Process Modelling and Adaptive Control Of A Metal Milling Process

David Drury

A dissertation submitted to the University of Bristol in accordance with the requirements of the degree of Doctor of Philosophy in the Faculty of Engineering, Department of Mechanical Engineering.

November 2005

Word Count: 45,000

Abstract

Within the aircraft industry, a large number of the aluminium components are milled entirely from single solid billets of metal. Current practice is to machine at conservative and constant feed-rates. This avoids damage to the workpiece and therefore reduces costly scrap. On-board monitoring systems on milling machines within the aerospace industry have introduced the possibility of continuously and adaptively varying the feed-rate on-line. It is proposed that this variation could be based on cutting power. Machining parameters, such as depth and width of cut, and tool efficiency, can vary considerably during the manufacture of a single component. It is therefore likely that an adaptive controller should be used. MCS is an adaptive controller algorithm that has been under development since 1990 Stoten *et al.*. It is known to have good properties with respect to robustness and controller performance and is therefore being investigated for use on the milling machines for aluminium components.

Substructuring is a dynamic testing technique that combines numerical models and physical tests into a single hybrid experiment. Briefly, it allows the engineer to "glue" a real component (in a lab) and a virtual component (implemented on a computer) together. These real and virtual components can then be tested dynamically and in real-time as if they were a single, complete component. Hence, substructuring provides the engineer with a framework to allow testing of individual components from entire structures at full scale without requiring the complete structure to be physically present. Accurate, hi-fidelity control is essential to the successful reproduction of structures using this technique.

Hence, the goal of the work presented in this thesis is the development and implementation of control strategies for use in the field of metal machining. A scheme that the controls the cutting force transmitted to aluminium workpieces by varying the feed-rate is developed. A requirement of this scheme is that it be simple to set up and implement whilst, at the same time, regulate the cutting power in the face of process parameter variations. The ability of the adaptive controller to meet these requirements is demonstrated both in simulation and on a pilot rig developed in the work. A model that relates peak cutting force to measured cutting power is developed for use with the aforementioned control scheme along with high-level control software implementing this scheme.

Further, controllers both fixed-gain and adaptive, are developed and tailored for use in the substructuring technique. The performance of the developed controllers is investigated both in simulation and in the laboratory on a linear large-scale hydraulic system. The advantages of using the adaptive controller scheme over a fixed-gain linear equivalent are presented. An example demonstrating the use of the substructuring technique in the field of machining is discussed, including a specific application.

ACKNOWLEDGEMENTS

The author would like to thank:

Dr John Morgan for providing me with the motivation, guidance and advice to write up the work for this thesis. Dr Simon Neild for his generous support and guidance, particularly in the field of substructuring. Prof. David P. Stoten and Dr. Andrew J. Harrison for providing me with a rich research environment and advice in the field of control. To Clive Wishart, Michael Lim, Andrew Hillis, Max Wallace and Anthony Croxford for all of the down to earth advice and for passing on their invaluable ability to solve complex problems using simple techniques.

Finally, I also wish to thank my family for their constant support and to Ruth Chapman for her help, advice and patience while I was preparing this dissertation. Without you all I would never have gotten this far.

This work was jointly funded by the University Postgraduate Scholarship Programme, BAE SYSTEMS, Consort Controls, the Seibel Award and by the European Commission under FUDIDCOEEF (Further Development in Dynamics and Control of Earthquake Engineering Facilities, Grant number ERB-FMGE-CT-980103) and NEFOREEE (New Fields of Research in Earthquake Engineering Experimentation, Grant number HPRI-CT-2001-50023). Thank you all for your support, both financial and academic.

AUTHOR'S DECLARATION

I declare that the work in this dissertation was carried out in accordance with the Regulations of the University of Bristol. The work is original except where indicated by special reference in the text and no part of the dissertation has been submitted for any other degree. Any views expressed in the dissertation are those of the author and in no way represent those of the University of Bristol. The dissertation has not been presented to any other University for examination either in the United Kingdom or overseas.

SIGNED:

David Drury

December 18, 2005

PUBLICATIONS

- Neild, S., Drury, D. and Stoten, D. P., An improved substructuring control strategy based on the adaptive minimal control synthesis control algorithm, *Proceedings of the I Mech E -Part I: Journal of Systems and Control Engineering*, 219:305–317, August 2005

- Neild, S. A., Stoten, D. P., Drury, D., and Wagg, D. J., Control issues relating to real-time substructuring, *Earthquake Engineering and Structural Dynamics*, 34:1171–1192, 2005

- Neild S. A., Drury D., Wagg D. J., Stoten D. P. and Crewe A. J., Implementing real time adaptive control methods for substructuring of large structures, *Third World Conference on Structural Control*, Como, Italy, 2:811 817, 2002

- Drury D., Stoten D. P., Wagg D. J. and Gomez E.G.. Advances in numerical experimental substructuring techniques using MCS control. *Twelfth European Conference on Earthquake Engineering, London*, paper 277:110, 2002

- Stoten D. P., Neild S. A., Wagg D. J. and Drury D., Dynamic substructuring via the adaptive MCS algorithm. *Third World Conference on Structural Control*, Como, Italy, 2:819825, 2002.

Contents

List of Figures

List of Tables

Notation

Chapters 2 and 4

Variable	Description	Units
a	(Radial) width of cut	mm
b	(Axial) depth of cut	mm
D	Diameter of cutting tool	mm
f	Feed per tooth	mm/tooth
$F_R(t)$	Radial cutting force	N
$F_T(t)$	Tangential cutting force	N
$h_c(\theta)$	Undeformed chip thickness at tool tip angle θ	mm
K_{mat}	Specific cutting pressure of workpiece	N/mm^2
L_c	Length of the cutting tool	mm
N_{flutes}	Number of cutting teeth on cutting tool	
N_r	Rotational speed of spindle	rev/min
P_{cut}	Total cutting power	kW
P_{spin}	Spindle spin power	kW
P_T	Total spindle power consumption	kW
r	Radius of cutting tool	mm
τ	Spindle torque	Nm
v	Workpiece/tool feed-rate	mm/min, mm/s
v_{surf}	Cutting tool/workpiece surface speed	m/s
θ	Angular position of tool tip	°
β	Cutting tool helix angle	°

Chapter 3

Variable	Description	Units
$e(t)$	Error signal	
$r(t)$	Reference signal	
$u(t)$	Control signal	
$x(t)$	Plant state vector	
$x_m(t)$	Reference model state vector	
K_{px}, K_{py}	Low-level proportional gains for x & y-axes	
K_{dx}, K_{dy}	Pilot rig LVDT gains for x & y-axes	
$K(t)$	MCS variable feedback gain	
$K_r(t)$	MCS variable feed-forward gain	
α, β	MCS adaptation weightings	
$y_e(t)$	Output error	
A, B	Real plant parameter matrices	
A_M, B_M	Model plant parameter matrices	
C_e	State output error matrix	

Chapter 6

Variable	Description	Units
a	Plant transfer function denominator coefficient	
a_m	Ref. model transfer function denominator coefficient	
b	Plant transfer function numerator coefficient	
b_m	Ref. model transfer function numerator coefficient	
c	Emulated system damping constant	Nm s^{-1}
C_e	State output error matrix	
F	Transfer system force	N
k	Emulated system spring constant	Nm^{-1}
k_d	Linear substructuring controller derivative gain	
k_{er}	Substructuring controller error feedback gain	
k_i	Linear substructuring controller integral gain	
k_p	Linear substructuring controller proportional gain	
$K(t)$	MCS variable feedback gain	
$K_e(t)$	Er-MCSI variable state error feedback gain	
$K_I(t)$	Er-MCSI variable integral state error feedback gain	
K_P	Inner-loop controller proportional gain	
$K_R(t)$	MCS variable feed-forward gain	
K_t	Displacement transducer gain	m/V
m	Mass present in physical substructure	kg
M	Mass of emulated system	kg
$r(t)$	Input excitation signal	
s	Laplace transform variable	
t	Time	s
t_s	Settling time	s
$u(t)$	Substructuring control signal	
$x(t)$	Physical substructure response	
$x_e(t)$	Model tracking error signal	
$x_m(t)$	Numerical substructure response	
$y(t)$	Emulated system response	
$y_e(t)$	Adaptive substructuring controller output error	
α, β	MCS adaptation weightings	
Δ	Algorithm sampling interval	s
λ	Eigenvalue	
ϕ	Phase lead/lag	rads
ω	Frequency	Hz
ξ	System states	
ξ_0	System state at stationary point	
ζ	Damping ratio	

Chapter 1

Introduction

SUMMARY: An overview of the themes of research with the main topics and objectives is given. The thesis structure is presented.

1.1 Introduction

In the early 1970s, metal machining within factories went through a revolution. The availability of affordable digital computer technology allowed the engineer to manipulate the parameters of machining on-line and automatically during a cut. Termed "Numerical Control" (or NC), parts were designed and turned into a series of numerical commands. These numerical commands were then entered manually into the automated machines and the part could then be reproduced accurately as many times as required. Since this time not much has changed. Computers, along with CAD/CAM packages, are now used to automatically generate the NC commands, allowing complex tool paths in up to 5 axes of motion to be produced. These commands are then downloaded to the machine directly by the computer allowing extremely complex components to be manufactured from single billets of material. This process is called "Computer Numerical Control" (CNC). The computer generated paths are optimised based on a vast database of cutting criterion. However, in the majority of cases the final cut itself remains an open-loop process with no parameter feedback. Thus, on-line alteration or refinement of the cutting path or parameters is not possible.

In this work it is proposed that it is now time to move the machining process on, with particular reference to an aluminium milling process.

Looking at and extending some of the process modelling work already carried out in this field, this work will set out to derive a fast method of deriving peak tooth loading on simple cutting tools from the electrical power being drawn by the cutting tool spindle. It is believed that cutting power is related primarily to cutting feed-rate and geometry. As a result, a controller strategy can be designed that modifies the feed-rate to allow the machine to satisfy a particular cutting power demand. The modified feed-rate will thus allow regulation of the peak tooth loading. Regulating peak tooth loading allows the machine operator to make maximum use of the available cutting power from the spindle without burning material or causing premature cutting tool failure. Due to the continuously varying nature of the geometry of cuts in a typical tool path, and therefore the plant, it is believed that an adaptive controller algorithm will be necessary.

A considerable amount of experience with such an algorithm called Minimal Control Synthesis (MCS), developed at the University of Bristol, highlights it as a possible candidate for such a method of control. One of the main strengths of the MCS algorithm a that it requires little knowledge of the controlled plant for implementation. This offers benefits in the field of machining as parameters usually required for reference models can often only be determined from empirical parameters that must be determined experimentally. For optimum stability during control, the order of the reference model and the plant (and hence the order of the controller adaptation mechanism) must be determined and matched. Once this has been achieved, successful implementation requires only a similar amount of programming code as for a PID controller.

As mentioned above, in a conventional set-up, the tool paths are pre-determined to ensure the geometrical quality of the final workpiece. Altering the feed-rate on-line will affect this geometrical quality. Software allowing multiple axis cuts to be performed to investigate this area is discussed and presented.

Due to the smaller forces involved during high speed machining, much smaller values of wall thickness in the final machined workpiece can be achieved. An example of this can be observed on the ribs on wing spars for Airbus aircraft. In this example, the wall thickness can be as small as 2 mm for a 80 mm high feature. Also, long, slender components such as turbine blades can be machined. However, it should be noted that, during machining, these components could be subject to a significant deflection due to the force imposed on the workpiece by the cutting tool.

In order to allow tests to be carried out to improve the accuracy of the cutting process when these conditions exist it is proposed that a new dynamic testing technique called *real-time substructuring* be used. The technique is still under development at the University of Bristol. Briefly, the real-time substructuring allows the components whose dynamic behaviour is understood and/or cannot be tested physically due to cost or practical reasons of implementation to be modelled in real-time within a computer. The parts that are less well understood or that are available for testing can then be tested as a physical experiment. Advanced control and numerical modelling techniques allow the two components to run side-by-side interacting with each other as if they were a single experiment.

A development of this substructuring technique using the MCS algorithm is constructed and presented. An implementation of this testing technique is then proposed that would allow testing of cutting techniques to improve the accuracy of cutting when forces imposed by the cutting tool are important such as those described above.

1.2 Background - Aluminium Aircraft Component Machining

When manufacturing some of the components used in their aircraft, one main difference still exists in the methods used by Boeing and Airbus. Boeing use techniques involving the assembly of prefabricated parts into final components, in much the same way that cars are made today. Within the Airbus range of aircraft, however, many of the major components are machined as single parts from a solid billet of metal, principally aluminium.

Looking at a specific case, British Aerospace machine their wing skins for the Airbus A300 Series from solid billets of aluminium alloy at their manufacturing plant in Chester (Figure 1.1). These billets can measure up to 30 metres in length and may weigh several tonnes, having a height corresponding to the highest dimension on the finished skin. As a result, the production of a typical skin make take 24 hours, and 75% percent of the billet will be machined away as swarf. It is vital, therefore, that as few of the final workpieces as possible are damaged in the machining process and scrapped.

Until recently the machining process was carried out "blind" and with the milling machines working at cutting speeds and feed-rates that were considered to be effective (maximising metal removal rates whilst minimising tool abuse) at the same time as being conservative. These conservative feed rates were generally chosen empirically, based on

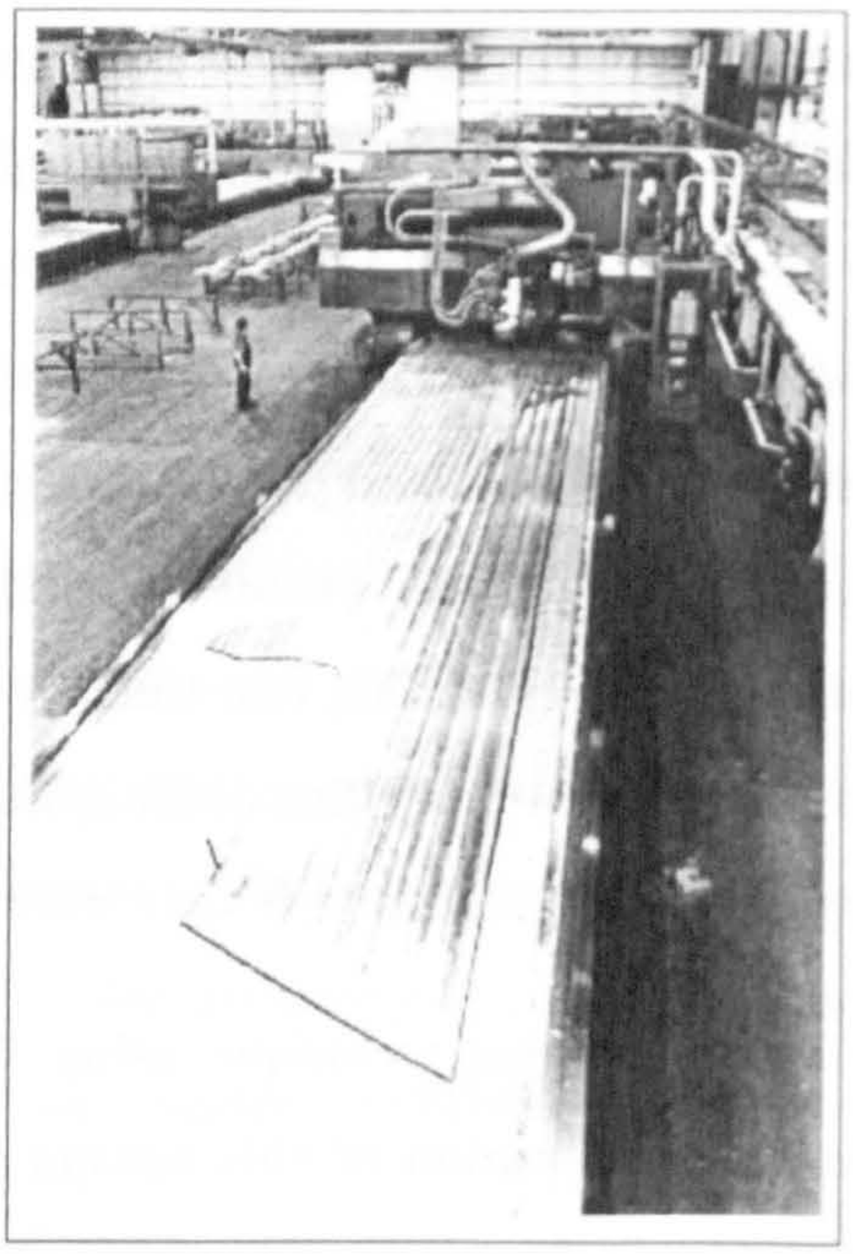

Figure 1.1: Large aerospace metal component milling machining

data supplied from the tool manufacturers that would ensure maximum tool-life and minimum chance of workpiece burn. All of the remaining parameters for a particular cut were determined within CAD packages off-line. The selected parameters were then loaded onto the milling machine's control computer which controlled the position of the milling head in a closed-loop manner. However, traditionally no other variables were either recorded or controlled on-line. Recent renovation of a series of five-axis milling machines used at BAe Airbus in Chester included the installation of an on-board monitoring and rudimentary control system. This system allows the continuous monitoring of parameters such as spindle torque, spindle speed (and therefore spindle power) and actual spindle running time amongst others, parameters measured for the first time on these machines.

The monitoring system brought to light the fact that the spindle was only running for around 6 hours per day, due to various factors including tool and workpiece change-overs. It was also believed that during these 6 hours the conservative feed-rates applied resulted in metal removal rates as low as 25% of the maximum values predicted for the spindle. Combined, these two factors show that there is potential to improve greatly both machining throughput and efficiency.

The main aim of the work in thesis is to explore ways of improving productivity during the process by:

- Improving throughput by continuously adjusting the feed-rate using both fixed gain and adaptive control methods.
- Modelling the cutting process.
- Developing a method of monitoring the variables of interest continuously during a cut.

1.3 Control Methods

The various types of control are presented here for clarity. This is mainly due to the ambiguous used of the term "Adaptive" when described feedback controllers in machining literature.

1.3.1 Open-Loop Operation

Open-loop operation, within a control engineering sense, is taken to mean a process in which no measurement is made of a particular 'output' variable and no attempt is therefore made to control or regulate it. Figure 1.2 shows a block diagram of an open-loop controller using a central heating system (without a thermostat) as an example.

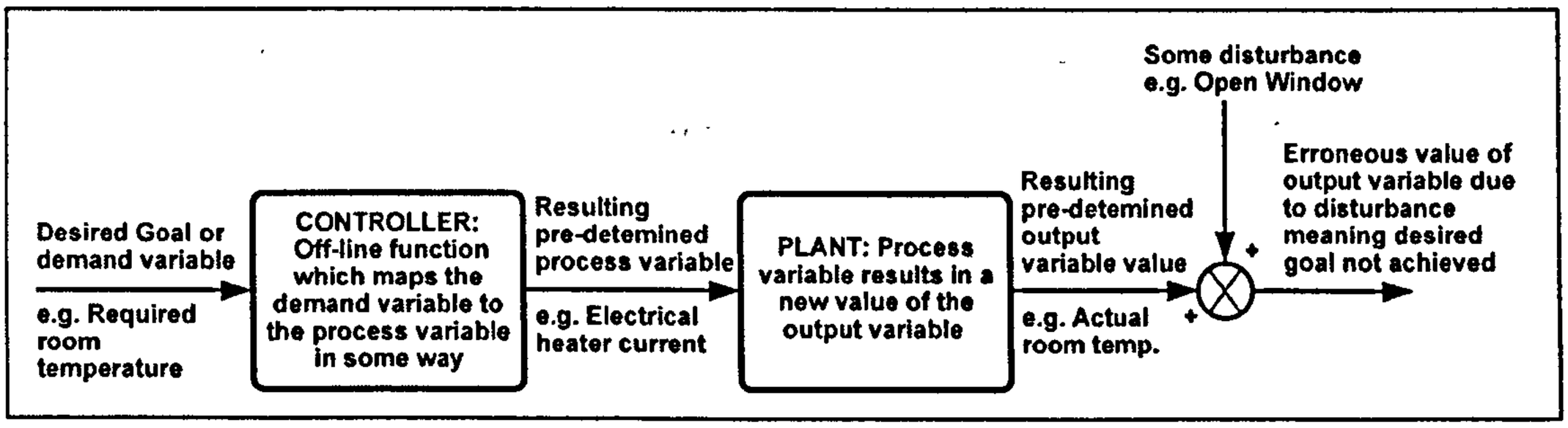

Figure 1.2: Open-loop control schematic

The majority of machining process until the late 1970s could be classified as either manual or automated (NC) open-loop control. That is to say that process variables were determined at the design stage of the cutting process and not measured or regulated during the cutting process itself. Whilst an argument could be made to say that closed-loop controllers are required for operation of automated NC machines these only maintain cutting paths and feed-rates based on a design determined before the actual cutting process was started.

1.3.2 Fixed-Gain Closed-Loop Operation

In fixed-gain closed-loop control a particular variable is measured, for example tool temperature, and another variable, such as spindle speed, altered via a fixed-gain algorithm such as a PID controller to achieve a desired goal with respect to the first variable (Figure 1.3). The majority of research into closed-loop control within the machining field

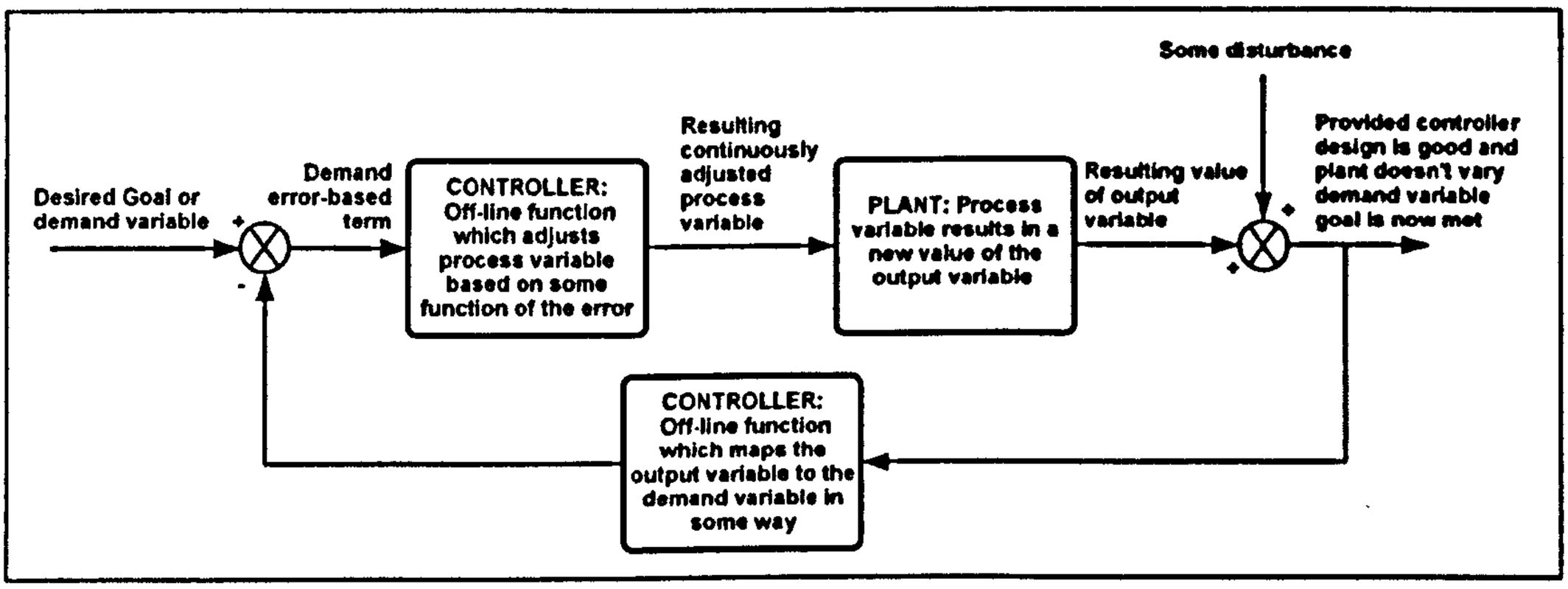

Figure 1.3: Closed-loop control schematic

during the 1980s and 1990s falls into this area. The techniques were named 'adaptive' because new the availability of small, fast processors allowed NC controllers to be used to change feed-rates, etc. during a cutting process and therefore 'adapt' cutting conditions to achieve a designed target such as tool temperature. However, this is not the conventionally accepted meaning of adaptive control and will be referred to as fixed-gain closed-loop control throughout this thesis.

1.3.3 Adaptive Closed-Loop Operation

Adaptive control, when used in the true sense of the term, takes fixed-gain techniques a step further. Using an pre-defined adaptation law, adaptive control varies the gains continuously over time within the control structure (Figure 1.4) to achieve a desired goal. This goal could be for example, to reduce closed-loop error and simultaneously minimize the energy in the plant. This continuous adaptation offers further advantages. Firstly, it allows the controller to compensate for changes in the plant being controlled. Secondly, it allows a controller with a linear structure to control a non-linear plant. This type of controller is particularly useful when unknown or unpredictable plant changes occur during

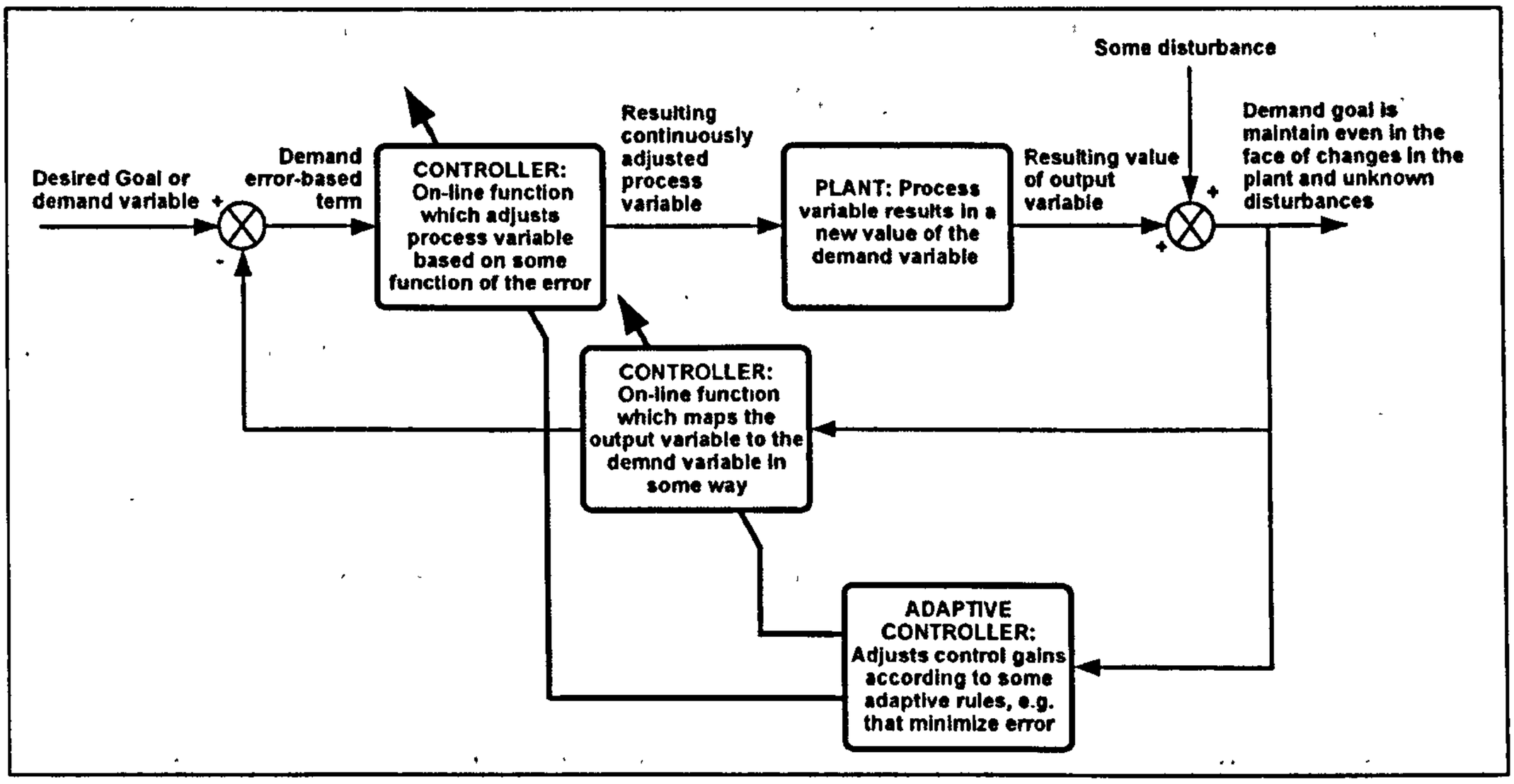

Figure 1.4: Adaptive closed-loop control schematic

a controlled process.

MCS Adaptive Control

MCS (Minimal Controller Synthesis) is an adaptive controller algorithm that has been under constant development at the University of Bristol since 1990 by Stoten *et al.* [7]. Derived from the MRAC family of controllers (section 3.1.2) and described further in section 3.2.1, the MCS controller delivers high robustness and good performance requiring no plant parameter estimations for successful implementation. It can reject high bandwidth disturbances as well as compensate for changes in the controlled plant parameters.

To date MCS has been successfully implemented in the a variety of situations including:

- Six axis (eight actuator) earthquake simulation rig
- Chaotic system control
- Servo-hydraulic control

1.4 Background - Substructuring Methods

Testing of systems or structures before construction or manufacture is essential for safe designs. Unfortunately, limits are often imposed on engineers in terms of cost, availabil-

ity of suitable testing equipment and time. Therefore, it is often not possible to test components/structures dynamically at full scale before manufacture.

Substructuring is a dynamic testing technique that aims to overcome these limits. Briefly, substructuring allows the engineer to "glue" a real component (in a lab) and a virtual component (implemented on a computer) together. These real and virtual components can then be tested dynamically and in real-time as if they were a single, complete component. Hence, substructuring provides the engineer with a framework to allow testing of individual components from entire structures at full scale without requiring the complete structure to be physically present.

Preliminary implementations of the technique have shown that accurate and fast control is essential to the successful reproduction of structures using this technique. Here the use of the MCS adaptive controller to achieve this is investigated using linear systems.

1.5 Research Objectives

The overall thesis object is to investigate the use of adaptive controllers in the field of metal machining. Given the points raised in this introduction the aims of the research presented here are:

- Examine the current opportunities for use of adaptive controllers within the field of aerospace machining.

- To develop an adaptive controller strategy that will vary the machining feed-rate to maintain a desired cutting power.

- To demonstrate that the aforementioned adaptive controller strategy achieves its goal in the face both of geometrical variations in the cut and in power demand changes.

- To develop a model that can be used in real-time to relate the mean cutting power to peak cutting force, the variable of interest to machining engineers.

- To develop a software platform that will allow testing of the strategies for multi-dimensional cuts.

- To investigate the use of adaptive controllers to improve the dynamic accuracy that can be achieved via the real-time substructuring technique.
- To tailor the basic adaptive controller algorithm to improve stability when used in the real-time substructuring technique.
- To demonstrate the potential of the real-time substructuring technique when applied to the field of metal machining.

1.6 Thesis Overview

The factors that drive the manufacturing process within the aerospace industry are presented in chapter 2. This chapter continues with a review of current aerospace machining technologies. Further, it focuses on the areas in which feedback control has been introduced and has played a key role in improving the quality of the final part and hence helped engineers to satisfy the drivers investigated at the beginning of this chapter.

The pilot study of adaptive control of a milling process to achieve constant cutting power is covered in chapter 3. A controller scheme is developed for use with both fixed-gain and adaptive controllers. A pilot rig facility is developed and used to implement the developed control strategy. The ability of the adaptive scheme to successfully achieve the required objective in the face of significant plant parameter variations is demonstrated. The performance of the adaptive scheme is compared to the fixed-gain scheme in experiments to demonstrate the advantages of the MCS algorithm.

The variable used for control in chapter 3 is cutting spindle electrical power. The variable of interest to manufacturing engineers is peak cutting tooth force. Hence, in chapter 4 an empirical model is developed that allows peak cutting force to be determined from cutting power and the geometry of the cut in real-time. The model is calibrated and validated using low-speed cutting experiments. A scheme for using the model in real-time is presented.

A software platform to define arbitrary cutting paths in multiple axes and control the pilot rig over these paths is presented and described in chapter 5.

A dynamics testing technique known as "real-time substructuring" and is introduced and discussed in chapter 6. The importance of good control in these experiments is

demonstrated. An application that would make use of the real-time adaptive substructuring technique to investigate the dynamics of machine tool-workpiece interaction during cutting is proposed. A linear scheme is developed alongside two adaptive schemes based on the MCS and Er-MCSI algorithms respectively. The performance of these schemes is tested and investigated on two individual test platforms, a multi-axis shaking table and and a custom-designed single degree-of-freedom hydraulic rig. The difficulties experienced by each of the controllers is examined and methods of compensation are proposed. Specifically,, a localised stability analysis is performed on the MCS implementation of substructuring and used to form three alternative controller schemes (MCSE, Alt-MCS and MCSmd) each of which out-perform the original MCS substructuring scheme proposed. Finally, the advantage of the adaptive scheme over linear, fixed-gain techniques is demonstrated experimentally.

The main conclusions drawn from the work are presented in chapter 7 along with suggestions for future work.

Chapter 2

Literature Review

SUMMARY: Factors driving the military and commercial sectors of the aerospace industry are presented. Methods currently used in the manufacture of aircraft components are investigated. Advances made in these methods, (both in industry and academia) are highlighted with particular reference to the role that feedback control plays in these areas.

2.1 Factors Driving Manufacturing Methods in the Aerospace Industry

The last 20 years has seen a large change in the aircraft/aerospace industry both in the commercial and military sectors. The major drivers in each market are presented.

2.1.1 Military Aircraft Drivers

The primary demand for combat military aircraft is a complex mix of performance criteria. These vary from the manoeuvrability and speed of the aircraft to ease of servicing and maintenance and further, successful execution of newer combat strategies. As military aircraft age, the advantage that a particular aircraft possesses will decrease as an enemy's familiarity with the aircraft and its capability improves. This would apparently lead to a self-perpetuating market.

Despite this, in the last 40 years the RAF has reduced its range of new aircraft from 27 different airframe types in the period from 1950 to 1959 down to 2 in the period from 1990 to 1999. Absolute numbers of aircraft within the RAF within a similar period have

fallen from 5,213 in 1954 to 1,013 in 1999 [8], a figure that has been roughly constant since the mid 1980's. This drop in number of military aircraft bought can be attributed to five main factors, each of which is summarised below.

The cost of individual military aircraft has spiralled with increased complexity of those aircraft. Augustine [1] demonstrated that, based on unit cost for military aircraft since the 1950, military aircraft cost increases fourfold in price every ten years. This is demonstrated along with the figures for civil and bomber aircraft in figure 2.1. The primary factor in this rise in unit cost is the increased proportion of the aircraft's weight being taken up by avionics. At the rate determined, Augustine hypothesised that by 2054 the US government's entire defence budget would only be able to purchase a single new aircraft and that would have to be shared by both the Navy and the Air Force.

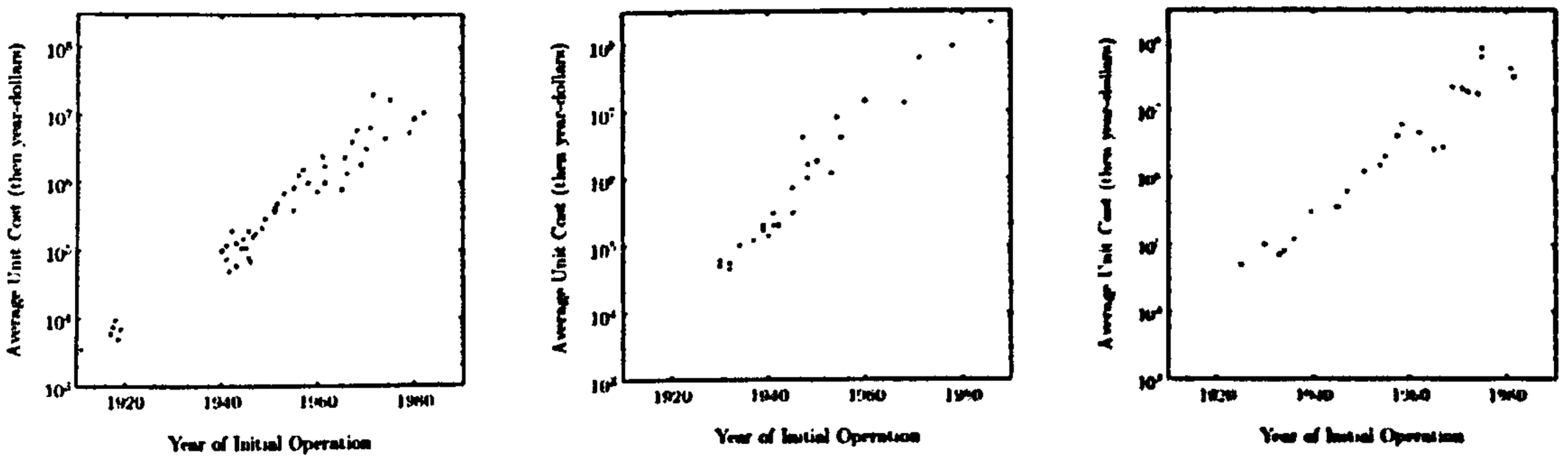

(a) Fighter aircraft (b) Bomber aircraft (c) Civil Aircraft

Figure 2.1: Unit cost of aircraft against year of initial operation, Source: [1]

UK defence spending has fallen by a significant amount since the end of the "cold war". When examined in real terms, the UK air defence equipment expenditure has fallen in the period 1986 to 1996 by more than 30% [8]. Whilst export of defence equipment may be an expanding market it is subject to a large degree of fluctuation based on the unit cost and need for the equipment as well as a good relationship between exporter and customer.

Military aircraft are being designed to fulfil the multi-role philosophy that is becoming common in all military vehicles. Multi-role aircraft the such as the Panavia Tornado are able to adapt to perform various tasks within a defence agency and have taken the place of aircraft specifically designed for a single role such as heavy bombers, fighters, etc. Coupled with the fact that a large number of missiles used in offensives can be launched from the ground and guided during flight reducing the need for large numbers of heavy bombers, it

is not difficult to see why the number of aircraft required is falling.

The life of the typical military airframe is becoming ever-longer. It is not uncommon for families of aircraft to have mid-life updates that involve some servicing of the airframe to extend service life and performance. These updates also include the replacing of avionics, bringing the aircraft up-to-date for a relatively low cost. The Panavia Tornado, F-16 and F-18 have all recently undergone or are currently undergoing mid-life updates. Beyond updates manufacturers often use older airframes in conjunction with newer technologies to produce new series of aircraft again at a low cost. The most recent addition to the Hercules family of aircraft, the Hercules C130-J, whose basic airframe has been around since the 1950s is a good example of this.

Traditionally governments would commission the design and manufacture of their military aircraft according to the cost-plus philosophy. Cost-plus indicates that the customer would pay total cost of the design and manufacture plus a profit margin to the supplier, upon delivery. This cost would be largely unknown to the buyer before delivery. Reduced government budgets for defence and an increased need to demonstrate transparency and good value for money to the public mean that projects must be broadly planned and costed. As a result, the majority of military aircraft projects are no longer planned and executed according this "cost-plus" philosophy commonly seen in the past (a move that has possibly saved the British tax payer £1b per year [8]). Longer production runs, iterative tendering and revision of contracts based on supplier's ability to achieve certain milestones provide better value for money to both customer and supplier.

A fairly typical example of a customer's need to control the final cost of a military aircraft project is demonstrated in the upgrade of the Nimrod aircraft to the MRA4. Following a request for information that was sent to 17 international aircraft manufacturers (and hence potential contractors), an "Invitation to Tender" for the contract to replace the ageing Nimrod MR2 was issued to British Aerospace (BAe), Lockheed-Martin, Loral and Dassault in 1995. The contract was awarded by the UK government to BAe and originally required the provision of 21 new Nimrod aircraft. The improved capabilities of the new Nimrod meant that fewer would be required than originally planned and, in 2001, the UK government reduced the number to be supplied to 18. Originally due to be in service by 2003, delays to the contract (possibly introduced due to BAe's decision to re-use the old Nimrod's airframe) the Nimrod aircraft is now planned to be in service by 2009, 6

years late. The UK government's response was to change the terms of the contract, now stipulating that only the first 3 research Nimrod would be paid for within the remit of the first contract. Provision of these first three fully functional aircraft would only then allow the UK government to negotiate the contract for the building of the remainder. In fact, in summer 2004 this contract was re-negotiated, reducing the final number of aircraft to only 12. The reduction in number was more than likely an agreement made both BAe and by the UK government to deliver a fleet of aircraft whilst keeping broadly to the original budget.

2.1.2 Commercial Aircraft Drivers

Direct-operating cost (combination of purchase price, operating and maintenance cost) is the main driver behind the purchase of new commercial aircraft. With the recent proliferation of low cost airlines introducing reduced fares and the reduced perception of the risk associated with flying, air travel is no longer the expensive "last resort" that it once was for the majority of commuters/tourists, etc. As with military aircraft, the unit cost of the average commercial aircraft is increasing exponentially with time (figure 2.1) whilst the expected cost to the end-user (air traveller) is decreasing [9].

Boeing has been dominant in the civil/commercial aircraft sector for a large part of the last half century, competing against many other companies for both commercial airliners as well as military transports. To remain competitive in this market (and in the military fighter/bomber market) the majority of these manufacturer's have consolidated or merged. The extent of this process can be seen in figure 2.2 which demonstrates the origins of the five main global aerospace airframe manufacturers. In the US, Boeing is the largest remaining commercial aircraft manufacturer with its main rival being AIRBUS. AIRBUS is a partnership between BAE SYSTEMS (itself evolved from 14 aerospace companies) and the European Aeronautic Defence and Space Company (EADS), a partnership or European aerospace companies. Since the introduction of its first family of aircraft in 1974 AIRBUS has grown to a point at which it provides more than 50% of the commercial airline market [10].

With two main competitors fighting for the majority of the market share, there is a strong desire to produce commercial aircraft more quickly and cheaply so that they yield more seat miles per gallon of fuel.

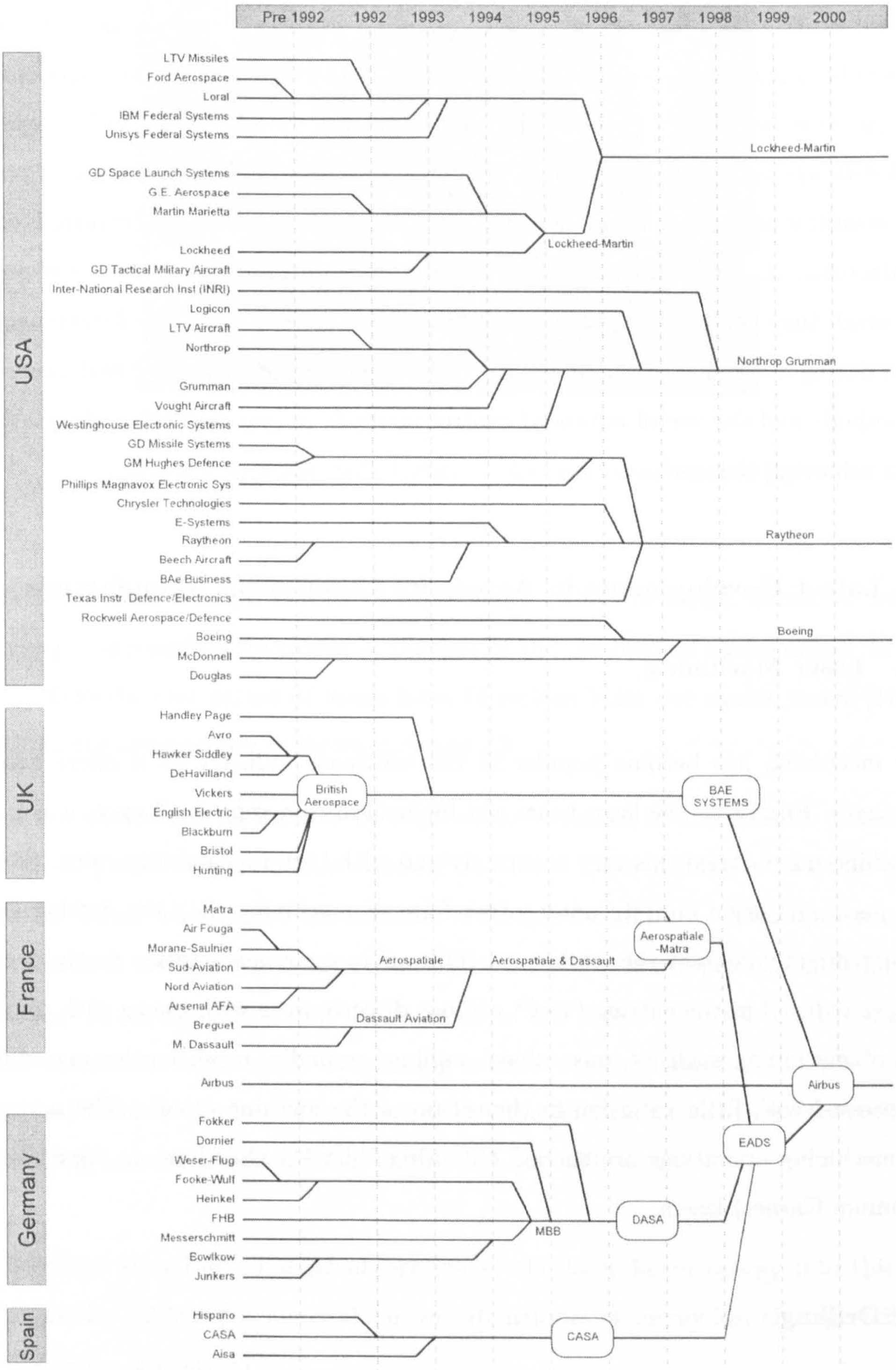

Figure 2.2: Consolidation of the USA and EU aerospace industries, Source: [2]

In summary, for both the military and commercial aerospace markets the increasing cost of aircraft can be largely attributed to the increased percentage weight of avionics included within the aircraft. Hence there is an increasing requirement on aircraft manufacturers in both markets to reduce not only the cost of airframe but also the direct operating cost associated with that airframe. The use of advanced manufacturing technologies combined with intelligent design can benefit both of these areas. With the increased precision and versatility of these new technologies parts for new airframes can be introduced and manufactured almost as easily as variations on existing airframes. If the degree of precision with which they can be manufactured could be increased then the use of interchangeable panels during maintenance would result in a lower operating cost. Improved manufacturing methods and the use of advanced control methods in manufacturing plays a definite role in achieving this goal.

2.2 Latest Developments in Aerospace Component Manufacture

2.2.1 Laser Machining

Laser machining has become popular in the aerospace industry as it offers two main advantages. Firstly, as the laser beam can be focused to a very small spot, it is possible to machine micro-structures very accurately and with high repeatability rates. Secondly, laser machining is an entirely non-contact form of machining, i.e. the cutting element does not directly contact the workpiece. This offers many advantages; firstly, recurrent costs are reduced as the cutting "tool" will not directly wear with use as with contacting forms of machining such as conventional milling; secondly, much harder materials can be processed with little variation in the set-up of the machine "tool". The majority of laser machining operations are carried out using Nd:YAG (Neodymium-doped Yttrium Aluminium Garnet) lasers.

Laser Drilling

One of the main areas of application of laser machining is in the drilling of effusion cooling holes in aero-engine components. Specific examples of these components include afterburner components, gas turbine blades and guide vanes. In all of these examples the component is subject to extreme temperatures (as high as 2000°C) and is hence often

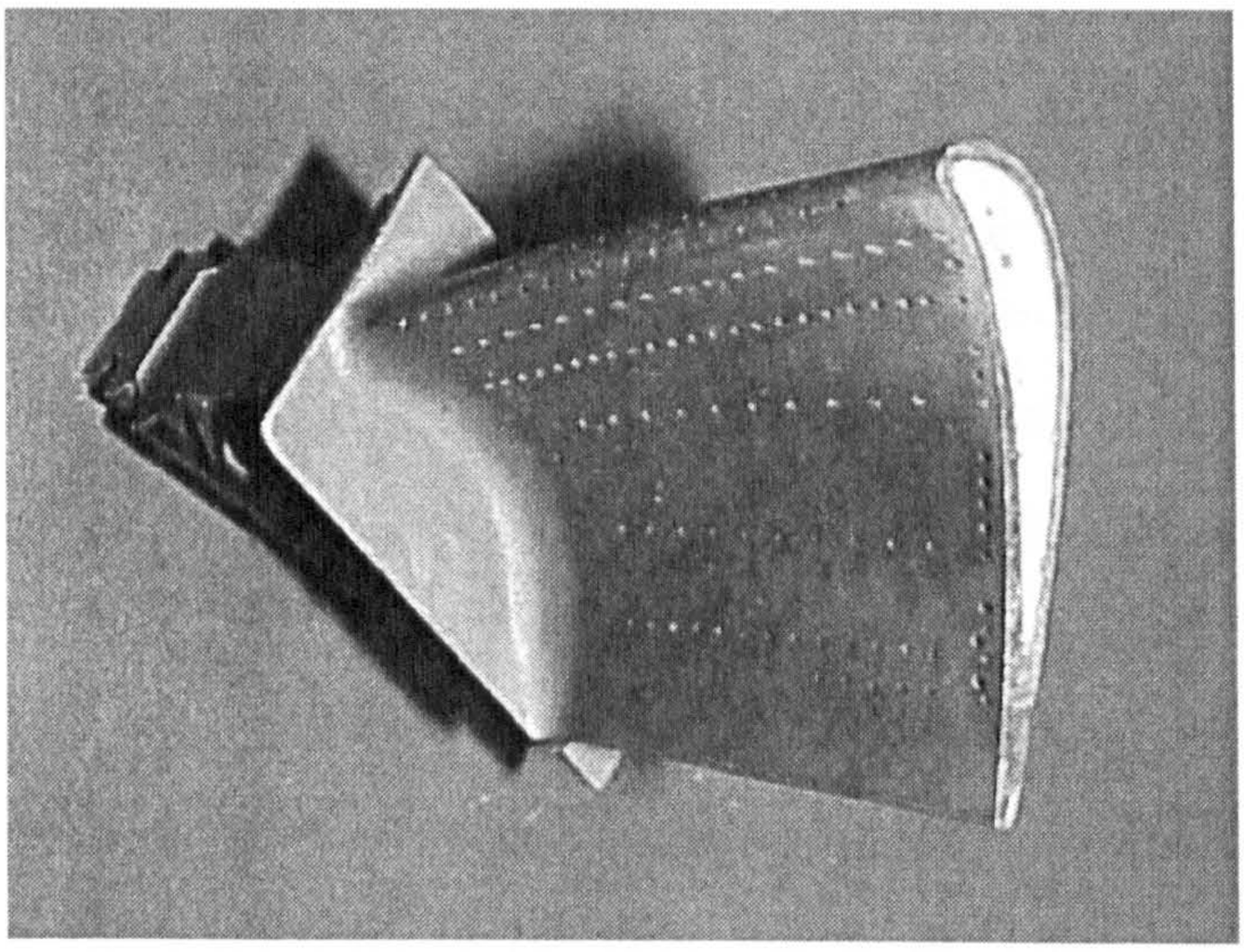

Figure 2.3: Laser drilled micro-holes in a turbine blade [3]

manufactured from a single crystal of super-alloys (alloys of nickel, cobalt or iron) to resist creep and maintain toughness in the face of the combustion environment. In order to cool efficiently, vast arrays of micro holes (4 million holes per square metre [11]) are drilled into the components as shown in figure 2.3.

It is not uncommon for holes to be required to be drilled at acute angles of incidence (down to 10°) with respect to the material's surface. Laser drilling allows this type of hole to be drilled where more conventional techniques would not. Two approaches are used when laser drilling depending on hole geometry. These are percussion drilling and trepanning. In percussion drilling the diameter of the hole to be drilled is the diameter of the focused laser beam spot. Trepanning is used when diameter of the hole required is large and involves the laser beam cutting out the hole rather than directly drilling it. Laser drilling broadly consists of four stages [12], [13]. These are:

- **Surface Heating** - Partial absorption of the laser beam energy into thin layer (typically <2-5nm) at material surface. Remainder of energy lost through reflection and beam scattering).

- **Surface Melting** - Given sufficient absorption of energy, surface heating leads to increased rate of energy absorption and melting of thin surface layer (with little conduction of heat into surrounding material)

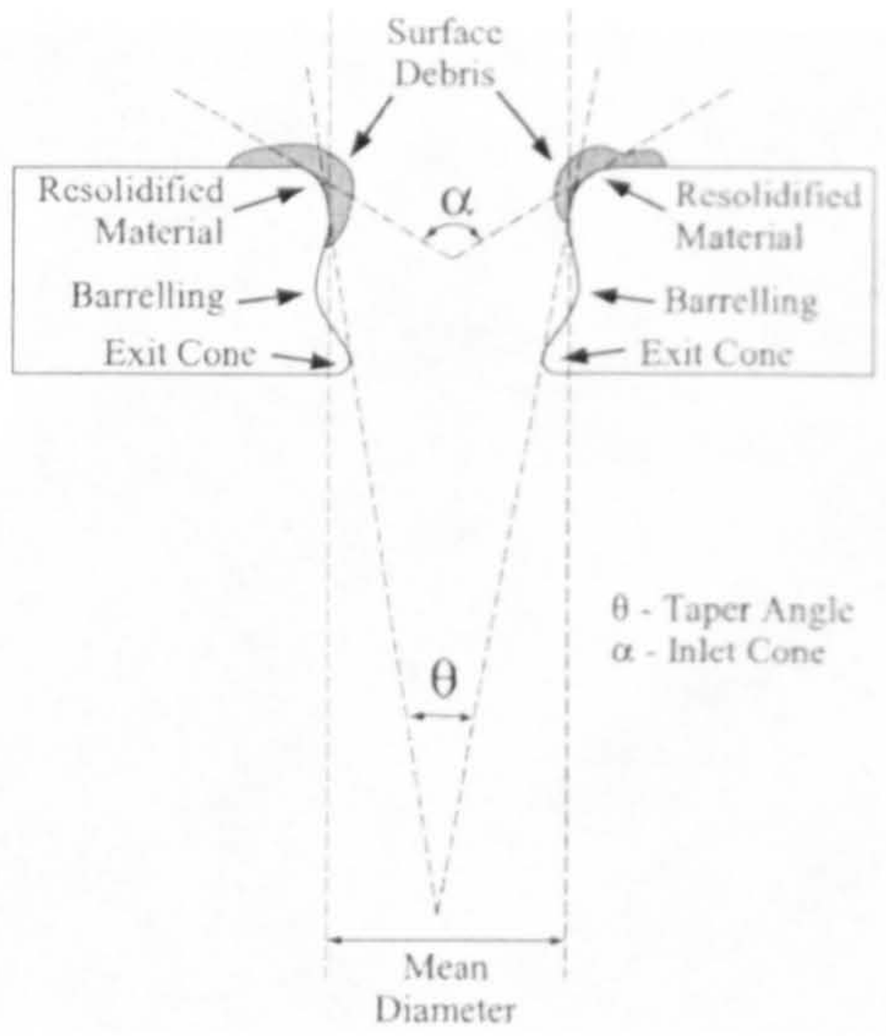

Figure 2.4: Parameters pertinent to laser drilled holes

- **Vaporisation** - Once the temperature of the molten material exceeds its boiling point it vaporises into the atmosphere and escapes from the hole area due to its vapour pressure being higher that the surrounding pressure.

- **Melt Ejection** - It is reported that two forms of melt ejection occur. Firstly, superheating of the material below the surface causes small vapour bubbles to form and burst ejecting molten material from the hole. Secondly, vaporisation of the material at the surface will result in a recoil momentum which has the effect of expelling molten material close to the surface out of the hole radially.

Despite its many advantages, laser drilling results in holes with imperfections shown in figure 2.4. Research has concentrated on improving the quality of holes produced when percussion drilling. The main body of research has focused on achieving this by manipulation of the process parameters such as laser type, pulse shape and duration, assist gas selection, etc. Problems seen when laser drilling metals include geometrical inaccuracies such as tapering and barrelling of holes as well as reduction in hole quality due to spattering of molten material leading to recast layers and micro-cracking.

Laser drilled hole taper, seen as an increase in hole diameter at the hole entrance point, decreases with hole depth and is mainly the result of material erosion at the mouth of the drilled hole due to the exiting vaporised/molten material. Barrelling in drilled holes is defined as a widening in hole diameter between hole entrance and exit. It is

caused by material erosion due to trapped energy as molten and/or vaporised material attempts to escape from the drilled hole. Various factorial studies have been performed that investigate the effects of combinations of laser drilling parameters [14–19] on hole quality. These studies demonstrated that the degree of taper in a laser drilled hole could be controlled by careful selection of the pulse profile of the laser machine tool, but that is extremely difficult to eliminate entirely. They also indicated that barrelling tends to increase with material thickness but can be reduced by the use of a lower pressure laser assist gas.

"Spatter" and "re-cast layer" are related and are primarily the result of molten material being ejected from the focal point of the laser (inside the hole) and subsequently re-adhering and re-solidifying on the hole. This re-solidifying process occurs either at the surface at the hole entry point of the drilled specimen (in the case of spatter) or to the interior sides of the hole (in the case of re-cast). Figure 2.5 shows a surface that has suffered particularly badly from spatter during a drilling operation. When laser drilled holes are used for cooling of aero-engine components both spatter and recast reduce the performance of the effusion cooling process and therefore need to be minimised. Studies have been conducted that examine the nature of the recast layers and spatter as well attempting to vary laser pulse lengths to minimise it with reasonable degrees of success [19–22]. However, the coupled nature of the effects of available laser parameters means that reduction in recast layers will affect hole geometry and drilling time. Low *et al.* [23] performed experiments that demonstrated the differing effect of two types of assist gas (inert gas and oxygen) would have on the amount and type of recast layers that would form.

More recent research has attempted to further improve general hole quality as well as applying the technology to new areas. Cooling holes in cavities are often required in situations where drilling through the back wall of the cavity would compromise the structure being drilled. The simplest method that allows these holes to be laser drilled uses lining materials within the cavity, such as PTFE. As more complex cavity geometries appear, lining materials become more difficult to apply and the use of some method of determining laser breakthrough becomes necessary. McNally *et al.* [13] summarise patented methods that have been developed to detect breakthrough when laser drilling including the use of optical, acoustic and magnetic flux sensors.

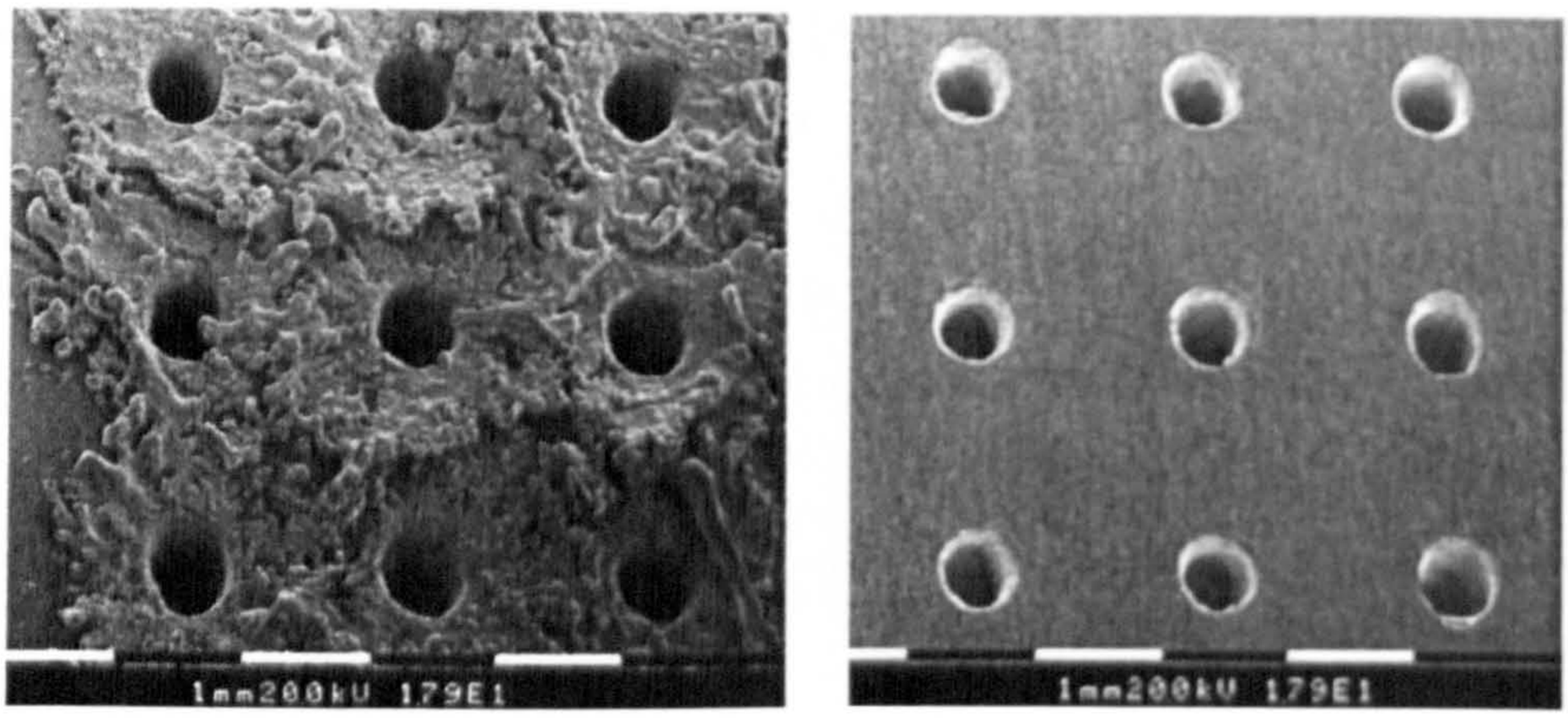

(a) with significant spatter (b) with no spatter

Figure 2.5: Laser drilled holes [21]

With engine temperatures increasing to improve efficiency there is a need for components to withstand these temperatures. It is becoming more common for manufacturers to coat components with a thermal barrier coating (TBC) to improve the resistance of the metal to such elevated temperatures. The most common mechanism of failure for these coatings is delamination from the host material. Cooling holes drilled into coated materials promotes the initiation of delamination at the holes. Corcoran *et al.* [24] examined the effects of pulse energy, width and shape as well as thermal barrier coating density and assist gas pressure on the final structure of a hole drilled into coated Rene80 substrate material. Most importantly it was found that the highest density TBC gave the minimum amount of coating delamination, with higher pressure assist gases yielding the lowest delamination, micro-cracking and recast layer thickness.

Future research in this area is also likely to include:

- Accurate blind drilling of holes of a predetermined depth
- Improvement of drilling times whilst retaining hole quality (given the number of holes to drilled in a single component this could drastically reduce cost to the end user)
- Drilling of holes at lower incidence angles to improve cooling characteristics.

2.2.2 Super-Plastic Forming with Diffusion Bonding (SPF/DB)

Superplasticity refers to the increased ductility seen in some metal alloys (such as Ti-6Al-4V) at high temperatures. Superplastic forming exploits this increased ductility to give stable strain values in the materials of the order 1000-2000%. This, on its own, allows panels to be formed with detail at a much greater depth than was possible with the more traditional cold and warm forming methods such as pressing. However due to the lower strain rates required (between 10^{-4} to $10^{-3}s^{-1}$) the forming process would be a time comsuming process and thus redundant for all but a few specific application areas. With only certain metal alloys originally exhibiting the superplastic behaviour a great deal of early reasearch attempted to identify the properties that led to a material being superplastically deformable. This led to the production of more useful alloys that could undergo superplastic deformation [25, 26]. However, it was not until the process of diffusion bonding was achieved that superplasticity became widely used.

Diffusion bonding is a process that is able to join parent materials (often of quite different composition) yielding a continuous join that retains the properties of the parent materials. To achieve a diffusion bond, good contact of the two parent surfaces is required. The parent materials are therefore cleaned thoroughly and pressure is applied to overcome microscopic roughness at the surface due to oxide films and any other substances. More complex joins can be used by applying a stop-off compound, using a silk screen process, to the areas at which a join is not required. As with superplasticity, diffusion bonding requires high temperatures (usually between 0.5 and 0.8 of the parent material melting point) and loading of the materials. Thus, diffusion bonding and superplastic forming can be combined into a single process that allows the production of hollow, and therefore light, complex parts. Components are generally formed from either two layer packs or, where higher rigidity is required, four layer packs. Using multiple-layers of material, treated at various points with stop-off compound, allows the engincer to first join and then superplastically form (by inflating the joined layers under pressure) the material to yield a hollow, honeycomb structure. An example of superplastic forming with diffusion bonding of a four layer pack in which a heat exchanger duct is joined and formed from a sandwich of profiled titanium alloy plate is shown in figure 2.6.

Currently the majority of components formed using SPF/DB are manufactured from titanium alloy as this is naturally superplastic at high temperatures and at controlled and

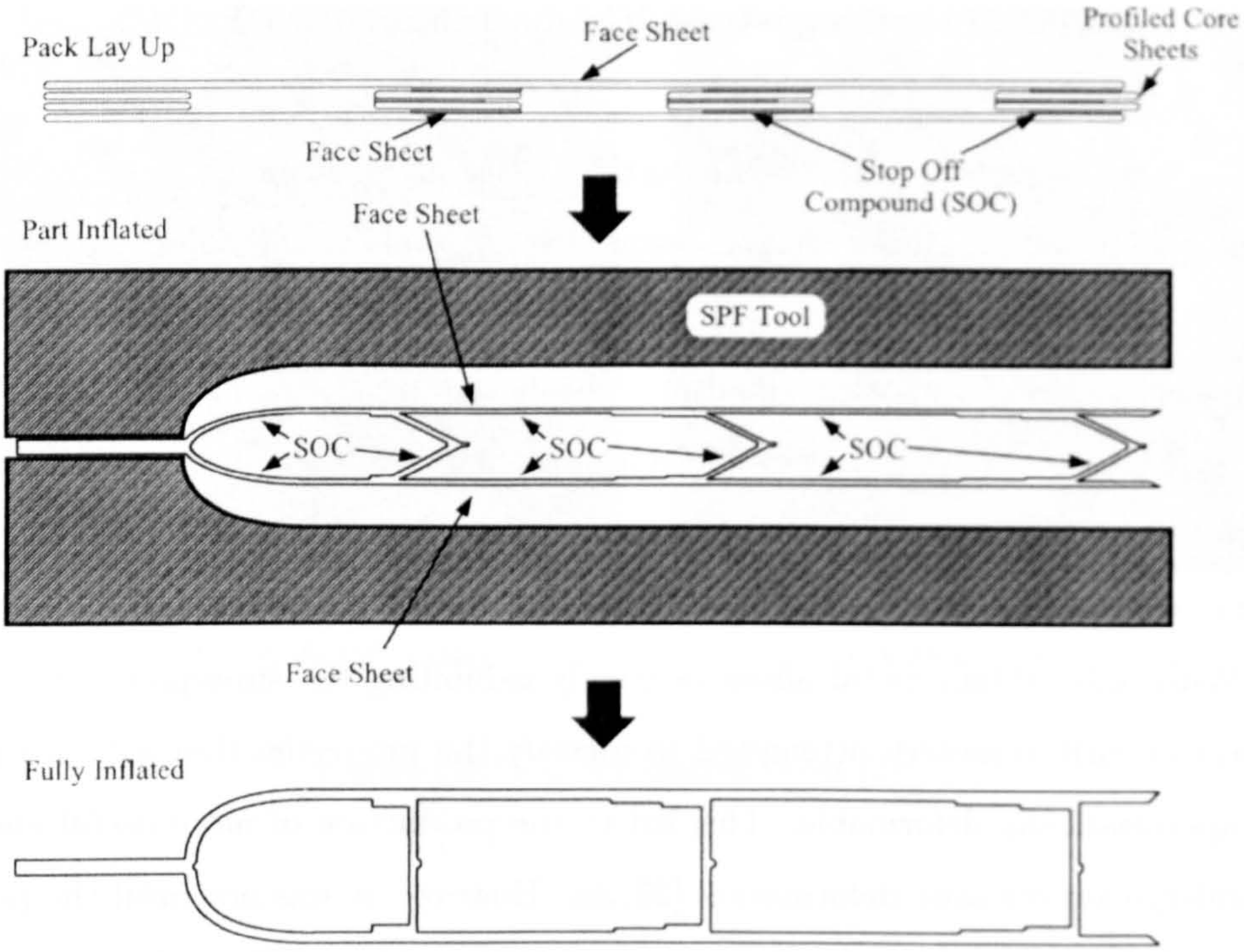

Figure 2.6: Schematic of diffusion bonding with superplastic forming of a hollow heat-exchanger duct from a four-layer pack [4]

moderate strain rates (10^{-5} to $10^{-3}s^{-1}$). A great deal of materials research is under way to broaden the range of materials that can be made to behave superplastically [27–29] as well as improving the strain rates achievable [30]. Also, research has been performed in an attempt to reduce the temperatures at which the SPF/DB process can occur yielding acceptable components [31, 32].

Initial attempts at SPF/DB used matched metal tooling to apply the pressure required for diffusion bonding to occur whilst simultaneously superplastically deforming the material. For good quality diffusion bonds to form, the tolerance on the thickness of the metals sheets used in the pack to form the component would have to be very small. In practice this level of tolerance was difficult to achieve which led to poor bonding quality especially if large areas of bonding were required [33]. Diffusion bond defects had also been found in areas at which contact between the plates in the pack was only made in the latter stages of the process [33–35], due to the bonding surfaces contacting during the superplastic forming stage. A key point of interest in superplastic forming is that of uneven thickness of the final component. This has been observed and investigated in a number of applications [33, 34, 36–38] with various methods of control proposed [39–41]. These

methods include variation of the thickness of the initial plates to account for thinning in forming as well as dies that move during the superplastic forming process to prevent thinning. An improvement in the success rate of the diffusion bonding process was seen when advanced, but relatively cheap, ceramic dies with induction heating were used to give fast heating of the material to be formed. This success rate was further improved when the diffusion bonding process was carried out before the superplastic forming phase using an inert gas rather than accurately machined metal tooling to apply the bonding pressure. Further, advances in finite element modelling [33] combined with a chemical milling process resulted in components with a much optimised geometry and hence weight and cost savings. General improvements in simulation by finite element analysis of the superplastic forming with diffusion bonding process have also been pursued [38,41–45] with a view to optimising the process and improving uniform thickness of formed components.

2.2.3 Electrical Discharge Machining (EDM)

Electrical Discharge Machining is a non-conventional machining process that makes use of the erosive properties when a spark is discharged across electrodes. One of the main benefits of EDM is that it is not affected by the hardness of the workpiece being cut. As a result it is used for applications that require forming of components that are either too hard be conventionally machined or cannot be machined for other reasons (e.g. ceramics). In EDM the workpiece to be machined is immersed in a dielectric fluid and connected into an electrical circuit. The electrode (or "cutting tool") is connected in the circuit as the opposite pole to the workpiece. Whether the workpiece forms the cathode or anode is decided by the engineer, based on relative rates of material erosion, with the workpiece requiring the higher rate of erosion. Kerosene is most often chosen as the dielectric fluid as it breaks down to yield relatively inert gases.

A pulsed d.c. current sufficient to generate a spark between the electrode and the workpiece is passed through the circuit. The effect of this spark is that it generates an plasma flume between the electrode and the workpiece yielding an instantaneous temperature of up to 20,000°, melting material at both the electrode and the workpiece. The pulsing nature of the supplying current means that each pulse will result in the spark and the plasma channel breaking down. This results in the molten material being ejected into the surrounding dielectric material. As with laser drilling (section 2.2.1) the molten material

leaves the workpiece before any significant amount of heat can be absorbed into it meaning that residual stresses in the final component are minimised. EDM is implemented in one of two forms as defined by the electrode used.

Die-Sinking EDM

The first of these is the most traditional form used, die-sinking EDM. In die-sinking EDM a profiled electrode is used as the cutting or forming tool. In most implementations of die-sinking EDM the profile of the electrode is the negative of the required form in the final workpiece. In its simplest form this could be a ball-ended cylinder (for cutting holes) with more complex forms possible. The electrode is mounted on a track that can be moved vertically and hence sunk into the workpiece, maintaining the correct electrode/workpiece gap required to form a spark as the EDM process proceeds, hence the name, die-sinking EDM. The concept is demonstrated schematically in figure 2.7

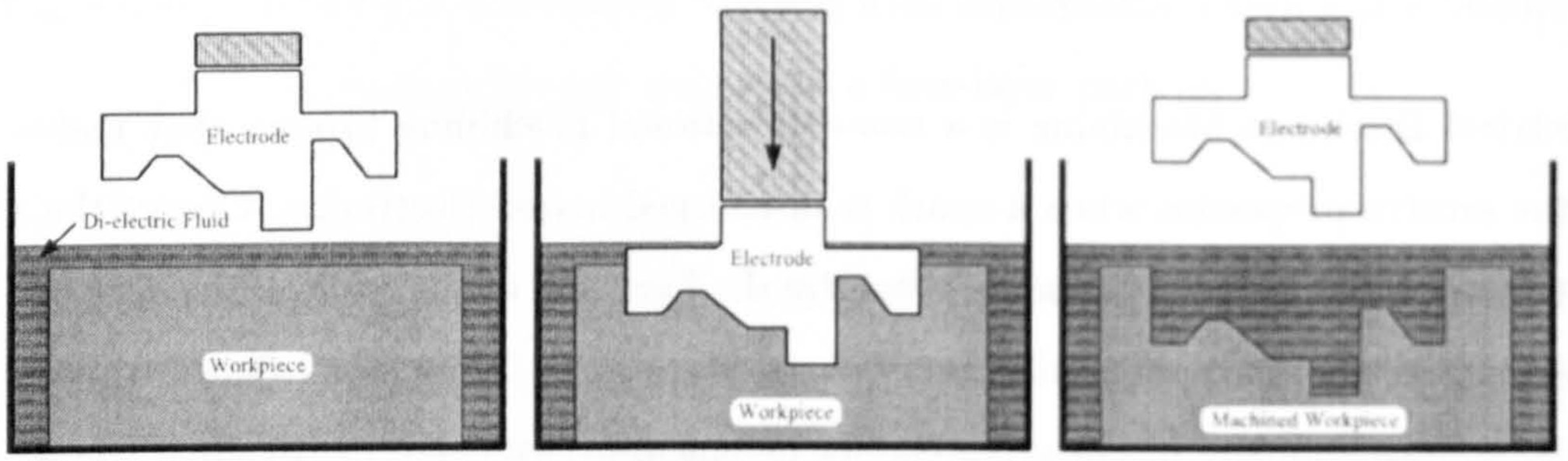

(a) Before EDM (b) During EDM (c) After EDM

Figure 2.7: Schematic of die-sinking EDM

Periodically the electrode is moved out of the workpiece to allow flushing of eroded discharge material. Traditionally the track on which the electrode was mounted would have been controlled using a ball-screw mechanisms. The slow speeds at which these systems operated meant that the eroded material in the dielectric fluid had to be manually flushed to prevent it causing unwanted discharge. More recent implementations of die-sinking EDM use higher speed and bandwidth linear motor drives. Using these drives the electrode can be made to "jump" extremely quickly in and out of the volume of erosion. Kaneko *et al.* [46] found that these modern drives reduced total cutting time and improved the quality of surface finish due to complete expulsion of eroded debris. Cetin *et al.* [47]

investigated the effect of the duration and shape of this "jumping" motion with a view to optimising it for improved machining speed and depth.

Various models of the EDM process exist and take one of two principle approaches. Firstly, there are models which focus on the fundamental thermo-electrical aspects. DiBitonto *et al.* 48] derived two models based on this principle. These models aimed to explain the process and led on to successful parameter selection when using EDM. The first model [5] was based on a cathode erosion model and defined two main useful parameters, optimum pulse time factor, g, and erodability, j. These were predicted with a reasonable degree of accuracy for a single electrode/workpiece combination over a range of peak electric currents and time between sparks. The second model examined the erosion of the anode pole [48] and made suggestions for parameter optimisation. For shorter pulse times (less than 5 μs), Singh *et al.* [49], predicted that the primary mechanism for material erosion was not melting as there was not sufficient time for heat to be conducted directly into the workpiece. Instead he developed a model that demonstrated that, for such short pulse times, the electrostatic force exerted on the surface of the electrode exceeded the yield strength of the cathode and was the main mechanism for material removal. Quantitative theoretical predictions of the volume of material removed via this mechanism were also made.

Other research has attempted to quantitively analyse the material removal rate during EDM by considering the process purely from a geometrical point of view [50, 51]. Considering the surface of the workpiece as a mesh of discrete points these models assume that the erosion always takes place at the point where the distance between the electrode and the workpiece is smallest. Earlier models assumed that the crater formed on the workpiece surface after a spark was a cube [50,52]. Improved surface finish estimates were obtained when the crater was assumed to be conical in shape [51]. The aim of this research was mainly to understand and control/improve the surface finish of components formed by EDM. As with many machining processes, optimization of variables to improve metal removal rate and surface finish has been attempted [53].

Wire EDM

In wire-cut EDM (WEDM) a wire is continuously fed between two spools along its axis and acts as the electrode which is fed through the workpiece. A schematic of this form of

EDM is shown in figure 2.8. In the majority of Wire-EDM processes the the dielectric fluid (usually de-ionised water) is continuously supplied at a moderate pressure which as serves to continuously flush the eroded material from the machining zone. The relative motion between the workpiece and the electrode is the continuously adjusted allowing complex parts to be "cut out" from billets of material with varying degrees of taper possible during the cut. Wire-cut EDM is particularly well suited to applications which require accurate machining of high strength and temperature resistive (HSTR) materials.

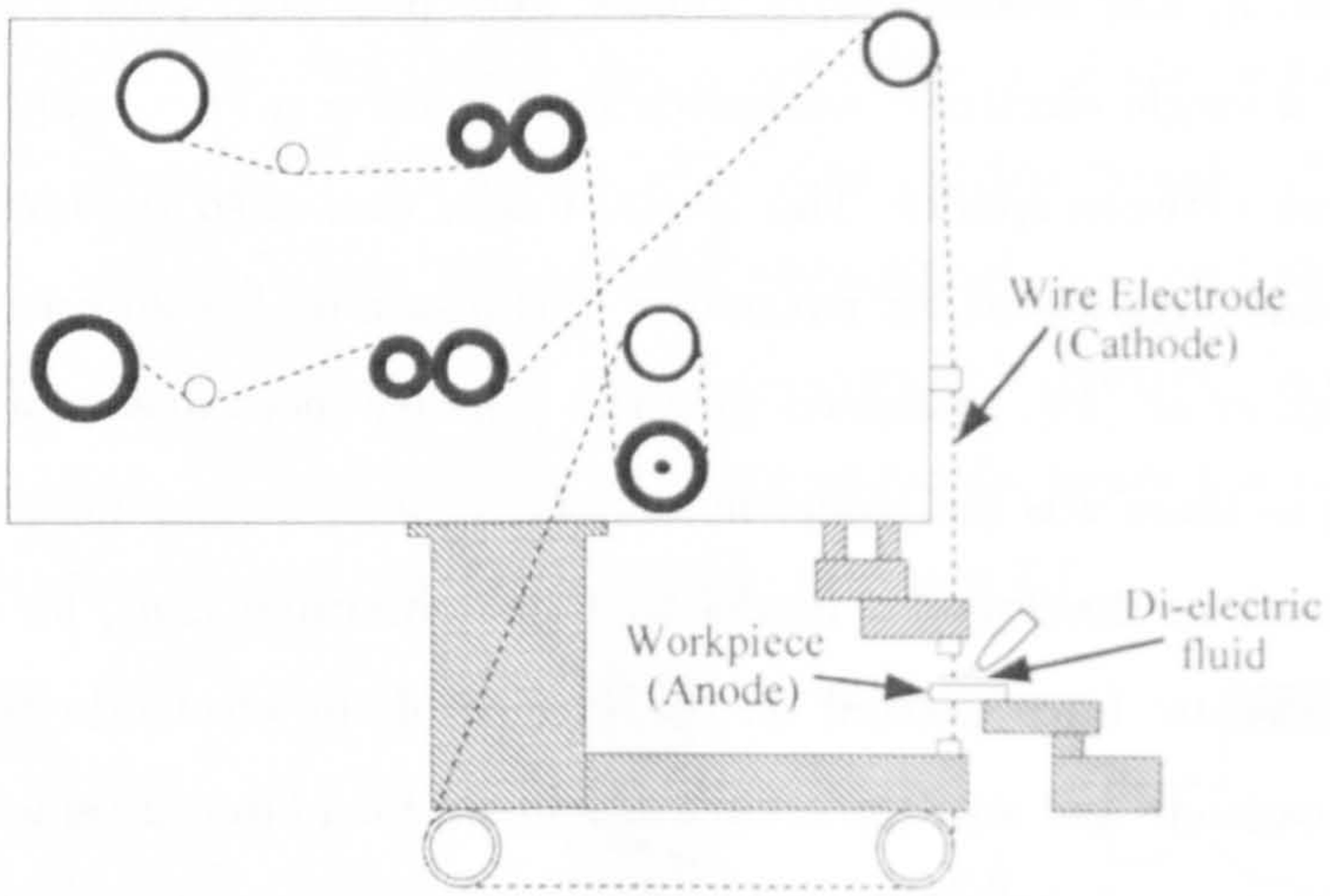

Figure 2.8: Schematic of wire-EDM [5]

A well-known problem with wire-EDM that has been the subject of much investigation [54–56] without resolution is the trade-off that is seen between material removal rate and surface finish. A large number of coupled process variables (including wire feed rate, electric pulse shape/duration and pulse current/voltages) affect the quality and speed of cut. As a result many researchers [57–59] have performed multi-variable analyses (such as factorial, Taguchi and neural-network studies) of the process in order to optimise these variables, ensuring the best compromise between surface integrity and machining speed. An often used compromise is to perform a fast rough cut followed by one or more higher surface quality trim cuts. As a result, it has been suggested [57] that WEDM cutting speeds have doubled every four years with quality of surface finish improving by a factor of fifteen in the same period.

Some research has extended this study looking looking to overcome the geometrical inaccuracies that can be caused by inaccurate positioning of the EDM wire due to wire

vibration and static-deflection (or wire-lag) [57,59–64]. Wire deflection occurs mainly due to a reaction force on the wire seen due to evaporation and movement of the dielectric fluid during electrical discharge. Alongside wire vibration, wire-breakage during EDM is a common cause of low metal removals rates and inaccuracy. It is believed that wire breakage is caused as a result of local temperature increases in the wire due to concentration of electrical discharges at a particular point in the wire. Also, changes in height of the workpiece leads to an corresponding increase in the thermal density of the wire which can cause breakage. Much work exists that attempts to predict and in some cases control the onset of wire breakage on-line [65–68] based on adaptive control [69,70] and fuzzy techniques [71] with varying degrees of success.

A recent body of research [72,73] has experimented with a technique called dry wire-EDM that reduces these forces and hence the vibration seen in the wire electrode. A much reduced gap between the electrode and workpiece can be used which increases the accuracy of the cut. Other advantages of dry-WEDM include reduced corrosion, as no dielectric is present, and reduced electrode wear. In contrast, the use of applying minute amplitude ultrasonic vibrations to the wire electrode results in multiple channel discharges resulting in a higher metal removal rate and improved surface finish [74–77].

Recent work has used the EDM process to form conductive ceramics such as Silicon Carbide in both die-sinking and wire-EDM [78–82]. This has been further extended by doping non-conductive ceramics with conductive materials allow them to be machined by EDM [83,84].

2.2.4 High-Speed Machining

Milling is one of the simplest and most conventional processes used to remove metal to form components of a pre-defined shape. Although the theory of high speed machining (HSM) has been under development since the beginning of the century, it is only since the end of the 1980s that the process has been practically possible. This is primarily due to the improved design of spindle bearings and availability of cutting tool coatings improving wear resistance. Direct benefits seen as a result of using HSM on the factory floor include a reduction in the number of different cutting tools required due to the higher volume removal rates possible from the same tools that perform some of the more precise cuts. In changing the manufacturing method from conventional to high-speed machining Boeing

$M.D.C. = \frac{\text{Dominant Natural Frequency (Hz)}}{\text{Tooth Passing Frequency (Hz)}}$	Machining Classification
$M.D.C. < \frac{1}{5}$	Low speed
$\frac{1}{5} < M.D.C. < \frac{1}{4}$	Midrange speed
$\frac{1}{4} < M.D.C. < 2$	High speed
$M.D.C. > 2$	Ultra speed

Table 2.1: Machining speed classification

reduced the manufacture time for a blocker door hinge from 16 hours to 2 hours [85]. A significant benefit of HSM, certainly with the softer materials, is that the majority of the heat produced during the cut is taken away from the workpiece in the chip or swarf before it can heat the remaining workpiece. This leads to a reduction (but not total elimination) of unwanted deformation in the workpiece due to residual stresses and thermal effects. As the chip loading is much lower during an HSM cut it is possible to use HSM to machine extremely thin walled components. Also, the lower chip loading results in a longer cutting tool life due to reduced wear. Surface finish is much improved when using HSM in comparison to conventional cutting methods, this reduces the amount of post-processing that component has to go through thus increasing efficiency.

Classification of a machining operation as high-speed-machining is dependent upon both the spindle speed, N_r, and the diameter of the cutting tool, D. Spindle manufacturers use a DN number (equation 2.1) to determine whether or not a spindle's performance will be classed as 'high-speed'.

$$\text{DN Number} = N_r \times D_{spindle} \tag{2.1}$$

where $D_{spindle}$ is the diameter of the machining spindle measured in millimetres and N_r is the spindle speed (rev/min). Another method used to determine whether or not a machining operation is classed as high-speed involves examination of the dynamics of the tool and spindle. Specifically the dominant natural frequency of vibration of the tool/spindle combination is compared to the tooth-passing frequency of that operation with classifications being made as shown in table 2.2.4 [86].

Within the aerospace industry HSM applications can be broadly categorised into three areas. Firstly, those in which large diameter face milling tools are used at conventional rotational speeds (1000-5000 rev/min) for finishing large areas such as finishing operations

in wing skin manufacture for commercial aircraft. Secondly, in applications where there is a high percentage metal removal (in the order of 90%). Here the cutting tools have a smaller diameter (10-20mm) but a higher spindle speed (10,000-30,000 rev/min). This is often the case in production of complex components in the aerospace industry made from solid billets of aluminium. Finally, the case in which much smaller cutting tool diameters are used (1-5mm) in conjunction with higher rotational spindle speeds again (50,000 rev/min and above).

Advances in both the machines themselves (introduction of fast response linear drive and stiff, high speed spindles) and the computer based tools for creating complex tool paths have more recently resulted in the latest generation of 5-axis machining centres. The flexibility offered by these machines combined with the ever-increasing precision available has led to high speed machining (specifically milling) becoming the favoured process for the manufacture of components made from softer metals such as aluminium in the aerospace industry. Research in the field of high-speed milling falls mainly into one of the following areas:

- Improved precision of the high speed machining process
- On-line Process Parameter Measurement and Control
- Cutting tool technologies
- HSM of hard materials

2.3 Research in the Field of High-Speed Machining

The typical hierarchical path followed from part design to manufacture using a high-speed machine tool is shown in figure 2.9. At the highest level, are the CAD/CAM systems which are used to generate the demands sent to the machine tool. These are shown as the input arrows to level 3 and traditionally consisted of just a series of pre-programmed position demands. More recently, the demands on the CNC system have increased to incorporate continuously variable feed, force and power demands amongst other variables.

The demands made by the CAD/CAM system are fed into the components shown in level 3 blocks. These are the adaptive (or closed-loop) controllers (covered in section 2.3.4 and the error compensation (section 2.3.2). These level 3 systems aim to ensure that

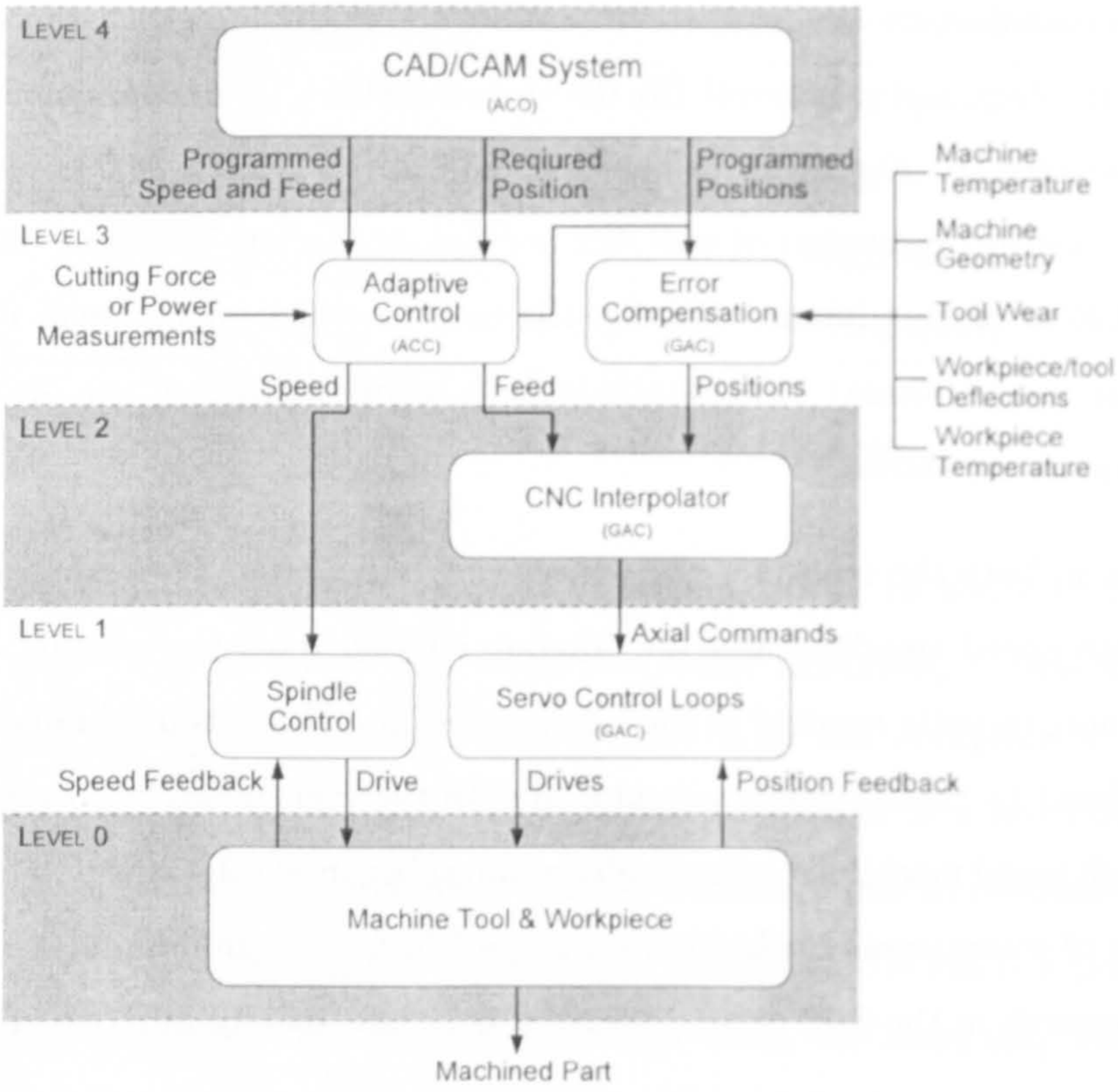

Figure 2.9: Hierarchical structure of CNC machining process [6]

demands sent to the systems at a lower level result in an accurate part being produced in the minimum time.

At the lowest level (referred to here as Level 0) is the machine tool. The machine tool is composed of a mixture of linear, prismatic and rotation drives/joints, as well as the cutting tool which is normally (but not always) mounted on a rotating spindle. Currently, most drives are ball-screw based and use gearing mechanisms to provide the required torque/speed combinations. These drives introduce a large amount of non-linearity in the form of friction, backlash and low fundamental frequency of vibration. As a result, they are being replaced on the workshop floor by direct-drive servo motors which reduce the aforementioned non-linearities. Each of these components will have its own associated dedicated hardware controller implementing basic control and safety features, these are contained in level 1. The accurate co-ordinated control of these servo-systems under variable loads has been the subject of significant research and is summarised in section 2.3.2

For improved precision (and to provide a interface between the software-based com-

ponents and the hardware-based components) interpolators (level 2) are used which take the demands generated by the higher-level systems and interpolate them (either linearly or as some spline function). This interpolation is carried out at a rate that the machine tool can accept to produce components to a specific quality/tolerance level.

2.3.1 Feedback Control and Machining

Control within the field of metal-machining has been of interest to engineers since the late 1970's when NC facilities began to appear on the shop floor. The main body of research in control applied to machining falls into three areas:

- Adaptive control with optimisation, ACO.
- Adaptive control with constraints, ACC.
- Geometric adaptive control, GAC.

In fact, the majority of the research in these areas used conventional, fixed gain techniques with truly adaptive controllers only making an appearance more recently. Therefore in this thesis they shall also be referred to as:

- Closed-loop control with optimisation, CLCO.
- Closed-loop control with constraints, CLCC.
- Geometric closed-loop control, GCLC.

The first of these areas, CLCO, involves the construction of a performance index that relates a cost function (metal removal rate, tool wear) to the process variables used in the machining operation [87–92]. Conditions upon the process variables that maximise the performance are then calculated and varied on-line using a controller strategy to obtain the best performance from the cutting machine.

The main drawback for this type of control is the direct measurement of tool wear on-line. Methods are only now being developed using neural network techniques that allow tool wear to be monitored and these are still in their experimental stages. Most recently, Yang *et al.* [93] implemented a controller that used neural networks to optimise tool wear based on an on-line estimator. Models exist that predict tool wear as functions of cutting tool temperature, rate of change of torque and metal removal rate but they fail to account

for workpiece properties and the nature of the active cutting process. Off-line experiments can be performed in order to obtain good estimates of these missing parameters. However, relating each cutting tool/workpiece combination in this way has the potential of removing any cost benefit that improvement in the machining process would lead to.

Closed-loop control with constraint, CLCC, is the most common form of control used in machining. Here, allowable limits for cost-effective manufacturing, such as an optimum peak torque, are identified as well as either one or a combination of process variables that allow its regulation, such as feed-rate. A controller strategy can then be designed that attempts to maximize the parameter that is constrained using the designated process variable.

Using CLCC, problems arise with the selection of the controller algorithm used to regulate the system. In order to function with a traditional linear controller, the non-controlled process variables would have to remain within tight constraints so as to keep the plant linear. Any large deviation in width or depth of cut as well as spindle speed would result in an erroneous choice of feed-rate by the controller possibly leading to premature tool wear. More recently these problems have been overcome via the use of self-tuning (or truly adaptive) controllers. It is this form of controller that is to be investigated in the following chapter of this thesis.

Geometric closed-loop control (GCLC), as its name suggests, is concerned with the dimensional aspect of machining and consequently used mainly in finishing operations. It is a subset of closed-loop control with constraint (CLCC) with a different goal. Here the aim of the control is not to maximise the efficiency of the process but instead to improve the quality of the finished surface and geometrical accuracy by varying the process variables. Using models that relate the deflection of the cutting tool to cutting force, nose radius effects it is possible to design a controller that will optimise the surface finish/roughness given the cutting conditions.

2.3.2 Improved Precision of the High Speed Machining Process

Improving the precision of HSM in the aerospace industry offers considerable benefits. Currently individual components are assembled in large jigs as generally they don't fit or line up exactly due to tolerance errors accumulated in the various components during

manufacture. One of the goals within the European aerospace industry is to reduce these errors to a level that would achieve a "jig-less" assembly mechanism.

In high-speed machining, two main factors lead to geometrical inaccuracies of the final part/component. The first of these is due to inaccuracies introduced by the physical properties of the machine tool structure. These can be geometrical variations of the machine tool, cutting tool flexibility, and/or errors in the control of the position of the machine tool. The second is due to the need to control the co-ordinated motion of the individual axes of motion of the cutting tool dynamically under varying loads.

Geometrical and Thermal Errors - Error Compensation

With current technology able to machine in five degrees-of-freedom, machine tool structures are extremely complex. For accurate knowledge of the position of the cutting tool, and hence production of accurate CNC paths off-line, an extremely good knowledge of the geometry and kinematics of the machine tool is required. In practice this is often difficult to obtain with the necessary degree of precision. This is further compounded by the continuously changing distortion that can occur both in the machine and the workpiece as they heat up during the machining operation. It is understood that the errors due to thermal expansion of the workpiece and machine tool are the most significant [94, 95]. These errors are generally known as the static errors. Errors due to dynamic effects also result in reduced precision of the machined workpiece. These include deflection of the cutting tool due to the average load imposed upon during the cut and inertial effects of the machine tool. The result is that the CNC path generated by CAD/CAM systems does not produce the part accurately enough. Much research has focused on being able to quantify and correct for such errors.

Initial work concentrated on being able to define the static errors in a generalised framework and compensate for them off-line using measurements made from a previously machined workpiece and comparing its geometry with the desired geometry [96]. For a three-axis machine it is understood that 21 error components contribute to the total volumetric error [97, 98]. This increases to 32 when considering thermal effects [99]. The majority of approaches to error compensation use rigid body kinematics to model the machine tool as a series of linkages, arms and prismatic joints [100]. Emam *et al.* [101] derived a generalised error model based upon Denavit-Hartenberg (D-H) matrices [102]

that accounted for both geometrical and motion related errors in all degrees of freedom in predicting the total volumetric error of the machine. Further work used homogeneous transformation matrices (HTM) to define a standard structure for volumetric errors. These were then compensated for off-line via CNC program manipulation simulation (assuming small angles) on a real milling machine for a three-axis system [100] and in simulation for a five-axis system [103,104] machine. In their work, Srivastava *et al.* [103] also highlighted the effect that machine design could have on maximising the effect of such compensation. Mou *et al.* [105,106] improved the off-line characterisation of errors using standard reference workpieces which lead to improved accuracy.

Once a good characterisation of the error components is found sensors that can (directly or indirectly) measure the errors are mounted on the machine tool. Laser inferometers [97] and/or co-ordinate measurement machines (CMM) are often used to measure geometrical errors. Ni *et al.* [98] developed a system using a laser inferometer in conjunction with beam splitters and mirrors with a dual-axis lateral effect photo-detector to allow on-line measurement of up to five error parameters in a single axis. Most compensation schemes that have been implemented are performed in three-axis machine as the difficulties associated with measurement of errors in the rotational axes make implementation of true five-axis error compensation the current challenge. Steps forward in measuring the rotational components of the error using 3D ball probes have been made by Lei *et al.* [107–110]. The scheme used a contact probe moving in pre-defined paths over a spherical test surface to characterise the errors of both the rotational and linear axes. The resulting compensation scheme [110] was implemented on a real machine with promising reductions in error. The optimal design and location of thermal sensors (usually thermocouples) to improve the characterisation of geometrical errors due to thermal expansion of the machine tool has been investigated [111]. Various approaches have been implemented to characterise the effect of thermal changes on error components based on practical temperature measurements. These have included finite-element models [112, 113], neural networks [114, 115] and reduced mode analytical models [94]. An off-line method based on a neural-network compensation scheme that could estimate and correct for error components on a real 3-axis machine including the effects of cutting tool deflection was proposed by Raksiri *et al.* [116]. In their work Raksiri *et al.* measured the errors due to cutting force using a camera. Given the errors a compensation scheme is then derived off-line and compensation is applied directly to the CNC program. This approach relies on errors being repeatable to be effective.

Also the technique has to be re-applied for each different part made on the machine tool.

Other attempts at correcting the tool path focus on doing so on-line. With measurements being made on-line, compensation for dynamic errors also became possible. In their work Mou *et al.* [105] included an adaptive on-line mechanism (based on off-line measurements) that changed the position demand sent to the machine tool servo-controller during the machining process, improving accuracy further. Using a method to measure and estimate the error components on-line and in real-time Chen *et al.* [99] implemented a similar real-time compensation mechanism for a three-axis machine with promising results. An on-line neural-network scheme was designed by Ouafi *et al.* [117] using a statistically selected subset of sensors that generated the required error components necessary for on-line compensation. Lechniak *et al.* [118] additionally accounted for errors in the geometrical description of the finished workpiece due to simplifications when implementing complex curves using Non-Uniform Rational B-Splines (NURBS). They also accounted for cutting tool deflection in their off-line compensation. Using a reduced mode analytical model Kim *et al.* [94] implemented a scheme for real-time compensation of thermal errors using a vertical-type high speed machine tool.

Drive Control Errors

As well as compensation of errors due to geometrical, thermal, and dynamics effects of the cutting process, errors can be introduced into the final machined component as a result of poor control and/or coordination of the individual axes of the machine tool itself. The principle error in machine tool control that can lead to geometrical inaccuracies is known as *servo lag*. Servo lag arises due to the dynamics and associated non-linearities (resulting from maximum velocities as well as limits on acceleration and deceleration) of the individual machine tool axes. Most servo-mechanisms can be simplistically modelled by a first-order lag transfer function with an integrator:

$$G_{axis} = \frac{k_{servo}}{s(s + \frac{1}{\tau_{axis}})} \tag{2.2}$$

where k_{servo} is the machine tool servo gain and τ_{axis} is the time constant for the axis of motion in question.

A simple way to quantify the amount of lag between the currently demanded position

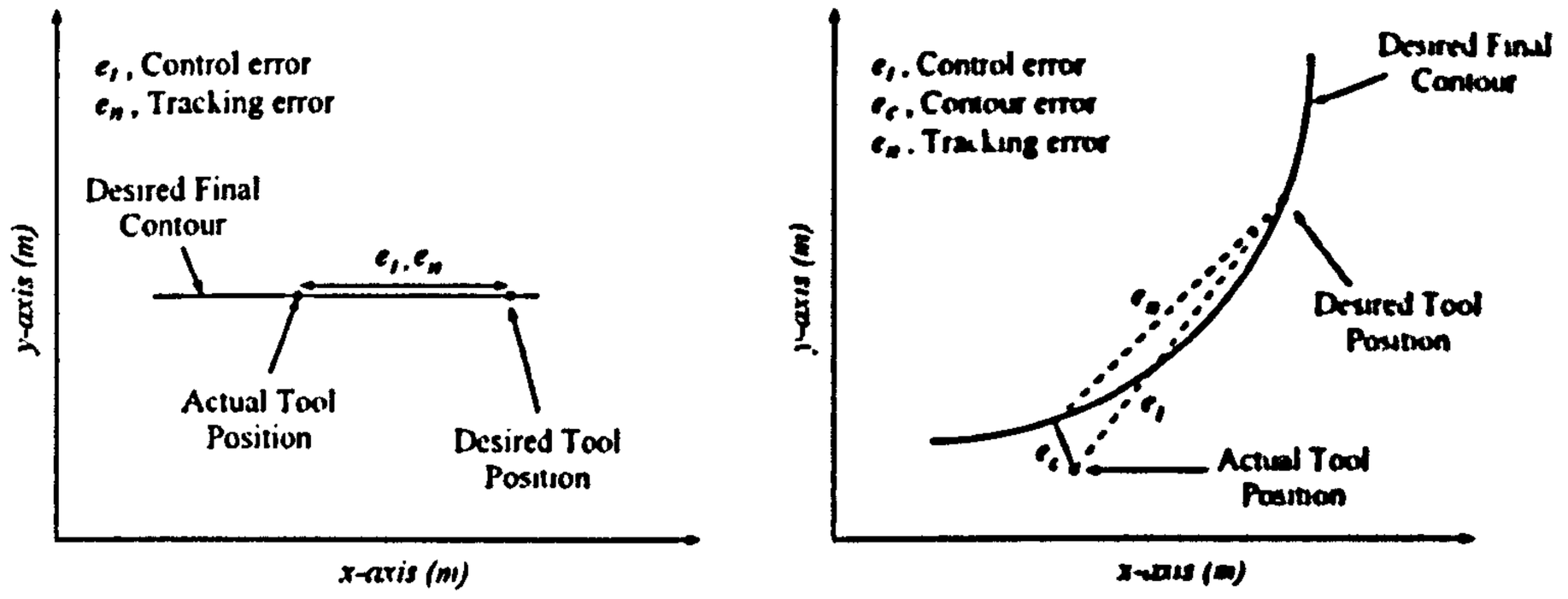

(a) Single Axis Errors

(b) Multi-Axis Errors

Figure 2.10: Single and multi-axis contour error definitions

of a particular axis and the actual position is to assume that it can be considered as a time constant, t_{LAG} [119] (when cutting at a fixed feed rate). Given this assumption the error in position (or tracking-error e_n) of the machine tool will be roughly proportional to the feed-rate for that particular axis. If motion along a single axis is considered (i.e. a cut along a straight line) then control of the rate at which the machine tools will only have an effect on the surface finish of the resulting cut with the geometry of the cut being unaffected. This is demonstrated in figure 2.10 (a.); the error, e_t, does not lead to an incorrect geometry.

Now consider a machine tool performing 2-axis motion in which a right angle corner, as shown in Figure 2.11, is to be followed. Current practice means that the cutting tool stops when it reaches the point at which the change in direction is required. It then proceeds in the new direction once a full-stop has been achieved. This leads to increased machining times and affects the surface quality of the final workpiece, leaving dwell marks. If this practice is not followed, then the servo-lag would result in the axes not being synchronised through the corner leading to a rounded-off or misshapen corner [120] as shown in figure 2.11. Further, if a complex profile using the latest generation of 5-axis machines is considered, then the problem of servo-lag becomes much more complex and leads to geometrical errors in multiple axes 2.10 (b.). When machining profiled surfaces in multiple axes the machine can no longer be stopped at arbitrary points. Therefore the feed rate at which these components are cut is reduced to minimise the effect of servo lag, leading to increased time for manufacture. In order to reduce the errors seen in machining

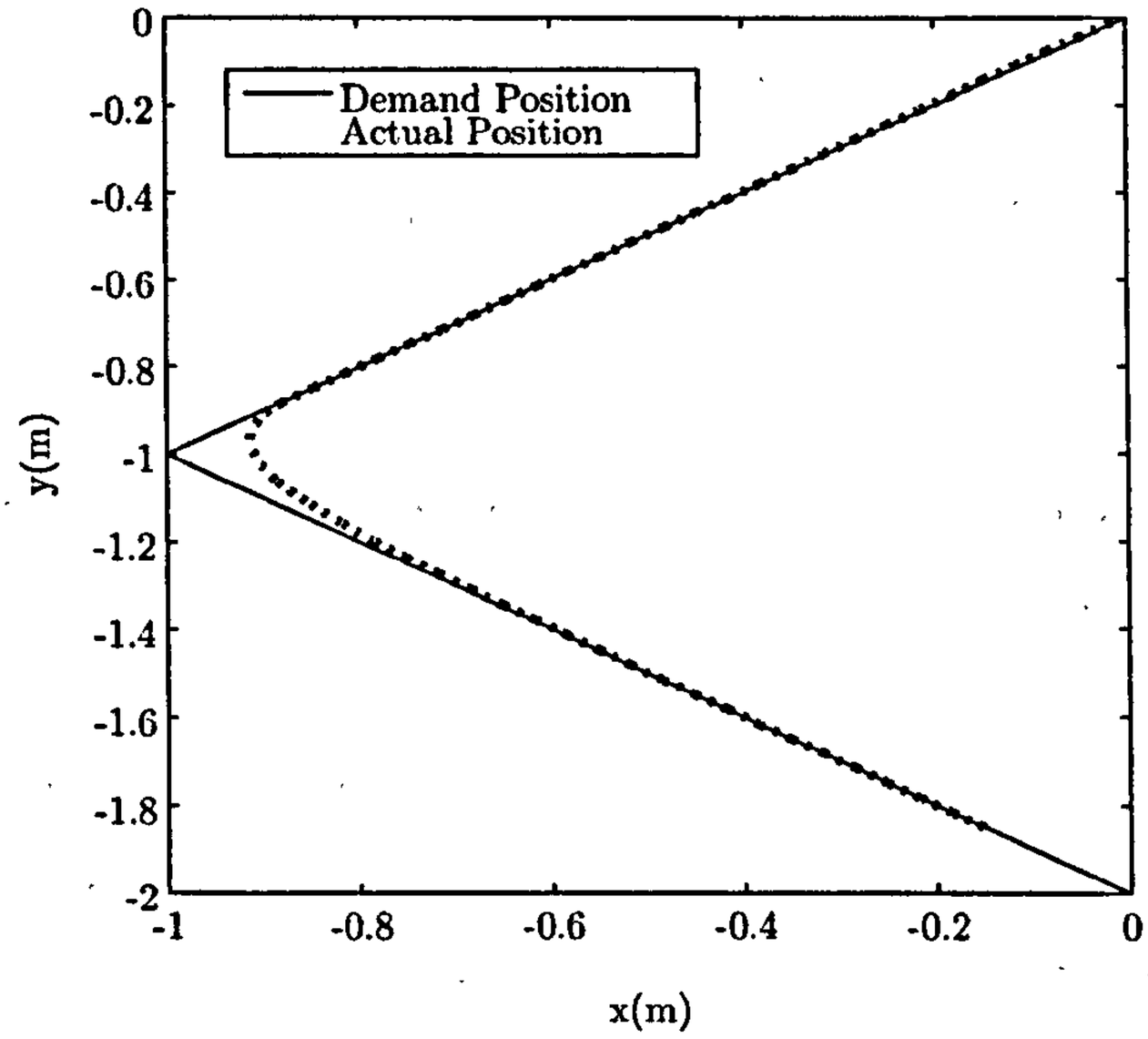

Figure 2.11: Typical errors encountered when milling a right angle corner

that result due to machine tool axis dynamics (or servo-lag), control techniques are applied to the individual axes to ensure that they remain co-ordinated. This area of research is broadly termed Geometric Adaptive Control (GAC). Due to ambiguity in interpretation of the word 'adaptive' in this phrase, this form of control is also referred to in this work as Geometric Closed-Loop Control (GCLC).

Geometric adaptive control for machining has traditionally taken one of two primary routes. The first of these is termed *'tracking control'* and operates on each of the axes of motion individually, attempting to reduce errors in each of those axes of motion independently. In CNC machining the demand vector is often known in advance, and hence the use of feed forward control is common [119,121,122]. For feed-forward control, given that the position demand for a particular demand can be represented by the variable $r(t)$, a model (normally linear), $G_{axis}(z)$, for the real control loop of the axis of motion in question can be derived such that:

$$y_{axis}(t) = G_{axis}(z) \times r(t) \tag{2.3}$$

where $y_{axis}(t)$ is the resulting real (and erroneous) motion of the axis in question. Feed forward control then attempts to derive the inverse of the this model of the real control loop giving $G_{FFD}(z)$, such that:

$$G_{axis}(z)G_{FFD}(z) = 1 \tag{2.4}$$

and:

$$y_{axis}(t) = G_{axis}(z)G_{FFD} \times r(t) = r(t) \tag{2.5}$$

Thus, the inverted model can be used off-line to generate a modified demand, $r_{axis}(t)$:

$$r_{axis}(t) = G_{FFD}(z) \times r(t) \tag{2.6}$$

that can be sent to the servo-controller improving the fidelity of control. The resulting motion will be improved on each axis but co-ordination of the axes (and hence accuracy of the complete machine tool) will remain poor. $G_{axis}(z)$ will possibly contain zeros that lie outside of the unit circle making implementation of feed-forward control complex. Tomizuka *et al.* [121] implemented a form of feed-forward control called Zero-Phase Error Tracking Controller (ZPETC) that overcame this difficultly based on a pole/zero cancellation technique, often involving high compensator gains at high frequencies with good results. However, the high amplitude, high frequency compensator often led to saturation of the control signal sent to the servo motor drives which resulted in reduced performance. The ZPETC controller is also sensitive to modelling errors and/or changes in plant parameters. Yeh *et al.* [123] improved the bandwidth of the ZPETC algorithm by placing it in series after a digital pre-filter, overcoming control signal saturation effects. Robustness was also improved by making the ZPETC algorithm adaptive using a real-time estimation technique. Off-line empirical feed-forward control (similar to off-line error compensation) was used by Bjorklund *et al.* [119] to generate a "Virtual Tool Path" based on previous cuts to ensure a more co-ordinated motion of the five-axis machine tool.

Optimal control [124, 125] associates a cost function with both the command signal sent to the servos and the error between the actual and desired position of each axis of the machine tool independently. Thus, as with feed-forward control, optimal control makes no attempt to co-ordinate the axes to improve the accuracy of the final workpiece and is therefore a tracking control strategy. Optimal controllers are designed to minimise each of the cost functions via adaptive or predictive methods. The techniques in this field rarely account for the non-linearities seen in machine tools such as backlash and saturation of signals. In a novel approach, Choi *et al.* [126] proposed a MIMO controller based on a H_∞ approach that used a force term (based directly on the velocity of the axes-of-motion) as the coupled feedback variable rather than position. The force feedback term was used to account for the change in plant machine tool parameters seen due to forces induced during machining resulting in a more accurate cut when performed in and out of cutting

conditions.

Renton *et al.* [120,127] demonstrated that the majority of tracking errors seen during cutting were principally due to velocity and acceleration limits imposed by the servo drives of the machine tool. Furthermore, they showed that the capability of machines could be enhanced if the velocity and acceleration capabilities across the full dynamic envelope (rather than limits based on a single feed-rate) were considered. In that case, accuracy could be maintained at much higher feed rates. The authors designed a feed-rate demand algorithm called Minimum-Time Path Optimization (MTPO) that made full use of the acceleration and velocity of a particular machine. A modified proportional-derivative (PD) controller was derived that used velocity feedback and was shown to yield smaller errors when tracking a ramped demand. Also, a controller whose design accounted for the acceleration and velocity capabilities named Minimum Time Tracking Control (MTTC) was derived. These two controllers (PD and MTTC) were used in combination with MTPO algorithm yielding accurate control at much higher rates of feed than conventionally possible. Consideration of robustness due to plant disturbances due to, for example, change in machine tool loading, symmetry or tool wear have been considered by various researchers [127–129] using observers. Erkorkmaz *et al.* [130] and Elfizy *et al.* [131] combined several of the above techniques (ZPETC Feed-forward, pole-placement controller, friction compensation, disturbance rejection) with a state-feedback controller using Kalman filters examining the improvement in performance at each step. Final experiments showed that this complex controller design could give a contouring error tolerance of $10\mu m$ when machining at 170mm/s but demonstrated the need for a simpler (computationally) controller design route. Further work in this area examined the robustness of the model-based control of non-linear piezo-electric drives over a wide parameter range [131]. Local models, whose structure was based on physical analysis and whose parameters are determined via an empirical system identification method, approximated closely the behaviour of the machine tool each over a narrow range of operation. For each model a corresponding ZPETC feed-forward and pole-placement based PID feedback controller was designed with the bandwidth set so as not to exceed the force limit of the drive. As with Renton *et al.* a disturbance observer was used to estimate and reject any disturbance exerted on the drive and a friction compensator used. In order to provide continuous control over the entire (and non-linear) operating range the local model-based controllers were switched to provide optimum local control with reduction in rise times (and hence response) of the

drive. As with many tracking controllers, this form of control suffered from saturation of the command signal if the design bandwidth was set too high.

In a bid to simplify control of the linear drives under varying conditions Jee *et al.* implemented an adaptive Fuzzy Logic controller (FLC) on a 3-axis milling machine [132]. This FLC algorithm adjusted the input and output membership functions on-line providing a robust controller again friction at low velocities and force disturbances.

The second tranche of CNC control is cross-coupled control (CCC). Originally proposed by Koren *et al.* [133] for a linear approximation to a tool-path and since developed [122,134] to account for curved paths, and arbitrary paths [135], CCC considers the error of the machine tool as being the smallest distance between the tool's current position and the nearest position on the desired cut path. This can be seen in Figure 2.10(b), labelled, ϵ_c and termed the *'contour error'*. The cross-coupled controller uses an accurate knowledge of the kinematics of the machine tools to implement a multi-variable (MIMO) controller that potentially gives a geometrically much more accurate cut at the maximum allowable feed-rate. However, it has been proposed [136, 137] that provided the bandwidth range is high enough, and that the algorithm in question is robust to changes in the plant due to loading condition, standard tracking controllers (such as feed-forward, ZPETC and optimal methods) provide similar capability without the need for the coupled kinematic model of the machine tool.

2.3.3 Interpolation

An additional area that can lead to an improved accuracy of the final cut is in the method used to define and interpret on-line complex surfaces. In the majority of previous research inverse kinematics and CNC programs used the cutter location (CL) as the point to control. This can lead to errors as it does not consider the actual point at which the cutting tool contacts with the workpiece surface. Lo *et al.* [138] developed an algorithm that could calculate the deviation seen and correct for it on-line on a 5-axis machine.

2.3.4 On-line Process Parameter Measurement and Control

This field of research is that referred to as Adaptive Control with Constraint (ACC). As mentioned previously current practice when designing CNC tool paths and feed schedules (and other process variables) is to err on the side of caution. Feed rates are specified in blocks with fixed values being based on a conservative estimate of the worst case scenario within a particular block. This results in under-use of the machine tools capabilities and, hence, extended processing time.

Algorithms that use a feedback variable, such as cutting force, to modify the CNC feed-rate have proved the most popular scheme to follow and became the subject of investigation in the late 1960's. Initial attempts used fixed gain feedback controllers [139–143]. The majority of research used a process model linking the feed-rate to either the measured cutting force or power to estimate the open-loop response. This model was then used to design the fixed gains for the simple (P, P+I) controllers. The results demonstrated that the cutting force could be regulated in this manner with limitations. Firstly, the steady-state gain of the open-loop system model was entirely dependant upon the geometry of the cut made. Hence, any change in the cut geometry could lead either to instability, or to an unreactive system. The fixed-gain attempts at ACC used steady-state compensators to overcome this phenomenon with limited success. More sophisticated controller design methods using linear model reference controller strategy were proposed [144] but suffered from similar limitations. The first parameter adaptive (or truly adaptive) controller strategy for ACC was proposed by Stute and Goetz [145] in which the output from a model estimating the force based on the feed was compared with the measured feed and used to modify (by simple division) the feed-forward gain of the closed-loop system. Many of the subsequent attempts (both adaptive and fixed-gain) at force based ACC were designed around this model-based approach [144,146] with model-reference adaptive control (MRAC) schemes proving most popular [147–151].

In 1986 Daneshmend *et al.*, [148], applied a series discrete SISO technique to a turning process estimating the transfer function between cutting force and feed as a first order system. A series of experiments were performed that allowed the sensitivity of different parameters in the MRAC algorithm to be tested. Results were mixed with the majority of set-ups controlling forces at a desired mean level but with large oscillations superimposed generated by the MRAC algorithm. Choice of the reference model was deemed critical

for good performance. The algorithm proved robust in the face of parameter variations due to cut geometry change. Lauderbaugh *et al.* [149], applied a similar approach to a milling process using a MRAC algorithm with adaptive based on a pole/zero cancellation approach using an on-line least squares algorithm. Good control was achieved when milling both a steel and aluminium billet as the workpiece material. Stable responses were observed when the controller was tested with both metals over a range of cutting conditions. However, due to measurement noise and non-linear effects, such as cutter run-out, the finally achievable bandwidth was lower than expected. Rober and Shin [151] discussed the limitations that are imposed on MRAC ACC systems by machine tool set-ups exhibiting non-minimum phase behaviour. They presented a modified MRAC algorithm based on a design originally proposed by Barthel and Shin [152] that used the zero phase-error tracking control algorithm to deal with uncancellable zeros present in machine tools. The ZPETC algorithm allowed good control of a plant that was close to instability due to the presence of zeros close to edge of the unit circle (and hence close to instability).

Other approaches to force-based feed-rate based ACC have used the model-based approach but relied on a different adaptation mechanism. Huang *et al.* [153] implemented a proportional-plus-integral-plus derivative (PID) controller using a neural-network to tune the pole-placement algorithm with parameter estimation based on a least-squares approach with good results. Luo *et al.* [154] extended this approach applying it to multiple axes on a milling machine, using the neural network to minimise the contour error simultaneously.

An adaptive strategy that regulated force via modification of both spindle speed and feed rate using fuzzy logic was proposed by Liang *et al.* [155]. The authors acknowledged the difficulty associated with modelling and hence controller design due to the large number of parameters required as well as hidden parameters in proprietary controllers that could not be derived. Hence their fuzzy controller defined seven fuzzy sets that were not based on a process model. More simply, the sets generated a control signal based on a rule set and whether the power error (at the cutting spindle) and the power change were large, medium or small and either positive or negative. The algorithm allowed regulation of a milling process along a single axis for various cutting geometries, workpiece materials and cutting tools.

Landers and Ulsoy [156] proposed stability boundaries of the force regulation process based on the force process gain of the closed loop system and two process models linking

feed-rate to cutting force. These models were the static form proposed by Elbestawi and Sagherian [157] which took the form:

$$F(t) = Kb^{\beta}v_{surf}^{\gamma}v^{\alpha}(t) \tag{2.7}$$

where F is the cutting force, b is the depth of cut, v_{surf} is the cutting speed and v is the feed rate with α, β and γ being coefficients describing process non-linearity. These coefficients are empirical, determined through experimentation. As with many of the similar constants in cutting force models presented in this thesis, they do not relate to individual material or process properties. Rather, they encapsulate a combination of the properties of the entire process, including machine tool structure, nature of the cutting process, workpiece material, etc.. K is a constant of proportionality for the process. The second form of model examined was a first order transfer function model, similar to that used in the majority of ACC designs, taking the form:

$$F(s) = \frac{Kb^{\beta}v_{surf}^{\gamma}}{\tau s + 1}v^{\alpha}(s) \tag{2.8}$$

For both forms, a model reference controller (non-adaptive) was designed and used experimentally to verify the location and form of this boundary of stability with reasonable fidelity. The controllers used were fixed-gain but the stability analysis allowed their design to be optimised in order to cope with large (and defined) parameter variations successfully.

In a later study [158], Landers *et al.* compared the stability and performance of four fixed-gain controller designs for force regulation. Specifically, these design methods were:

- linearisation based design
- log based design
- robust design
- non-linear design

The study showed (analytically and experimentally) that the log-based design method provided process stability over the widest parameter range and that stability margins decreased for all but the robust controller as the bandwidth requirements increased. Finally each of the controller designs were compared against an adaptive scheme similar presented earlier in this section. The study concluded that a major drawback of truly (or parameter) adaptive schemes for force regulation is the large number of parameters required as well as both controller and adaptation mechanism designs. For this reason the log-based fixed

gain controller design was recommended for the majority of machining operations due to its wide stability range and ease of design.

2.4 Conclusions

Factors that drive the economics within the military and civil aerospace sectors have been discussed. The need to reduce cost through the use of interchangeable parts and assemblies as well as versatile machine tool cells is apparent. In order to use interchangeable parts within the large structures, methods of manufacturing complex parts to a high degree of accuracy is vital. A wide survey of the recent advances in machining methods used in the aerospace industry, aiming to fulfil this criterion has been conducted. Within the manufacturing methods studied, the role of accurate feedback control strategies in enhancing machine bandwidth, and hence accuracy, whilst providing the versatility required from the machines is shown.

Within the field of high-speed machining this is most apparent. Use of more advanced controllers has allowed the machine operator to optimise the cutting process in a variety of ways. Attempts at using adaptive controller structures to vary the feed rate on-line have demonstrated that choice of reference model is always critical for stable operation of the machine tools. Moreover, process models that related cutting forces to process parameters often use and require experimental determination of empirical parameters that quantify the non-linear nature of the cutting process. The use of the MCS controller for regulation of the milling process is therefore attractive given the simple model structure assumed in its use.

Chapter 3

Regulation of an Aluminium Milling Process

SUMMARY: A summary of adaptive controllers is given. A control strategy is proposed that will regulate cutting power measured by adjusting the feed-rate. The pilot rig on which tests are performed is described. Results obtained using the described strategy are presented and discussed.

3.1 Introduction

For successful implementation of an ACC controller in milling, the literature review presented in chapter 2 demonstrates the need for a simple to implement and use adaptive controller. In this chapter, such an adaptive control strategy will be developed that can adjust the feed-rate of a cutting tool to meet a predetermined demand based on cutting power. This will be implemented and tested on a bespoke laboratory based milling rig.

The application of truly adaptive control techniques to the field of metal machining have, to date, fallen into two main categories; neural network techniques and model reference adaptive control.

3.1.1 Neural Networks

Neural networks represent an area that has attracted much interest in the last ten years since the increased availability of computer technology. The basic principal behind neural

networks relies on sets of properties being linked together via a network of 'neurons'. The strength of these neurons or links varies according to some specific function. This alters (or tunes) the whole system to behave in a specific manner or, conversely, allow recognition of a particular pattern of behaviour. One very good demonstration of the application of the use of neural networks is in the field of speech recognition, whereby the network will tune its already well defined idea of a particular work to suit a particular person's pronunciation of that word. In much the same way neural networks can be applied to the

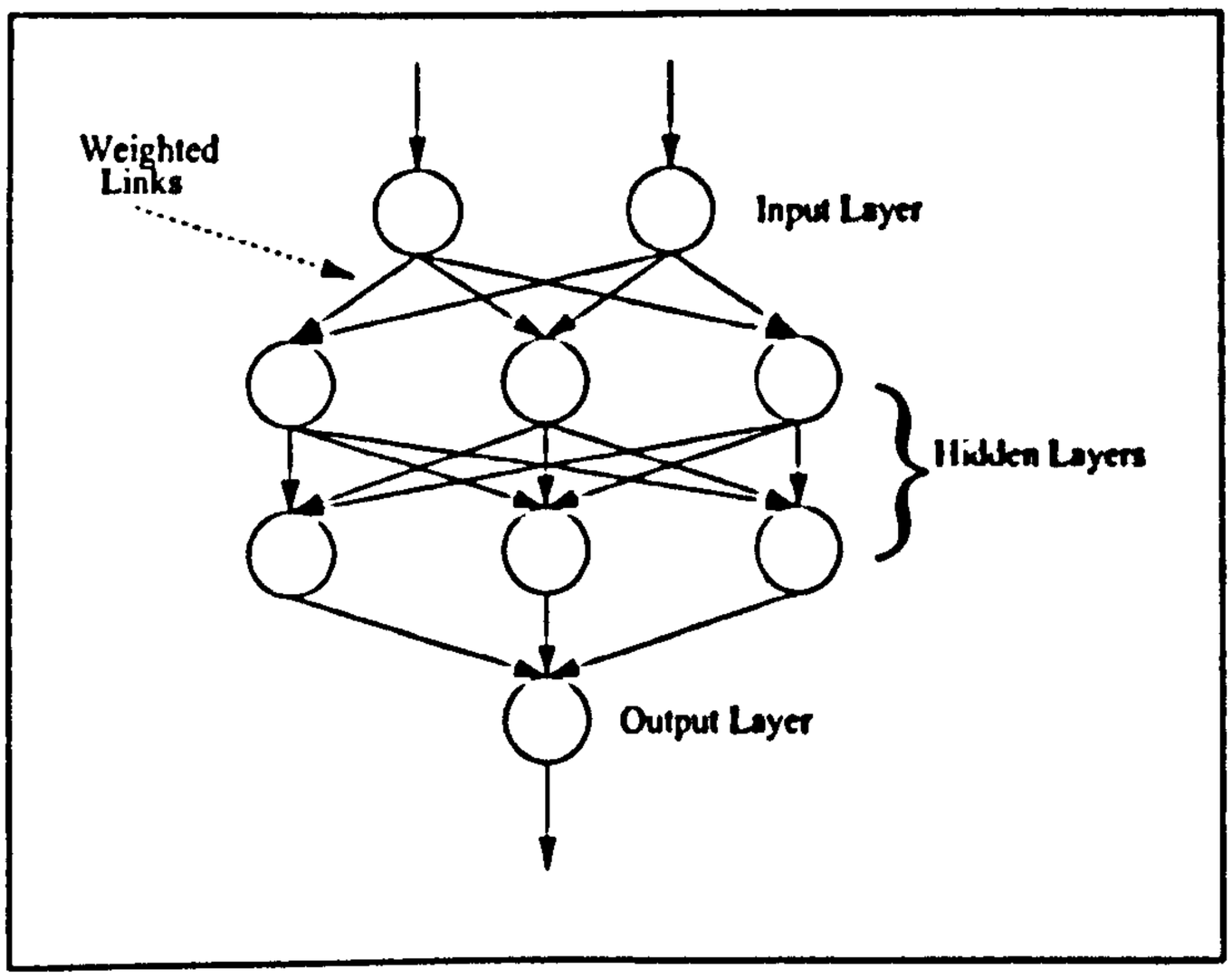

Figure 3.1: Back propagation neural network

field of control in order to tune to and then recognise particular patterns of behaviour. The controller can then adapt and correct for that behaviour. The most popular form of network used within the field of control is multi-layer back propagation. The structure for this particular type of control is shown in Figure 3.1. It consists of three distinct layers of nodes, with no connection between those nodes within a particular layer. The first layer is the input layer which, in the case of a controller, would have the demand signal and the feedback signal as its inputs. These signals then propagate through successive hidden layers of neurons via a series of weighted links, with each neuron in one layer having a possible effect on every neuron in the next. The chain ends with the last hidden layer of neurons feeding into the output layer, again via a system of weighted links and, in the case of control would result in a control signal. Each neuron in the network will behave in a specific manner, for example it might sum the inputs. The learning rules (some of which can be found in [159]) are applied to each of the links connecting the layers and it

is the choice of these rules that will determine the method of adaptation of the controller.

One advantage of this particular form of controller over other types discussed here is that they have the ability to provide the plant with a non-linear control law meaning that after initial adaptation the weightings in the network can be held constant and still allow control of a non-linear plant. MRAC and similar algorithms allow control of non-linear plants but only via the continuous variation of the controller gains.

Looking at the application of this technology to the field of metal machining three main branches of research appear. These are

- Process monitoring
- Process optimisation *akin to CLCO*
- Process control *akin to CLCC.*

Neural networks have been used to monitor machining processes for some time and their use in the first two of the above areas has become more popular especially for detecting tool wear. However faster computer processing technology has allowed the more recent jump into the field of the control of the machining process using network techniques. Initial research concentrated on the control of the relative motion between the spindle and the workpiece [153], [160] on retro-fitted automated milling machines. Using neural networks the trajectory error of the tool due to the non-linear elements of the motion due to backlash in the actuating lead screws and irregular coulomb friction was significantly reduced to acceptable levels. More recent research [161], [154] has applied neural network control techniques to the regulation of cutting forces via on-line variation of process variables (such as feed-rate) with a good degree of successful control in the relevant areas.

Neural networks require a large amount of training off-line before they can be implemented on-line and it is imperative that the data used to train the network are of good quality demonstrating a large range of the expected behaviour. As summarised above research is beginning to expand into the regulation of various aspects of the machining process but it is currently only in its infancy most probably due to the high level of complexity involved with the technique when compared with more conventional controllers.

3.1.2 Model Reference Adaptive Controllers (MRAC)

The Model Reference Adaptive Controller family of algorithms [162], [163] can be implemented in a variety of forms, one of which can be seen in figure 3.2. Various researchers have applied MRAC controllers to the adaptive control of machining processes [147–151]. The technique relies on a reference model to supply the required closed loop dynamics of the controlled system. The performance index is, in this case, the output error, x_e, the difference between the output state of the reference model, x_m, and that of the controlled plant, x. The aim of the controller is to adapt itself to allow the control of the plant such that the performance index is minimised in a fast and stable manner.

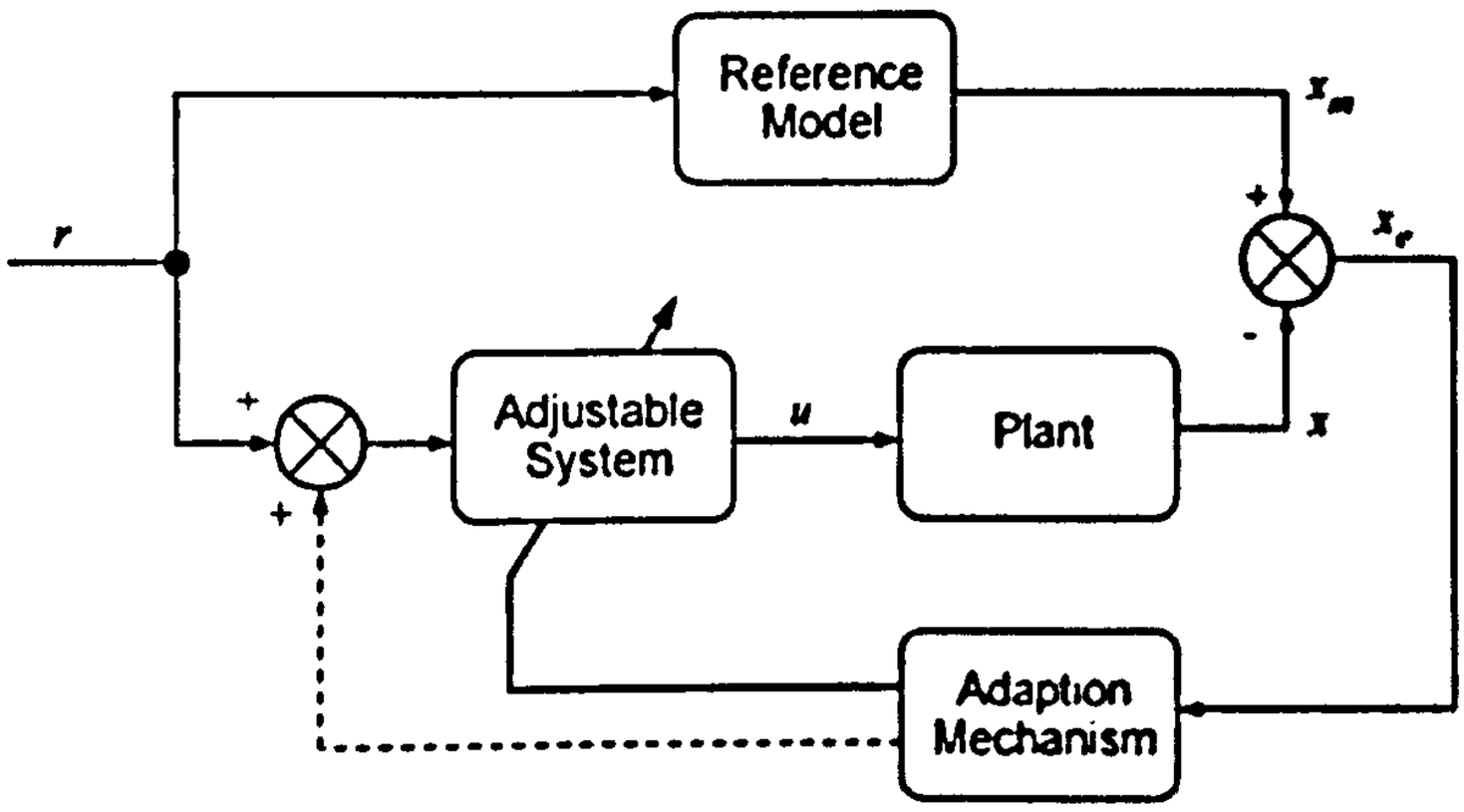

Figure 3.2: Basic MRAC configuration

Examining a multi-variable state-feedback form of the controller whose structure is shown in figure 3.3 it is possible to see how this is achieved. A multi-variable system and a reference model of the given system can be represented as:

$$\dot{x}(t) = Ax(t) + Bu(t) \tag{3.1}$$

$$\dot{x_m}(t) = A_m x_m(t) + B_m u(t) \tag{3.2}$$

$$x_e(t) = x_m(t) - x(t) \tag{3.3}$$

$$y_e(t) = C_e x_e(t) \tag{3.4}$$

where $[A, B]$ characterises the plant, $[A_m, B_m]$ the modelled system and u is the control vector given by:

$$u(t) = K^*(t, x_e)x(t) + K_R^*(t, x_e)r(t) \tag{3.5}$$

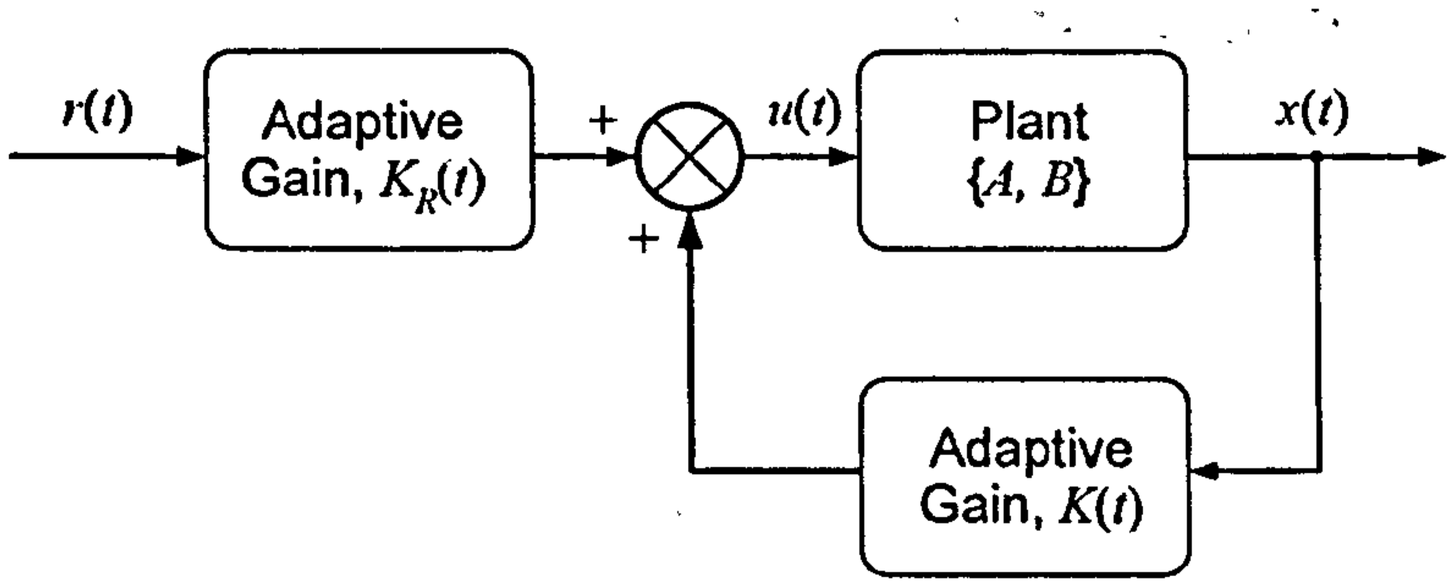

Figure 3.3: Internal structure of an MRAC controller

where $K(t,e)$ and $K_R(t,e)$ have constant and variable parts:

$$K(t,x_e) = K + \Delta K(t,x_e) \tag{3.6}$$

$$K_R(t,x_e) = K_R + \Delta K_R(t,x_e) \tag{3.7}$$

Upon further analysis the problem of adaptation reduces to a linear part and a non-linear part. The linear part involves the choice of parameter C_e such that:

$$C_e = B^T P \tag{3.8}$$

where P is a positive definite symmetric solution of the Lyapunov equation:

$$A_m^T P + P A_m = -H \tag{3.9}$$

H being a positive definite matrix. Initial values of K and K_R are also required. These are often chosen as the Erzberger values.

The non-linear part of the adaptation involves on-line calculation of the variable parts of $K(t,x_e)$ and $K_R(t,x_e)$ shown in equations 3.7. This non-linear part takes the general form:

$$\Delta K(t,x_e) = \int_0^t \Phi_1(y_e,t,\tau)\,d\tau + \Phi_2(y_e,t) \tag{3.10}$$

$$\Delta K_R(t,x_e) = \int_0^t \Psi_1(y_e,t)\,d\tau + \Psi_2(y_e,t) \tag{3.11}$$

The first terms in the above expressions provide the "memory" for the system with the latter terms being the transient terms that disappear as y_e tends to zero. The resulting controller allows control of both linear and non-linear plants using the reference model as the ideal behaviour.

3.2 Proposed Control Method

The method of control proposed for the regulation of cutting power is a first order Minimal Controller Synthesis (MCS) outer loop strategy. The details of the MCS algorithm including proofs of stability have been described in many papers [7, 164-166]. A brief overview of the algorithm is given here for completeness.

3.2.1 Minimal Controller Synthesis

The Minimal Controller Synthesis algorithm is a form of adaptive controller based on the Model Reference Adaptive Controller (MRAC) family described in the previous section 3.1.2. Conceived at the University Of Bristol in 1990 it extends the highly desirable properties of the MRAC series of controllers in the following ways:

- There is no need for plant parameter estimation either off- or on-line.
- It can cope with high bandwidth plant parameters.
- It will also reject the effects of high bandwidth disturbances on the system.
- The amount of coding required for successful implementation is small (similar amount to PID) making high sampling rates possible.

Previous experience with this form of controller has shown it to provide performance superior to that available from a standard, well-tuned PID controller [167]. This is mainly due to the adaptive nature of the algorithm and its resulting ability provide accurate control in the face of inaccurate plant modelling and/or unexpected changes to the plant during use (e.g. change in stiffness, etc.). The MCS algorithm simplifies the basic MRAC algorithm in the following ways. Firstly, the constant parts of the controller gains as described in equations 3.7 are set to zero. Secondly, a structure for the reference model and for the parameter C_e that assure robust stability is adopted. The combination of these simplifications reduces calculation times for stable, adaptive gains K and K_R (equations 3.12 and 3.13) and simplifies the design process reducing it to the choice of a pair of sensitivity parameters α and β and a settling time for the model, t_s.

$$K(t) \quad = \Delta K(t) \quad = \int_0^t \alpha y_e(\tau)x(\tau)\,d\tau + \beta y_e(t)x(t) \tag{3.12}$$

$$K_R(t) \quad = \Delta K_R(t) \quad = \int_0^t \alpha y_e(\tau)r(\tau)\,d\tau + \beta y_e(t)r(t) \tag{3.13}$$

To date the algorithm has been applied with successful results to a range of systems including a non-linear earthquake shaking table [167] and the control of chaotic systems [168].

3.2.2 Control Strategy

The chosen strategy for investigation in this work was an outer-loop strategy as shown in the schematic representation in figure 3.4. In this strategy the MCS controller forms the outer-loop which sits around the inner loop, this being the milling rig with its internal controller. One of the main advantages of this kind of scheme, and the main reason for its use here, is that it can be retrofitted around the existing equipment without modification of the inner loop's control. The outer-loop MCS would modify the position demand of, in the first case, a single axis of the rig in order to achieve the new feed-rate. It was intended that this new feed-rate would result in the desired power at the cutting tool.

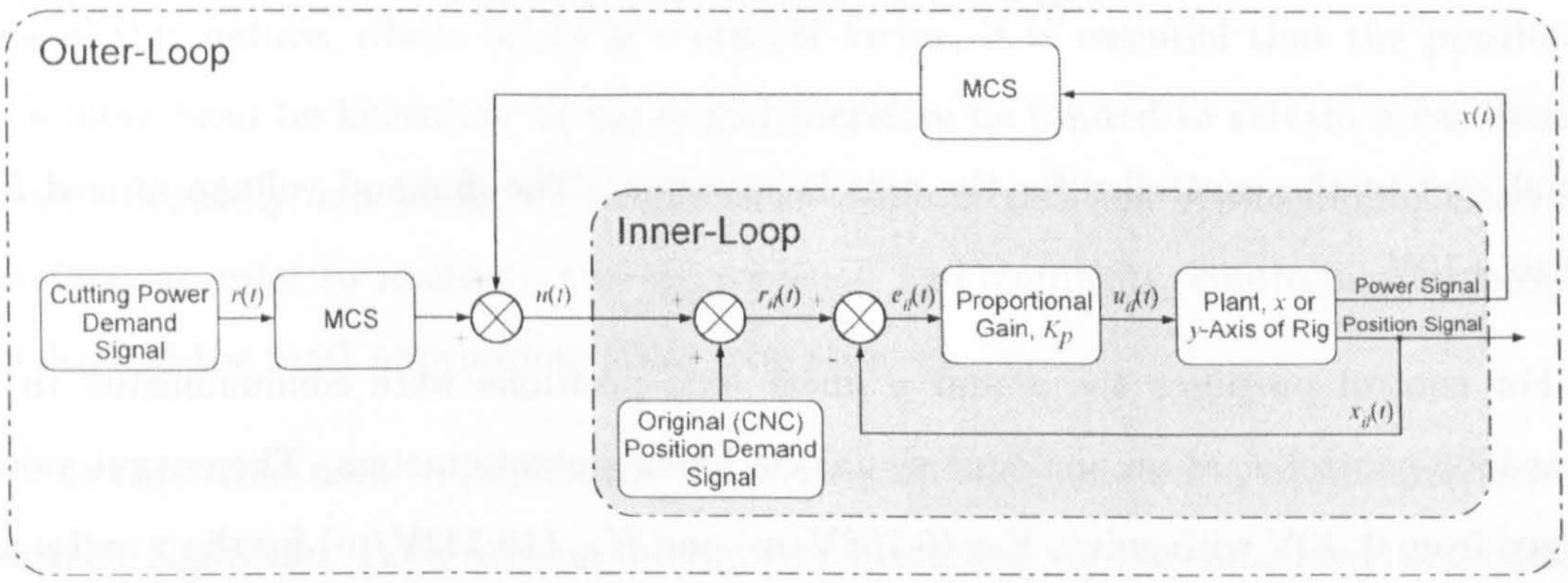

Figure 3.4: Outer loop overview

3.3 Pilot Rig Description

The pilot rig (Figure 3.5) that was used for the main body of the research work was a custom designed solution by BOSCH Automation Ltd in August 1997. It possessed a milling envelope of 1285mm (x-axis) by 895mm (y-axis) with a z-axis whose position could be adjusted manually via a slideway. It was a belt-driven two axis milling rig with each axis powered by a 1kW BOSCH Servodyn a.c. servo motor. Each of these motors was driven via a proprietary embedded controller. These controllers output a pulse-width modulated driving current. This current resulted in a velocity proportional to the analogue demand

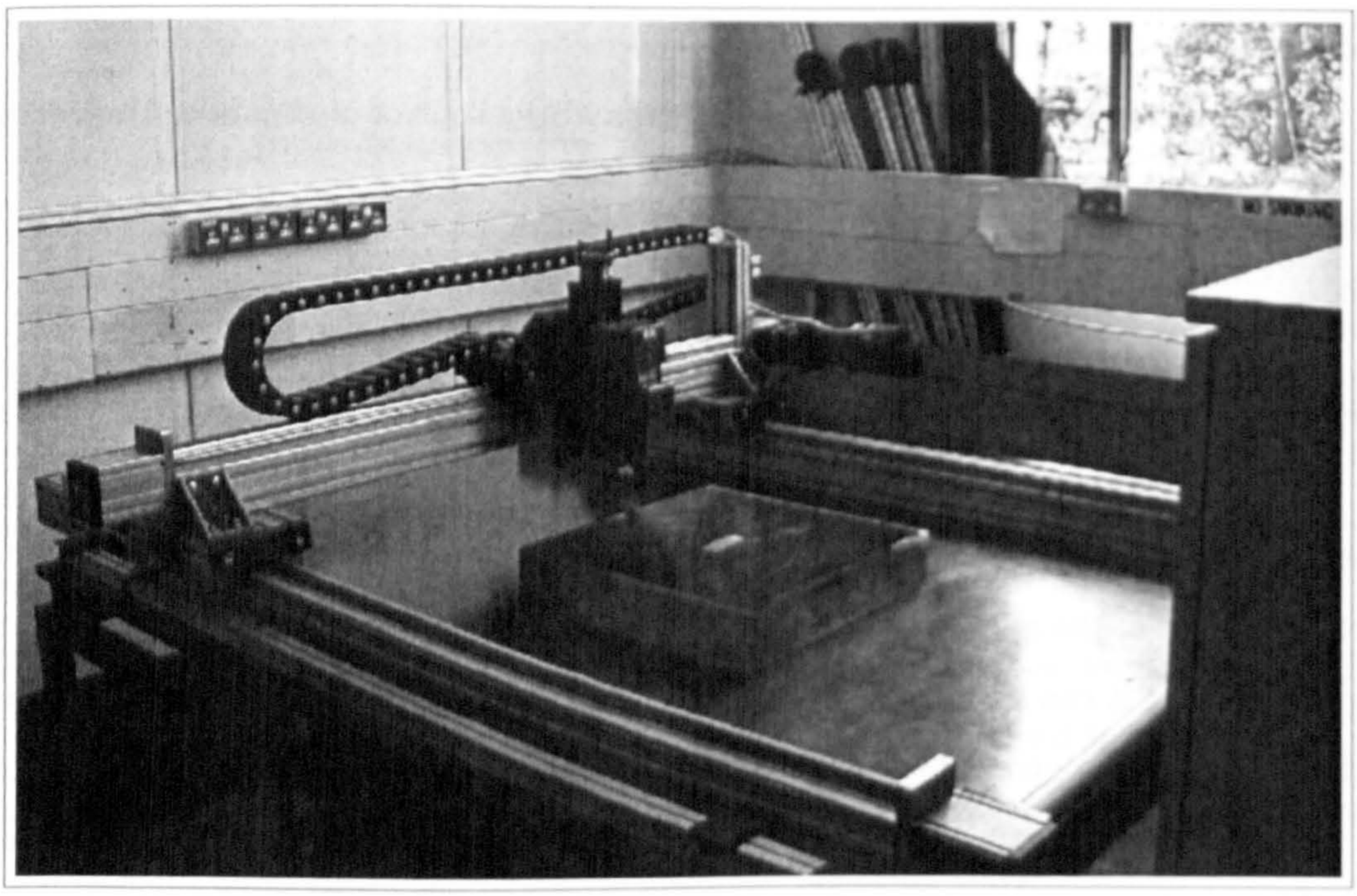

Figure 3.5: The two-axis pilot rig

signal sent to the controller for the axis in question. The demand voltage ranged from -10 to +10V.

For control purposes the x and y linear axis positions were communicated to the inner-loop controller as an analogue signal via linear potentiometers. The output voltage ranged from 0..10V with gains, K_{dx} (6.758V/m) and K_{dy} (10.142V/m) for the x and y-axes respectively.

The milling spindle was a Perske 2.2kW a.c. three phase motor with a maximum rotational speed of 18,000rev/min. It was powered by a BOSCH Servodyn-ASC three phase power supply. Its rotational speed was set via an analogue signal whose magnitude was proportional to the frequency of the a.c. current supplied to the router motor (0 volts = 0 Hz, 10 volts = 300 Hz). The embedded controller ensured that (after a brief settling period) the spindle current frequency was proportional to the rotational speed of the spindle.

Housed within the spindle was the $\frac{1}{2}$" tungsten carbide, 2 fluted, cutting tool with a helix angle of 60° that was used for all of the tests. The specific properties of this tool can be found in table 3.1. The main test specimen used during experiments was made from Aluminium 2024 T351, an alloy used in a large part of the manufacture of wing skins for

	Radial Dimensions	End Dimensions
Rake Angle	6°	7°
Primary Clearance Angle	10°	7°
Secondary Clearance Angle	20°	25°
Primary Width (mm)	0.71	1.27

Table 3.1: Cutting tool parameters

the Airbus A300 series. The test specimen measured 500 x 500 x 100mm and was bolted directly to the milling table at four points.

3.3.1 Low-Level Controller on the Pilot Rig

Each axis of the milling rig was controlled in position for two main reasons. Firstly, for a rig of this nature, where safety is a critical factor, it is essential that the position of the milling head be known at all times and therefore be limited to certain areas deemed as safe. Secondly, cut paths were defined in terms of position of the milling head and therefore, in order to maintain cutting precision and simplicity, controlling for position was deemed the most appropriate inner-loop strategy.

The algorithm used to implement the control on each axis was a simple proportional controller algorithm. Both axes on the rig were controlled via the embedded controllers as integrators in time (position being controlled via a velocity-based actuator), thus integral action was deemed unnecessary.

The choice of gains for each of the two axes was chosen via an empirical procedure. The values of the gains were set high to obtain a good dynamic performance and then systematically reduced until the effects due to noise were attenuated to acceptable levels. The final values that were used are:

$$K_{px} = K_{py} = 10. \tag{3.14}$$

The inner-loop set-up for each axis can be represented as in the figure 3.6 below:

Here, r, the reference signal is a voltage between 0 and 10 volts that indicates the demanded position of the relevant axis on the table, u is the analogue control signal sent to the servo motor drive and y is the current position of the axis, as measured by the

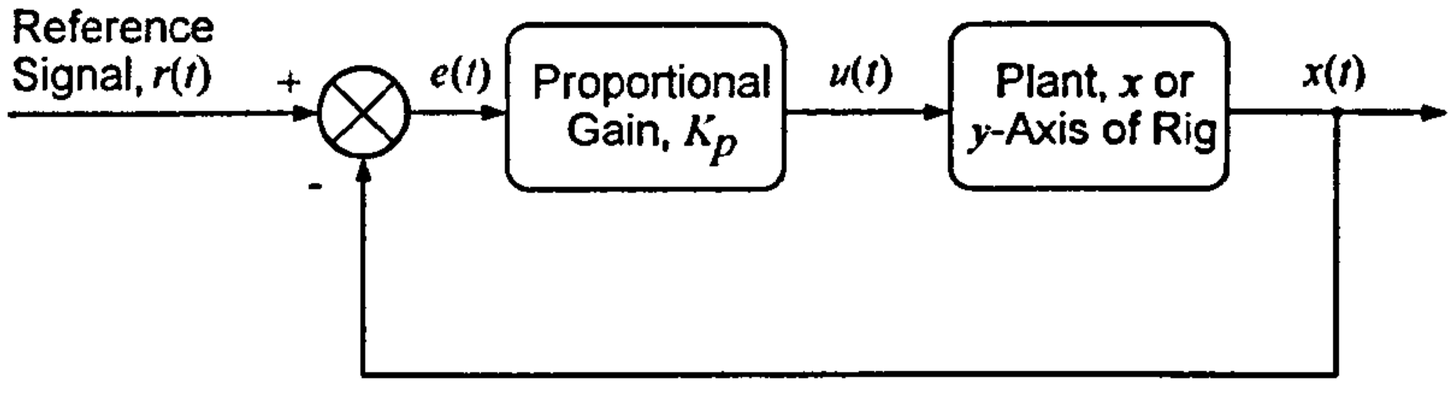

Figure 3.6: Pilot rig inner-loop control for x- and y-axes

LVDT.

3.4 Implementation of Proposed Control Strategy on Rig

3.4.1 Recovery of Cutting Power

A three phase Yokogawa 2533E Series digital power meter, supplied by Consort Controls was used on the pilot rig. This meant that the total electrical power being supplied to the spindle could be measured and hence the cutting power and torques calculated.

The power-meter was connected at the source of current for the spindle as shown in figure 3.7. In this figure the source is the BOSCH 3 phase power supply and the load is the spindle. As the spindle is a three wire load a total power measurement can be obtained by reading only two instantaneous currents, I_1 and I_3 and two instantaneous voltages, V_1 and V_3, the voltages being measured with reference to the second phase, NOT to ground. This is more commonly known as the *two watt-meter method.*

Given these quantities it can be shown that :

$$P_T(t) = I_1(t)V_1(t) + I_3(t)V_3(t) \tag{3.15}$$

where $P_T(t)$ is the total instantaneous power consumed. The mean power used in cutting, P_{cut}, is then equal to :

$$P_{cut} = P_T - P_{spin} \tag{3.16}$$

where P_{spin} is the free spin power of the spindle required to overcome friction, etc.. Values of P_{spin} were found experimentally for the spindle and a linear relationship between free spin power and rotational speed of the spindle was determined as:

$$P_{spin} = 30 + 0.0133N_r \tag{3.17}$$

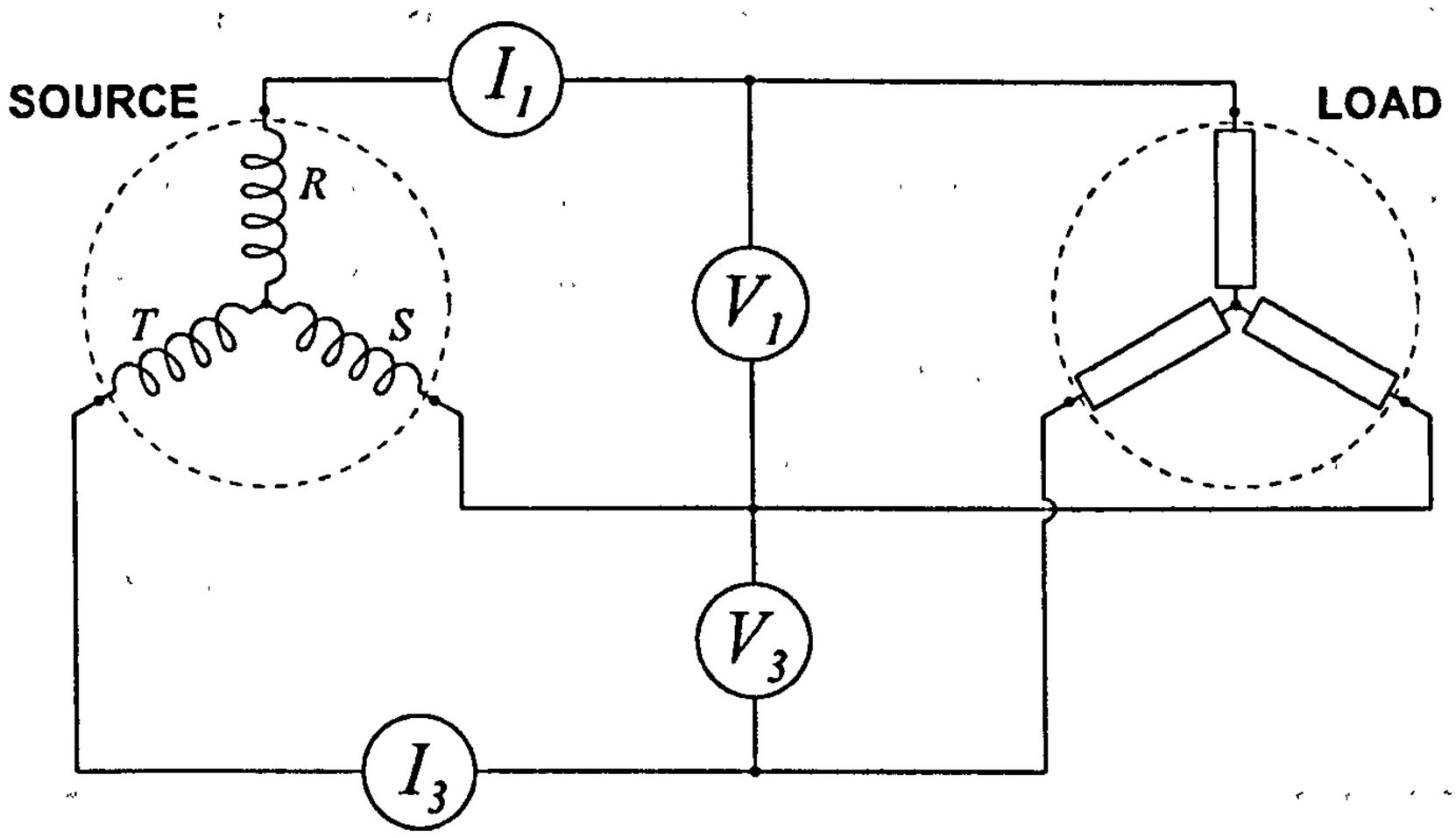

Figure 3.7: Three phase power meter connection

where N_r is the rotational speed of the spindle (rev/min). For all of the experiments performed it was assumed that any increase in spin power when cutting begins (due to extra friction on spindle bearings, etc.) is negligible and therefore that the spin power remains constant throughout cutting. It should also be noted that it was assumed that all current being measured was converted directly into cutting power. Losses in the wires transporting the current to the spindle as well as losses and inefficiency in the spindle were assumed small.

3.4.2 Software Configuration

The outer loop MCS controller strategy was implemented on a Pentium^{TM} class machine using 'ControlLab32', a piece of control software developed 'in-house' within the Department of Mechanical Engineering at the University of Bristol. A sample display of the software implementing a simple proportional plus derivative feedback (P+DFB) controller is shown in Figure 3.8. The software is modular, written in Borland Delphi around a fully object-oriented structure. The object-oriented approach to programming allows all of these blocks to be based on the same fundamental class structure ensuring signal integrity and synchronisation. Card drivers, signal generators, scopes, etc. all share the same basic code with the specific functionality being written on top of this code. In the final application, this allows control strategies to be built, or 'wired-up', without re-

compilation of the software, in a manner similar to that used in SIMULINK from a library of modules or blocks. A controller sampling rate of 1kHz was used in all of the experiments on the pilot rig. For data acquisition a ComputerBoards CIO-DAS1602/16 ISA interface card was written. A customised driver for the 'ControlLab32' software was written that allows recovery of 16 channels of data simultaneously via a 16-bit A/D converter. This allowed a theoretical resolution of 0.02mm on each axis.

For control output a modular driver was written for an Amplicon PC234 16-bit D/A card allowing output of up to four channels simultaneously.

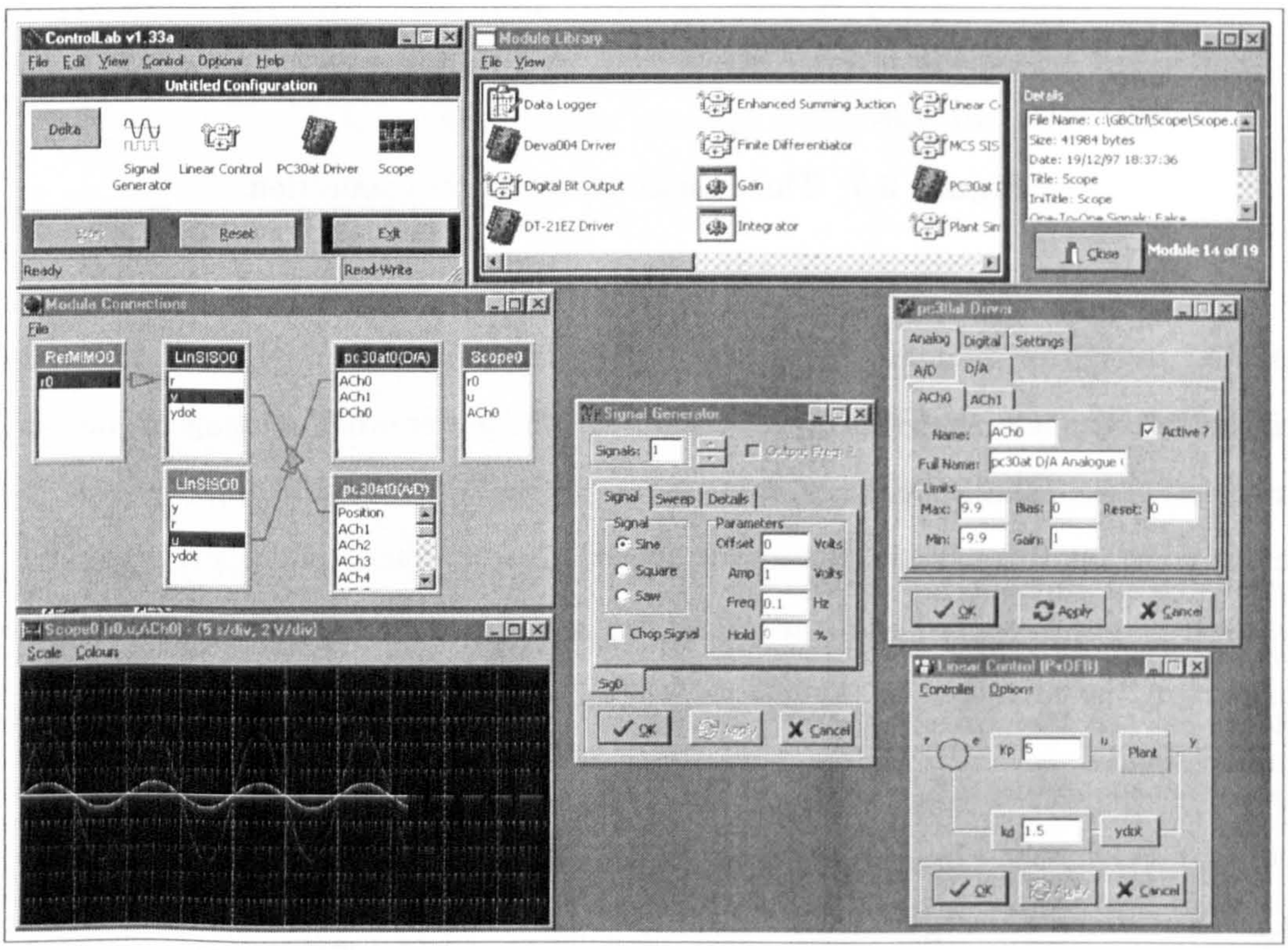

Figure 3.8: 'ControlLab32' implementing a P+DFB controller

Single Axis Demand Signals

The pilot rig detailed in section 3.3 was provided without a high-level controller, such as an NC controller seen on the majority of machines present in industry. In order to cut a continuous path along a single axis the low-level control strategy detailed in section 3.3.1 required an analogue signal representing the position of the tool at all times during a cut.

For non-adaptive milling, i.e.: simple open-loop cutting, this analogue demand was

achieved using the signal generator block provided by ControlLab32. This block output a triangular waveform whose amplitude, frequency and therefore gradient is equal to the required feed rate multiplied by the gain of the LVDT for the relevant axis (in experiments performed this was taken as the y-axis).

Suppose we require a feed rate of v m/min. This equates to:

$$\text{Voltage rate (V/sec)}, v_V = 60K_{dy}v \tag{3.18}$$

$$\text{Time period of half Triangular wave (s)}, P = \frac{A_y}{v_V} \tag{3.19}$$

$$\text{Frequency of triangular wave}, f_{feed} = \frac{1}{2P} \tag{3.20}$$

$$= \frac{2 * 60K_{dy} * v}{A_y} \tag{3.21}$$

where A_y is the peak to peak amplitude of the triangular waveform used.

When closed-loop milling is performed the control signal from the controller, be it a fixed gain or adaptive algorithm, is integrated with respect to time and added to the triangular wave forming a composite demand. This is shown in the schematic of the closed loop milling strategy in figure 3.9. To ensure that there is plenty of run-out for the test in the cuts performed in the pilot study, the value of A_y was set to 20V.

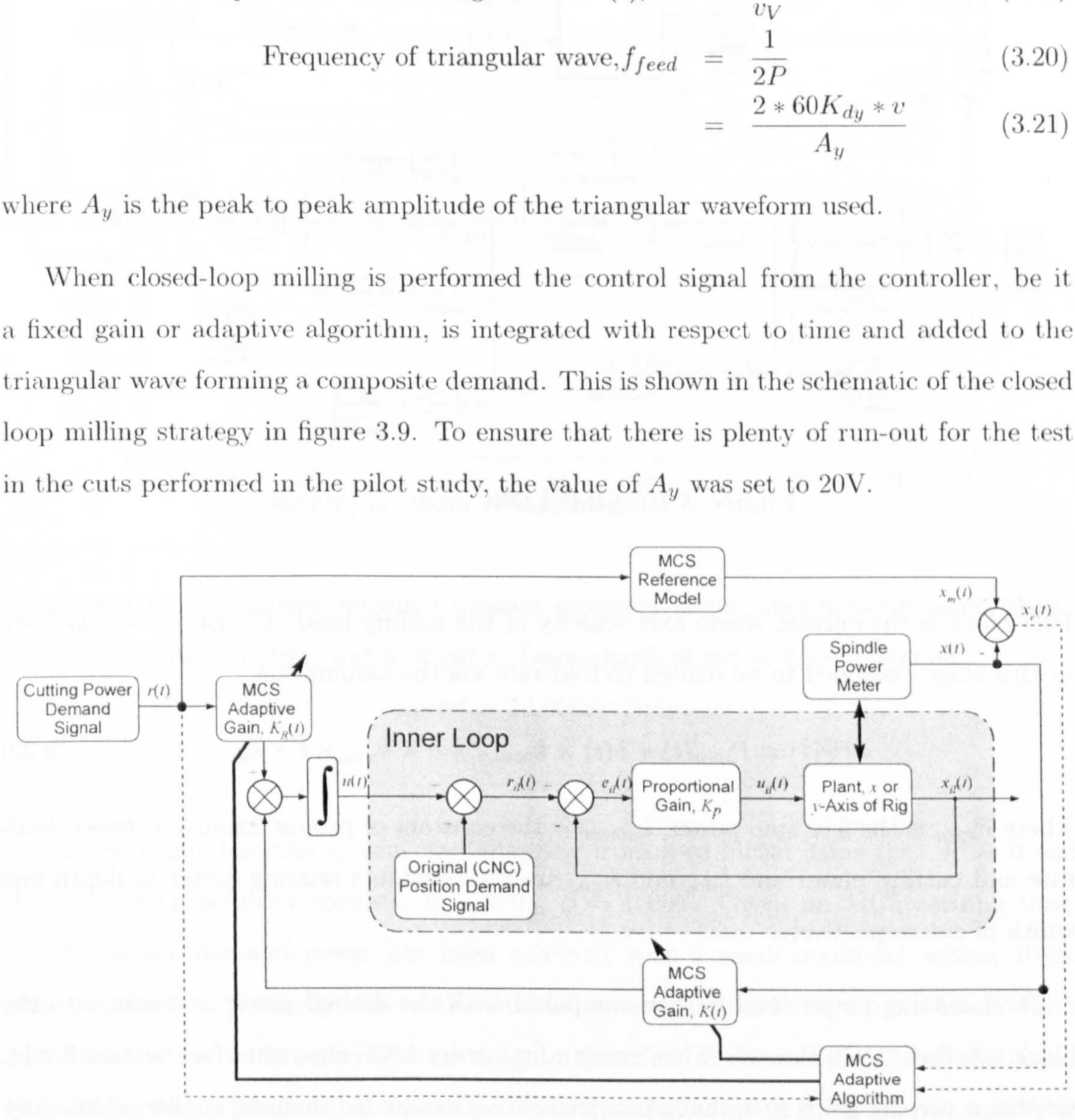

Figure 3.9: MCS outer-loop strategy implementation

In order to test the viability of the proposed strategy a MATLAB-Simulink model,

Figure 3.10, was constructed. This simulation can be compared directly with the strategy outlined in figure 3.9. The MCS outer loop can be seen around the block labelled MILL / PID. Within the MILL/PID block lies a model of a single axis of the pilot rig along with the proportional controller being used to regulate that axis. At the output of the MILL /

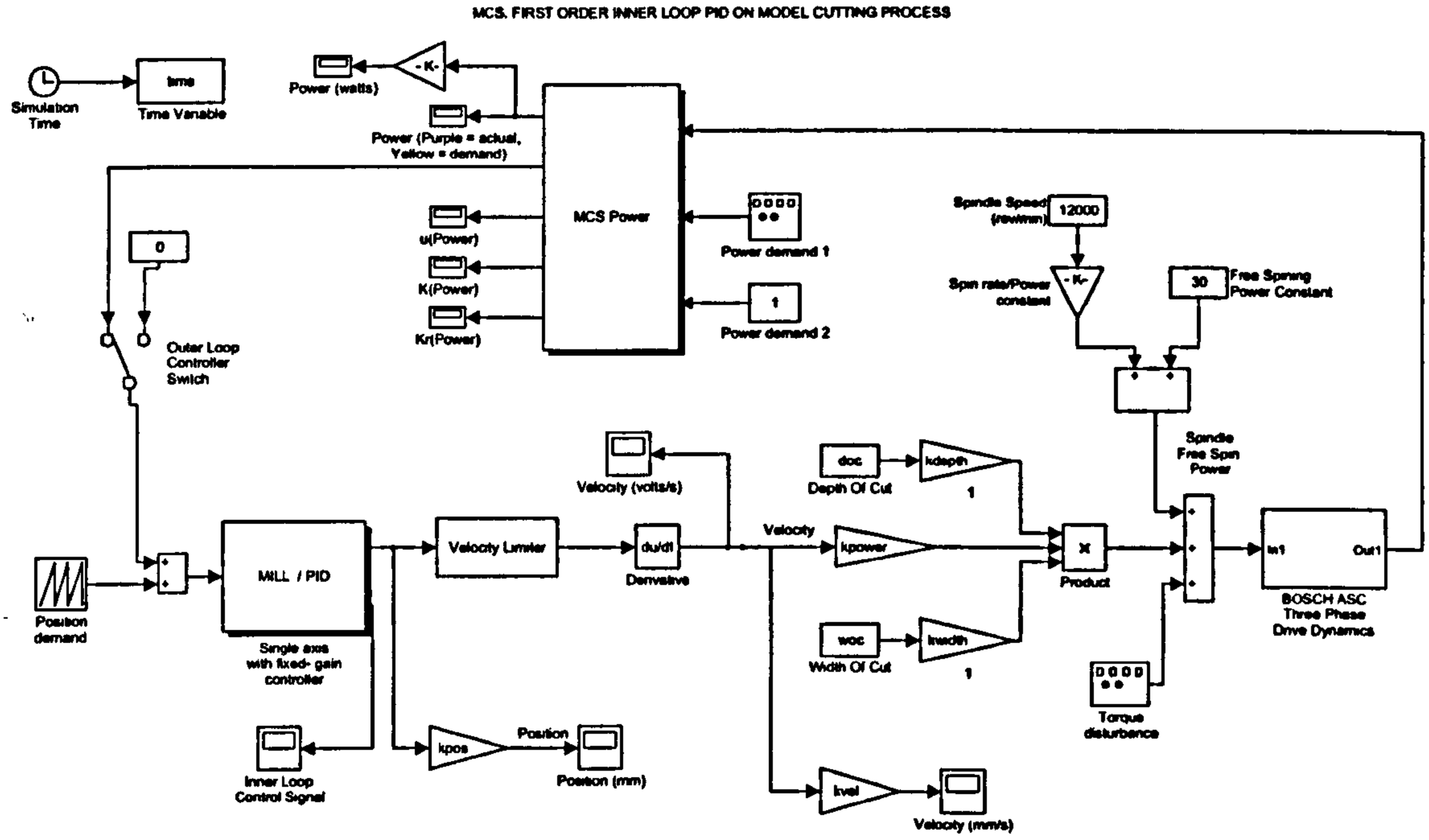

Figure 3.10: SIMULINK model of process

PID block is the current single axis velocity of the milling head. Cutting power is then, at this stage, assumed to be related to feed-rate via the assumption :

$$P_T(t) = P_{spin}(t) + v(t) \times k_{power} \times a \times k_{woc} \times b \times k_{doc} \tag{3.22}$$

where P_{spin} is the free spin power, k_{power} is the constant of proportionality between feed-rate and cutting power and k_{doc} and k_{woc} are the constants relating power to depth and width of cut respectively.

This cutting power level is then compared with the desired power and sent into the block labelled "MCS Power". This, using a first order MCS algorithm (see section 3.2.1), sets the controller gains such that a new feed-rate is demanded that will enable satisfactory tracking of the demand power. Finally, the signal produced is one which would be used to modify the feed-rate and therefore has to be integrated with respect to time so that it can be added to the inner-loop position demand in order to close the loop as described previously.

Figure 3.11 shows the results of a simulation where the demand power is being varied as a square wave for a constant geometry cut.

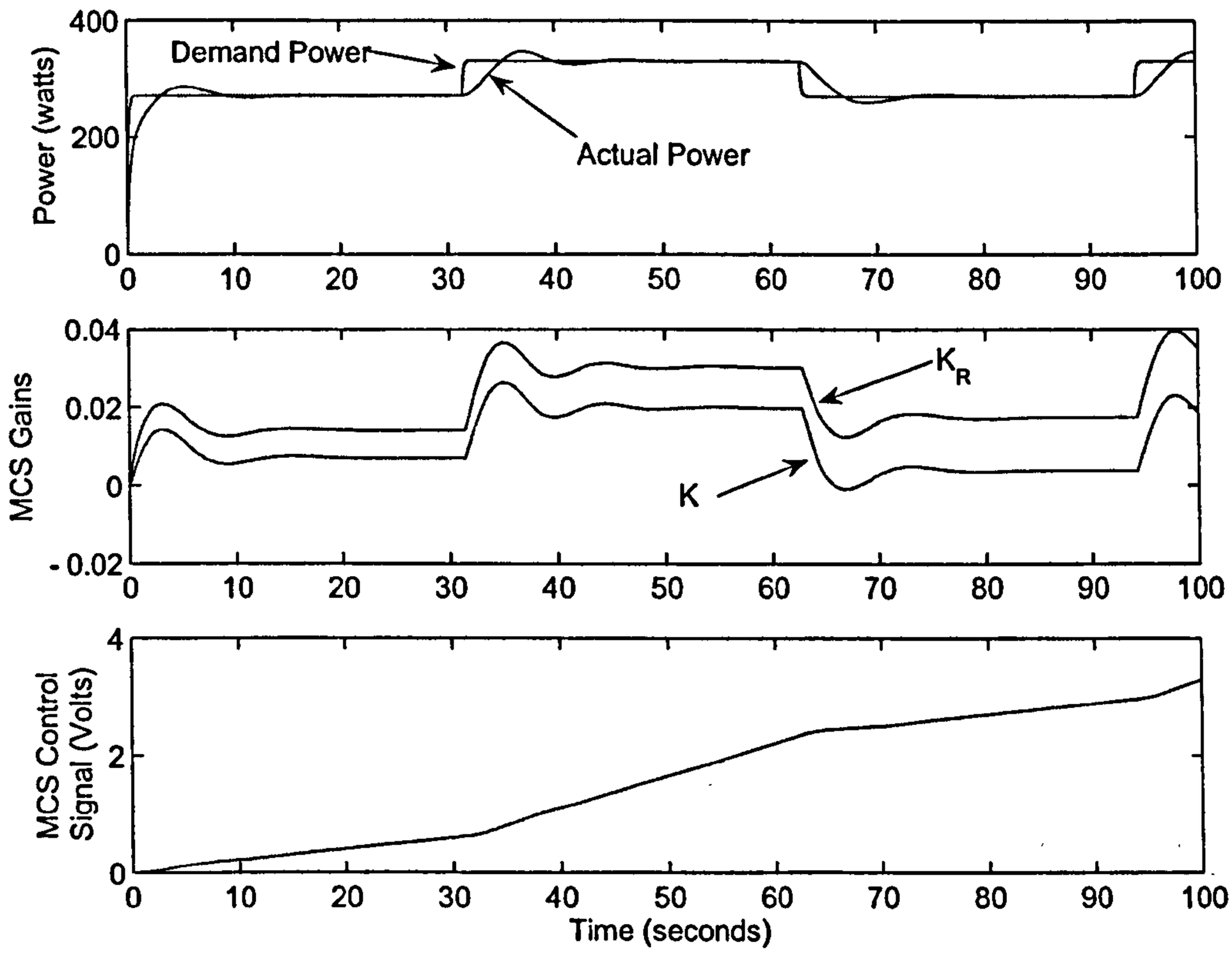

Figure 3.11: Simulation output: Constant geometry of cut, spin power present, MCS adaptive control, width of cut = 1mm, depth of cut = 3.9mm, spindle speed = 12,000rev/min

In this simulation the system was adapting from zero initial gains (i.e. $K = 0$ and $K_R = 0$) with adaptive weights, $\alpha = 0.05$, $\beta = 0.005$. Given an MCS settling time, t_s, of 1.0s the demand power has been achieved with a small overshoot within 10.0s. This overshoot is primarily due to the BOSCH three phase drive dynamics block which were included in the simulation to investigate the effect of drive dynamics on the closed loop. With the 3 phase drive dynamics block included, a good dynamic response from the MCS power loop is highly dependent upon correct selection of the MCS settling time, t_s. Another interesting point to note is that whilst the MCS controller gains reach quasi-steady state values after 10.0s, the change in demanded power results in a large change to the value of these gains. This change occurs even though the plant (pilot rig, geometry of

cut) has not changed.

This is due to the fact that in the above simulation, the free spin power of the spindle (spindle power under zero load) constitutes a high proportion of the total power consumed. This is the non-linearity that is being overcome by the MCS gains. Performing a similar simulation but without the free spin power yielded the results shown in Figure 3.12.

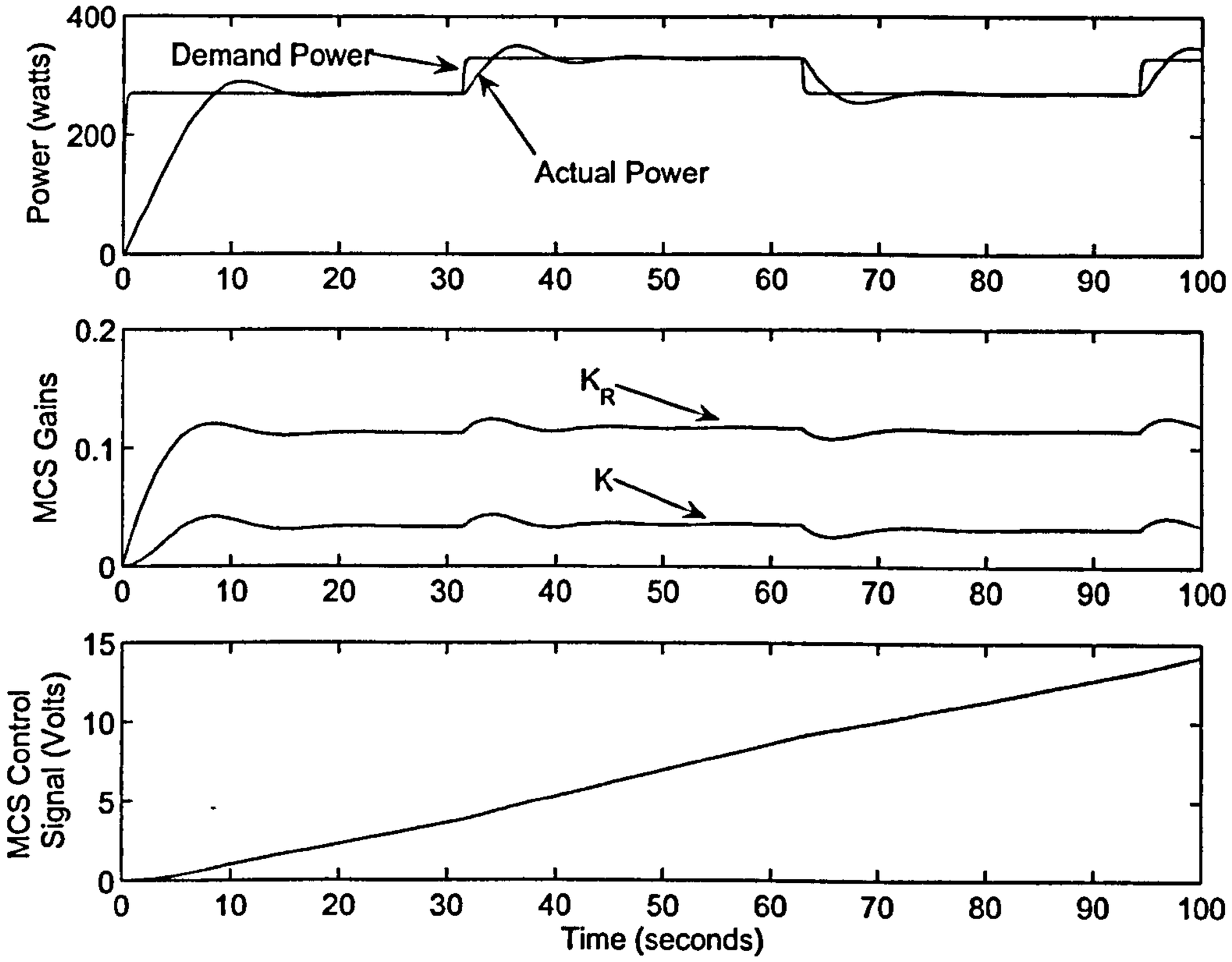

Figure 3.12: Simulation output: Constant geometry of cut, no spin power present, MCS adaptive control, width of cut = 1mm, depth of cut = 3.9mm, spindle speed = 12,000rev/min

Now it can be seen that adaptation takes slightly longer due to the fact that the constant spin power is no longer present. Also, figure 3.12 shows that this time the MCS gains reach their quasi-steady state values and, after a period of re-adaptation, remain at approximately the same values when the demand power changes. This is an important point as during finishing cuts performed in industry, the spindle free spinning power makes up a large proportion of the total power consumed. It is apparent from the above simulations that a conventional, fixed-gain controller would provide problems

for the control of power under these circumstances and demonstrates one of the possible advantages of using MCS.

3.5 Simple Single Axis Results

Presented in this section are the results of tests performed on a single axis of the milling rig under power control. Two types of controller were used throughout these tests. Firstly the MCS control strategy described in section 3.2 and secondly a fixed gain controller similar to a State Feedback Controller (SFC) based upon the same strategy. The purpose of using the SFC controller was to provide a benchmark with which the performance of the MCS controller could be compared. The values of the gains used in the fixed gain controller were obtained by completing trials under MCS control and noting the average steady state value of the adaptive gains.

The values of the MCS adaptive controller weights that proved most stable and that were therefore used for the range of MCS adaptive control tests carried out were :

$$\alpha = 0.01$$

$$\beta = 0.001.$$

These values were determined empirically, starting at low values of α and increasing it until noise amplification around the control loop deteriorated closed-loop performance. Experience with the MCS algorithm has shown that the relationship $\beta = 0.1\alpha$ yields the best closed-loop performance [169], therefore this relationship was used.

Demonstrating a fairly simple case figure 3.13 shows the results of a cut of constant geometry where the width of cut = 1mm, axial depth of cut = 3.9mm and the spindle speed = 10,000 rev/min. The demanded power was set at 240W for each of the cuts. The uppermost graph shows the cutting power in three cases. Firstly the case where no regulation of the power took place (open-loop), secondly the case whereby the power was regulated via a fixed gain controller and finally power regulation via the proposed MCS controller. The middle graph shows the values of the MCS and fixed gain controller gains. The lower graph shows the signal that was added to the position demand for both the MCS and fixed gain controllers in order to achieve the new feed-rate. The gradient of the lines in this bottom graph therefore represent the modification to the milling feed-rate.

The open-loop cut shows the level of power achieved at the base feed-rate of 0.24m/min.

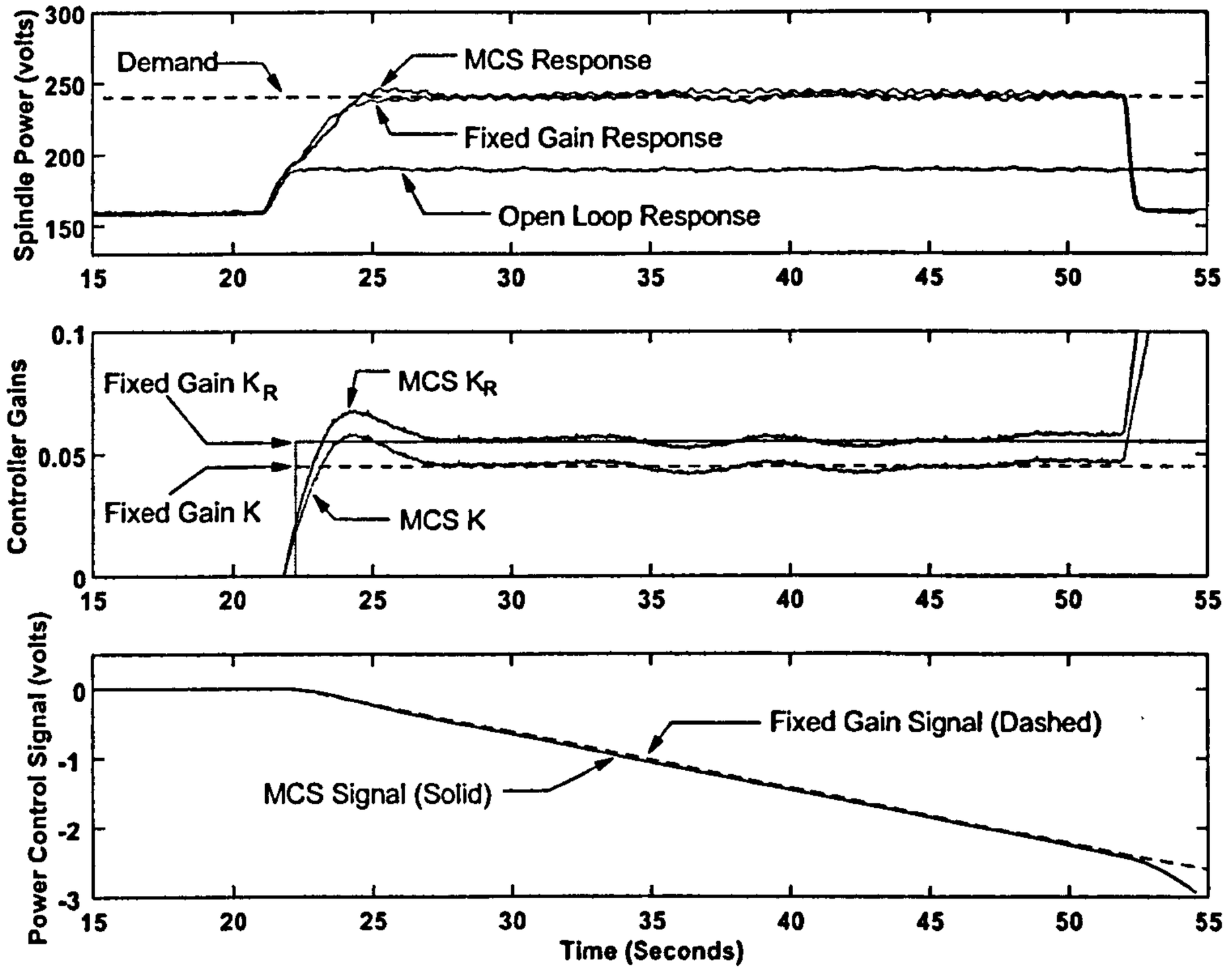

Figure 3.13: Results of tests carried out over constant geometry with a constant power demand for open-loop, fixed gain-control, MCS adaptive control. width of cut = 1mm, axial depth of cut = 3.9mm, spindle speed = 10,000rev/min.

Here the free spinning power of the spindle can be seen before 21.0s as 160W. When cutting actually started at around 21.0s this rose to a constant 190w. As in the simulation demonstrated previously the MCS adaptive gains started at zero and, when released at around 22.0s, arrived at their quasi-steady state values within around 5.0s. Successful tracking of the demanded power was achieved within around 3 - 4s with a good transient response, giving only one very small overshoot. This is due to the fact that the MCS controller gains were slightly over-compensating for the combination of two effects. Firstly, the response time of the pilot rig to the new feed-rate demand and secondly, the slow response of the power to the increased feed-rate, a point mentioned earlier when looking at the simulation and 3 phase power controller dynamics (section 3.2). The fixed-gain controller also achieved the target power with a slightly better transient behaviour in roughly the same time when it was switched on at 22.0s. At this stage the performance of the fixed-gain controller matched that of MCS, however, as the figure 3.14 shows, when

the power demand is not a constant value the benefits of the MCS controller begin to become apparent.

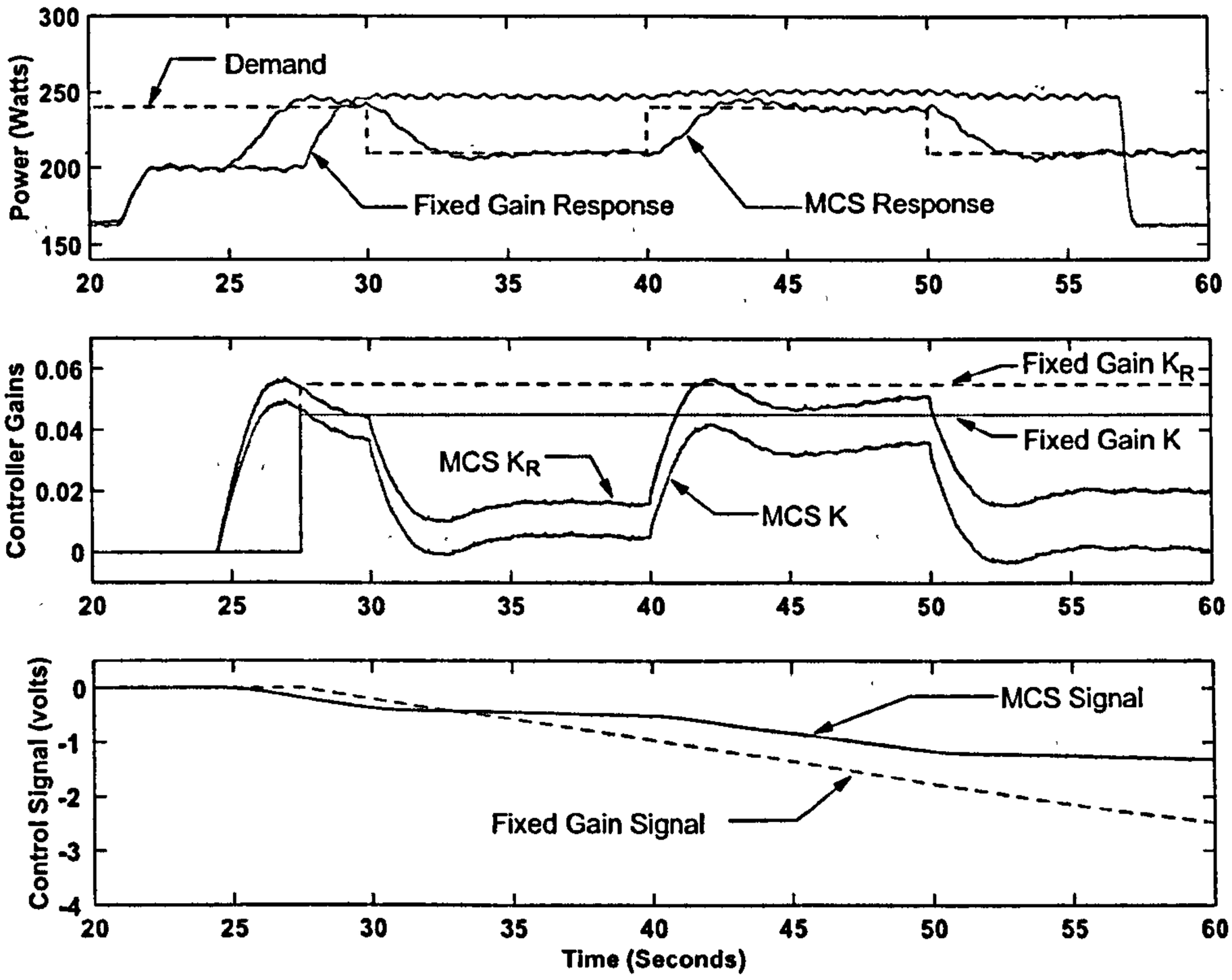

Figure 3.14: Results of tests carried out over constant geometry with a variable power demand for fixed-gain control, MCS adaptive control. width of cut = 1mm, axial depth of cut = 3.9mm, spindle speed = 10,000rev/min.

In figure 3.14 the graphs are arranged as before (power, controller gains, control signal) with only the fixed-gain and MCS controller responses being shown (no open loop). With both controllers the cutting tool entered the metal at around 21.0s. The MCS controller was switched on at 25.0s and the fixed gain controller was activated at 28.0s. As the power levels being demanded were similar to those in the previous case the fixed-gain controller gains were left at the same levels. As with the previous test the adaptive gains started at zero and reach the steady state values within five seconds, allowing successful tracking of the demand power with a settling time of roughly 3.0s.

The fixed-gain controller modified the feed-rate to roughly the correct levels after 2.0s with a small steady state error up until 30.0s. At this point the demand power underwent

a step change to a lower level of 200W. In response to this change the fixed-gain controller modified the feed-rate by an extremely small amount leading to a corresponding change in power of roughly 5W. This effect can be seen more clearly at points later in the test where the demand power changed (at 40.0s and 50.0s).

The MCS controller, however, successfully tracked the new demanded power level after only 2.5s with a good transient behaviour. The inability of the fixed-gain controller to respond to the demand change was due to the effect of the spin power making up a large proportion of the total cutting power.

In order to ensure a more effective use of the fixed-gain controller the spindle free spin power would either have to be a very low proportion of the total power, or would have to be constantly subtracted from the total power before being fed into the power regulation controller as was demonstrated in the simulations whose results are shown in figures 3.11 - 3.12, section 3.2. Another possibility would be the inclusion of integral action onto the fixed-gain controller which would offer benefits in the rejection of the effect of free spin power. However it is likely that introduction of such a measure would be to the detriment of closed-loop stability.

Looking closely at the power signals for each of the two tests shown above, a variation on the signal with a frequency of around 1.5Hz can be seen. Testing has shown that this variation was not a direct result of the power feedback loop but that it was due to the proprietary control algorithm used by the embedded BOSCH power controller.

In order to investigate the ability of the two controllers to provide stable control given a change in the plant parameters a series of tests (figures 3.15 and 3.16) were carried out at a higher loading factor. This took the form of an increased width of cut of 4mm with the axial depth of cut being maintained at 3.9mm. In order to compensate for the increased tooth loading the spindle speed was increased to 12,000rev/min.

Figure 3.15 shows the results of the fixed-gain controller strategy where the initial power demand was 450W. Once the controller was switched on at 14.0s it adjusted the feed-rate and realised the demanded power within 3.0s giving no overshoots and a good transient behaviour. The values of the gains used for this test ($K^{'} = 0.012, K_R^{'} = 0.018$) were quite different from those used in the previous tests ($K^{'} = 0.045, K_R^{'} = 0.055$) where a shallower cut was used. In fact, when the previous gain values were used, the controller

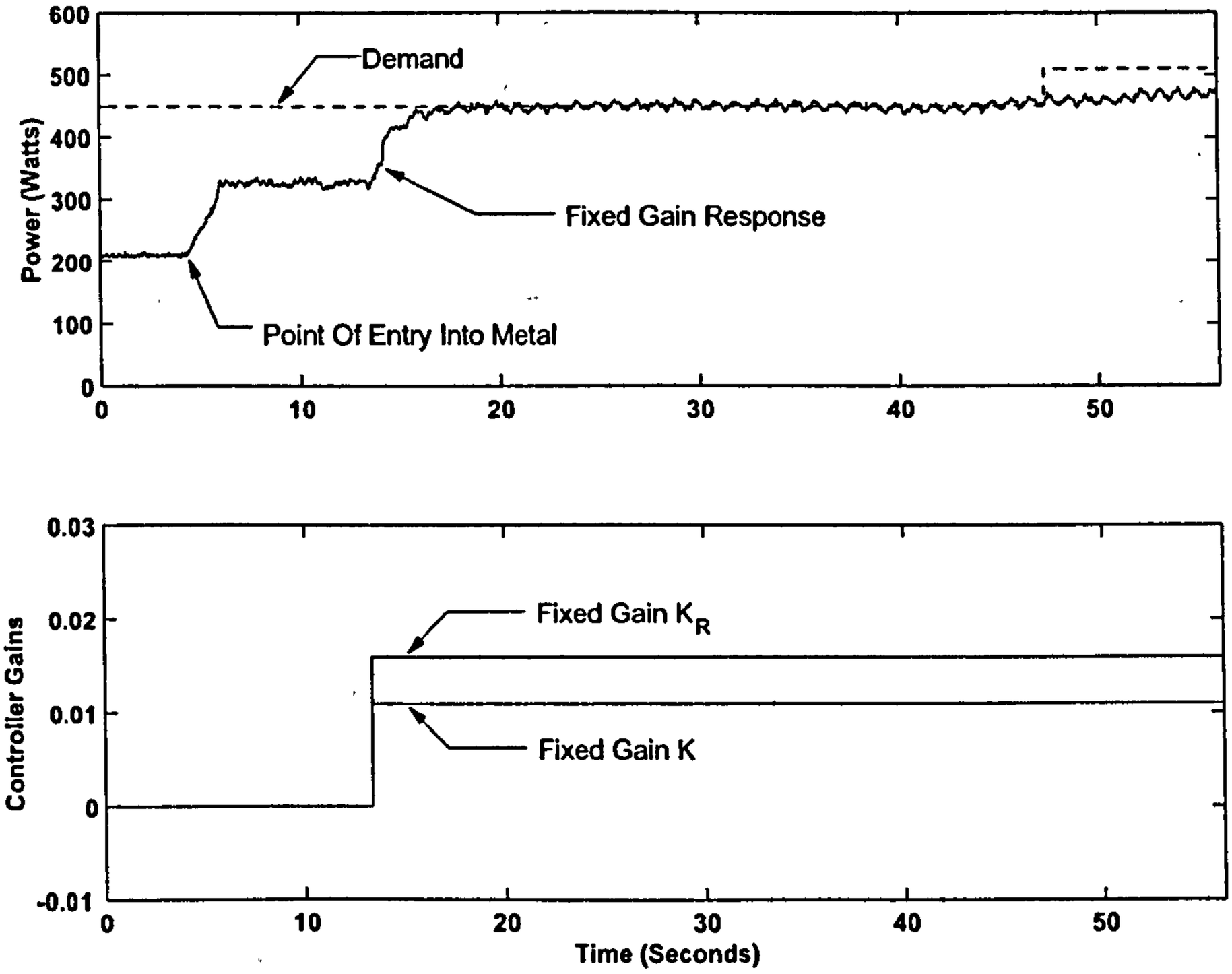

Figure 3.15: Results of fixed-gain controller regulated power cut, width of cut = 4mm, axial depth of cut = 3.9mm, spindle speed = 12,000rev/min

set the new feed-rate at a high level and never recovered within the life of the cut. This means that if a fixed gain controller of this type were to be used the geometry of cut would have to remain fairly constant throughout the machining cycle. This is certainly not true in the manufacture of wing skins where the profile of the cut constantly changes as well as the type of cut. Towards the end of this test the demanded power changed to the sightly higher level of 510W. As with the lower loaded cut (Figure 3.14) there was an initial period wherein a small amount of modification to the feed-rate took place, resulting in an increase in power of roughly 20W. After that period an error remained in the desired and achieved cutting power which was never recovered. This test indicated the need for integral action in the power loop so that the fixed-gain controller could overcome this error. Simulations have shown that introduction of integral action does indeed remove the errors seen in the steady state and also reduce the effect that the free spinning power of the spindle has on the efficiency of the fixed gain strategy. However, this is at the expense of the closed loop stability.

Looking at the first case in figure 3.16 the demanded power was set initially to 450W, varying from 390W to 510W later on in the test. The cutting conditions for this case were the same for those in the previously demonstrated test, axial depth of cut = 3.9mm, width of cut = 4mm, spindle speed = 12,000rev/min.

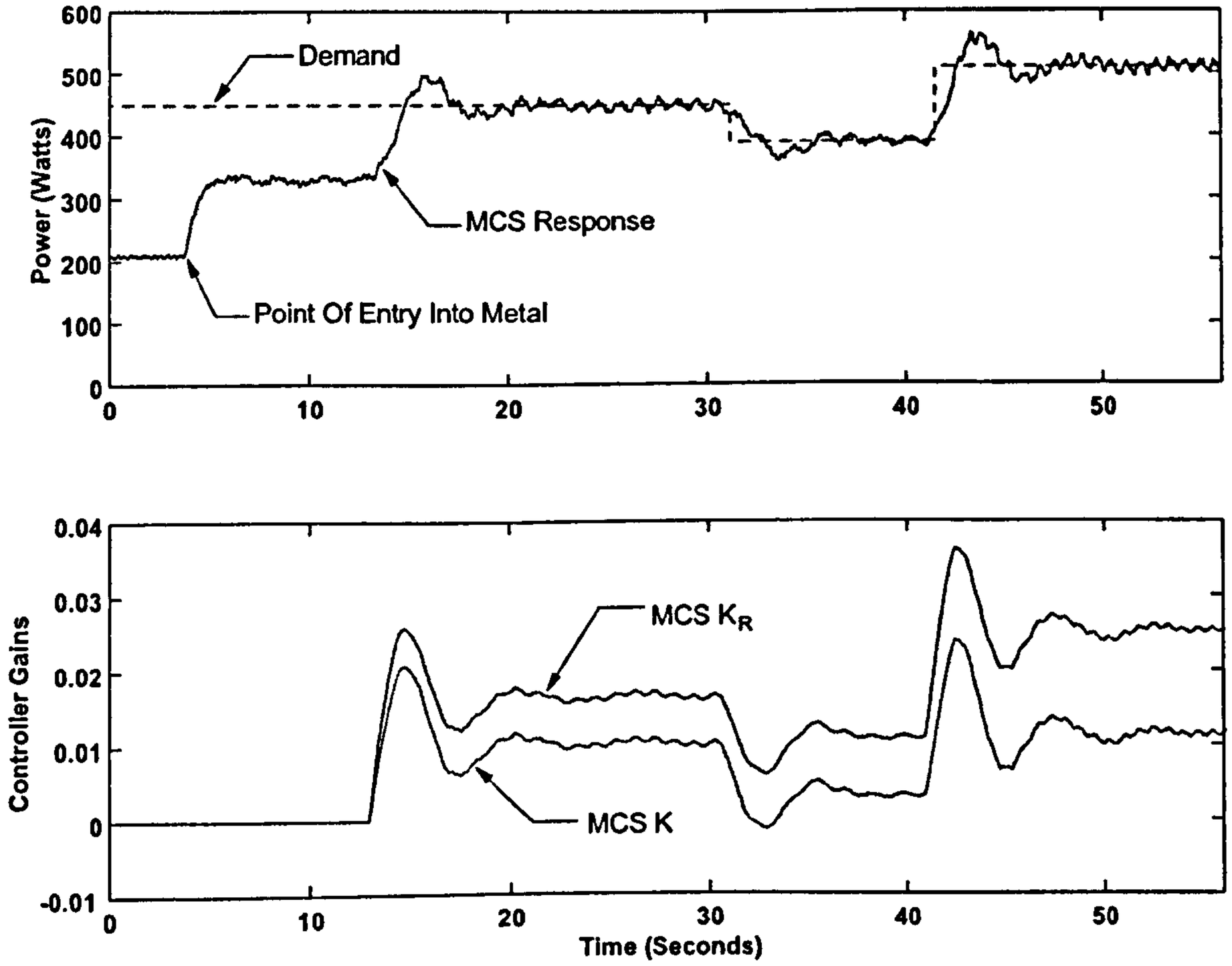

Figure 3.16: Results of MCS controller regulated power cut, width of cut = 4mm, axial depth of cut = 3.9mm, spindle speed = 12,000rev/min

With the MCS adaptive controller regulating the feed-rate, tracking of the demand power was achieved for each of the three demanded powers after a settling period of around 5 to 6s. This performance was achieved, unlike with the fixed gain controller, without any internal parameter changes. The transient behaviour in this case, however, was not a good as that seen with the smaller cuts. With each change in demanded power an overshoot was seen with a amplitude of roughly 50W. This was a result of the slow response of the pilot rig in arriving at the new demanded feed-rate. As mentioned previously, this resulted in the MCS power controller over-setting the desired feed-rate and not being able to recover quickly enough when that feed was achieved. Once again simulations confirmed this effect. If the proportional gain K_p used on the position control of the relevant axis (section 3.3.1)

was increased the performance of the system was much improved in terms of settling times and transient response. However increasing this gain led to problems due to noise on the relevant signals. Another proposed solution is the inclusion of an MCS loop around the pilot rig that would regulate its velocity. An important point to note, however, is that the pilot rig, and indeed any machine of this sort, will be subject to restriction on the maximum rates of acceleration and deceleration. This will certainly affect the stability of the MCS adaptive strategy over a range of desired feed-rates and should be investigated further in the future. Along the same lines, the controller being used to regulate the power sent to the spindle will play a fairly similar role. If the delay in which the BOSCH on board controller takes to achieve a constant spindle speed given, say, a change in the depth of cut, is large enough then a similar effect will be seen.

3.6 Further Single Axis Results

Figure 3.17 shows a series of tests during which the radial depth of cut was varied linearly throughout the cut. Given the previous results these tests were designed to look at the ability of the two controllers to cope with a constantly changing plant parameter, an area where MCS should perform well. Starting at a width of cut of 3mm at 20.0s and ending with 0mm at 85.0s the upper graph, as before, shows the levels of power obtained in three cases; open-loop, with a fixed gain controller and with the MCS controller. The lower graph shows the evolution of the MCS gains throughout the cut. The fixed gain controller gains were set at a value that gave good power tracking at the mean radial depth of cut.

The change in power due to the decrease in radial depth of cut can be seen on the open loop result. It is also worth noting that initially the demand power was equal to the open loop cutting power which means at the start of the tests neither of the controllers should have been doing any work in the regulation of the feed as the demand power was already being achieved. Firstly, the performance of the fixed gain controller performance is examined after it was activated at roughly 25.0s. It can be seen that after only 2.0s, as the difference between demanded and actual power slowly increased, the fixed gain scheme yielded unacceptable behaviour, increasing the feed to such a high level that it was deactivated at 31.0s. By contrast, however, the MCS controller yielded a good closed-loop response. The demand power was achieved throughout the duration of the cut, even at the latter end of the test where the width of cut was small. Eventually at 77.0s there

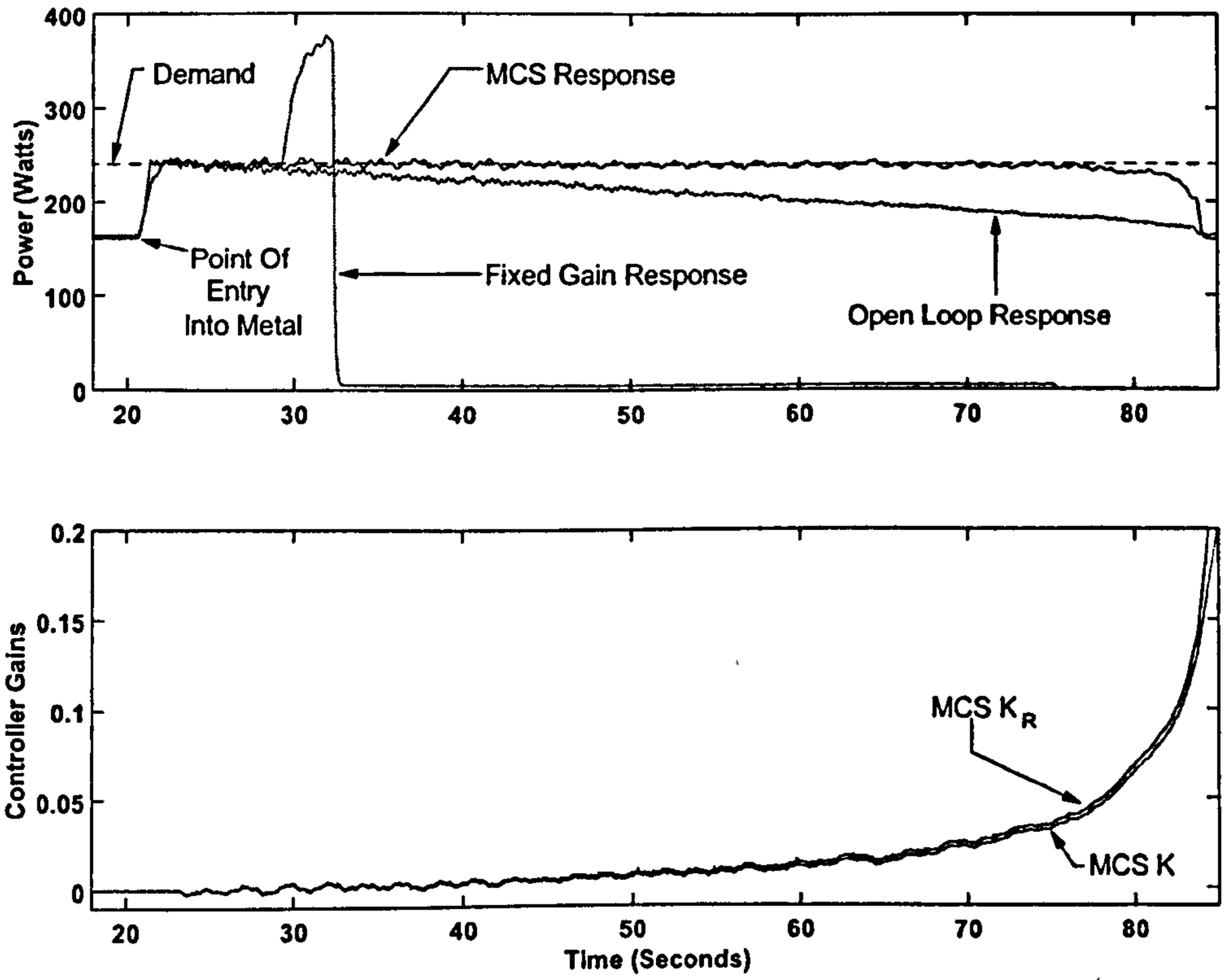

Figure 3.17: Results of tests carried out on a tapered cut, initial width of cut = 3mm, final width of cut = 0mm, axial depth of cut = 3.9mm, spindle speed = 10,000rev/min

was not enough metal to physically achieve the desired power given the limitations of the pilot rig and the actual power fell slightly under (77 - 82 seconds). The gains reflect this behaviour in that at the beginning of the test they were practically zero, indicating no need for control. As the cut narrowed so the gains increased in what appears to be, for a period, a roughly linear manner. At around the 70.0s stage the gains then increased at a much higher rate reflecting the point made earlier about the demanded power being almost unobtainable. The stable manner in which the gains compensated for the changing geometry of cut is very encouraging and is the main advantage that this form of controller over the more conventional types such as SFC.

In the previous test the variation in geometry was continuous, the next set of results come from a test in which the change in geometry of cut was instantaneous and unpredictable. It took the form of a step change in width of cut from 4mm to 2mm, whilst there was a constant depth of cut of 3.9mm. This test was only performed with the adaptive

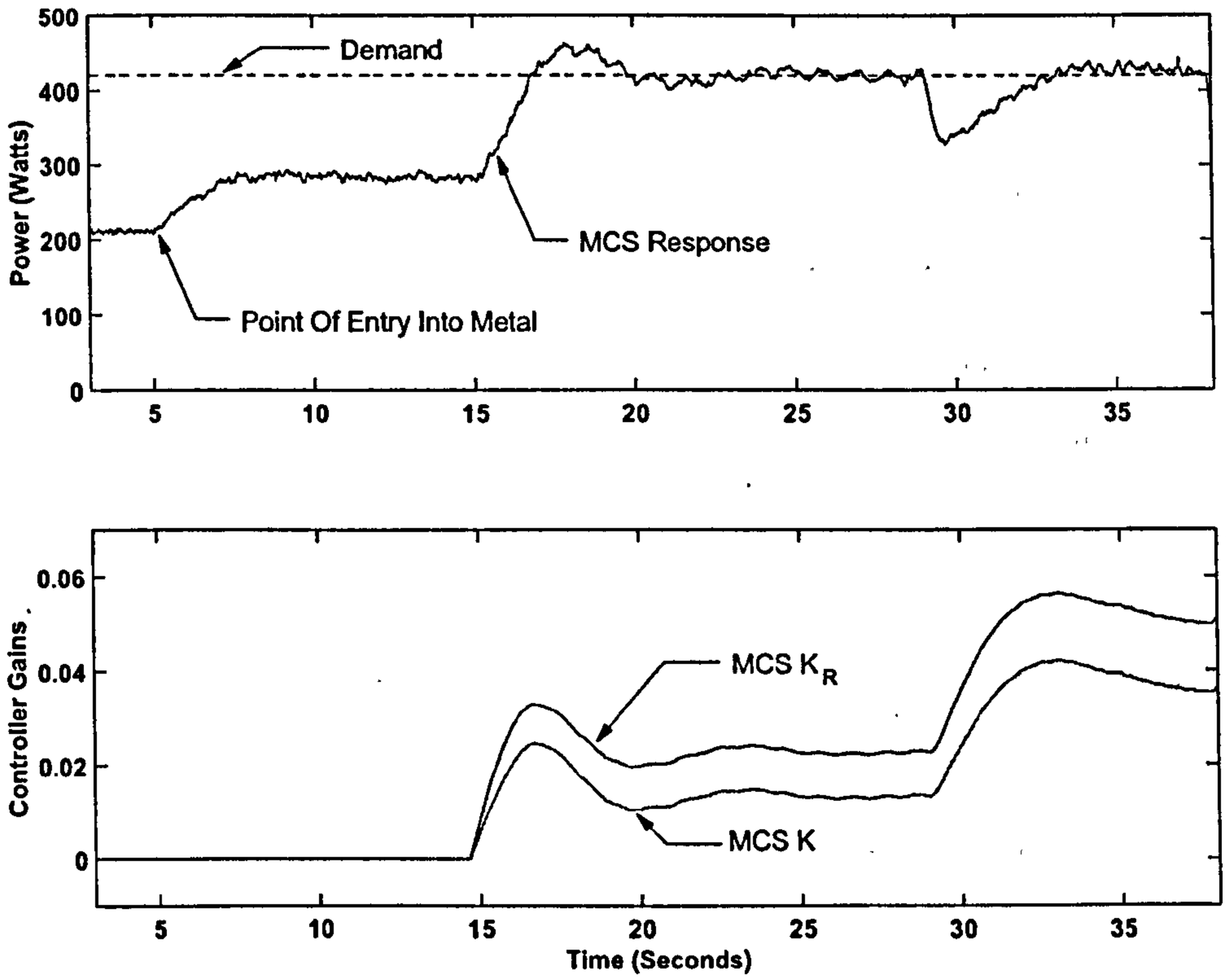

Figure 3.18: Results of MCS power regulated cut with step change in width of cut from 4mm to 2mm, axial depth of cut = 3.9mm, spindle speed = 12,000rev/min

controller as trials indicated that tool damage would result if the fixed gain controller were to behave in a fashion similar to that in the previous test. Results from this test are presented in figure 3.18. In this test the demand power was constant at 420W. The spindle entered the metal at 5.0s and the MCS controller was activated at 15.0s. The step change in width of cut occurred at 30.0s. As with the previous experiment, the demand power was satisfied and maintained after 5.0s with a small overshoot in the transient phase. On entering the new width of cut the demand power fell to a lower level as expected and after only 4.0s the MCS controller adjusted its gains in order to compensate for the instantaneous change in the plant. Once again it is encouraging to see that the response is stable even over the large change in depth (100%).

3.7 Conclusions

Metal machining and particularly the milling process is being used more and more to replace conventional metal processing methods such as castings a assembly from pre-fabricated parts. The majority of cutting process performed on the factory shop floor are still performed in an open-loop manner resulting in unnecessarily long machining times.

A pilot rig has been commissioned for use in experiments investigating ways of improving and regulating the metal milling process, specifically for aluminium components.

A controller strategy that provides a method of regulating the mean cutting power by continuous variation of feed-rate has been developed and tested in simulation. The strategy has been demonstrated on the pilot rig for single axis cuts under various conditions including:

- Constant demand power
- Variable demand power
- Variable cut geometries
- Continuously varying cut wrap angle

using either a fixed-gain or adaptive controller algorithm.

The advantages of using an adaptive MCS strategy over standard fixed-gain technologies have been demonstrated. The adaptive controller strategy considered performed well in a single axis for a range of types and geometries of cut. Limitations on the speed at which changes in power could take place were imposed on the MCS controller due to the unknown dynamics of the cutting spindle power controller. This unit uses an unknown non-linear algorithm to maintain a constant spindle angular velocity that results in its own set of dynamics. The lag with which the spindle controller responded introduced a de-stabilising effect into the power regulation MCS loop. No data on these dynamics is available as it is industrially sensitive information. However if these dynamics could be investigated and quantified it is possible that they could be taken account of by placing them in the reference model of the MCS controller routines. This would ensure that the MCS algorithm did not "over-demand" the feed-rate as was seen in experiments where either α set too sensitive and/or the settling time, t_s was set at to fast a value.

The machines in industry use spindles capable of delivering powers to the cutting tools

of up to 100kW. In order that the algorithms can be considered for use on these machines a stability study should be performed.

Currently the physical dynamics of the spindle are not accounted for when calculating cutting power from electrical power. Electrical machines consume power when accelerating and will also consume power to overcome bearing loss and drag losses. In order to refine the cutting power measurement these variables should be taken into account. Also a negative feed-rate does not lead to a negative cutting. In fact, negative feed-rates will not be acceptable in industry. Methods that make to MCS algorithm more robust to such non-linearities are essential before the algorithm can be used in safety critical (and non-experimental) applications such as this.

Chapter 4

Process Modelling of a Metal Milling Process

SUMMARY: A review of existing cutting force models is given. The need to derive peak cutting force from spindle power is presented. A single axis model linking the main process variables to the cutting power and cutting force is presented with calibration against milling experiments. An empirical model relating cutting power to peak cutting force based on the cutting tool/workpiece combination discussed is presented.

4.1 Theories of Metal Cutting - Past and Present

Investigative research in the area of metal cutting started in the mid 19^{th} Century with the compilation of empirical work relating the work expended to geometry of cut for a twist drill.

4.2 Microscopic Level

The publication of Ernst and Merchant's work in 1941 [170], summarising the bulk of the work carried out to that date on the analytical study of chip formation during metal cutting, marks the start of the more recent phase of research in that field. In this and subsequent papers, [171–173] the author identified the three basic chip types accepted today :

- Type 1 : Discontinuous chip
- Type 2 : Continuous chip
- Type 3 : Continuous chip with built-up edge

and went on to develop a system of equations for Type 2 chips that described the orthogonal cutting process relating cutting forces to tool and material properties. He established the idea that there were two main processes involved in chip formation. These were firstly, continual plastic deformation of the metal along a shear plane that runs from the tool tip to the surface of the workpiece (figure 4.1), and secondly a force required to overcome friction at the tool-chip interface. In so doing he dispelled the notion that it was a process akin to that seen when splitting wood with a hatchet. This analysis was added

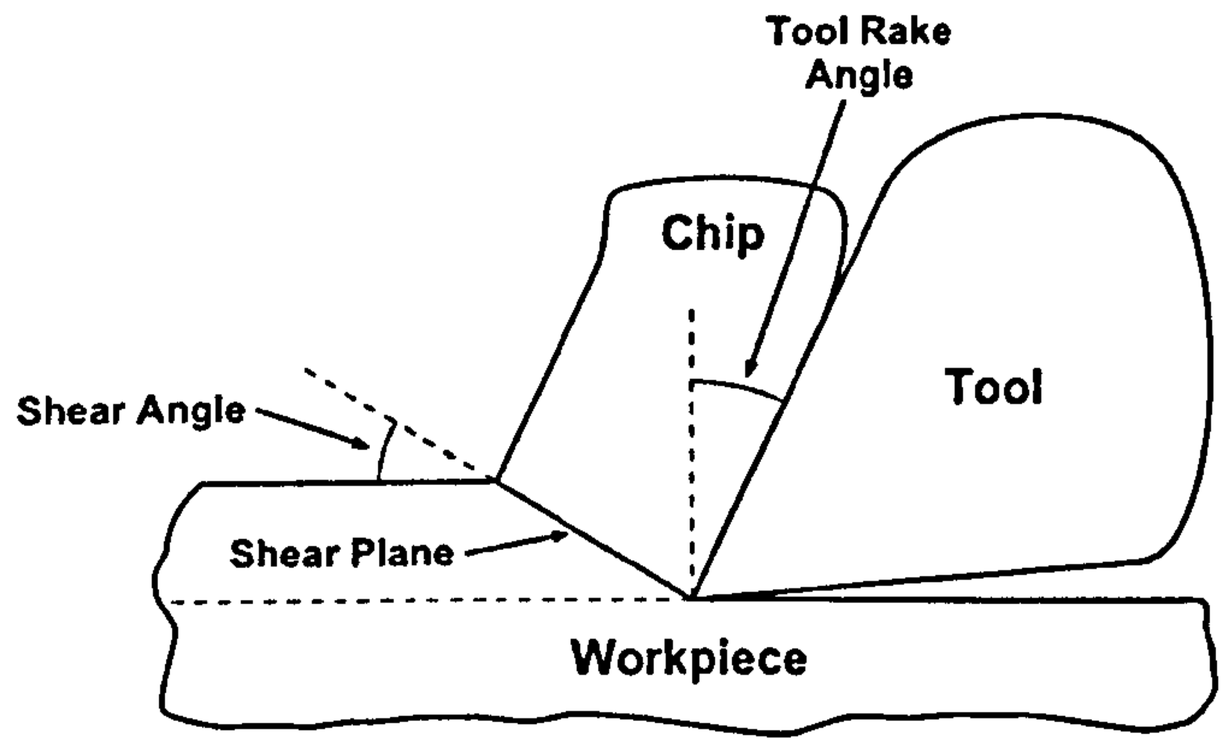

Figure 4.1: Schematic representation of Merchant's chip formation model

to by Lee [174] who, via the theory of plasticity, extended the notion of a single shear plane to include a zone of quasi-plasticity above that plane. This allowed the derivation of a similar solution for shear angle but, in addition, provided the means for the analysis of the cutting process where built-up edge (Type 3) chips were produced. The resulting system of equations, however, included parameters that where not obtainable by any independent means reducing their usefulness and subsequently allowing experimental data to be fitted in the desired manner. In a further effort to understand the basic processes that occur when cutting metal Palmer and Oxley [175] performed experiments and an analysis without the majority of assumptions previously adopted. In their experiments metal was filmed whilst being cut at very low feed rates and individual metal crystals followed from undeformed work through to chip. By following a large number of crystals they identified

a relatively large zone within which plastic deformation occurred in the formation of a chip. Using the ideal theory of plasticity in conjunction with their experimental picture they broke this zone into two distinct slip line fields. However, they could not make these two fields meet in the middle without reducing the problem to that of a single shear plane, a situation which their experiments clearly disproved.

In an attempt to overcome this disagreement the effect of work-hardening was included in the plastic analysis resulting in a detailed picture of the process. One disadvantage of this picture was that it took a long time to interpret for each material, for different tool properties, etc.. Therefore a simplified approximative method based on the main factors of this analysis was generated allowing the calculation of machining forces from metal and tool properties. Once again, however, some of the parameters required came from their particular experimentation only and were based on some questionable assumptions, one of which implied that the tool edge was not involved in the cutting process. The extreme cutting conditions used (0.02mm/min) can also be regarded as a source of inconsistency with respect to the general process.

In response to these points further work was carried out [176,177]. The main objective of this work was to define a standard method of determining parameters that could be used in a model to determine cutting forces based, as before, solely on tool, workpiece and cutting conditions. The experiments were carried out at more realistic cutting speeds and also effects of temperature on the shear strength of the material were included. The results predicted trends in machining well but generally proved too specific to be applicable to a range of cutting processes.

This is, in fact, true of a great deal of the research of this type and seems to be due to the fact that the process is not entirely constrained in the way other processes such as extrusions, drawing, etc. are. Whilst giving a valuable insight into the physical processes involved when cutting metal the analyses give only estimates of trends for what is a very simple case of cutting, that is to say orthogonal cutting.

Most real cutting operations are much more complex. In milling the cutting edge is curved, sometimes with quite a small radius of curvature. Also the depths of cut during a typical milling operation will be continuously changing through the cut. In the majority of the research of this type no account is made of the fact that the tool is not perfectly sharp and that the cutting force will contain a component due to the force exerted by

the tool on the newly cut surface (size effect). Friction on the tool face/chip interface is largely assumed to be coulomb friction with a constant value over the whole surface of the tool.

It is most likely for these reasons that, when referring to a particular metal cutting operation, the majority of models formed more recently have moved away from the microscopic level. Instead they look at the more general process level concentrating on process variables such as geometry of cut, feed, etc. with tool and material properties being incorporated into some form of constant of specific energy or pressure, K_{mat}. The remainder of this section will concentrate on the work carried out in this area.

4.3 Higher Level Modelling

One of the first models of this type was proposed by Boston in a phase of research that began in 1932, [178], [179]. The main outcome from this research was an expression that linked the energy expended in a very simple case of milling (single tooth, single cut) to the geometry of the cut. Specifically, this expression took the form:

$$E = K_{mat} b a^x f^y \tag{4.1}$$

where f is the feed per tooth, b is the length of the cutting edge (or axial depth of cut) and a is the width of cut as shown in Figure 4.2. K_{mat}, x and y are constants specific to a particular workpicce and tool combination. A range of tests was carried out for various metal/lubrication pairs identifying good milling practices, however no trends were highlighted linking K_{mat}, x or y to any material properties. Further, the method of experimentation provided a great deal of room for error in the results. Moving a step further a geometric analysis of the milling process was carried out in 1941 by Martellotti [180], [181], who examined the kinematics of the tool tip through several revolutions of the cutter. Concentrating on the fact that the locus of such a point is trochoidal he proposed a set of formulae that gave the undeformed chip thickness of the chip at any point during a revolution of the tool for both up and down milling. Also the dependence of the specific cutting pressure, K_{mat}, on the average chip thickness was demonstrated along with a comprehensive investigation into the process that marked a major step forward in the understanding of the milling of metals.

In the majority of research that follows attempts to model cutting forces during milling

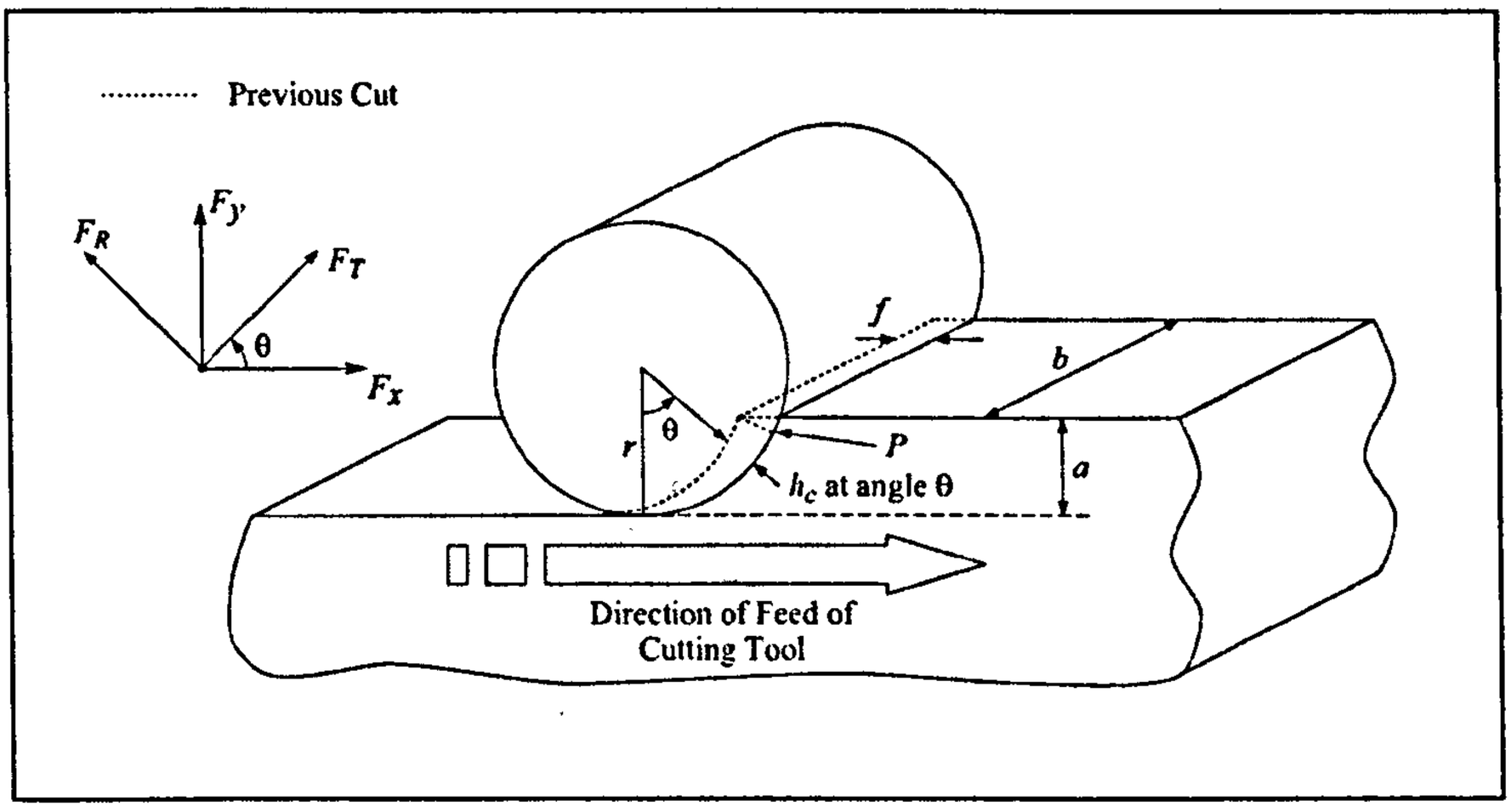

Figure 4.2: Definition of milling parameters

fall into two main categories. The first of these is a fully analytical approach. Assuming a milling tool with a constant helix angle is used, the milling operation for a single tooth will consist of three discrete regions of continuity. Figure 4.3 shows the cutting plane under scrutiny with figures 4.3 (b) and (c) showing each of these regions in the two cases of cut that can exist when a single tooth is cutting. Area WXYZ represents the plane of the cutting edge for a single tooth. In figures 4.3 (b) and (c) the upper part of the figure represents the cut at several stages were it to be flattened out. The dotted lines show the boundaries for the three regions of cutting, the bold lines represent an example of the length of the cutting edge when the tool is cutting within that region. The lower part of each figure shows an example of the cutting forces exerted during these regions of cutting.

The first region begins when the tool tip enters the workpiece and the length of the cutting edge that is in contact with the workpiece is increasing (region A). During this phase the force will increase slowly at first with the rate of increase in force getting larger as more of the tool enters the cut and the undeformed chip thickness at the tip increases. The next region occurs when the length of the cutting edge in contact with the workpiece remains constant (region B). Here the magnitude of the milling force with respect to the current angular position of the tool tip can assume one of many forms depending on the geometry of the cut. Two different cases are presented here both having a width of cut, a, which is less than the radius of the cutting tool. If the axial depth of the cut, b, is large when compared to the width of cut, a, (Figure 4.3(b)) then during this second phase the cutting edge will be a constant length moving up the workpiece with the net undeformed

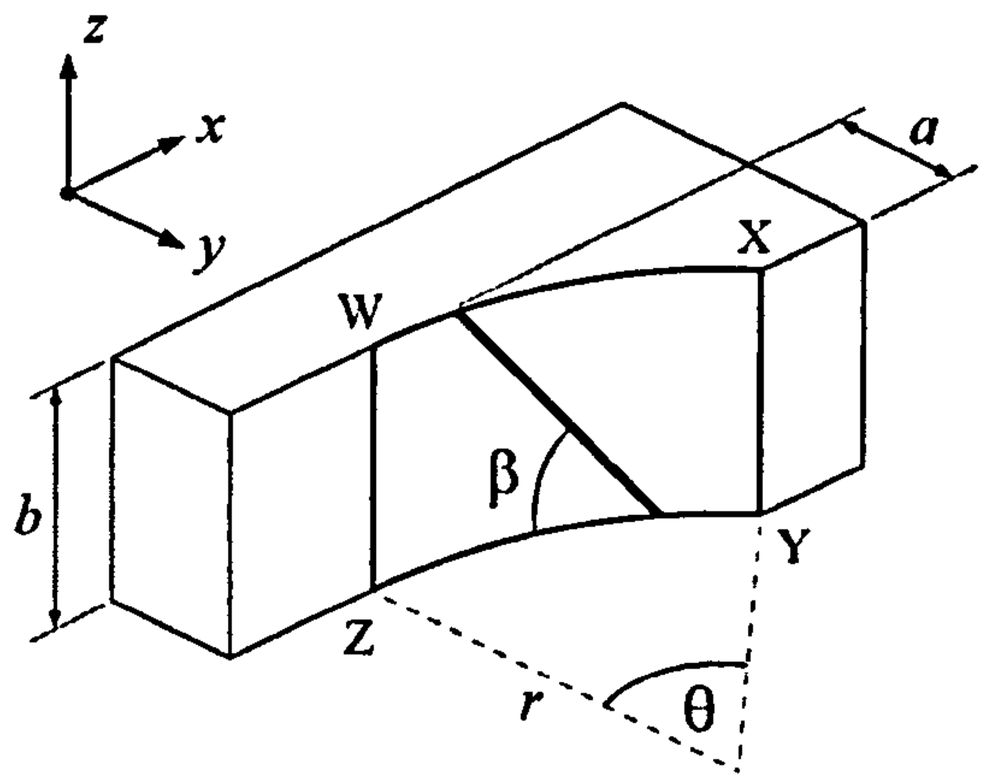

(a) Schematic of Cut Showing Specific Regions

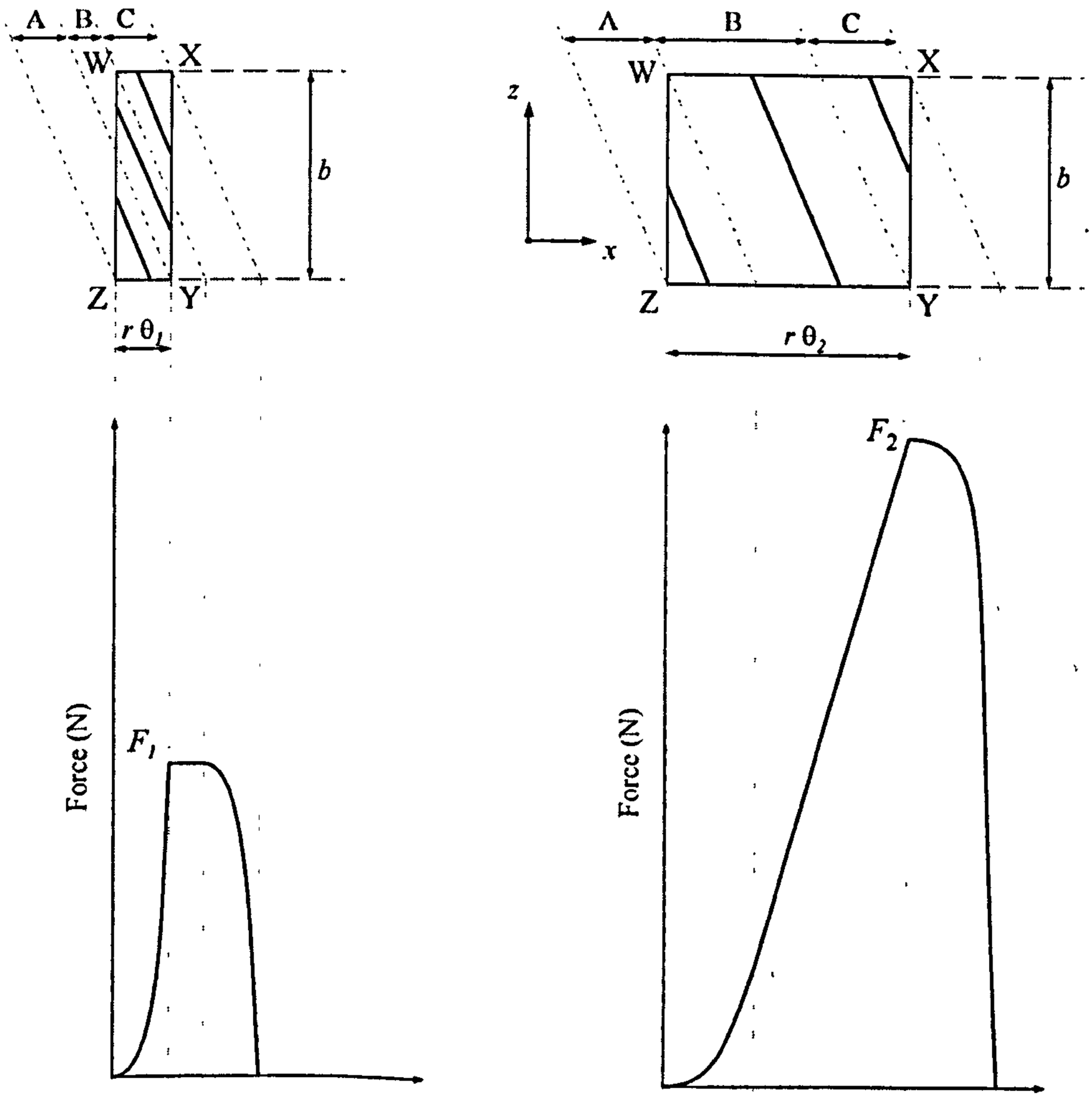

(b) Case 1: $b > \frac{b}{tan\beta}$

(c) Case 2: $b <= \frac{b}{tan\beta}$

Figure 4.3: Force shapes for two different geometries of cut

chip thickness remaining constant. This results in a constant tooth force. However if the width of cut is large in comparison with the axial depth of cut a very different pattern of behaviour will occur (figure 4.3 (c)). As before the length of the cutting edge remains constant during this phase but because the cutting edge is now moving across the cut the undeformed chip thickness will be increasing at all points as a function that can be approximated by a sine wave. This means that there will be a large, sharp increase in the cutting force during this phase.

Finally a third r, as shown in region C in Figures 4.3 (b) and (c) will occur as the cutting edge exits the cut and therefore its length in contact with the workpiece decreases. The shape of this phase is the same for both types of cut.

In an early analysis [182], the cutting force was expressed for a single tooth in terms of the angular position of the tool tip for each of these three regions of cutting. The resulting force profiles (similar to those shown in Figures 4.3) for a complete revolution of the tool provided a good degree of accuracy when compared with experimental tests both in terms of the values of peak forces obtained and the shape of the force profiles. However, due to the nature of the analysis, no account was made for variations in the undeformed chip thickness that may occur due to deflection of the tool/workpiece as well as effects caused by tool run-out[1]

The second category of model used to approximate cutting forces is similar in approach to finite element techniques. It has recently become more convenient thanks both to availability of fast computers and due to the fact that it can be extended fairly easily to include phenomena that affect the forces seen at the tool tip.

The technique involves splitting up the tool along its length into i thin, discrete discs of equal thickness, dz, as shown in figure 4.4. The forces seen at the cutting edge of each of these discs are then modelled as a function of the specific cutting pressure, $K_{mat,i}$, and the undeformed chip thickness, $h_{c,i}$, usually of the form:

$$F_{cut,i} = K_{mat,i} h_{c,i} \tag{4.2}$$

It is the determination of the correct value of $h_{c,i}$ for each axial disc of the tool that forms the critical, time consuming part of the calculation. In the simplest case the tool

[1]The term *tool run-out* refers to small, local variations in the effective cutter radius caused by an incorrectly mounted tool, [183].

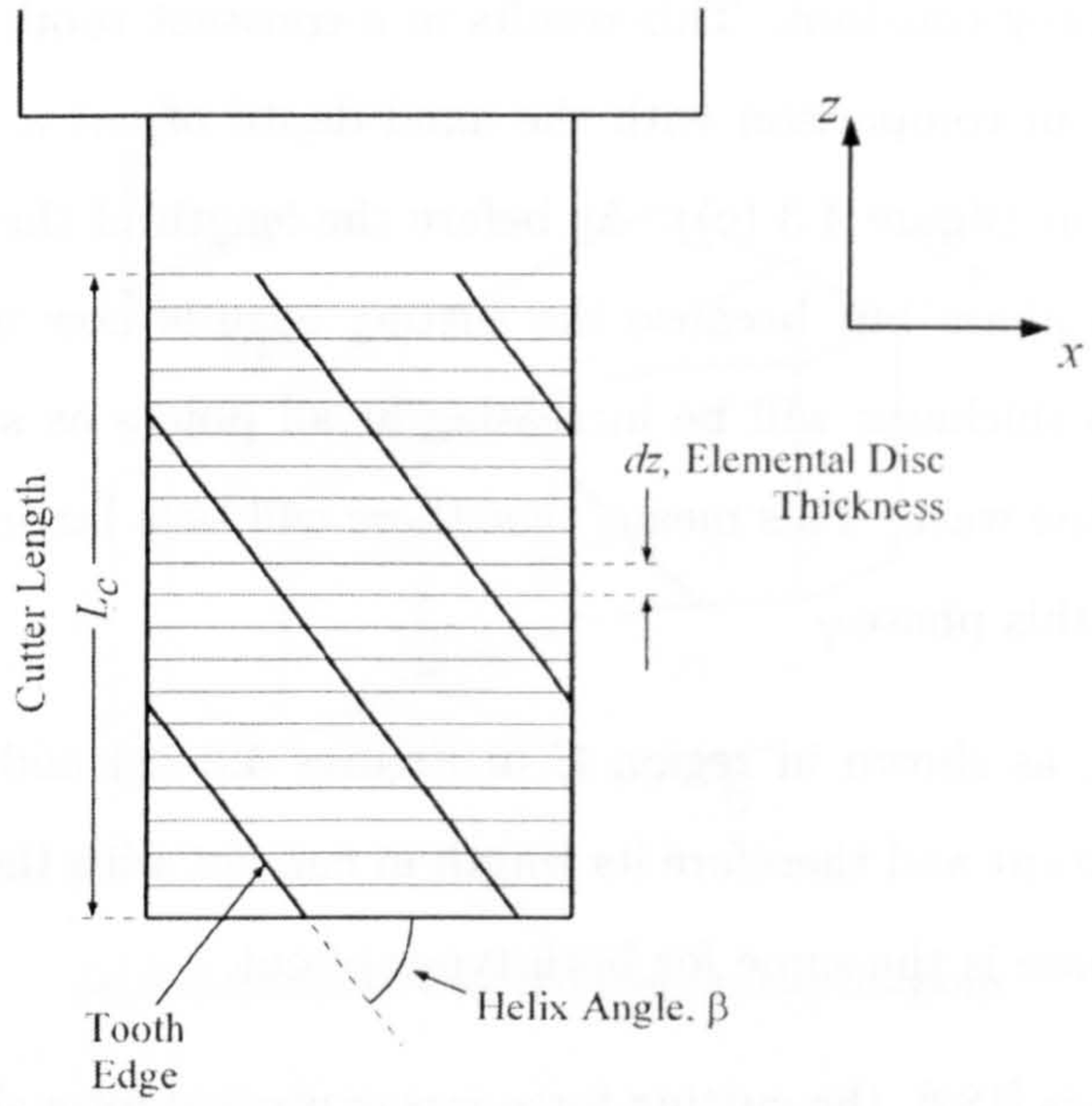

Figure 4.4: Discretisation of cutting tool

is assumed rigid with no run-out and a constant geometry of cut. The undeformed chip thickness can then be evaluated as:

$$h_{c,i} = f \sin(\theta_i) \tag{4.3}$$

where

$$\theta_i = \theta_0 + i \sin(\beta) dz \tag{4.4}$$

and $\theta_0 = \theta$ at the free end of the tool for the current cutting edge.

The finite model then checks which discs are currently cutting metal, via simple geometry, and sums the forces in each disc to give a final value for total cutting force. More recent models use a history that keeps a record of the path of the previous revolution's cutting edges. This allows a variable geometry of cut to be accounted for and therefore deflections of the tool and variations in cutter geometry due to run-out can be modelled successfully. This has been attempted [184, 185] using, in the first case, a static approach in which the cutting tool is assumed to behave as a cantilever beam in both x and y directions. The total cutting force, F_c is applied as a point load at the force centre, a point along the axis of the tool, z_c, defined as:

$$F_c z_c = \sum_{i=1}^{\frac{L_c}{dz}} F_{c,i} i dz \tag{4.5}$$

i.e. the point which allows the moment produced by the total force to balance the sum of the moments produced by the elemental discs. The resulting deflection of the tool leads to a new value of undeformed chip thickness. The force and cutter deflection calculations for that time step are repeated until the result converges. The resulting deflection at that time step is then stored for use in the calculation of the undeformed chip thickness in future time steps. A good agreement was seen in terms of the cutting forces and surface finish when compared with experimentation. Also the significance that run-out plays with respect to the peak cutting force during a revolution of the tool was confirmed, in some cases leading to forces on a particular tooth being double that of another. Taking the analysis a step further, a dynamic model, figure 4.5 has also been used to model deflection of the cutting tool using a similar approach, [186–189]. Here the dynamics of the cutting tool are modelled as a pair of second order differential equations:

$$M_x\ddot{x} + c_x\dot{x} + k_x x = F_x \tag{4.6}$$

$$M_y\ddot{y} + c_y\dot{y} + k_y y = F_y \tag{4.7}$$

which have allowed the effects of regenerative chatter to be included in the model as well

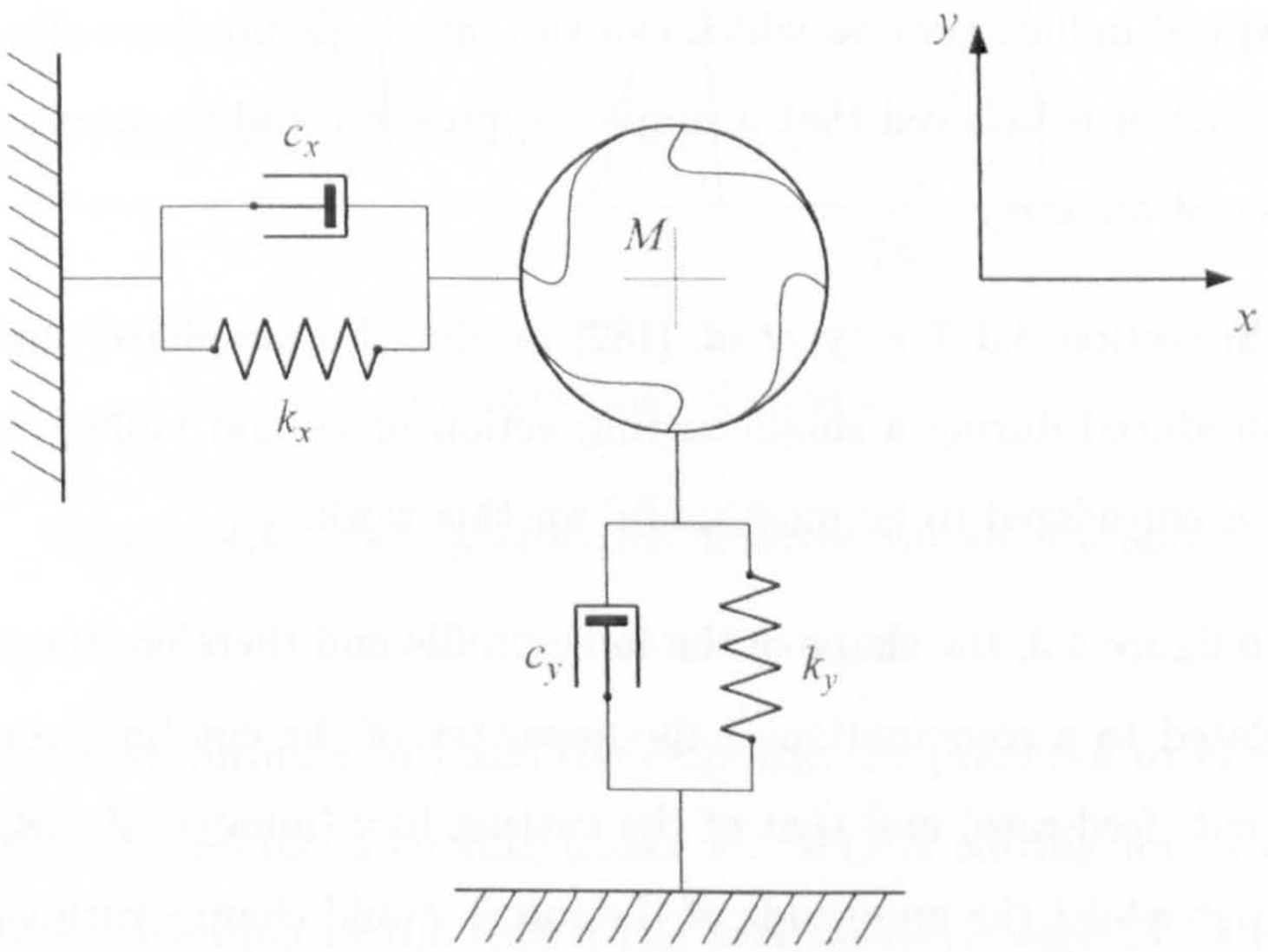

Figure 4.5: Dynamic cutting tool parameters

as consideration of the effect of ploughing forces, a force caused by the underside of the cutting tool rubbing against the newly cut surface.

4.4 Proposed Process Modelling - Linking Power to Force

As can be seen from the review presented in this chapter milling force is dependant on a large pool of process parameters including material and cutting tool properties and well as the geometry of the cut in question. Experience on the workshop floor has determined that the aim of an adaptive milling process would be to increase throughput whilst maintaining a suitable tool life. As tool paths in industry are mainly determined by the finished workpiece geometry and the geometrical capabilities of the relevant cutting machines the main method for increasing the throughput is via on-line manipulation of feed-rates. The factors limiting the rate at which the metal can be cut away are workpiece surface damage, machine power and cutting tool life. However it is the tool life which can be related directly to the peak tool tooth loading that dominates the limits the rate at which a cut can proceed.

With electrical spindle power consumption being the available variable for regulation a method of relating this variable back to the peak tooth loading is required so that an adaptive strategy using this variable can be justified.

Rather than attempting a full analytical model that accounts for all of the parameters present in a typical milling process which can run into large numbers of parameters for a even simple model, it is believed that a simpler approach could be attempted resulting in a similar degree of accuracy.

As shown in section 4.3 Tlusty *et al.* [182] produced a simplified analytical solution to the forces produced during a single cutting action of an end milling tooth. It is this approach that is considered to be most useful for this work.

As shown in figure 4.3, the shape of the force profile and therefore the peak tooth load is primarily related to a combination of the geometry of the cut (in terms of width and axial depth of cut, feed-rate) and that of the cutting tool (number of teeth, helix angle). It is believed that whilst the amplitude of the forces would change with variations in the cut and tool geometry there exist discrete regions for which the shape of the force profile remains the same. For example, the force profile shown in figure 4.3 a.) would retain the same shape provided that:

- The ratios of the depths and widths of cut and tool helix angle remained the same

- Variations in these ratios remain localised.

Figure 4.6 shows theoretical force profiles for cuts having two different series of values of widths, a, and depths, b, of cut. Figure 4.6 (a) shows the forces for a cut having large values of a and b with 4.6 (b) having small values for these parameters. The parameter

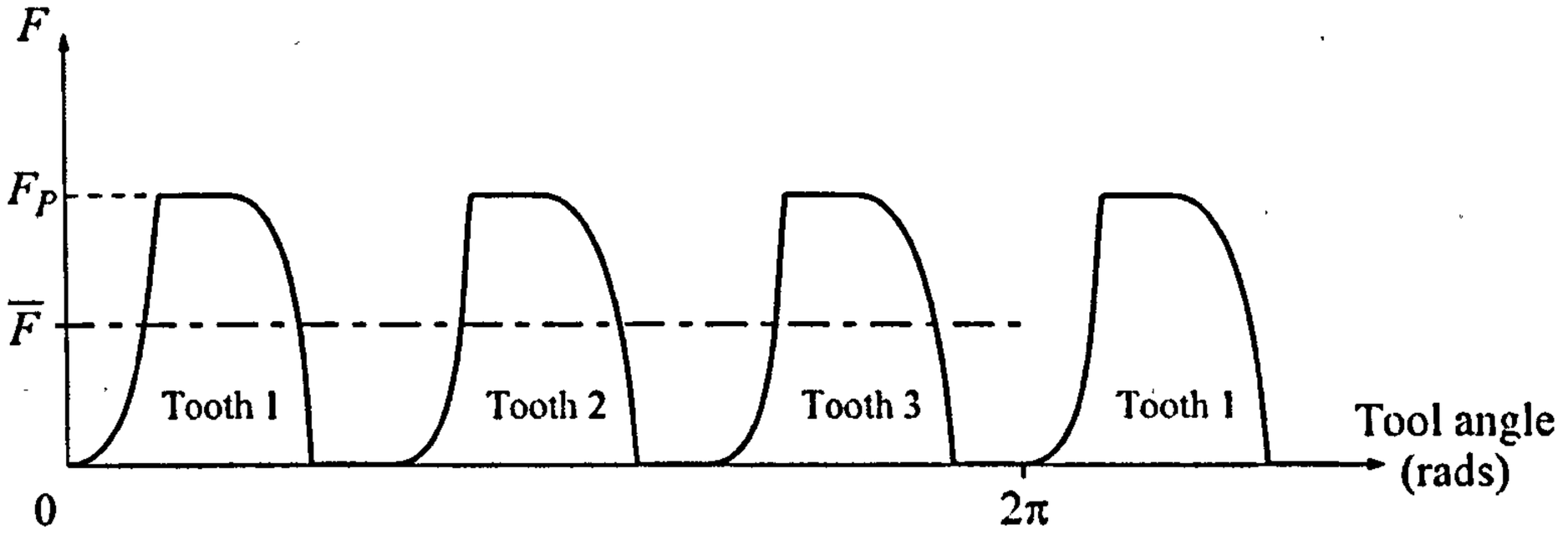

(a) Large Values of a and b

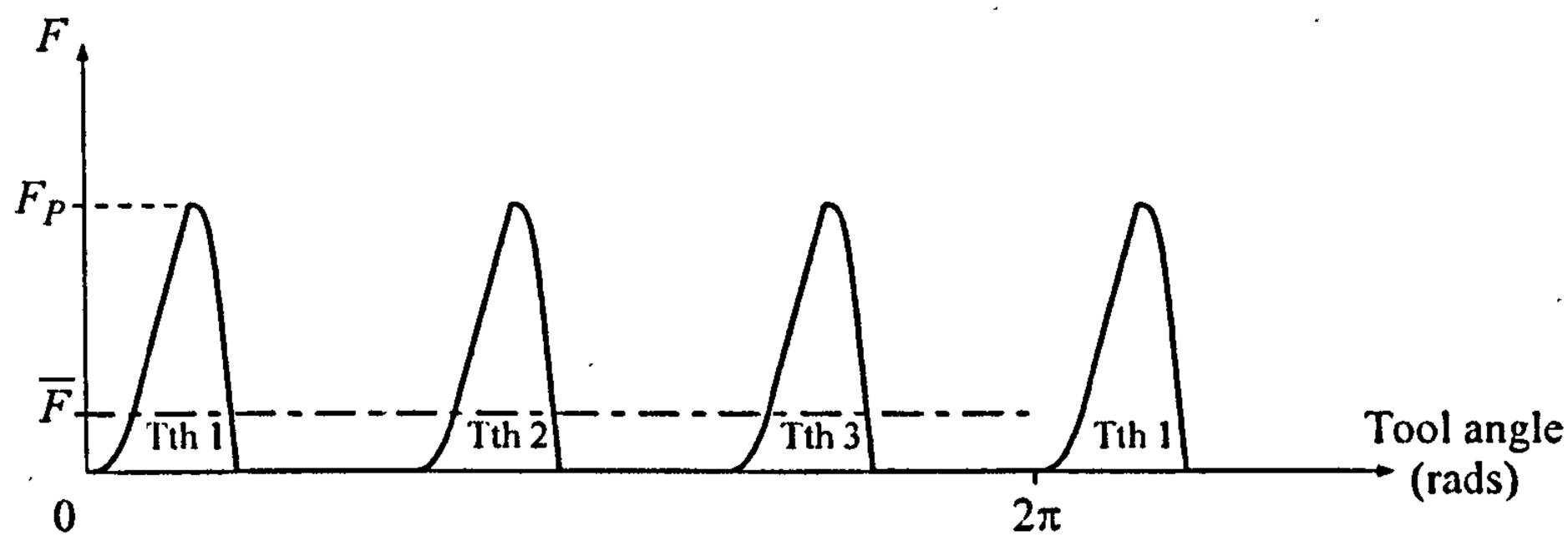

(b) Small values of a and b

Figure 4.6: Force profiles for different values of a and b

that can be measured during a cut, and therefore has the potential to be regulated using closed-loop control is the mean cutting power $\overline{P}$. Whilst cutting forces change at high rates during each revolution of the tool if the average force were to be computed for a complete revolution of the cutting tool it would result in a mean cutting force, $\overline{F}$ which should correspond to that given by:

$$\overline{F} = \int_0^{2\pi} \frac{F}{2\pi} d\theta \tag{4.8}$$

Assuming that the majority of cutting occurs on the outside helix of the milling cutter

and not on the underside, mean cutting force, $\overline{F}$ could also be extracted as:

$$\overline{P} = \overline{F} r \omega \tag{4.9}$$

where r is the tool radius and ω the tool's angular velocity.

Relating that mean force back to a peak cutting force, F_p as seen in figure 4.6 is a complex task which is highly dependant upon the geometry of both the cutting tool and the tool/workpiece interaction, see section 4.1. However, for a single cutting tool, a good estimate of the peak cutting force is possible by identifying and grouping together certain cutting geometries and applying assumptions as to the shape of the cutting force profile at various stages of the cut. This would provide a fast means of allowing peak cutting force regulation via the measurement of power. However this measurement would be insensitive to the extra forces produced by tool run-out (mis-aligned mounting of the cutting tool in the spindle) and cutting tool deflection.

4.5 Development and Testing of a Process Model

4.5.1 Machine Tool Dynamics

To allow investigation of the power-peak force relationship over a range of conditions, and to provide a simulation platform for control strategy development and testing, a simple mechanistic model of the cutting process was developed in SIMULINK/MATLAB. The model considers the static force produced on a thin slice, dz of the cutting tool as previously described in section 4.3. Referring to figure 4.2, the static tangential force, $F_T(t)$, produced by the ith slice of the cutting tool and the jth cutting tooth can be approximated by [182]:

$$F_{T,ij}(t) = K_{mat} * dz * f^y * sin(\theta_{ij}) \tag{4.10}$$

where θ is the angle between the point at which the cutting edge entered the cut and current position of the cutting edge for cutting tooth j and slice i of the tool in question (see Figure 4.2). The radial force is then approximated by:

$$F_{R,ij}(t) = K_{rad} * F_{T,ij}(t) \tag{4.11}$$

with the total forces exerted on the cutting tool being:

$$F_T(t) = \sum_{i=1,j=1}^{i=N_{flutes},j=\frac{L_c}{dz}} F_{T,ij} \tag{4.12}$$

$$F_R(t) = \sum_{i=1,j=1}^{i=N_{flutes},j=\frac{L_c}{dz}} F_{R,ij} \tag{4.13}$$

Average forces and hence cutting power and torques could then be calculated based on equations 4.8 and 4.9.

In order to calibrate the parameters of the model a series of cutting experiments using a billet of 2024 aluminium as the workpiece and a 2-fluted, 14mm diameter carbide cutting tool on a milling machine were commissioned. A Tektronix 3014, 4-channel scope was used to collect 3-axis data simultaneously from the Kistler Type 9257A 5kN, 3 component force transducer, shown in figure 4.7. The transducer uses four series of three piezo-electric

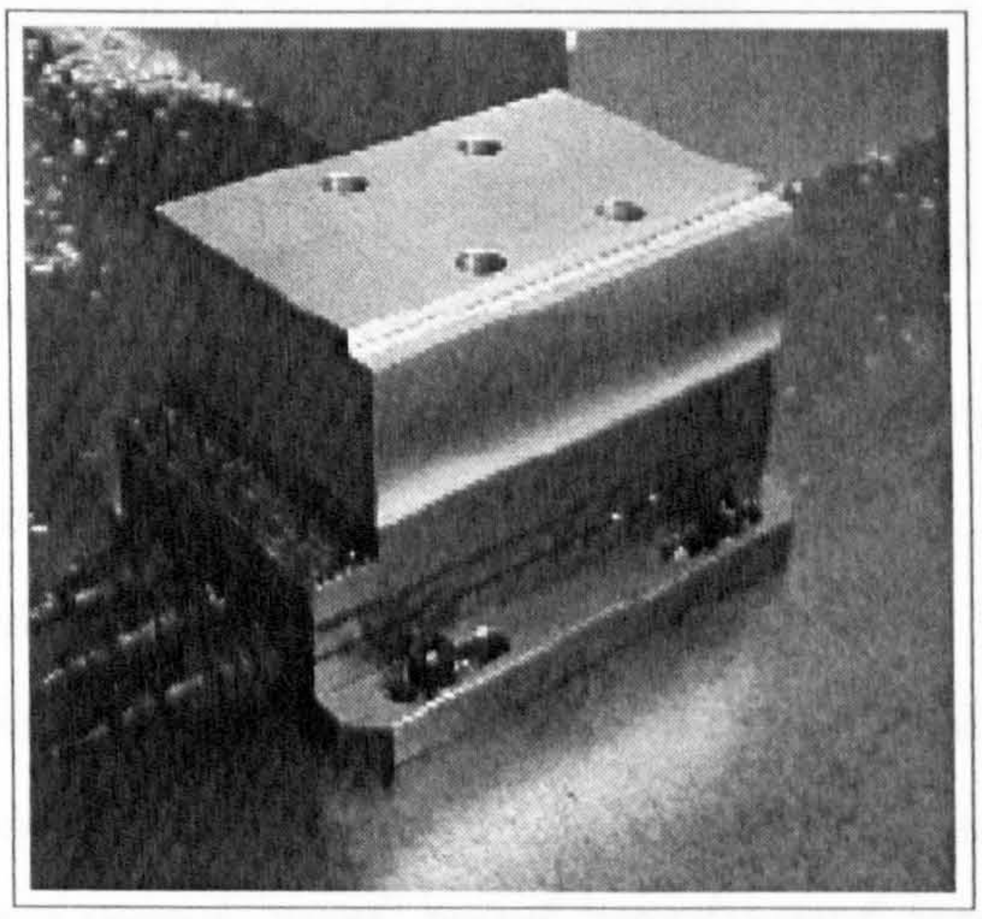

Figure 4.7: Kistler force plate used to recover cutting forces

crystals arranged orthogonally within a rigid steel mounting plate, to allow measurement of forces at high frequencies. Three Kistler Type 5001 charge amplifiers were used to convert the output from the force transducer into a voltage that was linear with respect to force in each of the three orthogonal components. The Tektronix scope used permitted simultaneous measurement of the forces at the high-sampling rate of 100kHz. This allowed the shape of the force profile of individual cutting actions to be examined. One limitation of acquiring data via the Tektronix scope was that it uses 8-bit A/D converters which resulted in visible quantisation across its range, particularly visible in the z-component of force shown in figure 4.10.

Initial experiments were performed on a high-speed milling rig (described in detail in section 3.3 at 12,000 rev/min. With the 2-fluted cutting tool the tooth-passing frequency

was 400Hz. An example of the results obtained from these tests (after filtering) is shown in figure 4.8. Examining figure 4.8 it can be seen that one tooth on the cutter appears to

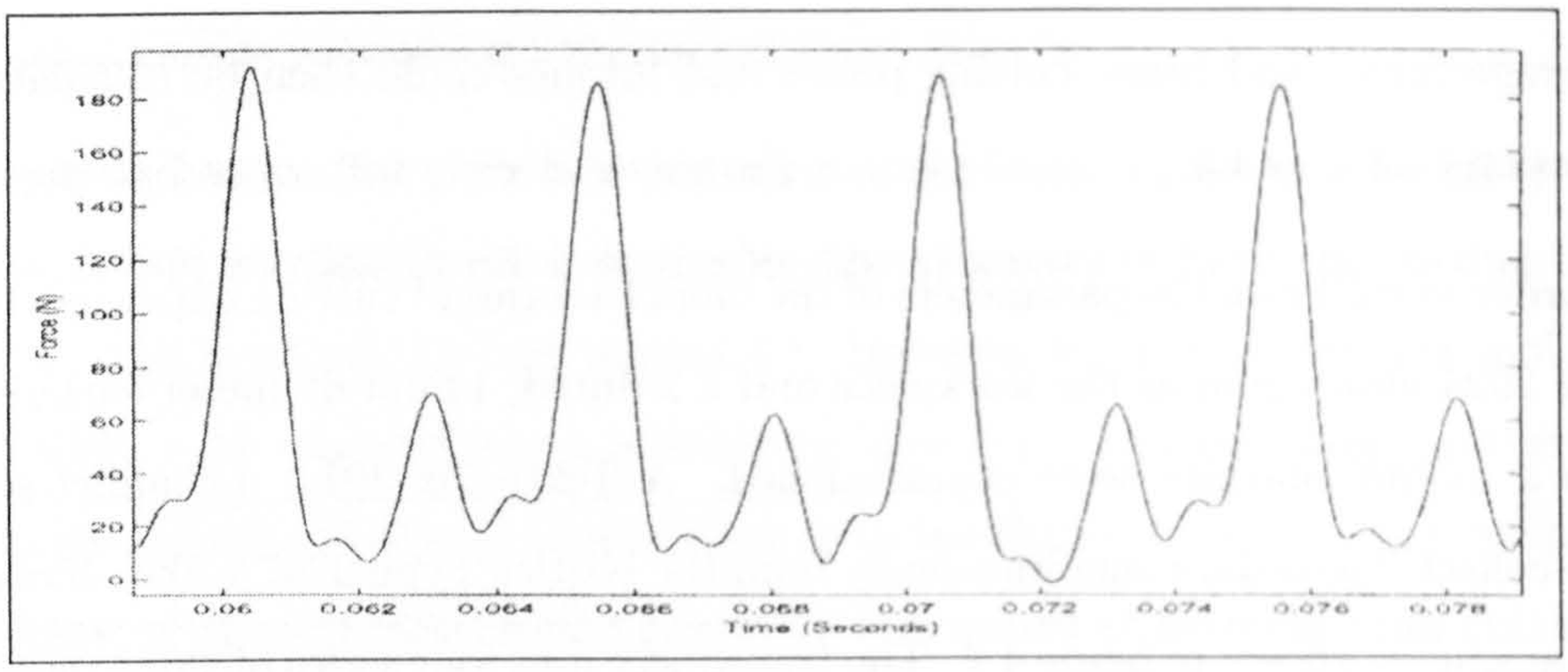

Figure 4.8: Cutting force data obtained on high speed milling set-up

be doing the bulk of the cutting work. Also the shape of the force profile does not seem to coincide with the theoretical shapes presented earlier in section 4.1. This was due to the fact that the raw output from the oscilloscope has been treated to remove a high amplitude unwanted component of force with a frequency of 800Hz. The high frequency component was introduced as a result of a high frequency instability introduced during cutting, based on the relative stiffnesses of the force plate and the cutting tool. The spindle used on the milling rig suffered from low torque at spindle speed values beneath 12,000 rev/min and the instability remained present throughout the remaining usable speed range of the spindle. Therefore, an alternative experimental set-up was sought to calibrate the force model. This alternative set-up used the same Kistler force measurement plate but was performed on a low-speed Bridgeport mill, shown in figure 4.9.

The Bridgeport mill benefited from a much higher stiffness and therefore the instability seen when measuring forces on the high speed machine was not observed. Tests were conducted at spindle speeds of around 1,200 rev/min using a feed-rate that would result in an equivalent feed-per-tooth value to that used on higher speed machines and at similar depth and widths of cut. A cutting tool with virtually identical parameters to that used on the high-speed machine was used for these tests. An example of the raw data retrieved using this set-up can be seen in figure 4.10.

Using MATLAB, the experimental data obtained from these tests was low-pass filtered to remove the unwanted noise and quantisation effects introduced during data logging. The

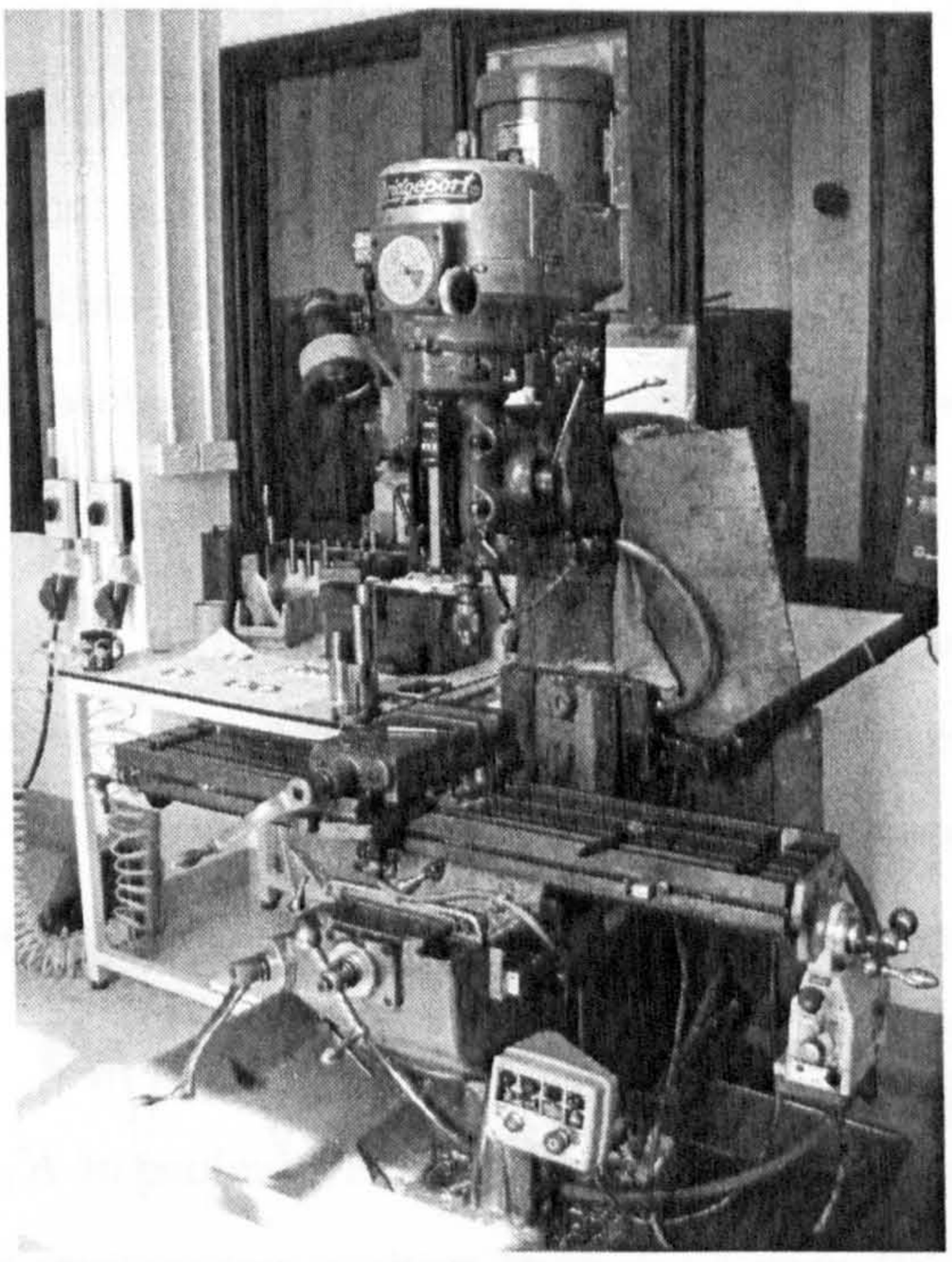

Figure 4.9: Low speed force measurement mill

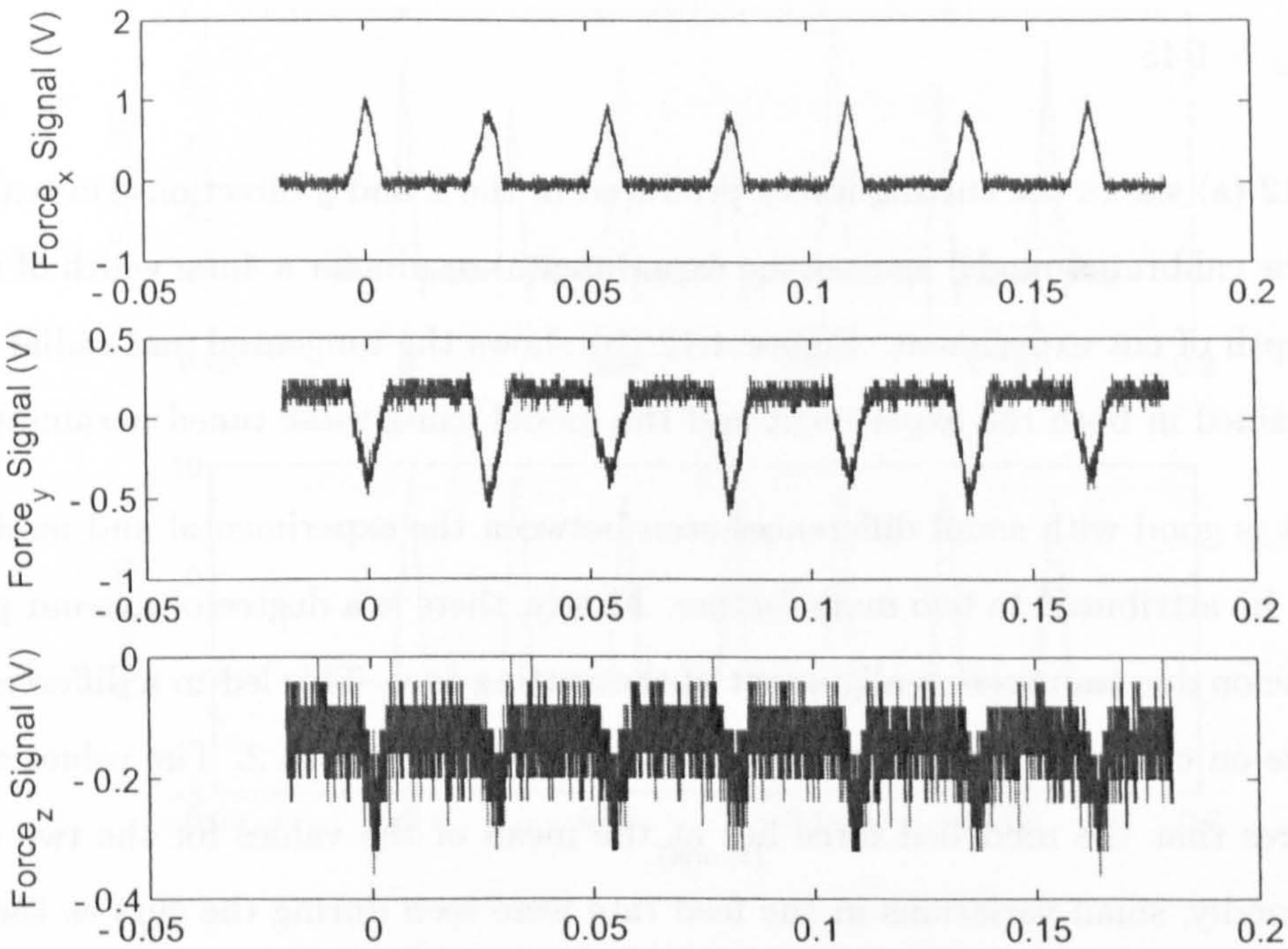

Figure 4.10: Raw cutting force data obtained on the low speed set-up, (x, y and z forces for a low-speed cut where $a = 1$mm, $b = 5.2$mm,m $N_r = 1050$rev/min

filter used was a first-order, low-pass design, with a cut-off frequency of 10,000rad/sec. The filtered force data was then transformed from an x, y and z co-ordinate system to a tangential and radial force system for the cutting tool. This tool-based co-ordinate system used the angular position of the first point of contact of the cutting tool with the workpiece as it's zero datum. Figures 4.11 show the filtered data, before (Figure 4.11(a)) and after (Figure 4.11(b)) transformation.

The model described in this section outputs tangential force (and hence radial force) as its primary variables. Hence the transformed data acquired from the experiments performed on the low-speed mill could be used to calibrate it. Given the force model as described in equations 4.10 and 4.11, model calibration required the tuning of three parameters. These were K_{mat}, y and K_{rad}.

This transformed data could then used to derive values of K_{mat}, y and K_{rad} for force calculation (equation 4.10) over a range of process parameters within the model. Final values chosen were:

- $K_{mat} = 500$ N/mm^2
- $y = 1.35$
- $K_{rad} = 1.45$

Figure 4.12 (a) shows the cutting forces produced in the x and y directions (measurement axes) of the calibrated model against the experimental results for a 4mm width of the cut, 5.2mm depth of cut experiment. Figure 4.12 (b) shows the tangential and radial cutting forces obtained in both the experiment and the model using these tuned parameters.

The fit is good with small differences seen between the experimental and model data which can be attributed to two main factors. Firstly, there is a degree of run-out present, a phenomenon due to incorrect alignment of the cutting tool. This led to a difference seen in the force on cutting tooth 1 of the tool to that at cutting tooth 2. The values selected have ensures that the modelled force lies at the mean of the values for the two cutting teeth. Secondly, small variations in the feed rate were seen during the cuts as they were being performed on a older milling machine at low feed rates. Once again, the values used in the model are based on the average value of feed rate for the whole cut.

As data for the cutting power was not available for the low-speed cuts the values of power calculated by the model was calibrated using data gathered during the feed rate

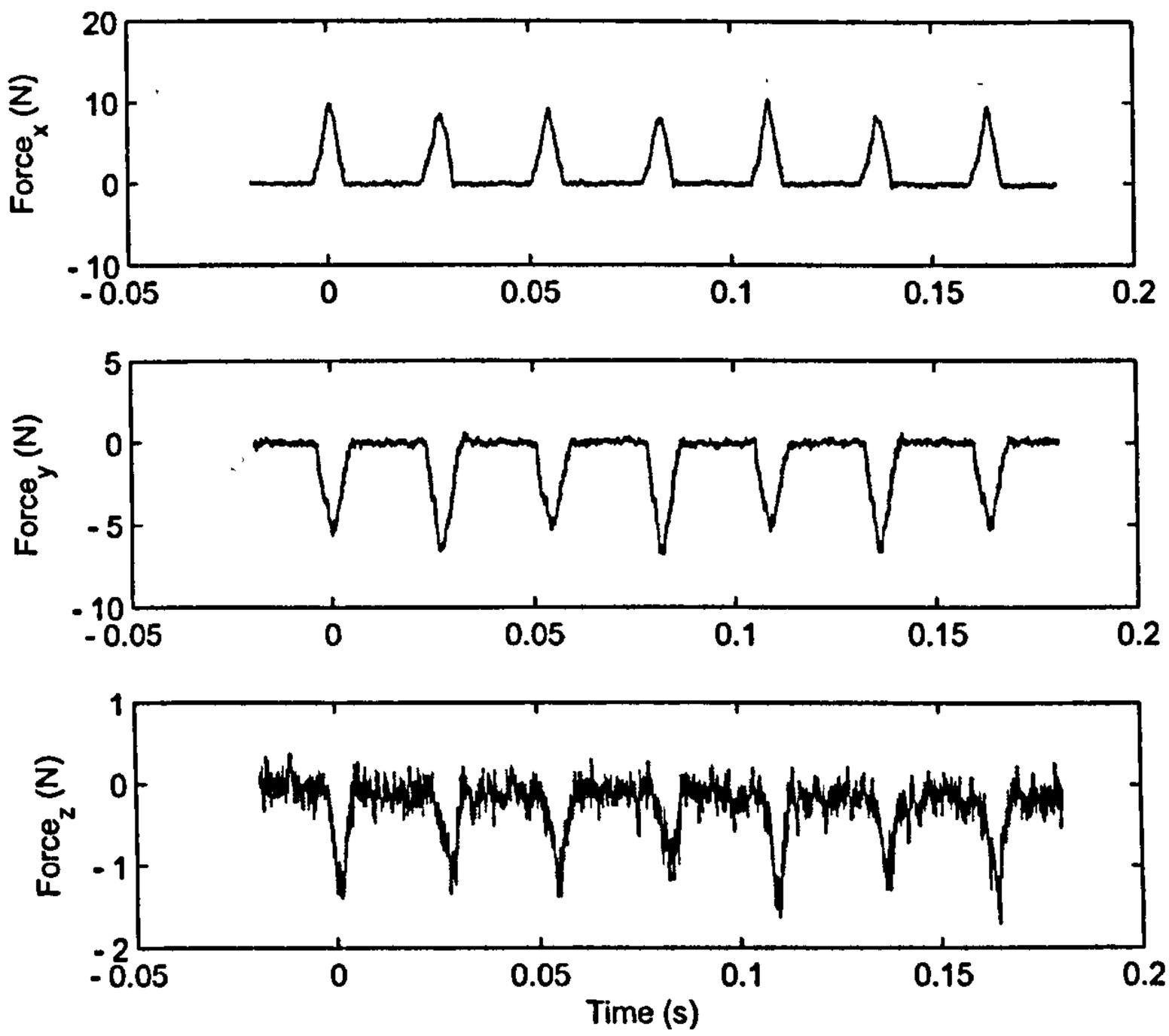

(a) Filtered, x, y and z data

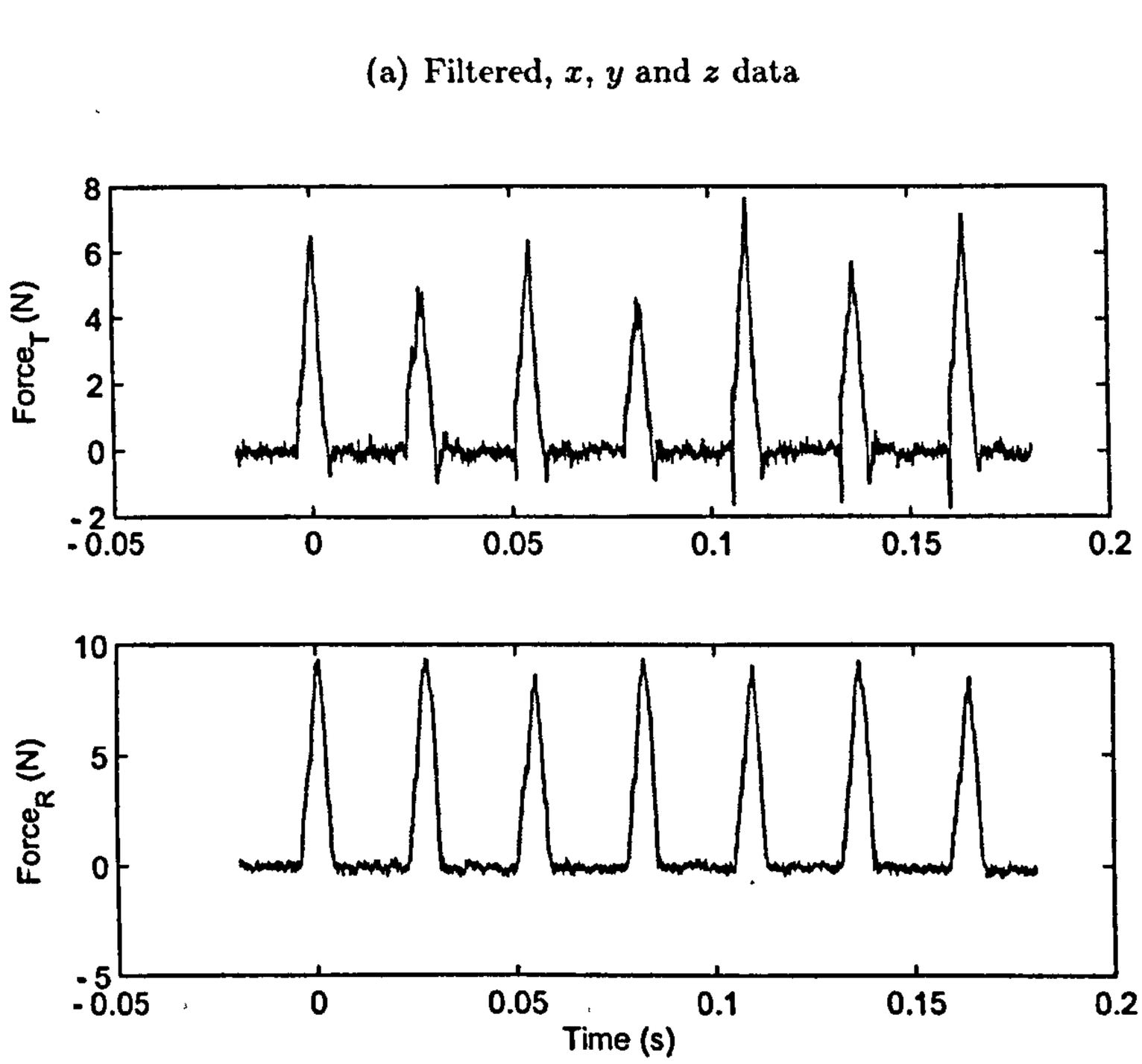

(b) Transformation of filtered, x, y and z data into tangential and radial co-ordinates

Figure 4.11: Filtered and transformed experimental cutting force data for a low-speed cut where, $a = 1\text{mm}$, $b = 5.2\text{mm}$, $N_r = 1050\text{rev/min}$

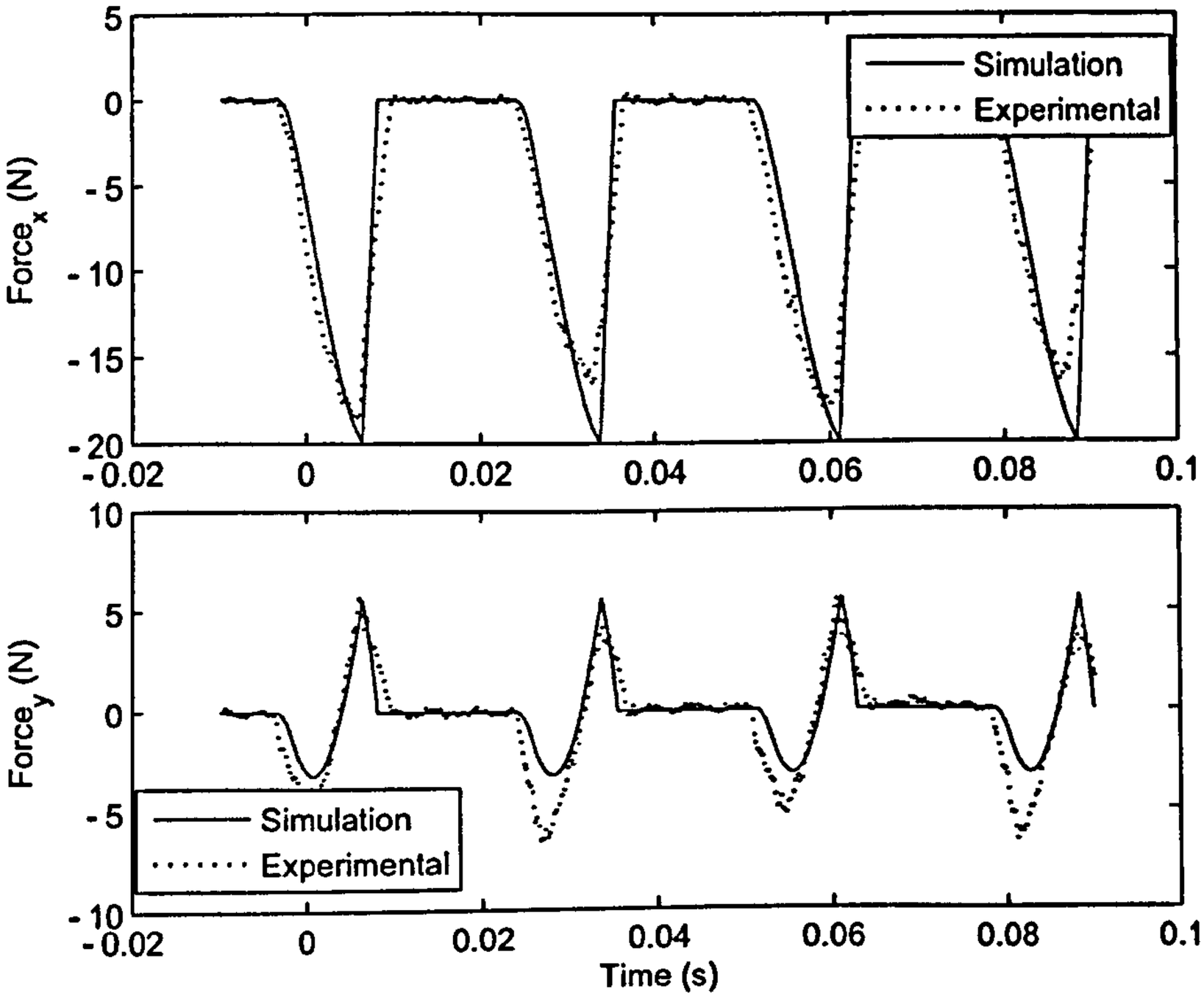

(a) x and y components of cutting force

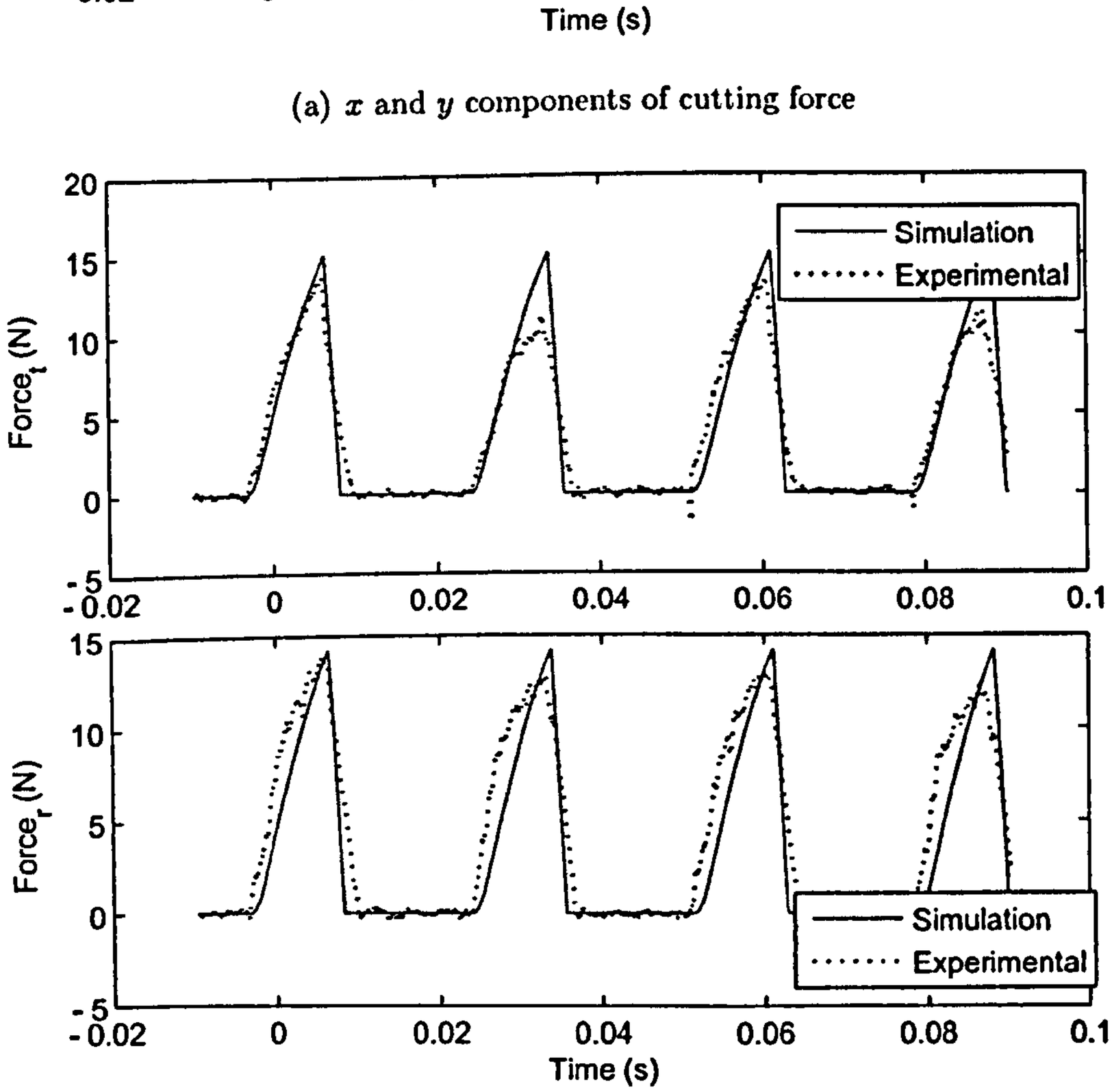

(b) Tangential and radial components of cutting force

Figure 4.12: Simulated and experimental cutting forces for a low-speed cut where, $a = 4\text{mm}$, $b = 5.2\text{mm}$, $N_r = 1050$ rev/min

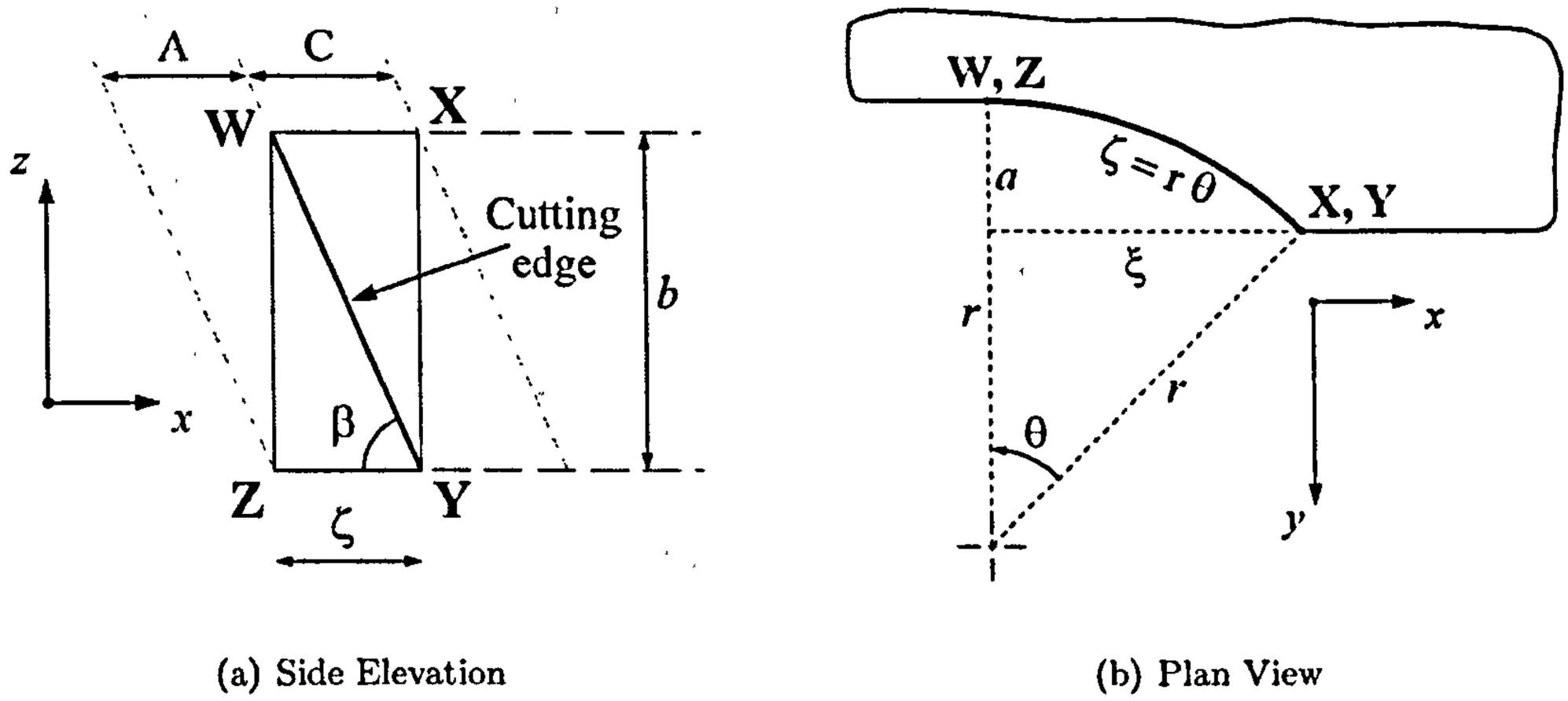

(a) Side Elevation (b) Plan View

Figure 4.13: Views of the cut surface highlighting useful parameters

control experiments (on the high speed milling rig) and seen to replicate the trends and values obtain during those experiments.

4.5.2 Empirical Model Relating Peak Cutting Force to Power

The aim of this section is to investigate a empirical relationship, that holds for a range of parameters, between peak cutting force and cutting power. This was achieved using the calibrated SIMULINK model described in section 4.5. As detailed in section 4.3 for simple geometries of cut, two main types of force profile exist, depending on the ratio of the width of cut, a to the depth of cut, b. Figure 4.13 (a) shows surface of a cut that is at the transition between the two types of cut described in section 4.3.

This transition occurs when the bottom of the cutting edge exits the cut at exactly the same time as the top of the cutting edge enters the cut. This is shown in figure 4.13 as a bold line spanning between points **Y** and **W**. The angle that the cutting edge makes with the horizontal (or x) axis is determined by the helix angle of the cutting tool, β. Making the assumption that the axial depth of cut, b is fixed then it is possible to find the width of cut, a_{crit} at which the transition occurs.

$$\zeta = \frac{b}{\tan \beta} \tag{4.14}$$

Figure 4.13 (b) gives a plan view of 4.13 (i.e. looking along the z-axis). From this view it

Depth of Cut, b (mm)	Width of Cut at Transition, a_{crit} (mm)	Depth of Cut (mm), b	Width of Cut at Transition, a_{crit} (mm)
0.5	0.00656	4	0.4153
1	0.0262	8	1.607
2	0.1047	16	5.6147

Table 4.1: Width of cut at transition between force profiles, a_{crit}

can be seen that:

$$\zeta = r\theta \tag{4.15}$$

giving

$$\theta = \frac{b}{r\tan\beta} \tag{4.16}$$

From figure 4.13 (b) it can also be seen that:

$$r\cos\theta = r - a_{crit} \tag{4.17}$$

Hence

$$a_{crit} = r(1 - \cos\theta) \tag{4.18}$$

and from equation 4.16:

$$a_{crit} = r\left(1 - \cos\left(\frac{b}{r\tan\beta}\right)\right) \tag{4.19}$$

Table 4.1 shows values of width of cut at which the transition between the two types of force profile occurs for a tool with a helix angle of 60° and a radius of 6.35mm ($\frac{1}{4}$" at various depths of cut, hereafter referred to as the transitional width of cut, a_{crit}

The structure of the SIMULINK cutting force model was such that many runs of the model could be made during which the width of cut (or any other specific parameter) could be stepped up in discrete amounts whilst keeping the other cut parameters constant.

The linear ratio between cutting power and peak cutting force was investigated for a range of depths and widths of cut using the SIMULINK model. Given that the force profiles at values above and below a_{crit} have different shapes it is likely that the relationship will change significantly at this point. Therefore, the model was run at similar levels of detail both above and below this value for each depth of cut with a view to obtaining different relationships above and below a_{crit}.

Figure 4.14 shows the ratio of cutting power, P, to peak cutting force, F_{peak}, for the simulations with the following geometries of cut:

- Cutting tool helix angle, $\beta = 60°$
- Depth of cut, $b = 0.125 \ldots 16$
- Width of cut, $a = 0 \ldots 2 * a_{crit}$
- Feed-Rate, $v = 4$ mm/s
- Tool Radius, $r = 6.36$ mm

Figure 4.14 (a) shows the data for cuts where $a < a_{crit}$, with figure 4.14 (b) showing the data where $a > a_{crit}$.

The stepping effect seen on the data is an effect seen due to the fact that the instantaneous cutting force is measured once per revolution in the model whereas the cutting power is continuously measured and takes a full revolution to settle. The data shown was down-sampled to remove the stepping effect. Using a least squares based curve fitting algorithm the following fit was obtained for cuts in which $a < a_{crit}$:

$$\frac{P}{F_{peak}} = (P_1 b + P_2)\left(\frac{a}{a_{crit}}\right)^{(P_3 b^{P_4} + P_5)} + P_6 b + P_7 \tag{4.20}$$

where:

P_1	P_2	P_3	P_4	P_5	P_6	P_7
-5.53×10^{-4}	-1.64×10^{-3}	0.1892	-1.153	-0.8334	0.0199	-2.8×10^{-4}

Table 4.2: Coefficients for empirical power-cutting force relationship in which $a < a_{crit}$

For cuts in which $r > a > a_{crit}$ a different fit was obtained:

$$\frac{P}{F_{peak}} = (P_1 b + P_2)\left(\frac{a}{a_{crit}}\right)^2 + (P_3 b + P_4)\left(\frac{a}{a_{crit}}\right) + (P_5 b + P_6) \tag{4.21}$$

where:

Figure 4.15 shows the power to peak cutting force ratio for the two empirical models when compared to the data obtained from the SIMULINK model for the a cut with depth, $b = 4$ mm. As predicted, due to the different basic force profile involved, different empirical models are required above and below a_{crit}. As can be seen from figure 4.15 the empirical

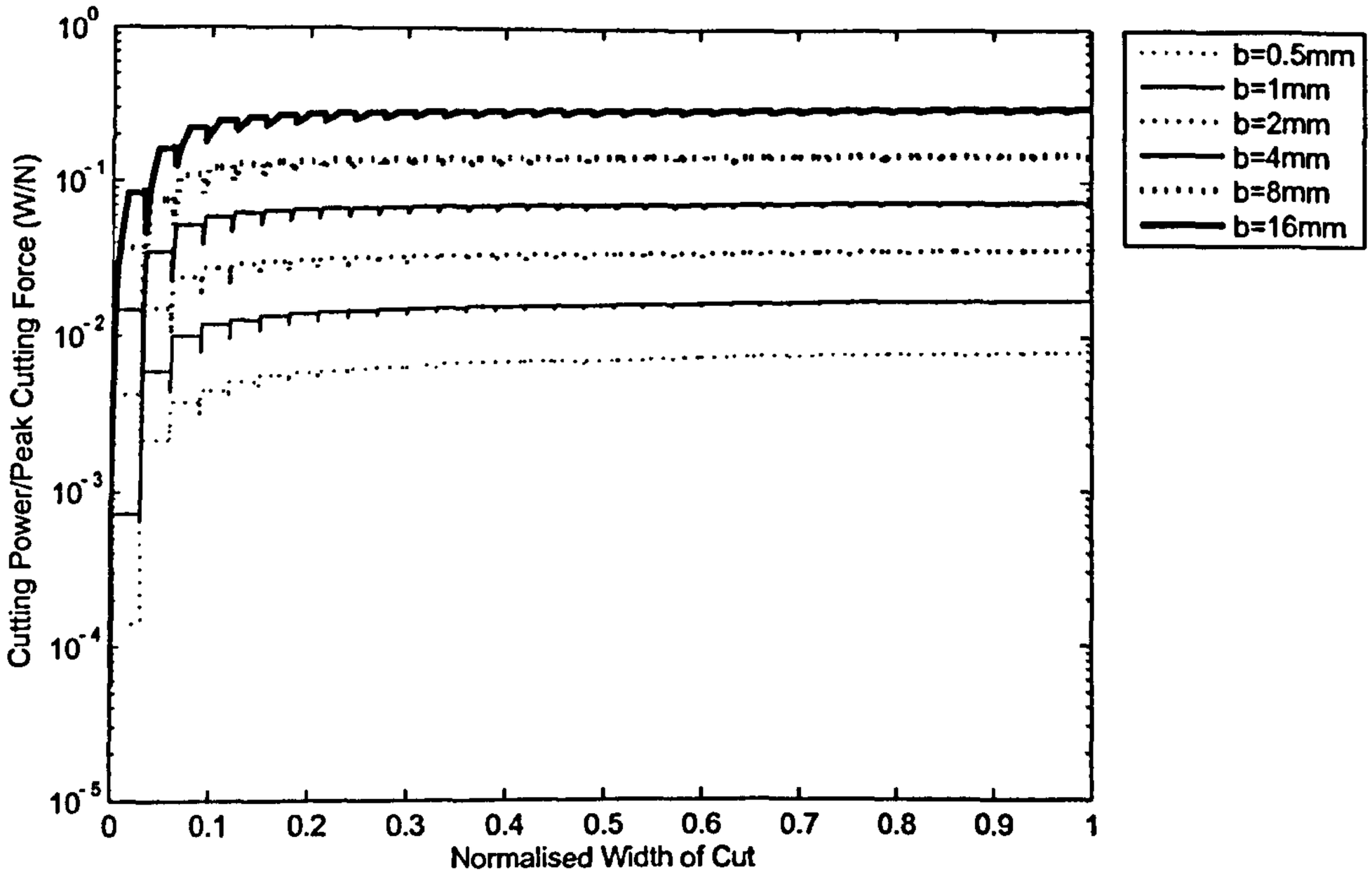

(a) Widths of cut below the critical width of cut, a_{crit}

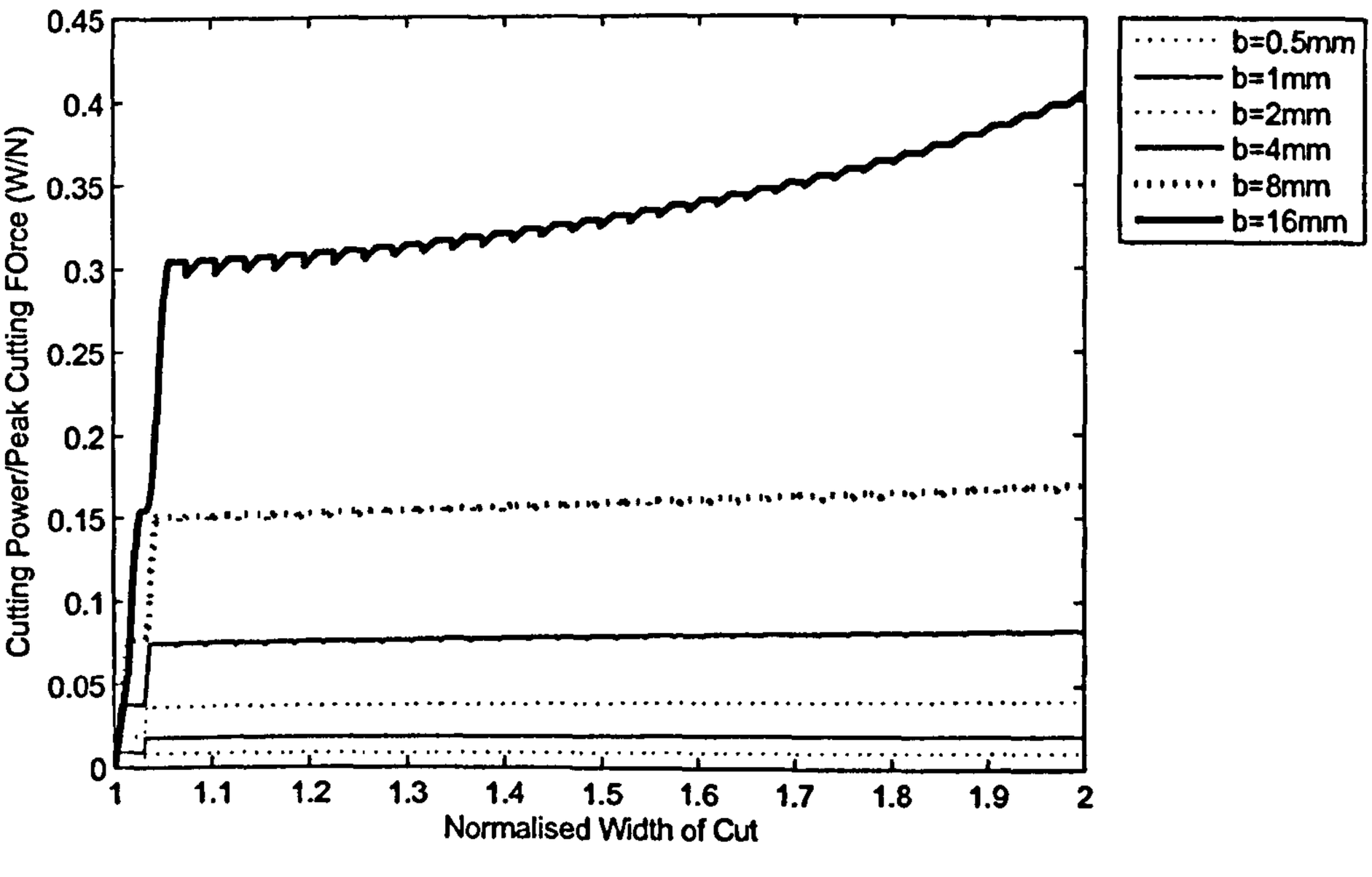

(b) Widths of cut above the critical width of cut, a_{crit}

Figure 4.14: Cutting power/peak cutting force ratio vs. width of cut, a for a range of axial depths of cut, b

P_1	P_2	P_3	P_4	P_5	P_6
1.13×10^{-3}	-6.87×10^{-4}	-9.16×10^{-4}	-2.13×10^{-3}	1.87×10^{-2}	5×10^{-3}

Table 4.3: Coefficients for empirical power-cutting force relationship in which $r > a > a_{crit}$

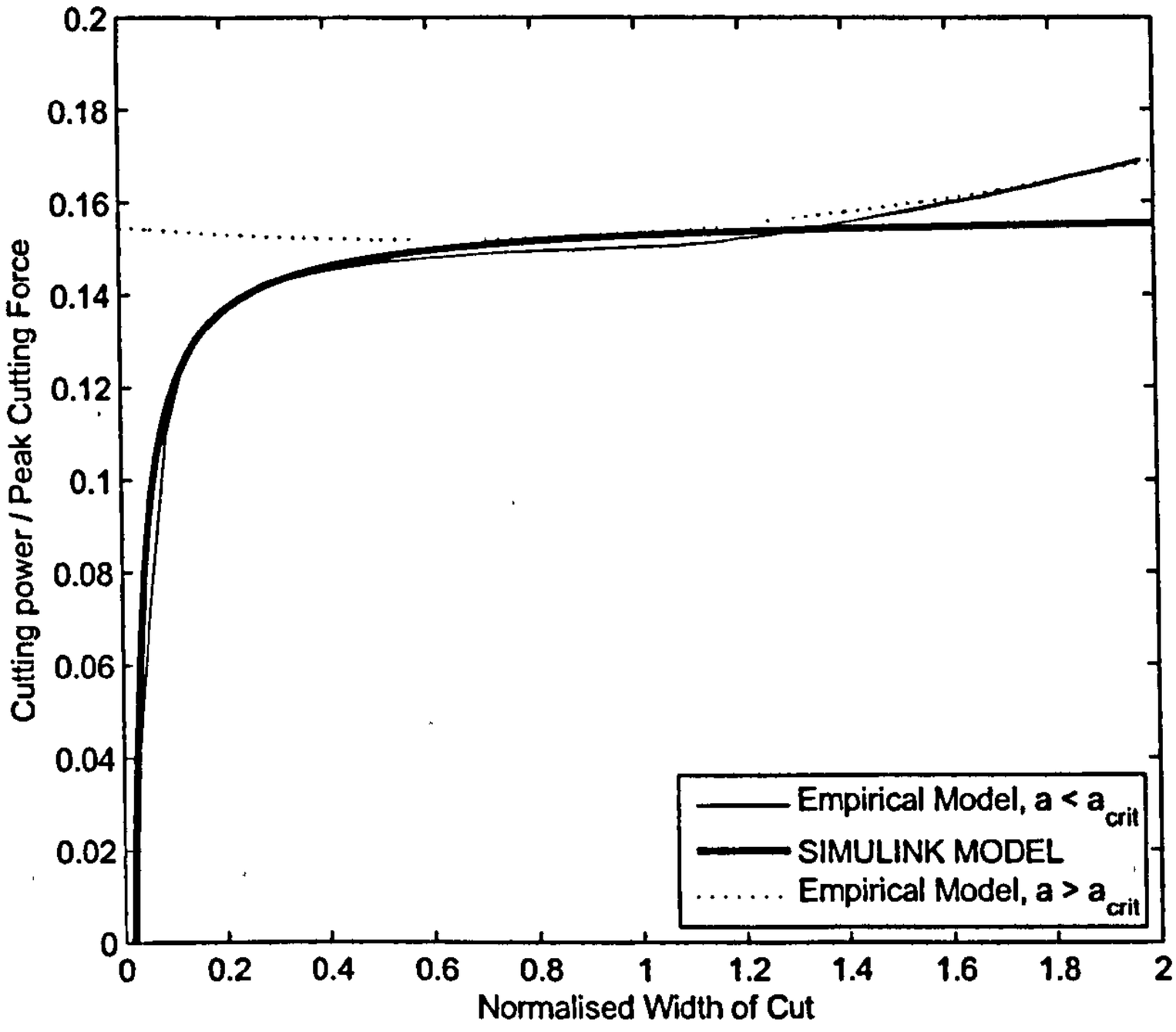

Figure 4.15: Comparison of the empirical and SIMULINK models for a cut where $b = 4\text{mm}$, $a = 0 \ldots 2a_{crit}$

model fit is good for both empirical models in their active areas (i.e. above and below a_{crit}.

The fit for all data where $b = 1$ remains good, with depths of cut below 1mm suffering from a poorer fit when $a_{crit} > 1$. This has been attributed to the reduced resolution of the SIMULINK data available below $b = 1$. This resolution could be increased in a further study in order to obtain a more robust parameter fit.

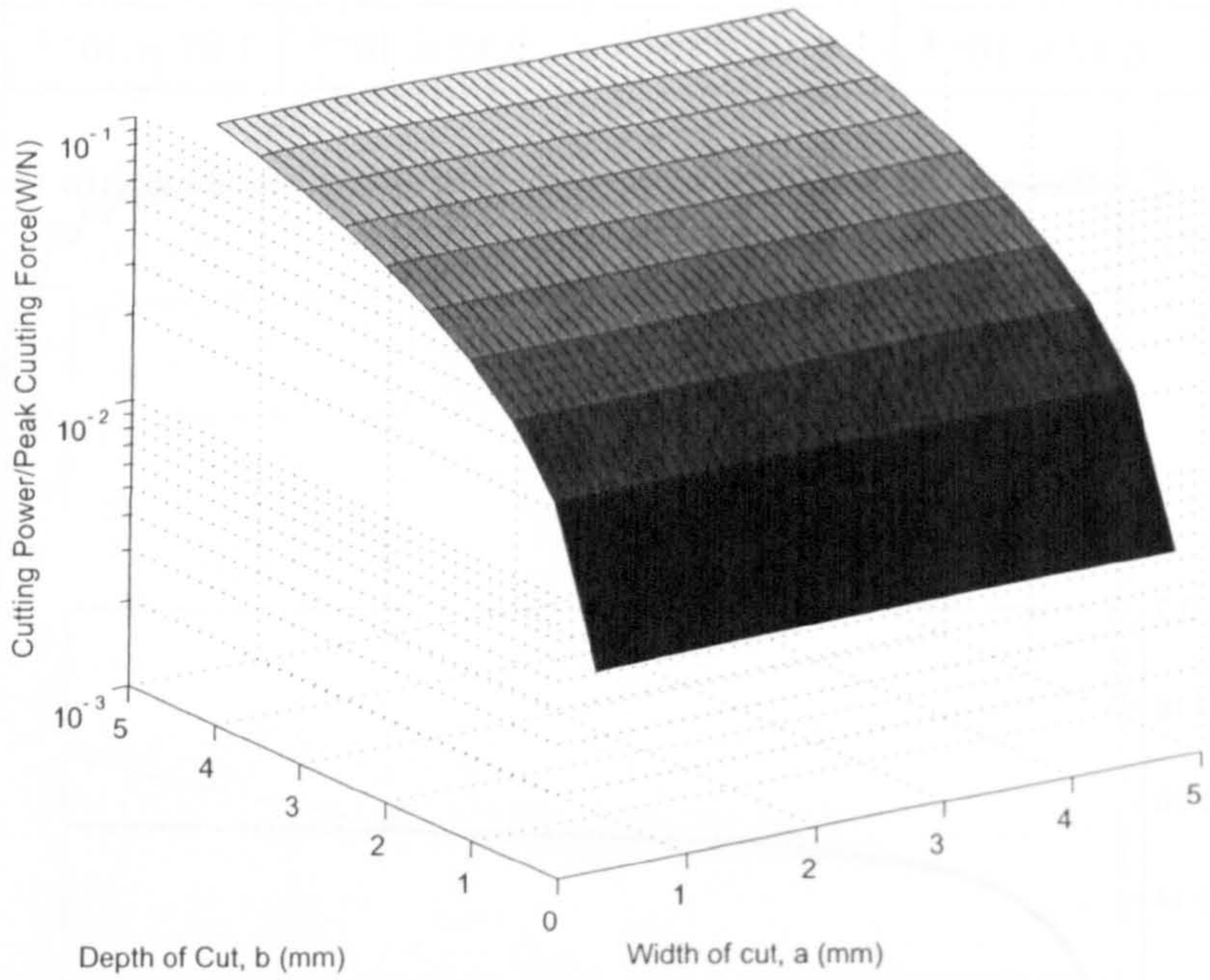

Figure 4.16: Power - peak cutting force surface plot for $a = 0.1 \ldots 5$ mm, $b = 0 \ldots 5$ mm

4.6 Conclusions & Limitations of the study

Figure 4.16 shows a surface plot of the power-peak force relationship obtained over the range of widths and depths of cut sampled. It is this surface that could be used in real-time to predict the peak cutting force for a particular cut, based on the depths and widths of cut for a particular tool.

The study conducted was performed for a series of cuts for a single cutting tool (i.e. constant helix angle, β and radius, r). It is possible that, as these parameters vary the values of a_{crit}, that the power-peak force relationship will be similar to that derived in section 4.5.2.

Values of a for which the wrap angle exceeds 90° have not been considered here as these would require another empirical model. This is due to the fact that after the cutting edge reaches 90°, the total feed per tooth decreases. Also, above this wrap angle it is likely that more than one tooth edge on the cutting tool will be involve in the cut. The is effect has not yet been considered in this study.

Finally, whilst the SIMULINK model on which this study has been based has been

calibrated against a set of low-speed data, no calibration was performed at the higher speeds. Also, no final comparison of the empirical data with a high speed cuts has been possible (both with and without the adaptive controllers used in chapter 3). This was due to resource limitations and should be performed, when possible, to validate the models and control strategy proposed.

Chapter 5

Extension of Controller to more Complex Cutting Systems

SUMMARY: Cutting in multiple axes presents further challenges that must be resolved in order to used adaptive control effectively and safely. Software that allows the pilot rig to be used to investigate these issues is discussed along with a discussion of the areas that must be tackled.

5.1 A New Problem - Multi axis cuts

A method of regulating the power consumed during a particular milling cut has been demonstrated to work well for a single axis system. However cuts in industry are rarely so simple with the machines being capable of cutting in five degree of freedom simultaneously. This introduces a range of new factors that must be investigated and subsequently regulated to ensure that adaptive milling does not reduce the quality of the final component.

In order to allow investigation of such areas to begin a new way of controlling the pilot rig was required.

5.2 NC Style Interface For Pilot Rig

Section 3.4.2 describes the method used to generate the reference signal representative of a cutting tool path for a single axis cut using a triangular wave and integrated control signal.

Investigation of adaptive control of milling over multiple axes requires a method of generating tool-paths in more than one degree-of-freedom, co-ordinating those degrees-of-freedom and finally a method of varying the feed-rate of the tool path during a cut. As ControlLab32 was the control package that had been used for the single axis experiments a module and accompanying software was written to allow ControlLab32 to control the pilot rig in such a manner.

5.3 NC Commands

It was decided that the primary functions required from an NC-type controller for the rig would be:

- Ability of the tool to move in an arbitrary but defined straight line
- Ability of the tool to move in an arbitrary but defined portion of a circular arc
- Ability to vary the tool feed-rate continuously on-line

For each different type of command a two-letter code was assigned with each code has a defined number of parameters available. In order to be used by the NC module written for ControlLab32 the commands had to be entered into a text editor, one command per line. An customised editor called "GeniPath" that allowed easy creation of these commands was written for the Windows NT platform. A screen shot main interface of the software is shown in figure 5.1. Each of the commands is presented in turn along with the options provided by the customised editor software.

MetaData and Comments

These commands do not perform any function whilst the tool is running but provided a mechanism to keep track of various path files. They begin the line with a double hash character '##' and include attributes such as File Author, Tool Path Name, Path Notes and Date Created.

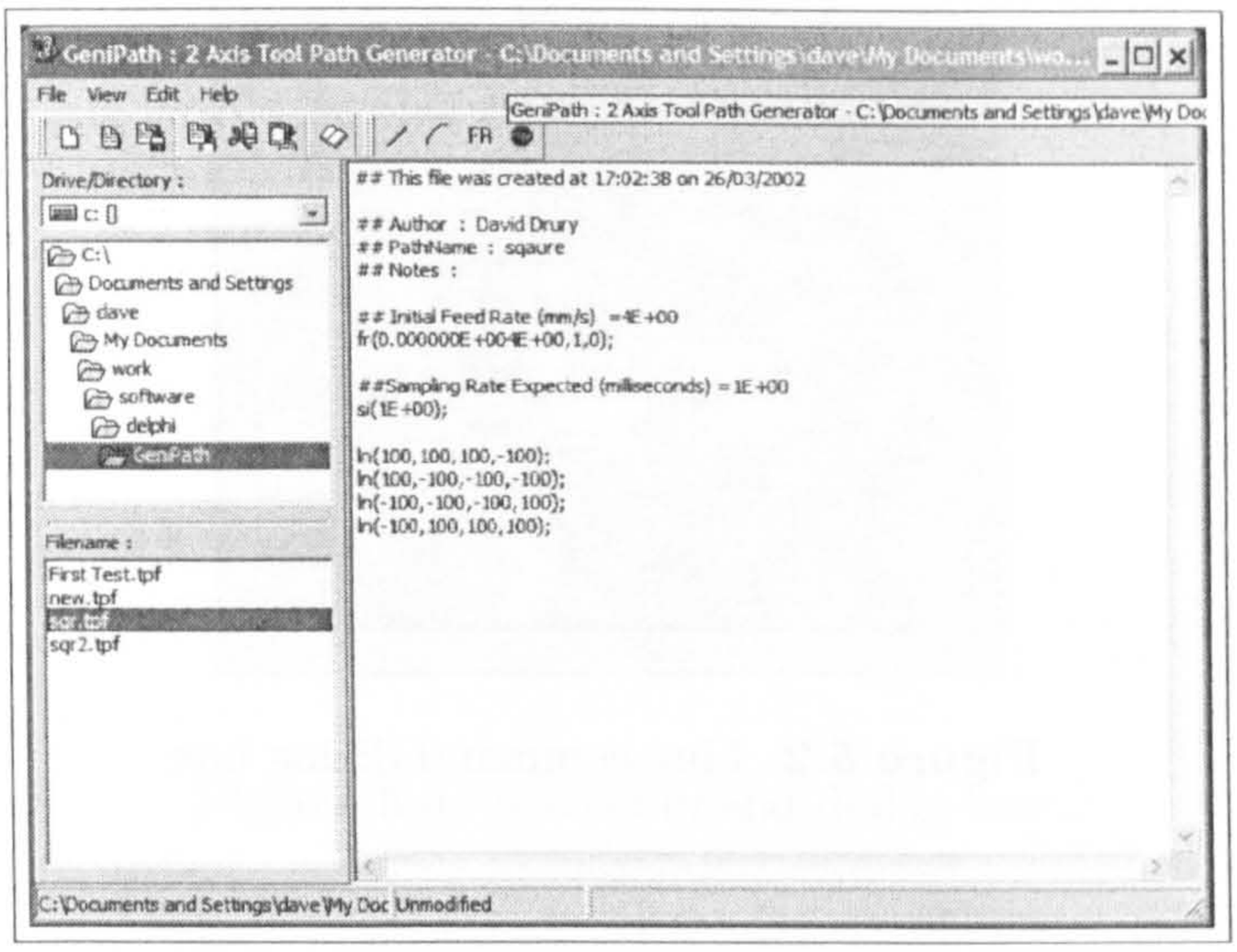

Figure 5.1: GeniPath: Customised editor for NC command generation

Straight Lines, *LN*

The command "*LN*" was assigned to define straight lines with four additional parameters being required. The command has the following structure:

$$\mathrm{LN}(X_1,Y_1,X_2,Y_2)$$

X_1 and Y_1 represent the x and y co-ordinates of start position of the tool head and X_2 and Y_2 the x and y co-ordinates of the end position of the tool head. Figure 5.3 shows the line dialog box provided by ControlLab32. In this software lines could be defined by:

- Start Position, End Position
- Start Position, Length, Angle

The convention used when defining x, y and angles on the milling table are shown in figure 5.3.

Portion of Circular Arc, *AC*

The command "*AC*" represents a portion of a circular arc with six additional parameters being required. The command has the following structure:

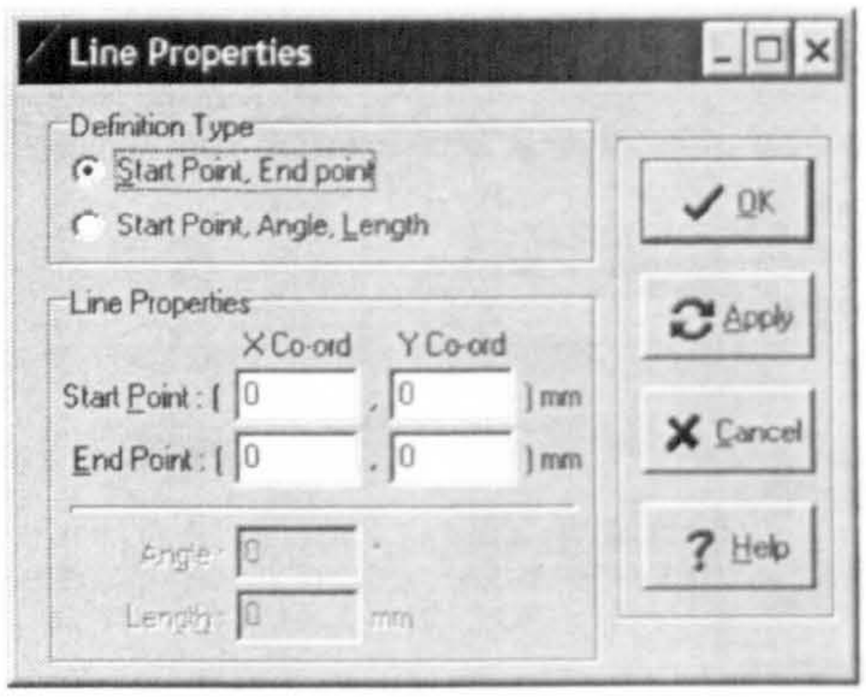

Figure 5.2: Line command dialog box

Figure 5.3: Axis and sign conventions for the milling table

$$\text{LN}(X_1, Y_1, X_2, Y_2, X_3, Y_3)$$

The co-ordinates X_1, Y_1, X_2, Y_2, X_3 and Y_3, represent the x and y-co-ordinates of the start point, centre point and end point of the arc respectively, travelling in a clockwise direction. Figure 5.3 shows the line dialog box provided by ControlLab32. In this software lines could be defined by Start Position, Centre Position, End Position only.

Feed Rate Change, FR

The command "FR" indicates a that a change in the base feed-rate is required. Four parameters are required with command structure being:

$$\text{FR}(Feed_{OLD}, Feed_{NEW}, \text{Transition Type, Transition Time})$$

The parameters $Feed_{OLD}$ and $Feed_{NEW}$ provide the controller with the old and new feed rates in mm/sec. The third parameter indicates whether the change in feed-rate is to be applied instantaneously or phased in linearly over a specified period of time with the

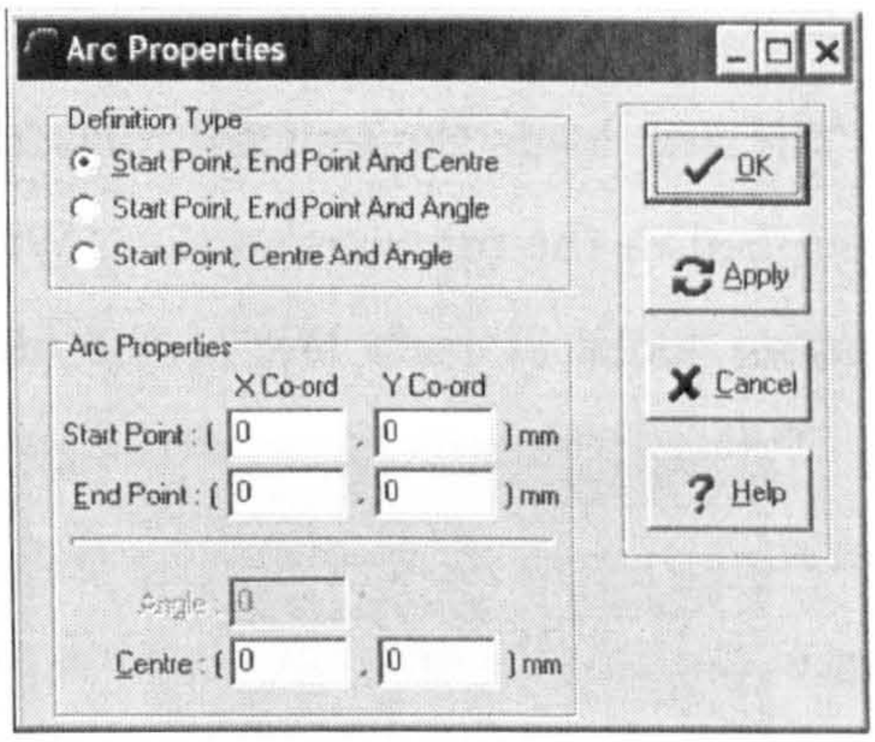

Figure 5.4: Arc command dialog box

fourth parameter indicating the time that the transition should take. The dialog box for this parameter is shown in figure 5.3

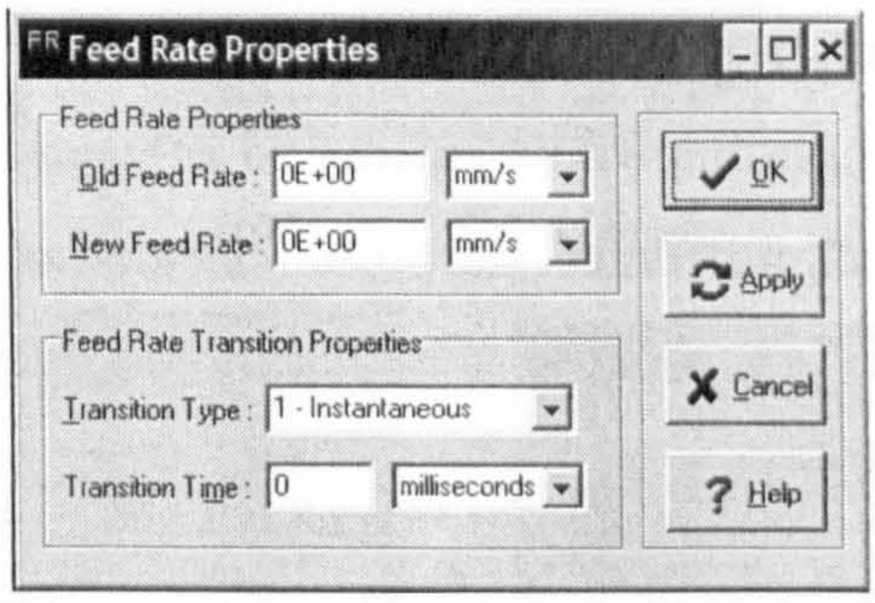

Figure 5.5: Feed command dialog box

5.3.1 ControlLab32 Dual Axis Control Module

Having generated a series of tool path commands it is now necessary to turn then into a series of tool path co-ordinates at a fixed distance interval so that they can be passed to the position controller for each axis of the pilot rig. This is achieved using the ControlLab32 Dual Axis Module which consists of three main parts. These are:

- NC Command loader and parser
- Scaling tool
- Instantaneous path point generator

When loaded into ControlLab32 the module appears as is shown in Figure 5.6 with the Path Set-up page showing. The user loads the text file containing the commands created using the GeniPath tool described in the previous section. When the file finishes loading the tool path file a path parser looks at each line of the file for one of the three NC commands (*LN*, *AC*, *FR*). When it identifies one of the geometric commands (*LN* or *AC*) it generates a stream of rows of x and y co-ordinates that the tool would follow line-by-line were it to be moving at a feed-rate of 1mm/s with a sampling interval of 100ms. This is called the pre-processing stage. Using these values keeps the number of rows of co-ordinates relatively small for a normal tool path and allows easy lookup of points were the tool either to be moving at a multiple of 1mm/s of sampling at a multiple of 100ms. For example were the desired feed-rate of the tool 6.5mm/s per second with a sampling interval of 200ms then the dual axis controller would refer to every 13th row of the stream of generated data. In the event that extra resolution is required linear interpolation between the nearest to points is used to provide it. This method was chosen in preference to generating the tool-path on-line whilst cutting so as to maximise the processing time available to the ControlLab32 for control purposes (calculating MCS gains, control signal, etc.) and is essential for the maintenance of high sampling rates.

Once the pre-processing stage has been completed the controller can be started and the on-line part of the software takes over. Acting as a reference signal generator this part of the software streams the rows of co-ordinates that were generated in the pre-processing stage (or relevant interpolated co-ordinates) to the controller as the reference signal according to the desired feed-rate. This feed-rate can then be adjusted manually via the user-interface in the dual axis dialog box or by an automatic method such as an MCS controller. This would be the proposed method by which MCS would be used to maintain a desired power for varying geometries, etc. under a multi-axis environment.

The x and y axis set-up and spindle set-up pages allowed the dual axis module to be calibrated for the milling table in question. The measured feed-rate was calculated numerically from the measured positions of the x and y LVDTs using the method proposed by Harrison *et al.* [190]. This feedback variable could then be used purely to monitor the actual feed rate, or in an outer-loop strategy to reduce the error between the desired and measured feed-rates.

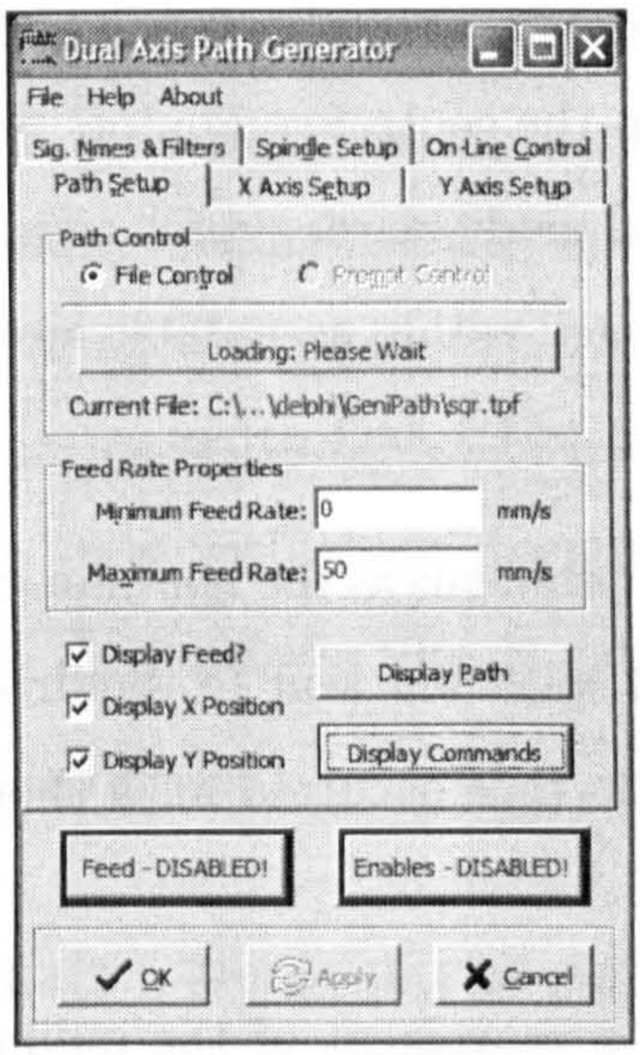

(a) Path Set-up Page

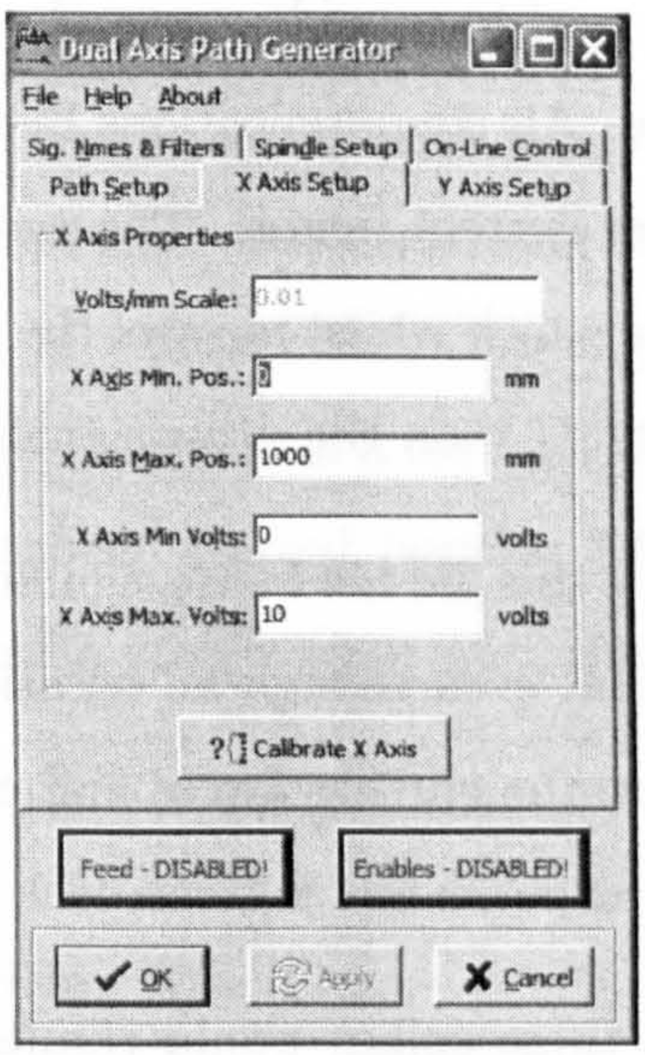

(b) X-Axis Set-up Page

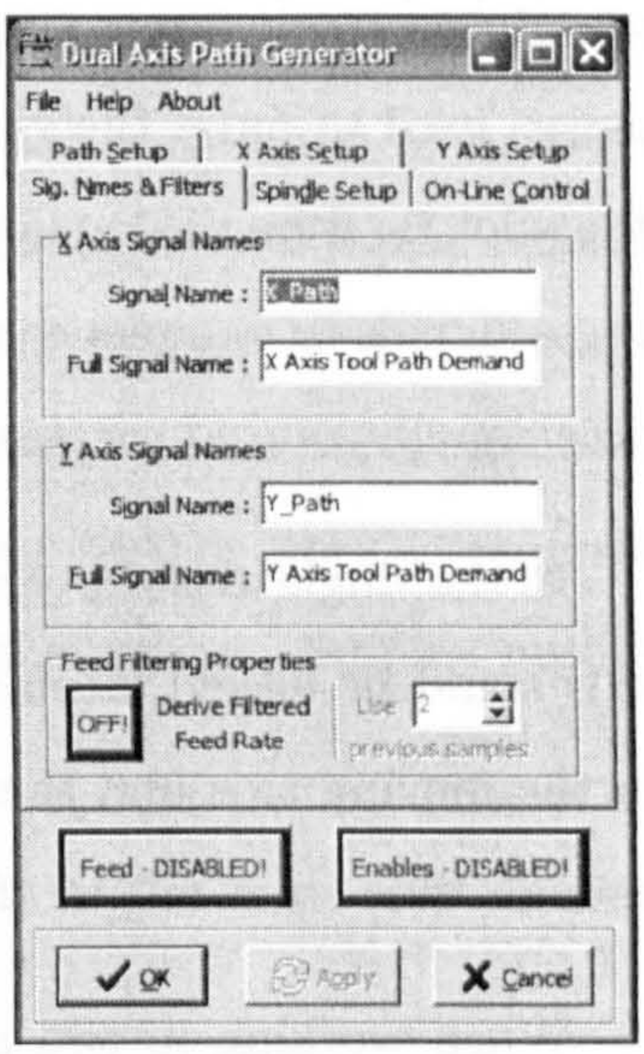

(c) Signal Names & Filters

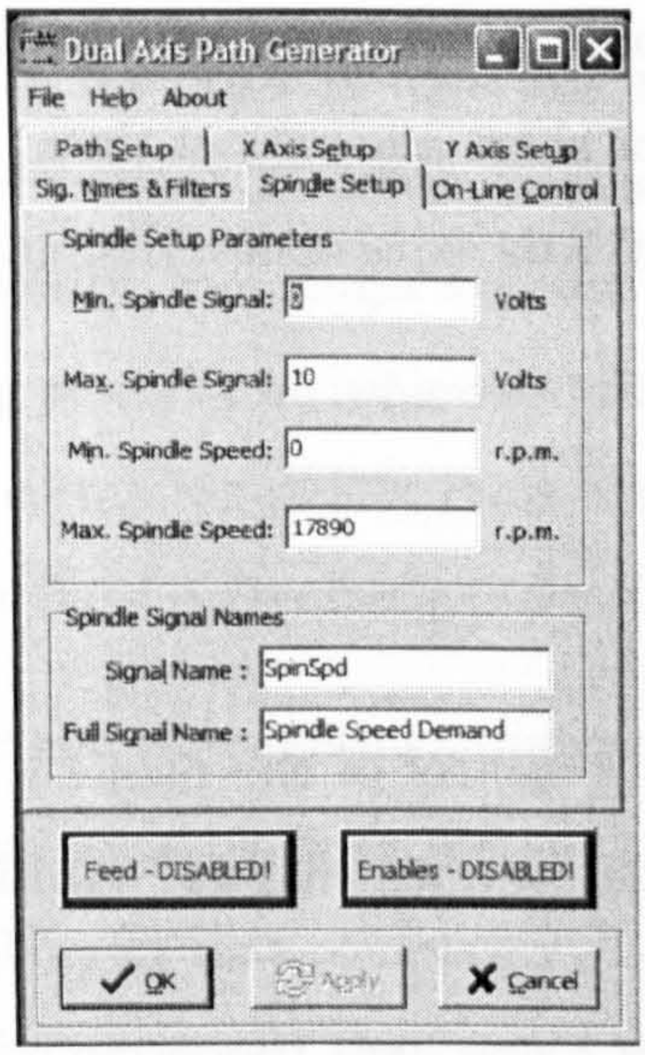

(d) Spindle Set-up

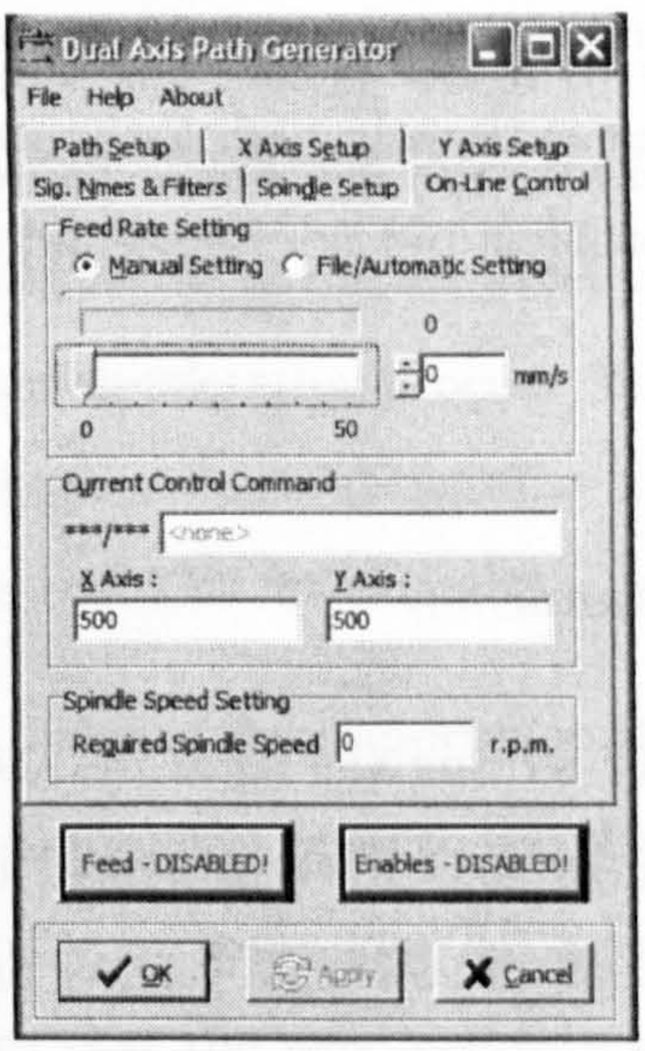

(e) On-Line Control

Figure 5.6: ControlLab32 dual axis module

5.3.2 Implementation Problems Encountered

No cutting experiments were performed using the dual axis module due to a problem seen with the analogue nature of the pilot rig. Contained within the control box of the rig was a switched mode power supply used to provide power the three phase spindle and the belt drives used to move the spindle. All communications between the control computers and the pilot rig were analogue, lower current signals. The switched mode power supply caused these signals to experience noise which whilst most of the time fell within acceptable levels occasionally caused surges of up 0.5V on the drive signals sent to the belt drives.

In the single axis experiments this did not cause significant problems as the non-moving axis could be locked meaning that even though an occasional spike was sent to the drive in the moving axis and therefore the cutting forces and powers thee occurred for a short enough time so as not to affect experiments a great deal.

When working in two axes these spikes would results in a movement of the milling head in an unpredictable direction. In practice, this would mean that the cutting tools which would be rotating at up to 18,000 rev/min could potentially be driven into a solid block of metal at extremely high feed-rates for short amounts of time. A resolution was sought to this problem but not found and multi-axis experiments discontinued for reasons of safety.

5.4 Conclusions

The main aim of writing the software allowing control of the pilot rig in two axes was to extend the single axis work presented in the previous chapter. Multi-axis cuts would enable investigation of two main further areas:

- Continuously varying wrap angle
- The effect of the dynamics of the milling machine

5.4.1 Continuously Varying Wrap Angle

Wrap angle is defined as being the proportion of the diameter of the tool that is actively involved in cutting. To clarify this definition, figure 5.7 shows two cuts. Figure 5.7 (a)

shows a cut in which the radial depth of cut is equal to half the diameter of the cutting tool. In this situation the wrap angle, marking as a bold line, is just over 90° due to the trochoidal nature of the cut. Figure 5.7 (b) shows a cut in which the radial depth of cut is equal to the full diameter of the cutting tool. Here the wrap angle would be 180°. To date only two series of experiments have been performed in which the wrap angle of the cut is changed during a cut. The two cases were in a single axis with the wrap angle change instantaneously in the first case, and decreasing at a constant rate in the second. During the life of a typical cut in industry the wrap angle will change non-linearly and continuously, e.g. when milling the outside of a corner. The ability of the MCS controller to cope with these changes has been started (section 3.6) but further work is required to demonstrate that it can remain stable when performing these more complex milling actions.

5.4.2 Dynamics of the Milling Machine

As mentioned before milling machines used in industry, especially those used in the aircraft industry, weigh in the order of tons. As a result, the rate at which they can accelerate and decelerate is limited. Moreover, how accurately controlled this rate of acceleration is an unknown quantity. In a single axis this would result in the incorrect value of feed and therefore cutting power to be achieved during the deceleration process. In a multi-axis cut it would almost certainly result in geometrical imprecision and therefore a badly machined part. Two methods of overcoming these effects could be investigated in the future.

Firstly a method of weightings that would balance the importance of geometrical accuracy for a particular block or section of a component against the desired to improve the speed of milling of that component. Secondly, an inner-loop MCS velocity controller strategy could be developed that would ensure that the new feed-rate generated by the strategies developed in the previous chapter were accurately achieved. This would indirectly improve the precision of the final machined part. This controller would sit outside the milling machine's proprietary position controllers but inside the MCS adaptive machining loop.

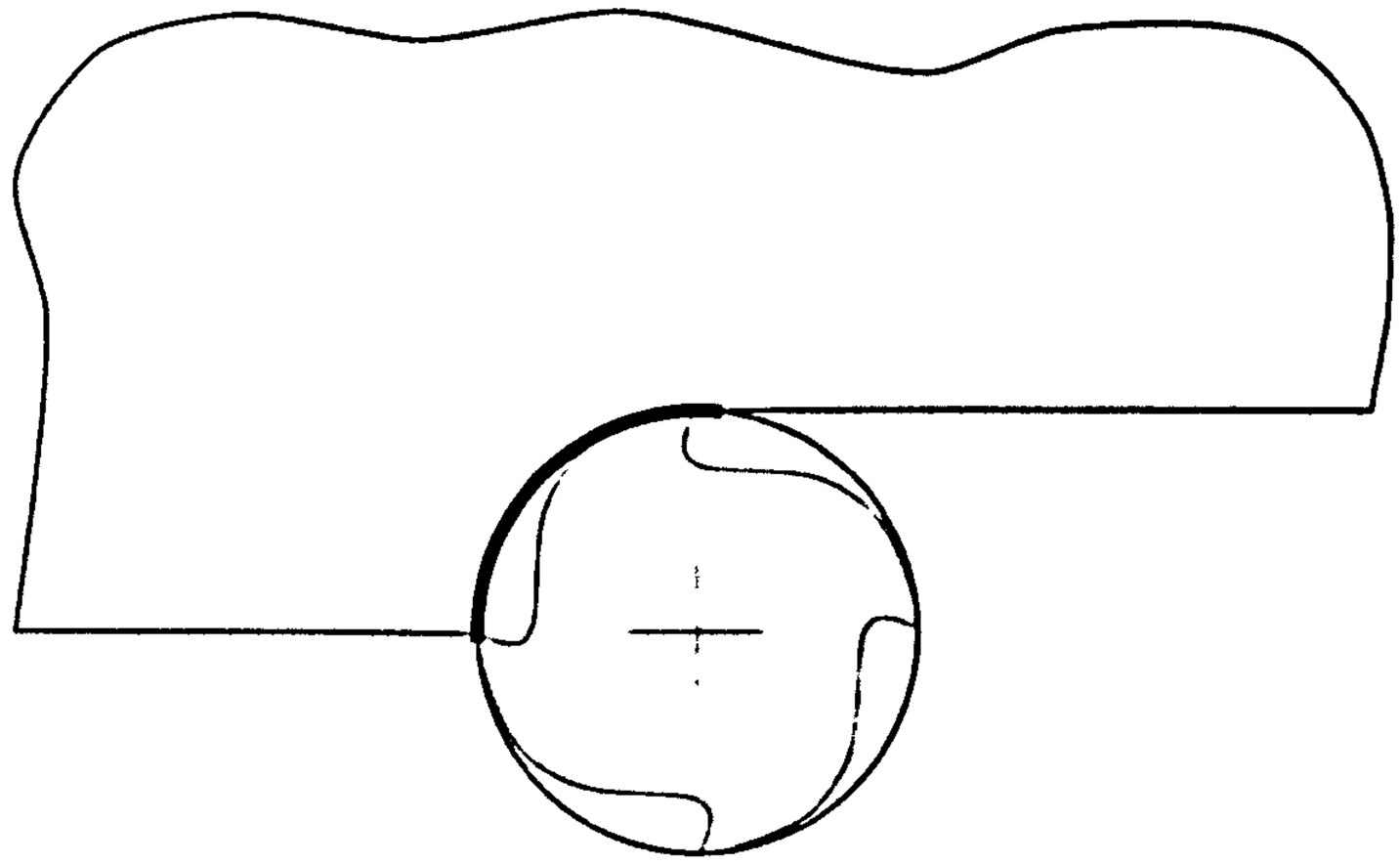

(a) Wrap Angle approx. 90 degrees

(b) Wrap Angle approx 180 degrees

Figure 5.7: Wrap angle definition

Chapter 6

Real-Time Substructuring using MCS

SUMMARY: A method that extends the use of MCS beyond the realms of pure control into the field of a new dynamic testing technique called real-time substructuring is presented. Relevance of the technique in the field of manufacturing presented along with example. Implementation methods and results achieved using this technique on various dynamic experimental set-ups will be presented and discussed.

6.1 Introduction

Few large scale testing facilities exist throughout the world that allow dynamic testing of full scale and complete systems whether those systems be civil engineering structures or mechanical components. This limitation means that experiments on larger structures, such as bridges, towers and aerospace frames are either carried out at a reduced scale or with a small part of the structure being tested in isolation. Testing at a reduced scale allows the entire structure to be tested, but adjustment to the dynamic excitation pattern and interpretation of the results are required to allow the inability to scale factors such as gravity, aggregate size in concrete structures, etc. Testing small parts of the structure at full scale in isolation overcomes these problems but again requires interpretation of results to account for the missing part of the structure. Similarly, when investigating the effect of cutting forces on the final geometry of a complex workpiece, the full workpiece may not always be available in its final form. However, in order to replicate the workpiece behaviour

when excited by imposed cutting forces, the dynamic response of the entire workpiece is required. Real-time Substructuring (also known as hybrid testing) is a method of dynamic testing conceived by Takanashi *et al.* [191] that aims to overcome these shortfalls.

6.1.1 Nomenclature

Figure 6.1 demonstrates how a system is broken down and tested using the real-time substructuring technique. The complete structure that is to be reproduced in real-time substructuring is referred to as the *emulated system* (figure 6.1 (a)). In a substructuring test, the emulated system must be broken down into smaller parts, referred to as *substructures*, shown in Figure 6.1 (b).

Substructures fall into one of two types. The first group are theoretically well understood, generally linear, and can be modelled accurately. They are called *numerical substructures.* The second group consists of systems which are either not well understood, non-linear, otherwise complex to model, or are simply not available for testing. This second group are known as *physical substructures.* Figure 6.1 (c) shows the example given in (a) when broken into a particular combination of substructures. As the names suggest, the physical substructure is the part that will be tested physically in a laboratory whilst the numerical substructure would be implemented via a computer model running in real time.

The recombination of the distinct substructures is achieved using a *transfer system* which would normally consist of a transducer and corresponding actuator that can measure and alter the *interface variable.* In the example shown, the force F on the physical substructure in the required degree of freedom(s) is the interface variable which could be altered using a hydraulic actuator. The substructuring experiment corresponding to the example detailed above, including the transfer system, is outlined in figure 6.1 (d).

Real-time substructuring is a subset of the Hardware-in-the-Loop Simulation (HILS) technique[1] [193, 197–199]. HILS has recently become popular due to the increased availability of digital signal processors and accompanying rapid-prototyping solutions such as dSPACE[2] and XPC[3]. Hardware-in-the-Loop simulation is typically used to allow equip-

[1] http://www.embedded.com/showArticle.jhtml?articleID=15201692

[2] http://www.dspaceinc.com/

[3] Product of The MathWorks - http://www.mathworks.com/products/xpctarget/

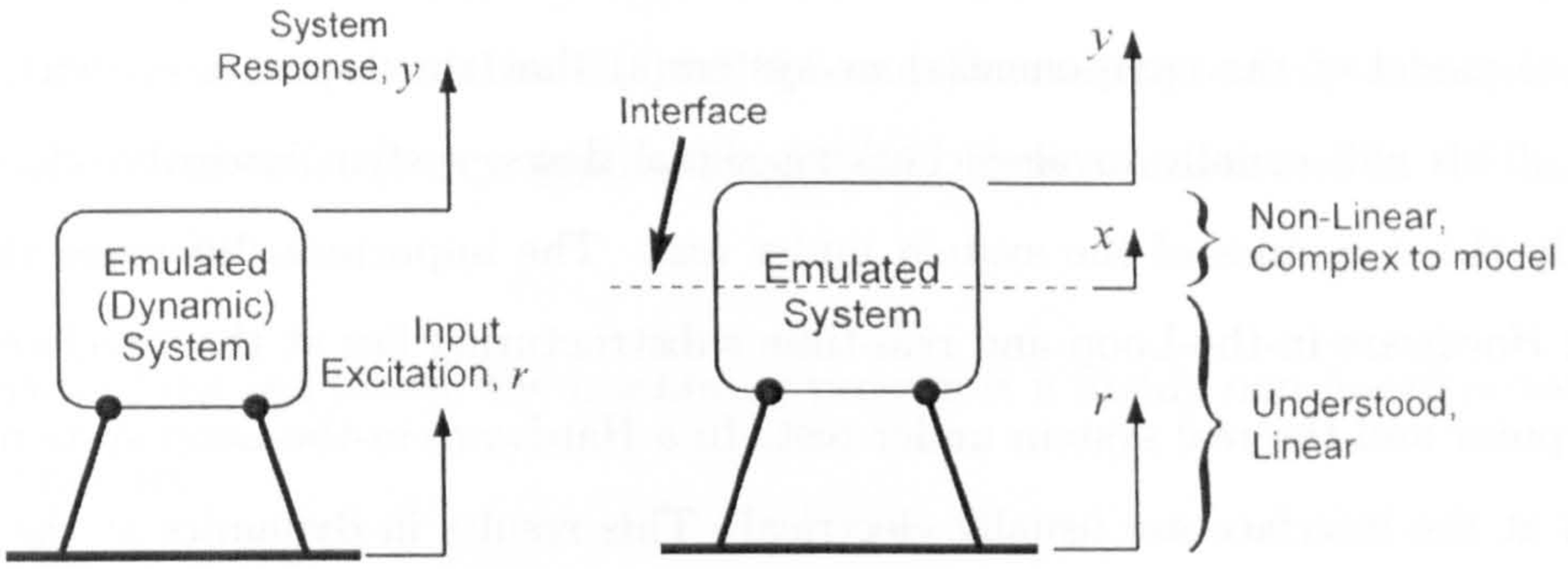

(a) Emulated System (b) Component Parts - Characterisation and candidate Substructures

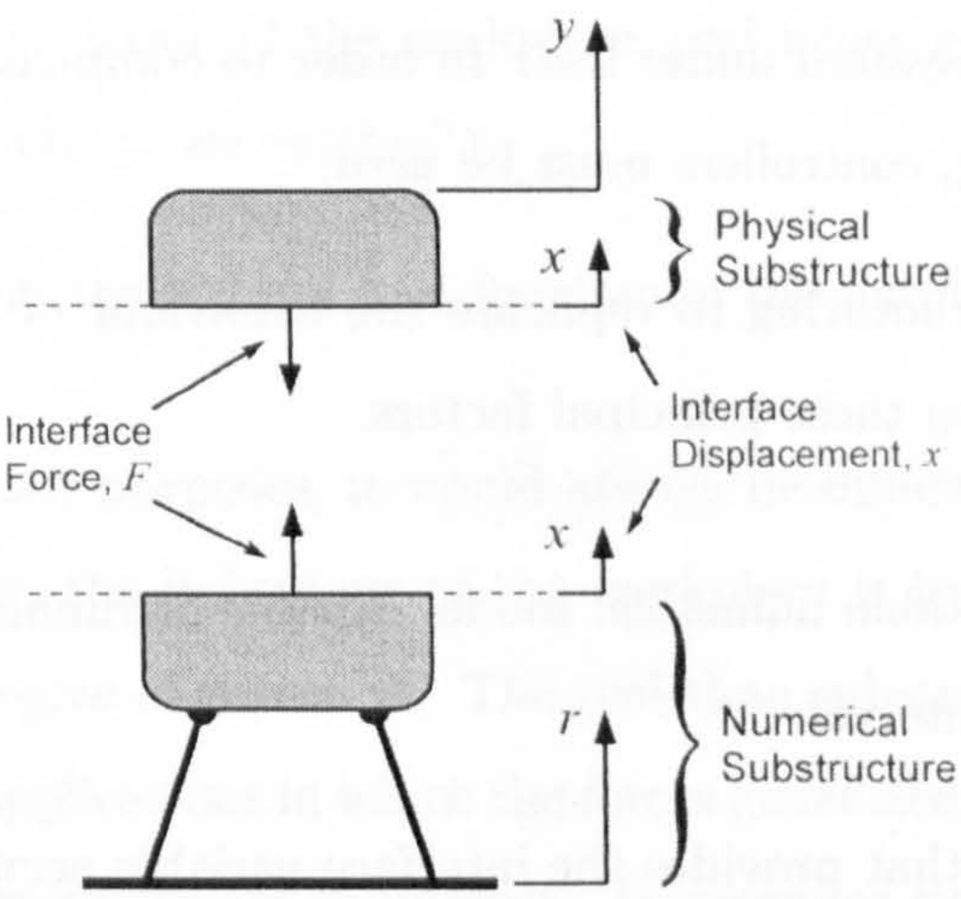

(c) Physical and Numerical Substructures

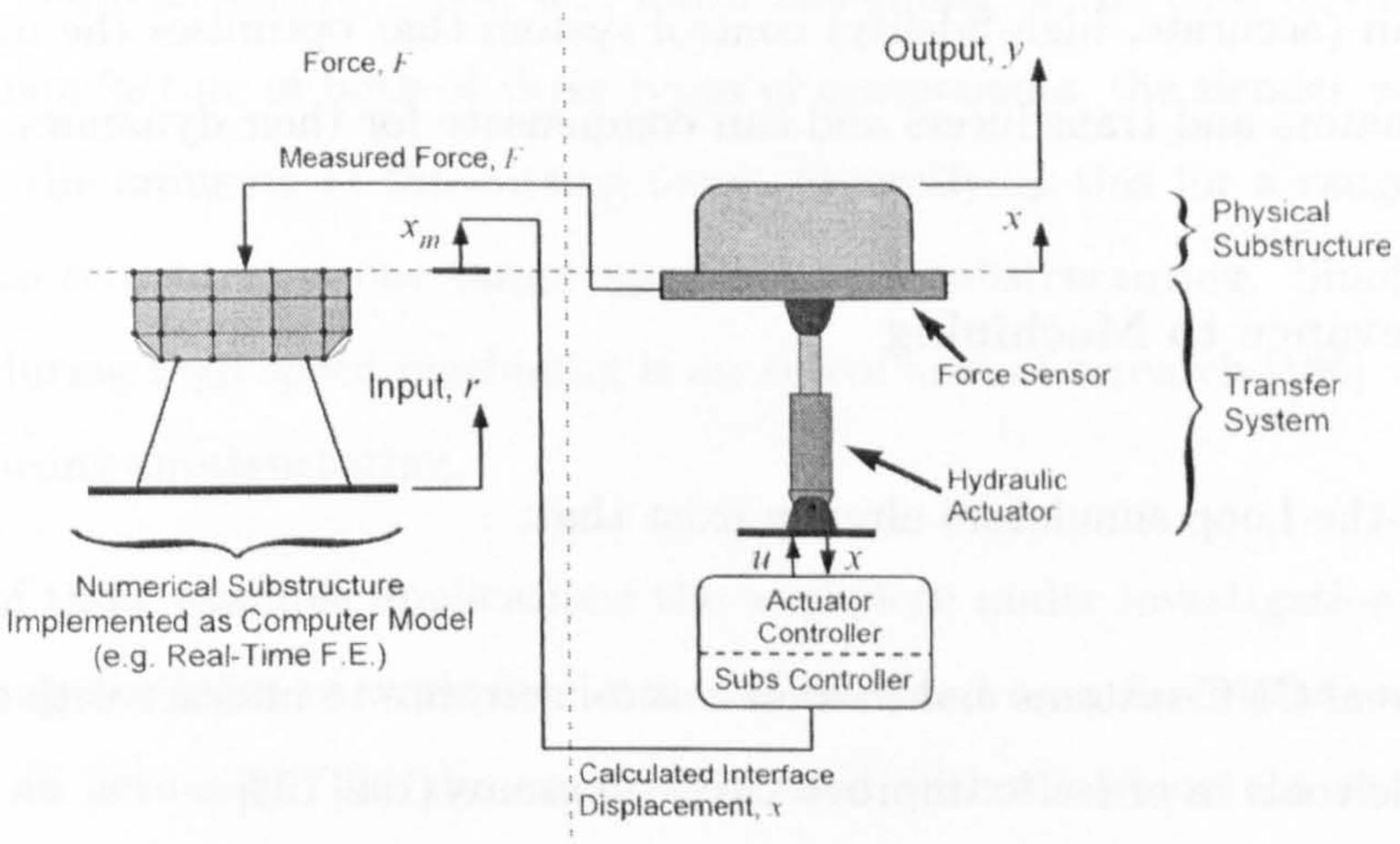

(d) Implementation of Substructuring Experiment

Figure 6.1: Substructuring example - from emulated system to experiment

ment manufacturers to test their systems (such as an Engine Management System) on a numerical model of the component(s) or system(s) that they operate on/with (e.g. an engine). This will usually involve checking signal flows, system integrity, etc. and occasionally the dynamics of the system under test. The important difference that exists between Hardware-in-the-Loop and real-time substructuring lies at the interface between the computer and the real system under test. In a Hardware-in-the-Loop system the connections at the interface are usually electrical. This results in dynamics at the interface whose bandwidth is far higher than the real system under test and hence can be ignored. In a real-time substructuring experiment the connections at the interface are physical (e.g. hydraulic actuator). The associated raw dynamics will have a bandwidth that lies in the same region as the real system under test. In order to compensate for these dynamics in real-time substructuring, controllers must be used.

The ability of substructuring to replicate the behaviour of the complete structure is therefore dependent upon these principal factors.

- An accurate and stable numerical model capable of running in real-time at a satisfactory sampling interval.
- A transfer system that provides the interface variable accurately.
  - A well understood set of high quality actuators and transducers
  - An (accurate, high-fidelity) control system that optimises the use of these actuators and transducers and can compensate for their dynamics.

6.1.2 Relevance to Machining

Hardware-in-the-Loop simulators already exist that:

- Allow real CNC systems and motion control software to interact with simple virtual machine tools in order to improve CNC programs [192, 193]
- Allow investigation of machine tool dynamics for chatter suppression [194]

Currently, the real-time substructuring technique described in this chapter has only been tested in applications with a low bandwidth (up to 15Hz). This is mainly a limitation

imposed by the speed of computation and the bandwidths of the actuators and transducers available. It is proposed that when the real-time substructuring testing technique develops to incorporate higher-frequency applications, it will form a useful tool in the high-speed machining research arena.

In terms of cutting forces, the machining process is a highly non-linear process. This is mainly due to:

- The form that the cutting tool takes, with discrete cutting edges that enter and exit the workpiece at unpredictable times
- The large range of variation of the workpiece, and hence geometry of cut, during a particular cut (including "air cutting")
- Variable dynamics in the n degrees-of-freedom of the machine tool

As a result, for research purposes, it would always be difficult to model the machine tool accurately. However, the behaviour of the workpiece is less complex and easier to model to a reasonable degree of precision. The real-time substructuring technique could lend itself to machining applications in which the forces generated by the machine tool, and hence defection of the workpiece are of interest. Two similar examples of this particular type of application are briefly discussed. These are the milling of thin webs and ribs on aerospace components [187, 195], and finish machining of the ends of turbine blades. During the manufacture of both of these types of components, the slender workpiece will deflect under the influence of the cutting force. Quantifying this for a range of machine tool workpiece structures is one target application of substructuring. Similarly, chatter suppression during high speed machining is an active area of research [196] that could be investigated using substructuring.

In both of these example applications the workpiece under investigation could be replaced by a regular billet of workpiece material mounted on a force plate which is itself mounted on an actuator. The dynamics associated with the structure of the emulated workpiece could then form the numerical substructure with the machine tool forming the real system under test (or the *physical substructure*). This is demonstrated in figure 6.2.

Note that, in this proposed application, the input excitation would be through the real system under test (*physical substructure*, rather than through the virtual system under

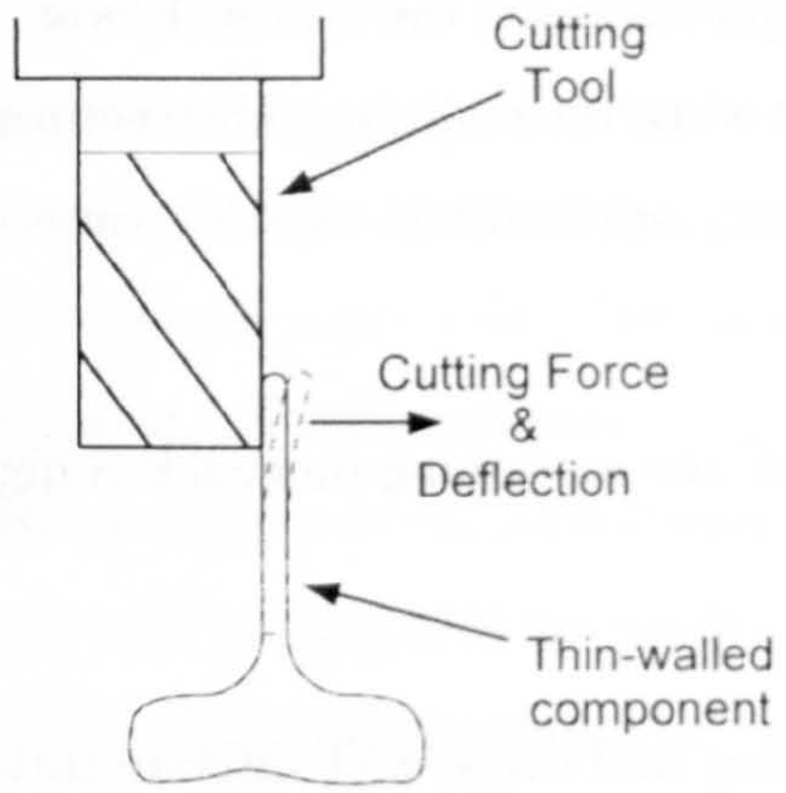

(a) Emulated System

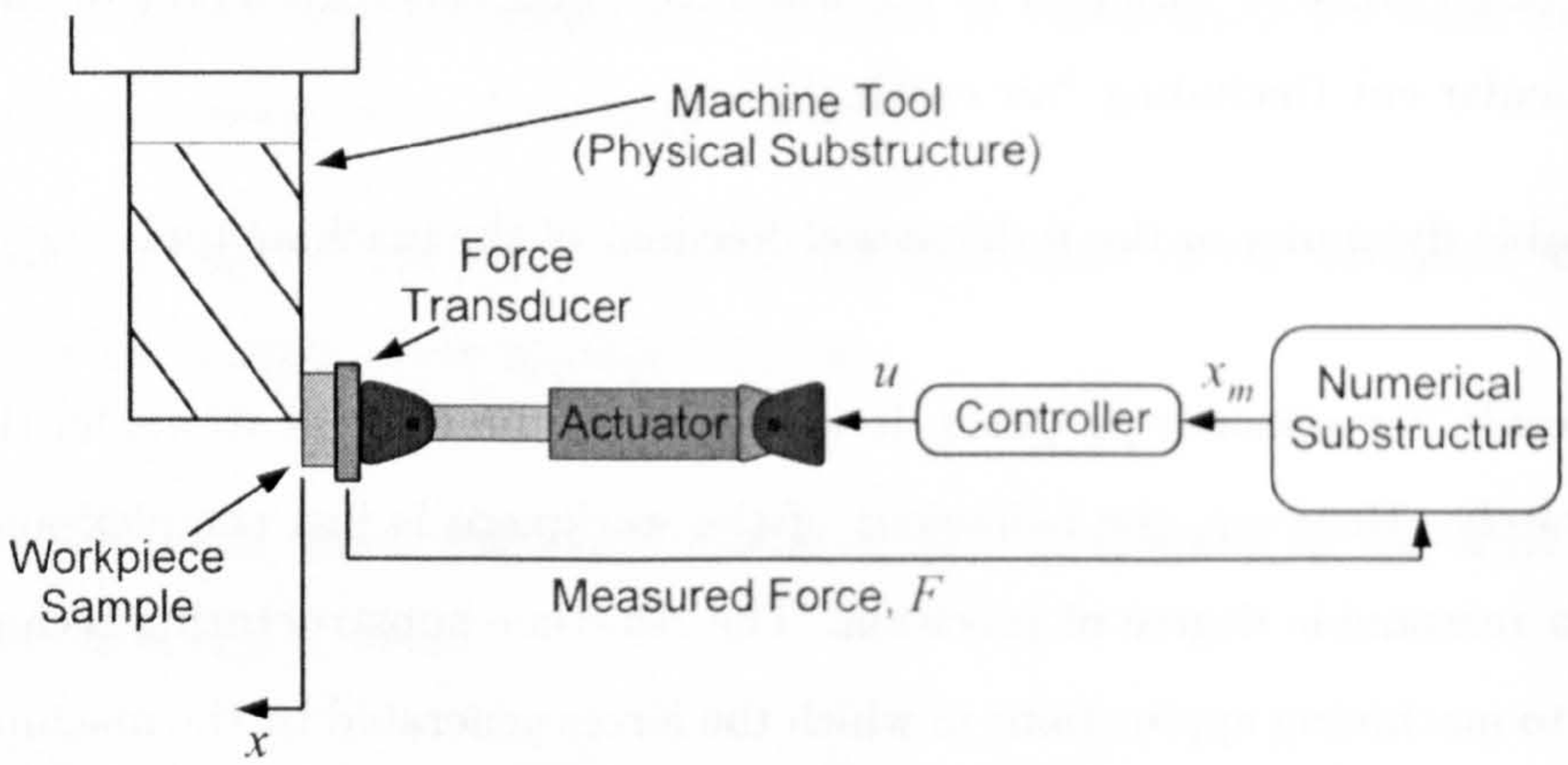

(b) Substructured System

Figure 6.2: Schematic demonstrating a case in which substructuring is applied to machining

test (or *numerical substructure*), as is been presented in the sample problem chosen for the work in this chapter. However, this change in configuration requires no change in the methods used to implement the substructuring technique.

The work presented in this chapter is a result of joint research carried out with Dr S.A. Neild[4].

[4]Research Assistant, Department of Mechanical Engineering, University of Bristol, Queen's Building, University Walk, BRISTOL, BS8 1TR

6.2 Control for Substructuring

The majority of research in real-time substructuring has concentrated on the first of the above areas, ie the numerical model [200], with investigators assuming that the control systems are sufficiently accurate.

The work presented here approaches the technique from the opposite angle, assuming that the problems and instabilities associated with implementing the required numerical model in real-time have been solved, and that the output of that model is perfectly accurate.

Most attempts to improve the control of the transfer system in order to improve substructuring performance have followed the ideas proposed by Horiuchi *et al.* [201]. Horiuchi *et al.* noted that the time difference seen in sending a demand signal to an actuator controller and the arrival of that actuator at the demanded position was significant in introducing inaccuracies and even instability during substructuring (or hybrid) experiments. For even a simple linear system, the time difference can have the effect of introducing a supplementary negative damping term into the structure providing it with additional energy. If this time difference and its associated negative damping term is large enough the effect causes the entire substructured system to effectively behave as if it had negative damping, resulting in experimental instability [202].

The method proposed by Horiuchi *et al.* for overcoming this effect was termed "actuator delay compensation". The term "delay" in Horiuchi's work referred to the frequency dependent lag associated with the dynamics of any particular actuator. A polynomial was used to predict a modified demand signal one time step ahead such that the actuator responded without a "delay". A sensitivity study that used polynomials of increasing orders to generate the new predicted signal showed that the technique itself slightly altered the accuracy of the final substructured system. This method assumed a fixed delay as a model for the lag of an actuator as it was based on a single frequency of excitation, possibly the main excitation or a representative frequency. Its applicability to systems where the lag of the actuator either varies greatly, or is non-linear over the excited frequency range, is undemonstrated. An self-tuning form of Horiuchi's work, proposed by Wallace *et al.* [203], successfully compensated for a delay of variable length, making this approach more robust.

The approach presented here is one that considers the true dynamics of the transfer

system and compensates for these dynamics using a range of feedback controller strategies.

6.3 Sample Problem

Using a single degree of freedom mass-spring-damper system shown in Figure 6.3 (a) as a complete structure, the technique has been demonstrated, tested in simulation and then performed experimentally with a variety of substructuring controllers. In the first instance a fixed-gain linear controller will be examined, followed by an MCS substructuring controller (and variants).

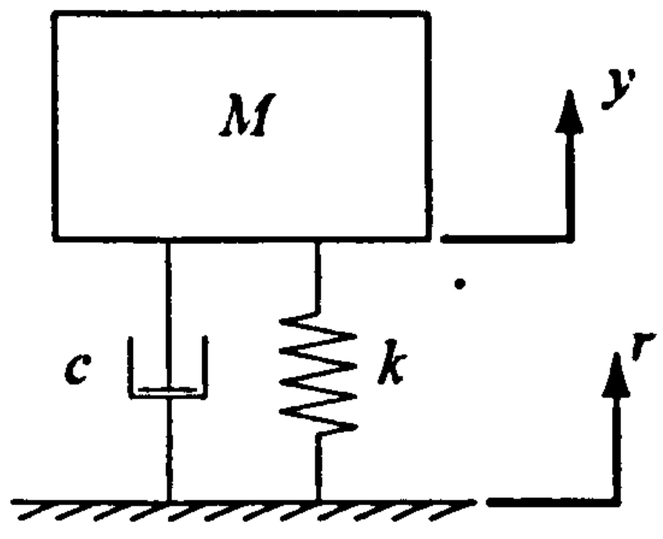

(a) Emulated system

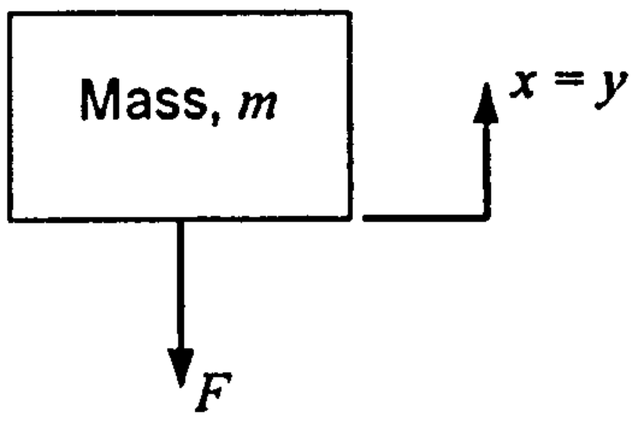

(b) Experimental substructure

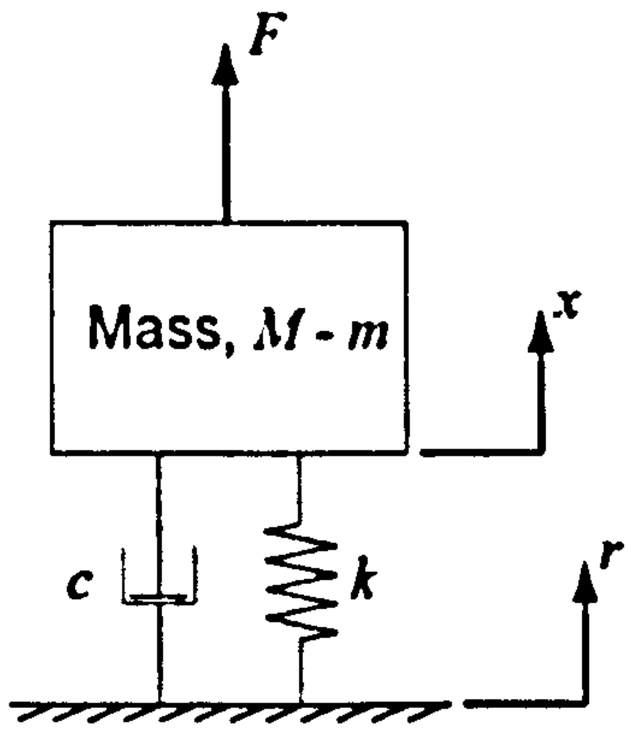

(c) Numerical substructure

Figure 6.3: Single degree-of-freedom mass, spring and damper system, emulated system and equivalent substructured single degree-of-freedom system

The system is broken down into two substructures. The numerical substructure is composed of the spring, with stiffness k, the damper, with damping coefficient c, and part of the mass, $M - m$. The experimental substructure consists of the remaining mass, m as shown in Figures 6.3 (b) and (c) respectively.

This particular choice of substructures has chosen to keep the experiments as simple as possible during this proof-of-concept state of the work. The following values have been chosen for the variables, c, k, m and M so that the emulated system is an underdamped structure (damping factor, $\zeta = 0.1$) with a natural frequency, ω_n, of 2Hz.

- Mass of the mass present in the physical substructure, $M = 20$kg
- Mass of the mass present in the numerical substructure, $M - m = 80$kg
- Spring stiffness, $k = 16{,}100$ Nm^{-1}
- Damping factor, $c = 254$ Nsm^{-1}

The continuous-time transfer function for the emulated system is:

$$\frac{x(t)}{r(t)} = G_T(t) = \frac{cs + k}{(M + m)s^2 + cs + k} \tag{6.1}$$

6.4 Proposed Substructuring Controller Algorithms

6.4.1 Linear Controller

A design process for substructuring using a linear controller, for a linear substructured system was conceived by Stoten *et al.* [204]. The work used a series of simulations to validate the design process and perform a sensitivity study. The design process is summarised here, and the work extended through a series of experiments in section 6.6.1.

By making a linear approximation of the "plant" (the transfer system and the experimental substructure), a linear controller may be designed. Performing a system identification, using a swept sine wave as the method of excitation, a first order approximation to this system was found to be:

$$G_t(s) = \frac{b}{s + a} = \frac{0.264}{s + 7.91} \tag{6.2}$$

where a and b are plant parameters determined experimentally and s is the Laplace transform variable. Figure 6.4 shows a schematic of a linear controller for the substructuring test, involving the one degree-of-freedom mass-spring-damper system. Using the first order plant transfer function, $G_t(s)$, it is possible to design the linear controller to enable the movement of the substructure mass to replicate the mass of the emulated system [204]. It is required that the closed-loop transfer function from the ground excitation r to the

displacement of the substructure mass x is the same as for the emulated system, $G_{emu}(s)$, therefore:

$$\frac{x(s)}{r(s)} = G_{emu}(s) = \frac{cs+k}{Ms^2+cs+k} = \frac{G_c(s)G_t(s)}{1+G_c(s)G_t(s)H(s)} \tag{6.3}$$

where $G_t(s)$ is the plant transfer function from $u(s)$ to $x(s)$, $G_c(s)$ is the feed forward gain and $H(s)$ is the feedback gain. An exact solution to this equation exists when a proportional + integral + derivative feedback strategy is adopted:

$$G_c(s) = k_p + \frac{k_i}{s}\ ,\ H(s) = 1 + k_d s \tag{6.4}$$

where k_p, k_i and k_d are proportional, integral and derivative gain terms respectively. By substituting equations 6.2 and 6.4 into equation 6.3 it may be seen that the closed loop transfer function exactly matches the transfer function of the emulated system provided that:

$$k_p = \frac{ck_i}{k}\ ,\ k_i = \frac{k-ac}{Mb}\ ,\ k_d = -\frac{a}{bk_i} \tag{6.5}$$

However, the controller has been based on a first-order linear model of the transfer system, and may not prove to be robust to changes in plant parameters $\{a, b\}$ or model parameters $\{c, k, M\}$. To overcome this, a high-gain error feedback strategy is proposed [204, 205], as shown in figure 6.5. The benefit of the high-gain error feedback term, $G_h(s)$, is that it enables bounded disturbances in the plant and numerical model to be rejected [204]. In this study, the error feedback block is assigned $G_h(s) = K_{ef}$ where K_{ef} is a fixed error feedback gain. The equation for the control signal may therefore be written:

$$u(s) = \left[k_p + \frac{k_i}{s}\right][r(s) + K_{ef}x_e(s)] - \left[k_p k_d s + k_i k_d + k_p + \frac{k_i}{s}\right]x(s) \tag{6.6}$$

One problem with implementing this controller in a discrete form is that the control signal includes an $\dot{x}$ term which leads to amplification of higher frequency noise if it is generated by differentiating the displacement signal. To overcome this, composite filtering [206] was used to generate the required $\dot{x}$ term from the measured shaking table displacement and acceleration. Using a composite filter [206] based on a second-order Butterworth filter with a cut-off of 20 rad/s (based on the performance of the transducers) the $sx(s)$ term was calculated using:

$$sx(s) = \frac{s}{s^2+28s+400}a_t(s) + \frac{28s^2+400s}{s^2+28s+400}x(s) \tag{6.7}$$

where $a_t(s)$ is the measured shaking table acceleration. A discrete version of this controller has been developed for use within the dSPACE control environment.

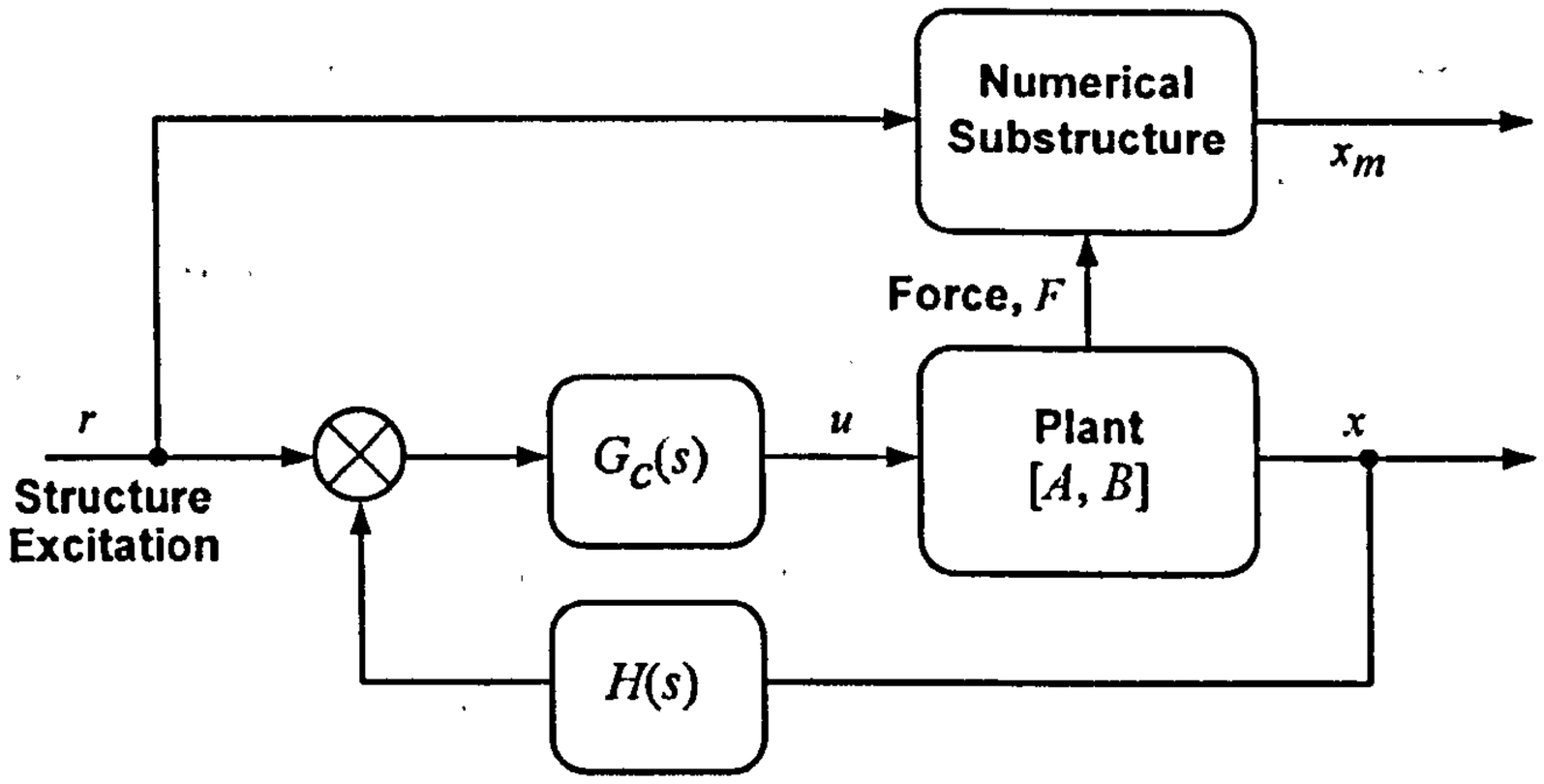

Figure 6.4: Block diagram of substructuring using a linear controller, $\{G_c(s), H(s)\}$

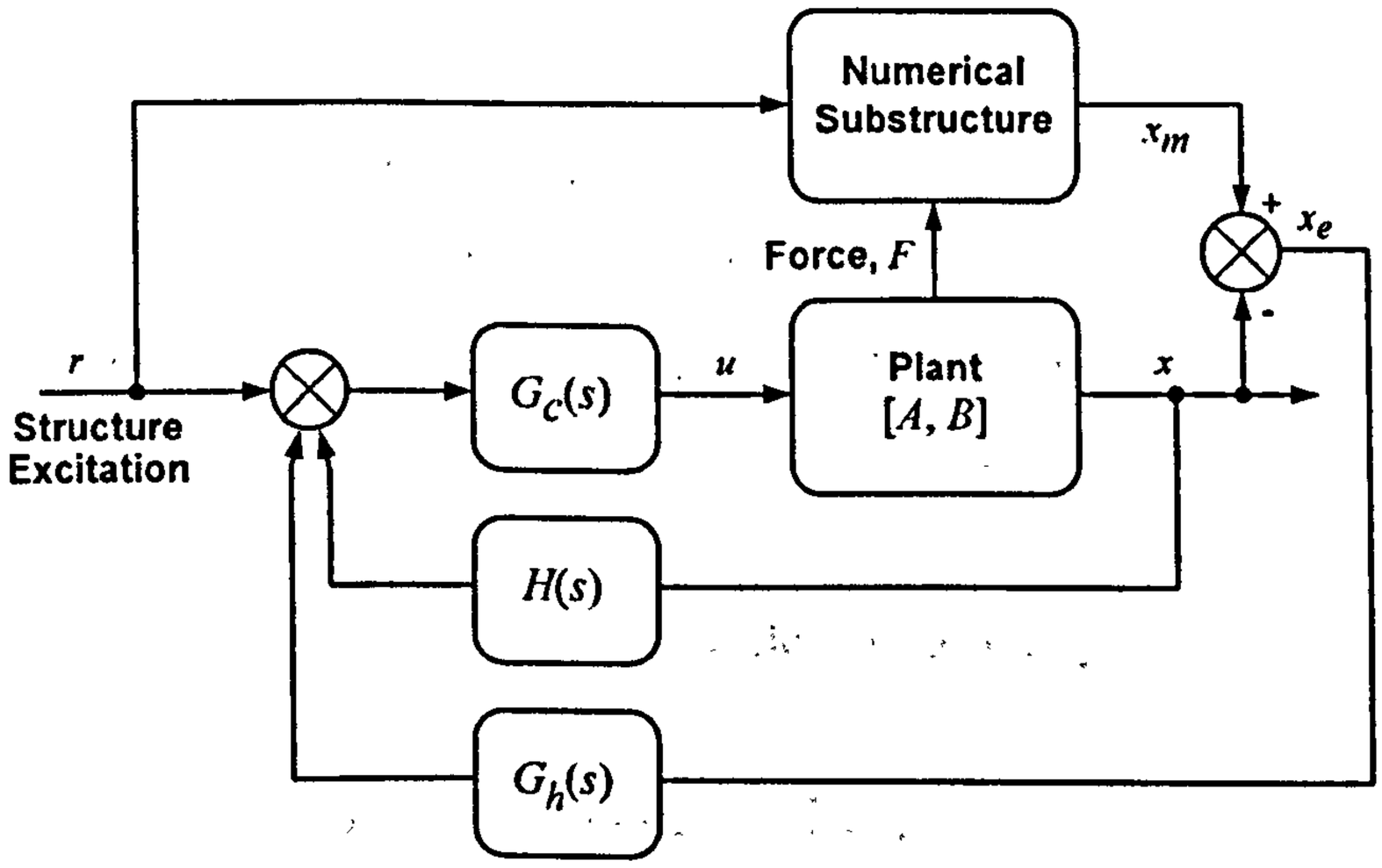

Figure 6.5: Block diagram of substructuring using a linear controller with error feedback, $\{G_c(s), H(s), G_h(s)\}$

6.4.2 MCS Adaptive Controller

As detailed in section 3.2.1 the MCS algorithm (figure 6.6) is an adaptive model reference control strategy. Two modifications have been made to allow it to be used in substructuring. Firstly the reference model has been replaced by the numerical substructure. Secondly, an additional feedback loop has been added allowing the force to be fed from the shaking table to the numerical substructure. First order control is implemented using this strategy. The resulting block diagram for the controller is shown in figure 6.7 and can be compared to the MCS strategy when used as a standard controller, shown in figure 6.6.

The relative ease with which the substructuring concept could be fit into the MCS algorithm is one of the reasons for its selection for use with this technique. For first order control, the control signal is calculated using the ground excitation, r, the physical substructure displacement, x, and the adaptive gains, K and K_R. In this one degree-of-freedom case, these adaptive gains may be expressed as:

$$K(t) = \alpha \int_0^t y_e(\tau)x(\tau)\,d\tau + \beta y_e(t)x(t) \tag{6.8}$$

$$K_R(t) = \alpha \int_0^t y_e(\tau)r(\tau)\,d\tau + \beta y_e(t)r(t) \tag{6.9}$$

where α and β are adaptive weightings and $y_e = C_e x_e$ where C_e is defined to ensure hyperstability of the closed loop error dynamics [164]. For first order control, C_e is normally defined as $4/t_s$ where t_s is a settling time, in this case 0.01s. The ratio $\alpha = 10\beta$, which has been shown to work well empirically [169], is used here. The higher the value of α the greater the adaptive "effort". However, in practice α is limited by the discrete nature of the controller and signal noise.

6.4.3 Er-MCSI Adaptive Controller

The Er-MCSI controller is a modified version of the MCS controller in which the control signal is based on the error displacement, x_e, the integral of the error displacement, x_i, and the corresponding adaptive gains. The objectives behind these modifications to the MCS controller are twofold. Firstly, the explicit integral term will prevent gain wind-up. This is desirable since gain wind-up results in the closed-loop bandwidth becoming excessively large, which leads to aliasing and also results in signal noise being amplified around the loop. Secondly, the use of the displacement error term rather than displacements x and r

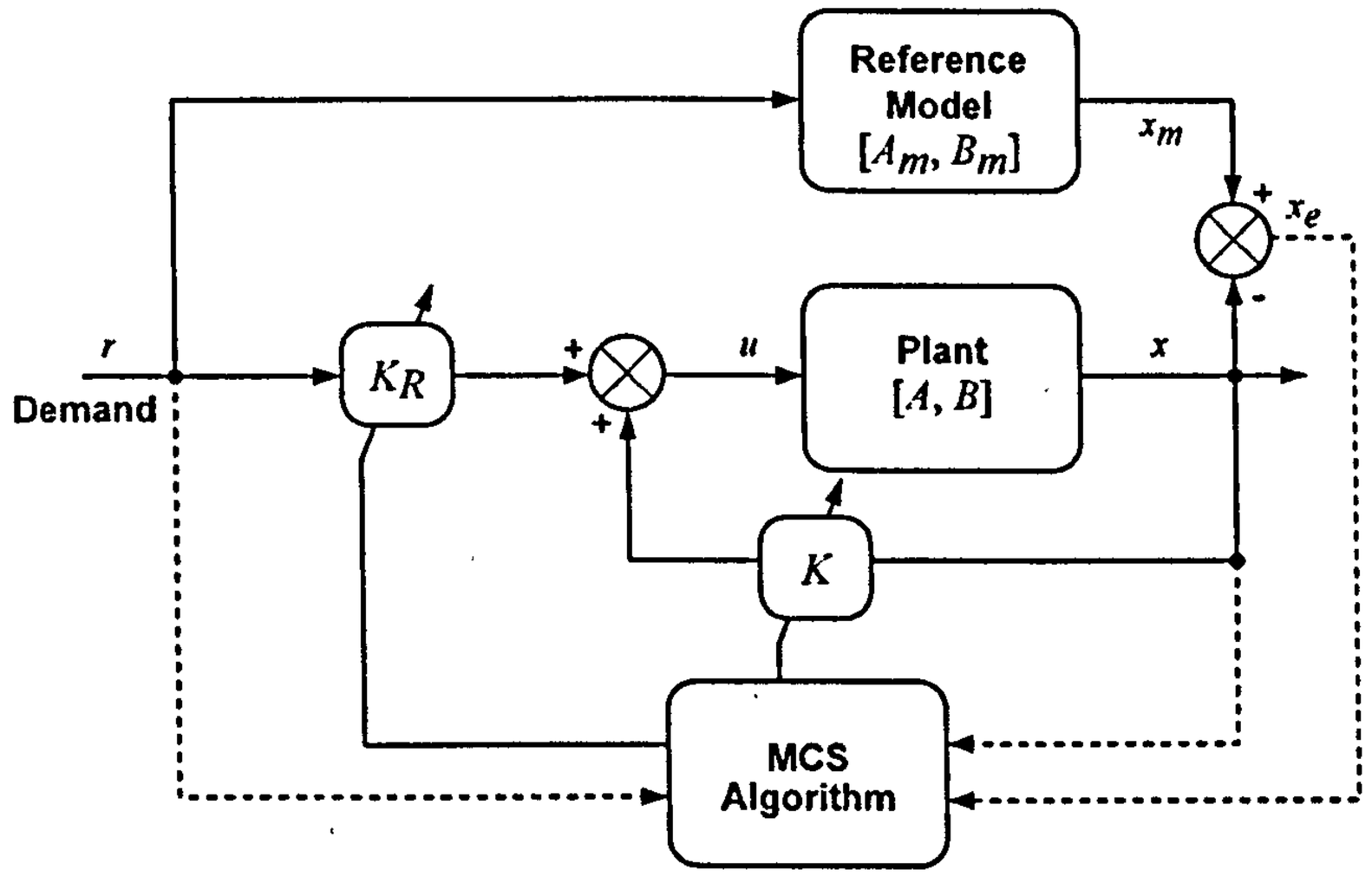

Figure 6.6: Block diagram of the basic MCS algorithm used as a standard controller

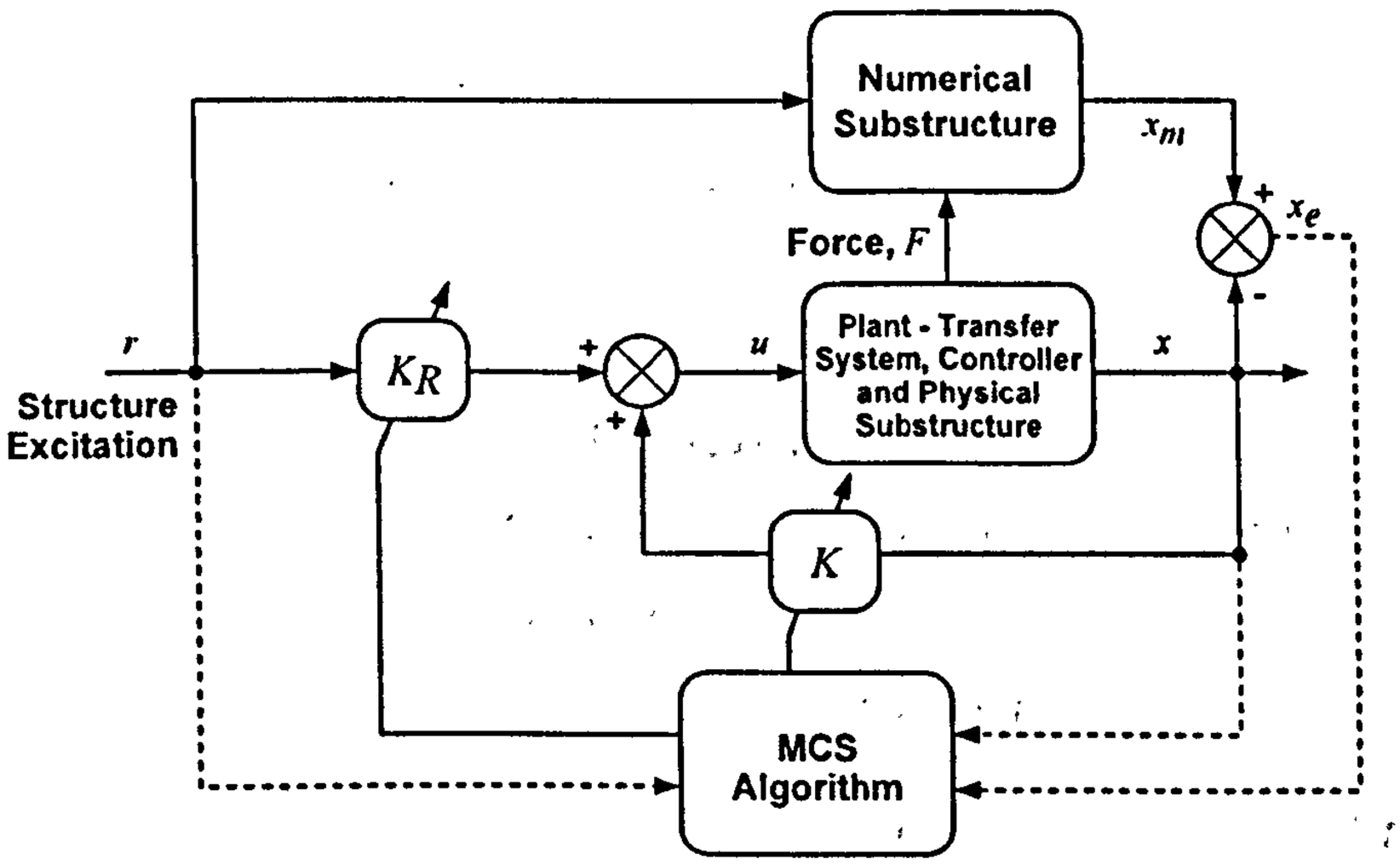

Figure 6.7: Block diagram of the MCS algorithm when used as a substructuring controller

overcomes the problem that both x and r potentially exist over a wide operating range. The effect on the gains across this range is not constant, but varies linearly with distance away from the origin. This can result in too much adaptation at the limits of the operating range and too little near the origin. The use of the error in displacement eliminates this problem since its magnitude is insensitive to the operating point [207]. As with the MCS controller, the Er-MCSI controller has been modified for use in substructuring, firstly by replacing the reference model with the numerical model and secondly by adding an additional force feedback loop from the plant to the numerical model. The block diagram for the controller is given in figure 6.8. The equations for the gains are:

$$K_E(t) = \alpha \int_0^t y_e(\tau)x_e(\tau)\,d\tau + \beta y_e(t)x_e(t) \tag{6.10}$$

$$K_I(t) = \alpha \int_0^t y_e(\tau)x_i(\tau)\,d\tau + \beta y_e(t)x_i(t) \tag{6.11}$$

where x_i is the integral of x_e with respect to time. As with the MCS algorithm the ratio $\alpha = 10\beta$ is used.

6.5 Implementation of Substructuring Controller Algorithms

All of the substructuring algorithms presented here were implemented using a rapid-prototyping system called dSPACE. dSPACE is a proprietary hardware and software platform on top of which real-time control applications can be developed. Briefly, control routines (or any other application type) are designed and written within the SIMULINK environment. This is a block-based modelling tool that runs within MATLAB, enabling simulation in continuous or discrete-time of dynamic systems. Using a library of blocks, systems are implemented simply by dragging them into the window containing the model and then "wiring" them together as necessary. An example of the SIMULINK model used to generate the software used at the University of Bristol to perform substructuring experiments is shown in Figure 6.9.

dSPACE extends this environment, allowing the systems designed in SIMULINK to be run in hard real-time via the following stages:

1. Provision of a hard real-time DSP hardware environment and D/A, A/D subsystems
2. Generation of C-code equivalent to the SIMULINK model via the Real-Time Workshop, (RTW)

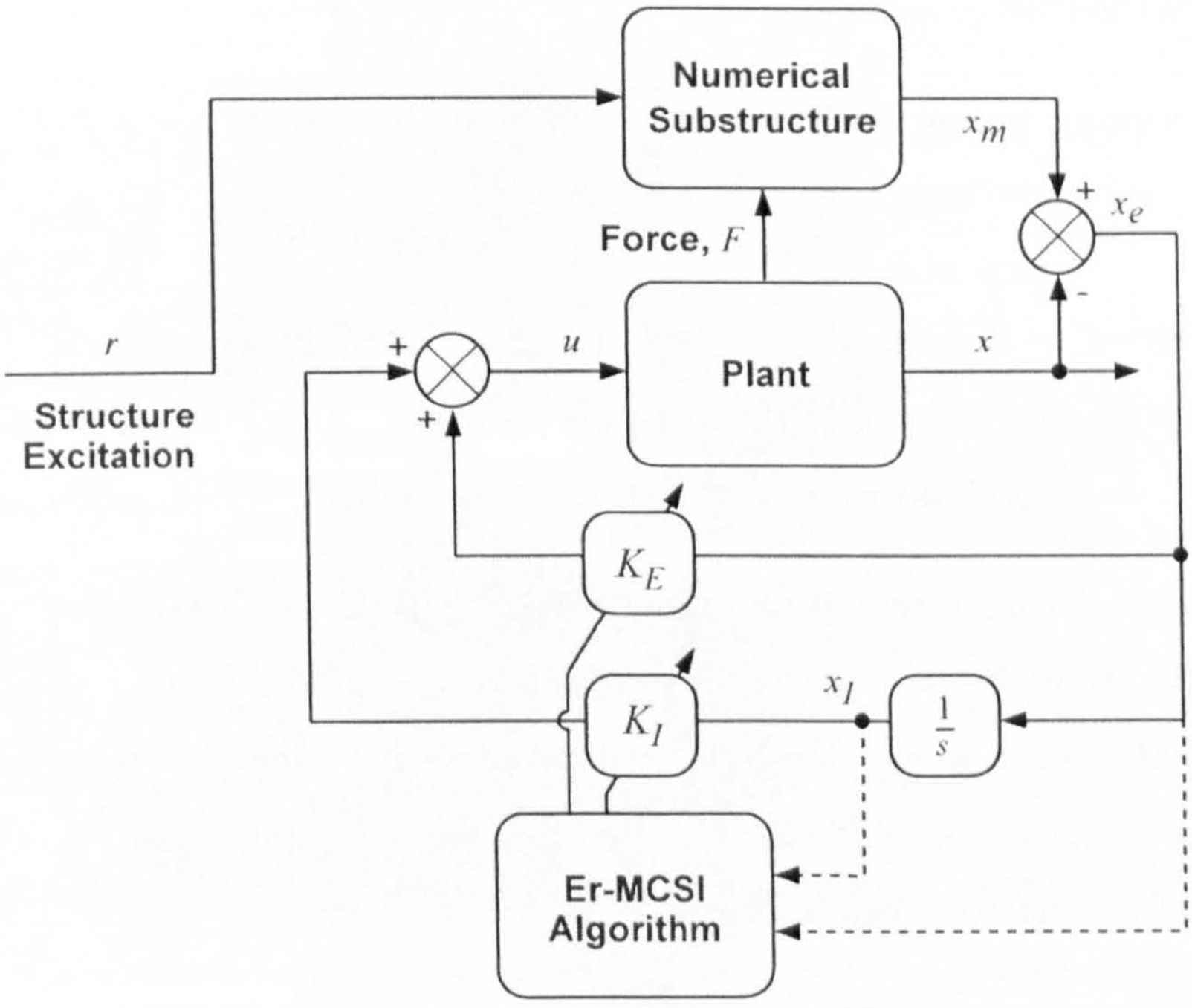

Figure 6.8: Block diagram of the Er-MCSI algorithm when used a substructuring controller

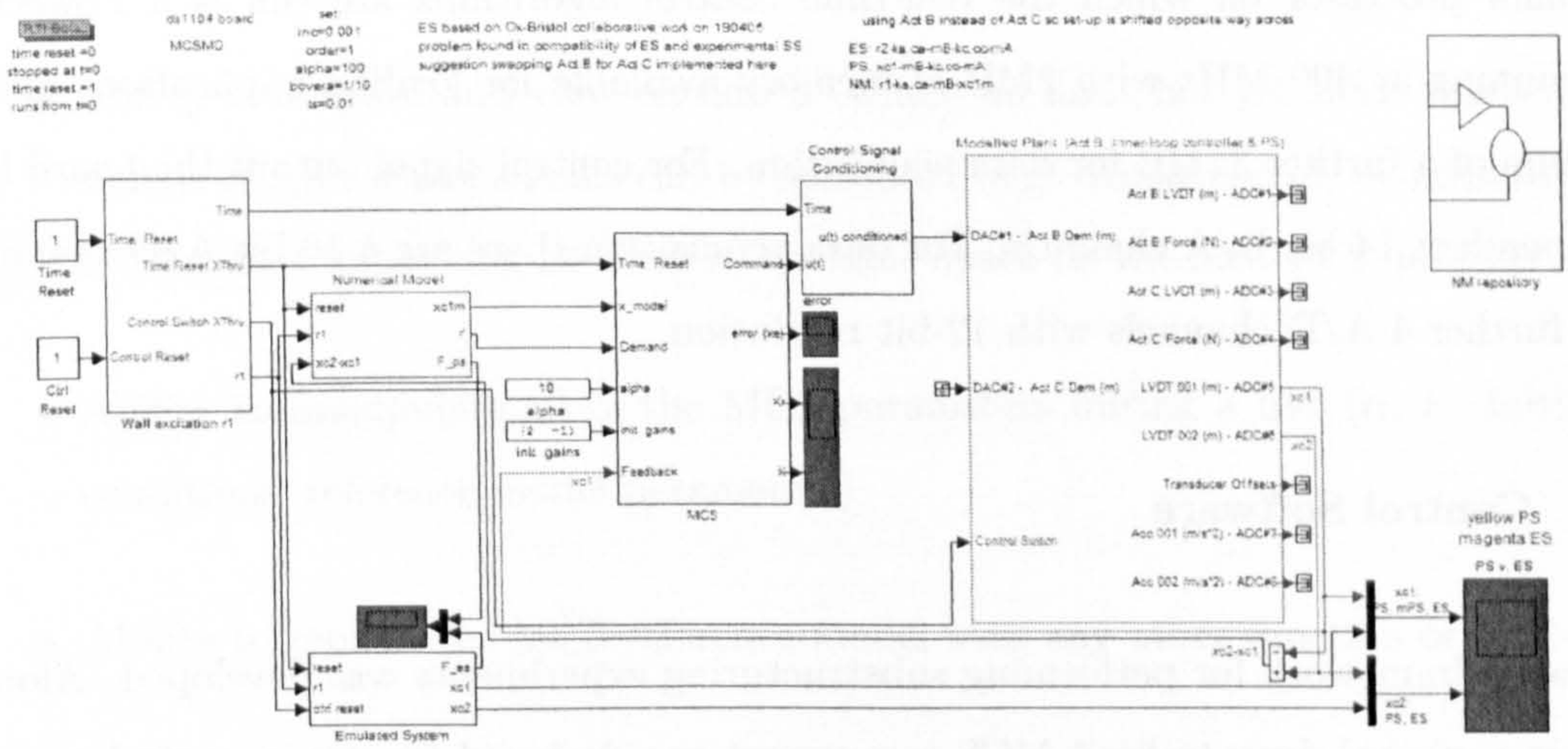

Figure 6.9: Simple Simulink model

3. Downloading to on-board memory and running of the generated C-code onto the dSPACE DSP processor

4. Monitoring, interaction and general control of the loaded C-code via the ControlDesk software environment

ControlDesk is the software provided by dSPACE to allow interaction of an end-user with the application running on the real-time processor. It provides basic GUI components such as buttons, check boxes, etc. as well as a data logging system and graphing tools.

Whilst windowing capabilities are not present with ControlDesk, the creation and use of several layers within a single application is possible. To offer the functionality required by a general control application individual levels of functions are assigned to particular layers in the ControlDesk software. The top layer is dedicated to the important functions allow use of the most important components.

6.5.1 dSPACE Hardware Platform

dSPACE produce a range of hardware platforms for implementation of control. For the substructuring experiments presented, a DS1104 system was selected. This is a single board solution which provides all the hardware necessary to control a host of systems. The main processor on which the real-time control algorithms are run is a PowerPC 604e running at 400 MHz with 2MB of memory available for loading applications and a minimum of a further 32MB for data acquisition. For control signal output the board has 8 independent 14-bit D/A channels. For data acquisition there are 4 16-bit A/D channels and a further 4 A/D channels with 12-bit resolution.

6.5.2 Control Software

A software framework for performing substructuring experiments was developed. Alongside this a general decentralised MCS component was designed for use in control experiments. Appearing as a single block the component is able to control n-degrees of freedom as a decentralised strategy. To accompany the model and its associated application a GUI was developed in ControlDesk to manipulate experimental parameters, acquire data and run the experiment. An example of this GUI is shown in Figure 6.10. The software's

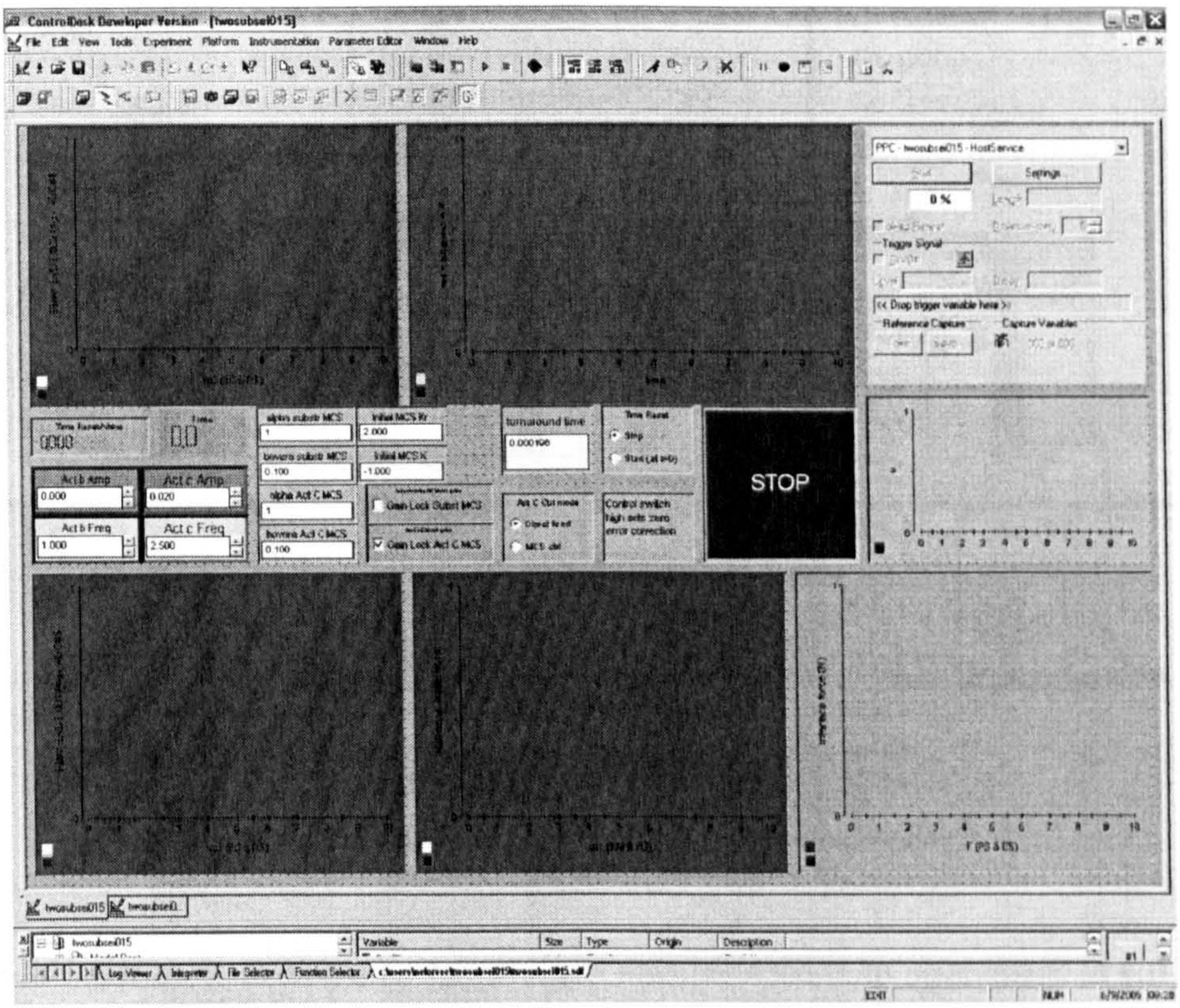

Figure 6.10: GUI implemented in ControlDesk for substructuring experiments

functionality included:

- Ability to acquire and view on-line n (where no limit has yet been reached on n) signals of data where signals can be measured (e.g. displacement) or generated (e.g. MCS gains) for as long as there is available space on the host PCs hard drive.

- Ability to manipulate all of the MCS parameters during a test (α, t_s, initial gain conditions, reference model parameters)

- Ability to replace the MCS reference model with any other function or model.

- Ability to include digital filters of various types (Butterworth, notch, composite, etc.) quickly and with the ability to vary parameters on-line

- Ability, with small modification, to control n degrees of freedom simultaneously either via the same controller block or each with its own independent block.

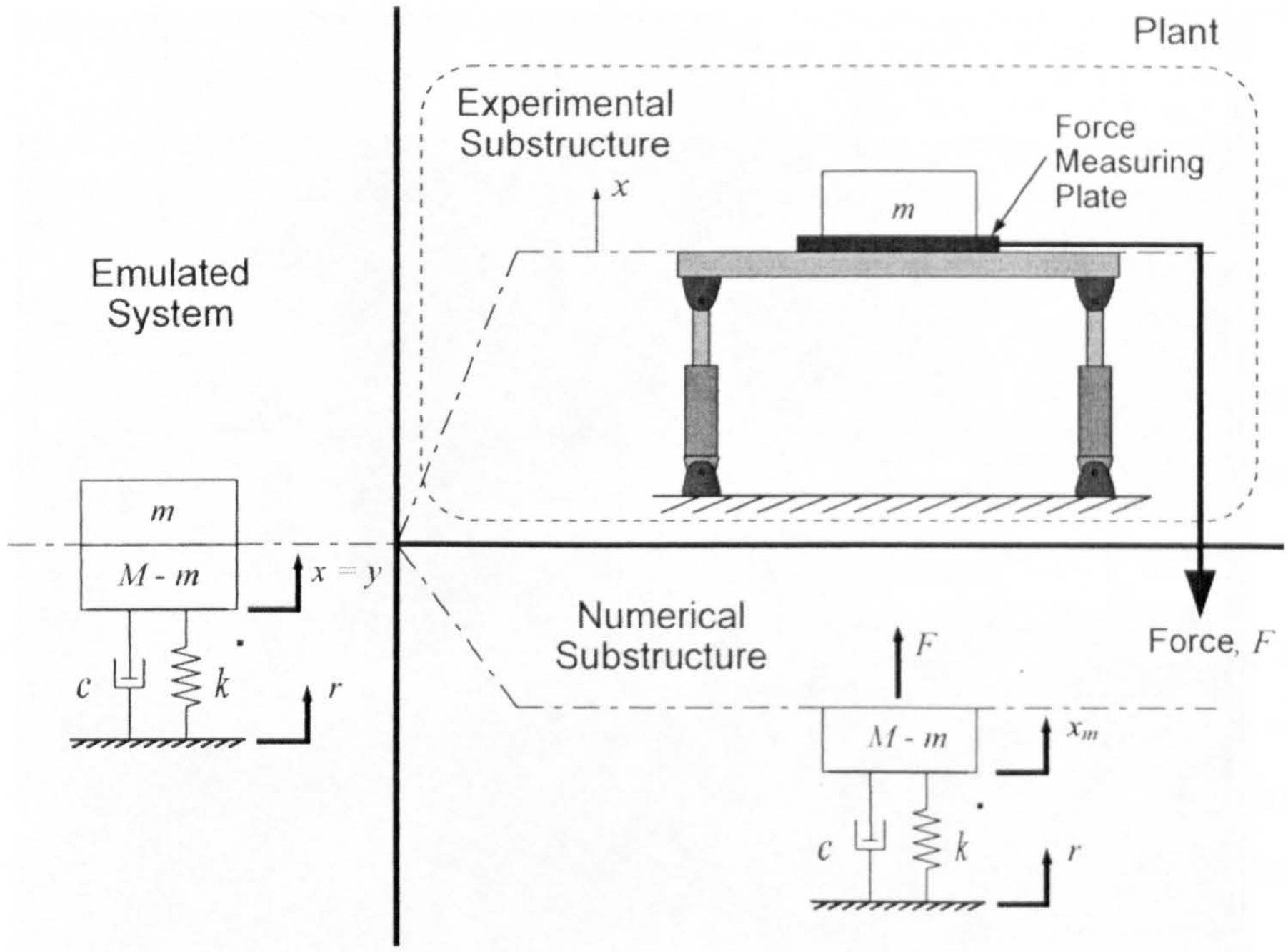

Figure 6.11: Schematic of substructuring experiment as performed on the University of Bristol shaking table

Within the University of Bristol, SIMULINK models of the rigs used for substructuring tests were designed that incorporate the rig itself, characteristics of the sensor and data acquisition equipment and the proprietary (or inner-loop) controllers. This allowed all tests to be simulated accurately using the new dSPACE controllers before commencing full-scale testing. Alongside development of the software was a phase of testing of the software/hardware platform provided by dSPACE ensuring real-time functionality as well as identifying any limitations and/or bugs.

6.6 Substructuring - Shaking Table Experiments

In the first instance the substructuring experiments detailed in section 6.3 were performed on the University of Bristol shaking table. The system described in section 6.3 was split up into the described substructure as shown in the schematic in figure 6.11. The numerical substructure and control algorithm were implemented in the dSPACE environment detailed in section 6.5. For the shaking table tests, rather than using a force plate, the mass was rigidly connected to the shaking table and the force was calculated from an

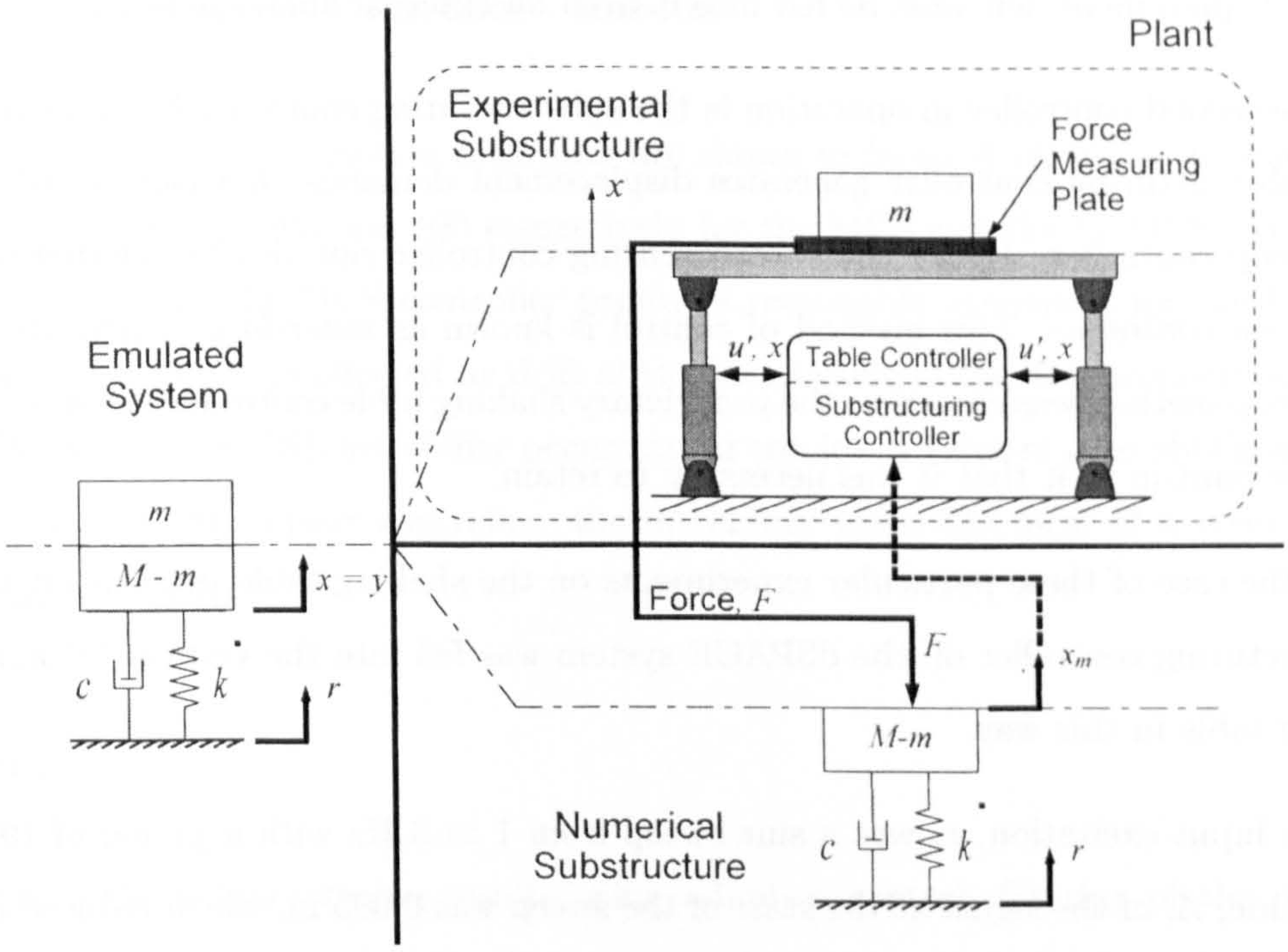

Figure 6.12: Schematic of shaking table implementation

accelerometer mounted on the table. This allowed a range of substructure masses to be tested without the need to alter the experimental set-up. A more detailed schematic showing the presence of the shaking table controller, substructuring controller and signal flow is given in figure 6.12.

Figure 6.12 shows that there are two controllers operating within this experimental set-up. The first is the low-level, or proprietary, controller used to control the motion of the shaking table. This controller contains:

- the kinematic and inverse-kinematic solvers used to convert motion to and from the degrees of freedom of the table (x, y, z, roll, pitch and yaw) to 8 actuator displacements
- low-level systems (such as pre-load pressure regulation, signal conditioning, etc.
- safety features
- PID controller allowing control in displacement or acceleration

This is referred to as the *inner-loop controller* for the system. This inner-loop controller

allows displacement demands be fed into it from an external analogue source.

The second controller in operation is the substructuring controller being investigated. The substructuring controller generates displacement demands that can be fed into the inner-loop controller. Hence the substructuring controller can also be referred to as the *outer-loop controller*. This method of control is known as *outer-loop control* [167]. This outer-loop method was chosen as the proprietary shaking table controller has several safety features built-in to it that it was necessary to retain.

In the case of these particular experiments on the shaking table, the output from the substructuring controller on the dSPACE system was fed into the vertical (z) axis of the shaking table in this way.

The input excitation, r, was a sine sweep from 1 to 3 Hz with a period of 19 s. The magnitude, A, of the signal at the start of the sweep was 0.005 m, which reduced over the sweep as a function of time, given by:

$$R = 0.005\left(\frac{19}{19+t}\right) \tag{6.12}$$

The reduction of amplitude over time ensured that the shaking table's response remained within its safe working displacement envelope throughout the experiment, even through resonance.

6.6.1 Linear Controller - Results

Figure 6.13 shows the results for the experiment when using the linear design for the substructuring controller with the substructured system described in section 6.3. For this controller, the beneficial effect of the error feedback gain is clearly visible. Without any error feedback gain, substructuring using the linear controller produces large interface displacement errors since the linear controller design was based on a first-order representation of the plant. With the inclusion of the error feedback there is good agreement between the shaking table displacement and the emulated system. However, with a feedback gain greater than 10, instability occurs in the form of a growth in a resonance at approximately 23 Hz. This corresponds to the frequency at which the oil columns within the actuators resonate on the shaking table.

6.6.2 MCS Adaptive Controller - Results

Initial results using the adaptive controller are shown in figure 6.14, using the maximum utilisable α values, 10,000 and 100 respectively for the MCS and the Er-MCSI controller. It can be seen that the MCS controller produces reasonable agreement for the first 12s, however for the last 7s is affected by drift of the mean value of the displacement over each cycle. With the Er-MCSI, instability occurs at far too low a value of α to obtain accurate results. As with the linear controller, the instability takes the form of a resonance at approximately 23 Hz.

Filtering

To improve the substructuring results using adaptive control, filtering of the displacement and force signals was used. To maintain the correct phase and amplitude of the corresponding signals within the system it is necessary to employ the same filter for both the force and the displacement signals. It should be noted that filtering using the linear controller was not possible without a redesign since the gains are dependent on the plant dynamics. However, with adaptive control, knowledge of the plant dynamics is not required.

Using the control signal and the shaking table displacement for the Er-MCSI test, a fourth order system identification for the plant was estimated:

$$G_t(s) = \frac{5495(s+10.92)}{(s^2+12.32s+2.109\times10^4)(s^2+18.26s+88.88)} \tag{6.13}$$

This approximation to the plant indicated that there is a distinct resonance at 23.1 Hz. Experiments were conducted using a variety of filters to reduce this resonance. Low-pass Butterworth filters with a break frequency of 16 Hz were tried as well as notch and pole cancellation filters. The pole cancellation filter was designed to replace the poles corresponding to the 23.1 Hz resonance, with more highly damped poles, thereby reducing the magnitude of the resonant peak. The filter took the form:

$$G_{pc}(s) = \frac{(s^2+12.32s+2.109\times10^4)}{(s^2+2\pi B_w s+2.109\times10^4)} \tag{6.14}$$

where B_w is the bandwidth of the replacement pair of poles, critical damping corresponds to approximately $B_w = 46$Hz.

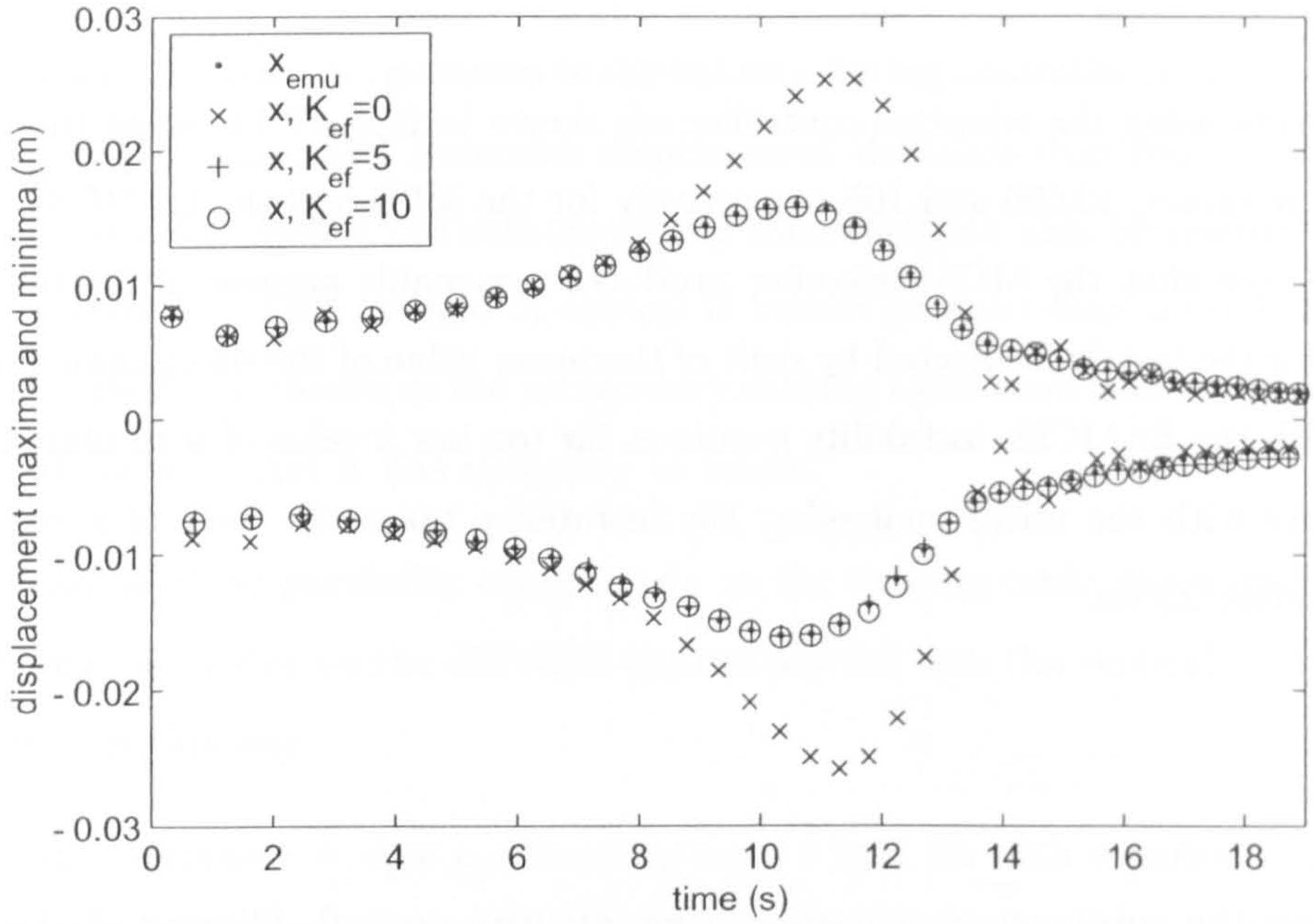

Figure 6.13: Experimental substructuring results using a linear controller, with a substructure mass of 20 kg, showing the effect of error feedback gain on the shaking table displacement peaks

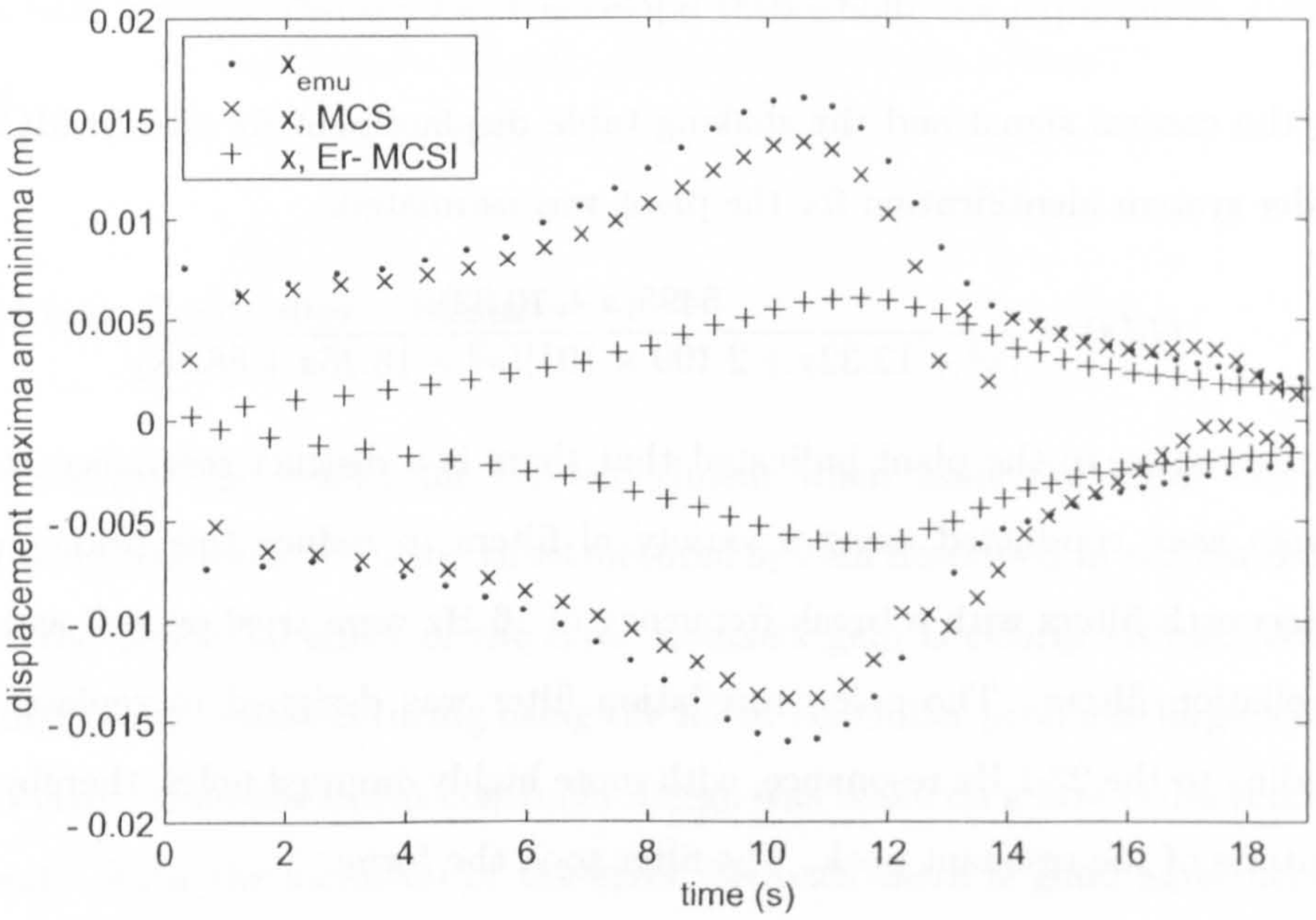

Figure 6.14: Experimental substructuring using adaptive control, with a substructure mass of 20 kg and maximum α before instability, shaking table displacement peaks

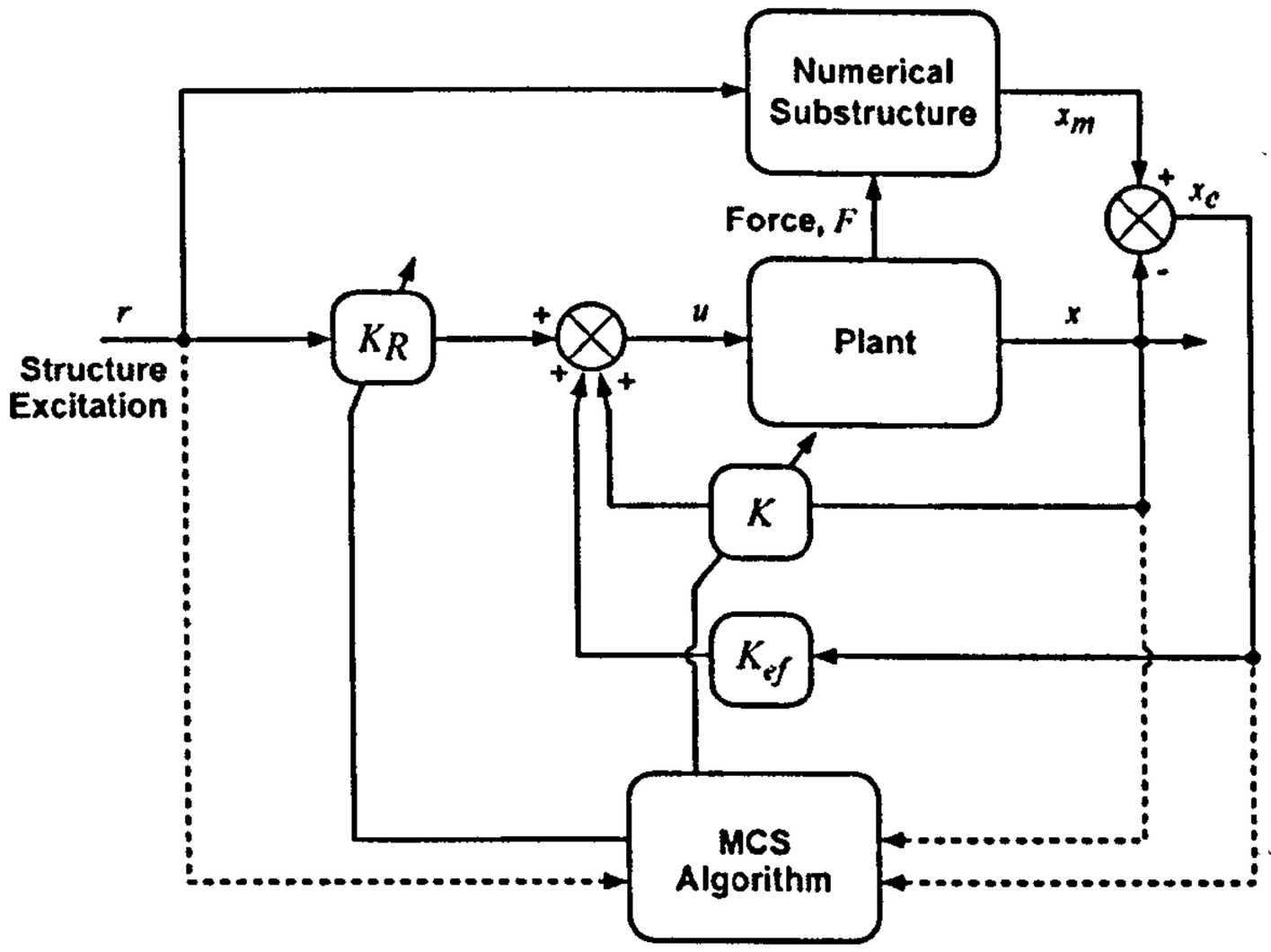

Figure 6.15: Block diagram of the MCS algorithm with a feedback gain, when used a substructuring controller

Error Feedback Gain

As with the linear controller, an error feedback gain can be used in conjunction with the adaptive controllers. For the case of the MCS controller the block diagram including the error feedback gain is shown in figure 6.15.

Further Experimental Results

Figure 6.16a shows the shaking table displacement peaks for the case where the MCS controller is used in conjunction with various filters. These results use the maximum utilisable α and K_{ef} values, {15000,50}, {25000,50} and {25000,0} for the 2-pole Butterworth low-pass filter, the pole cancellation filter with bandwidth of 20 Hz and the pole cancellation filter with bandwidth of 46 Hz, respectively. It can be seen that over the first 12s the test with the 46 Hz pole cancellation filter produces the best results. However, beyond 12s the 2-pole Butterworth low-pass filter test is superior. It can also be seen that for the tests with the 2-pole Butterworth low-pass filter and with the pole cancellation filter with bandwidth of 20 Hz there is drift of the average displacement over each cycle after around 12s.

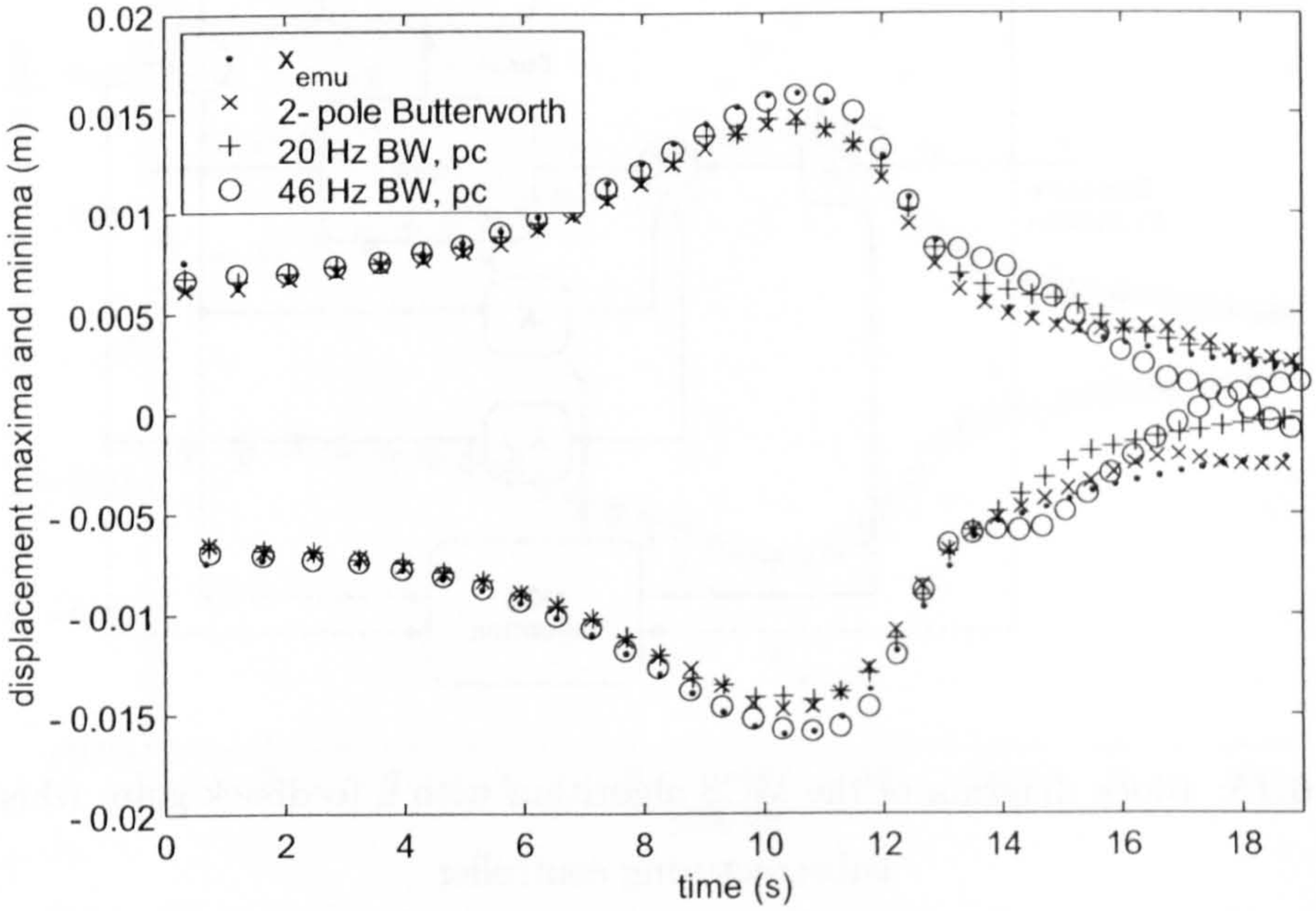

(a) MCS Controller

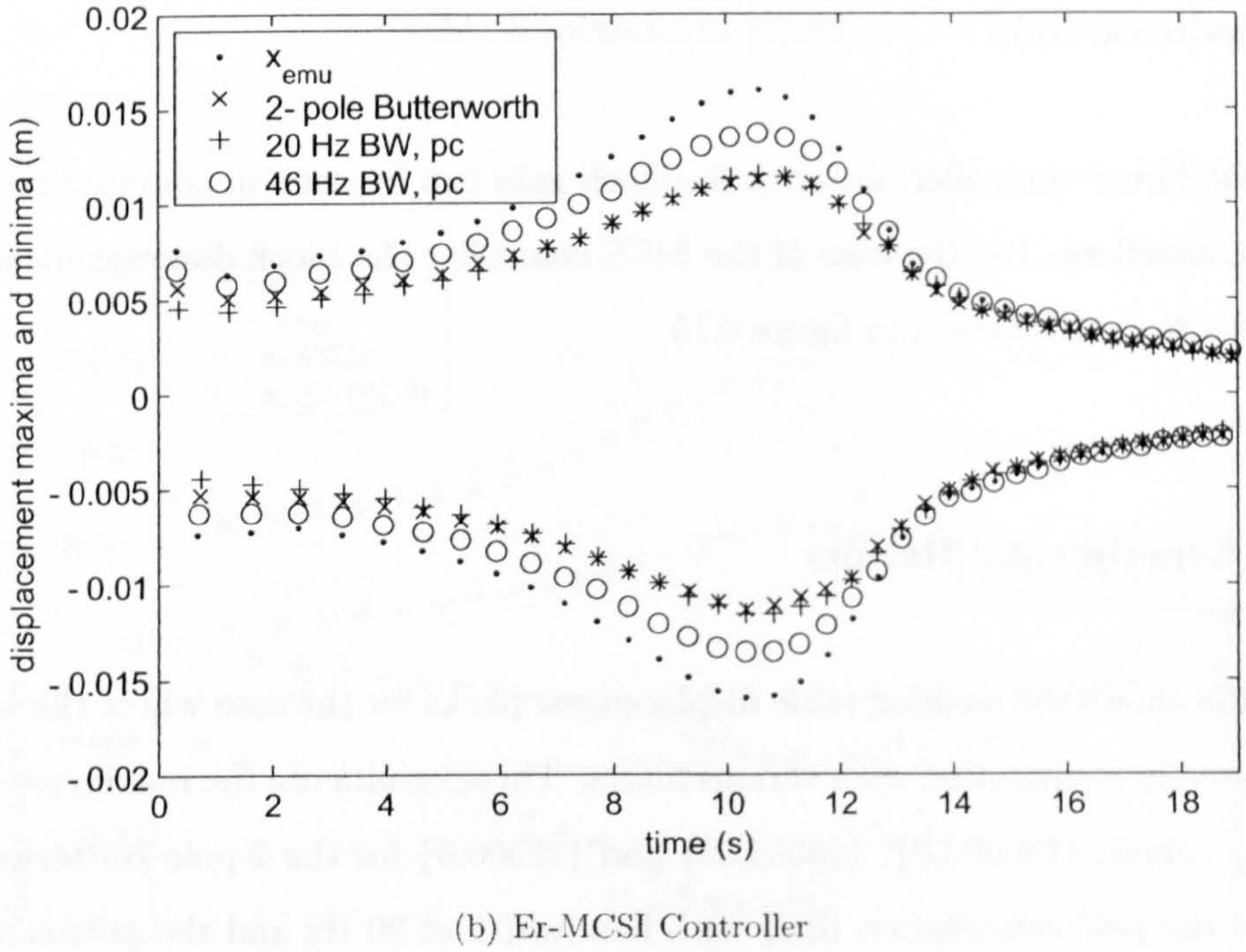

(b) Er-MCSI Controller

Figure 6.16: Shaking table displacement peaks for tests using maximum alpha and error feedback gains before instability for a range of filters, using (a) the MCS controller and (b) the Er-MCSI controller

6.6.3 Er-MCSI Adaptive Controller - Results

Shaking table peak displacements for tests using the Er-MCSI in conjunction with a range of filters are shown in figure 6.16 (b). These results use the largest utilisable α and K_{ef} values, {4000,100}, {8000,50} and {40000,200} for the 2-pole Butterworth low-pass filter, the pole cancellation filter with bandwidth of 20 Hz and the pole cancellation filter with bandwidth of 46 Hz, respectively. It can be seen that the test with the pole cancellation filter with bandwidth of 46 Hz gives the best results, however all the tests under-estimate the amplitude of the oscillations. None of the results using the Er-MCSI controller exhibit the drifting of the mean displacement that occurs in the MCS controller tests.

A second advantage of the Er-MCSI controller over the MCS controller is that the shape of the response at lower α values is similar to that at higher α values. This should mean that predicting the maximum utilisable value will be easier than for the MCS controller. Figure 6.17a shows the effect of increasing α up to its maximum value for the case where there is no feedback gain and 2-pole Butterworth filtering is used with the MCS controller. It can be seen the shape of the plots change significantly with increasing α. This is in contrast to the case where the Er-MCSI controller is used. As shown in figure 6.17b, where a 2-pole Butterworth filter is used with no error feedback gain.

6.7 Substructuring - Hydraulic Actuator Experiments

To allow a wider range of experiments to be carried out, and to remove effects seen due to oil-column resonance, a second rig was commissioned.

The system to be substructured was identical to that used on the shaking table except that the amplitude was scaled down by a factor of 0.4. Also, a single actuator was used as the transfer system rather than a shaking table.

As with the shaking table (section 6.6) there are two controllers operating in the system. Firstly, the inner-loop controller, which consists of a PID controller (and safety features) associated with the actuator. Secondly, there is the outer-loop substructuring controller. Only the proportional term of the inner-loop controller was active, and the gain was set to $K_p = 4$ unless otherwise stated. The pragmatic solution to C_e was adopted, $C_e = 4/t_s$, where $t_s = 0.01$.

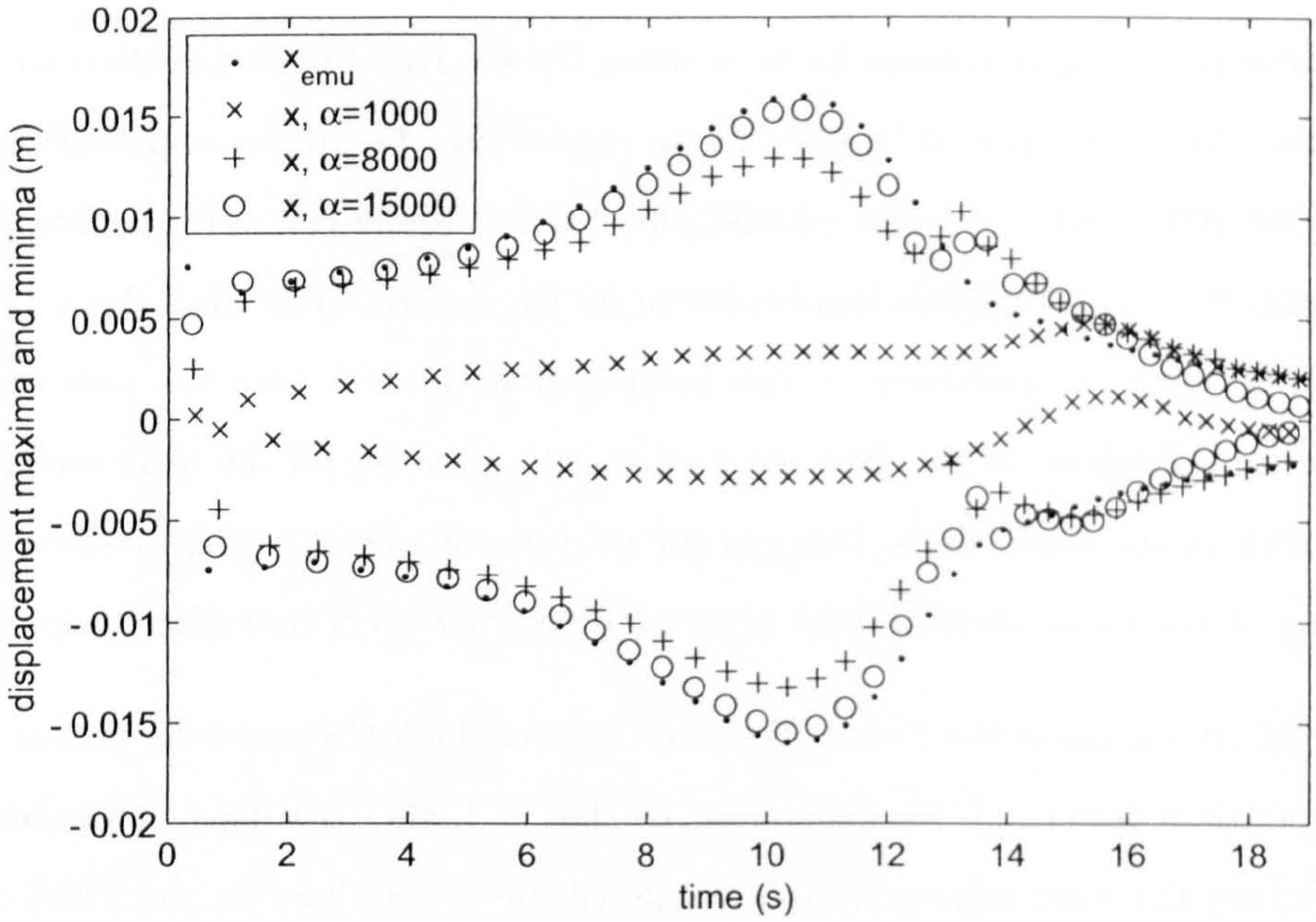

(a) MCS Controller

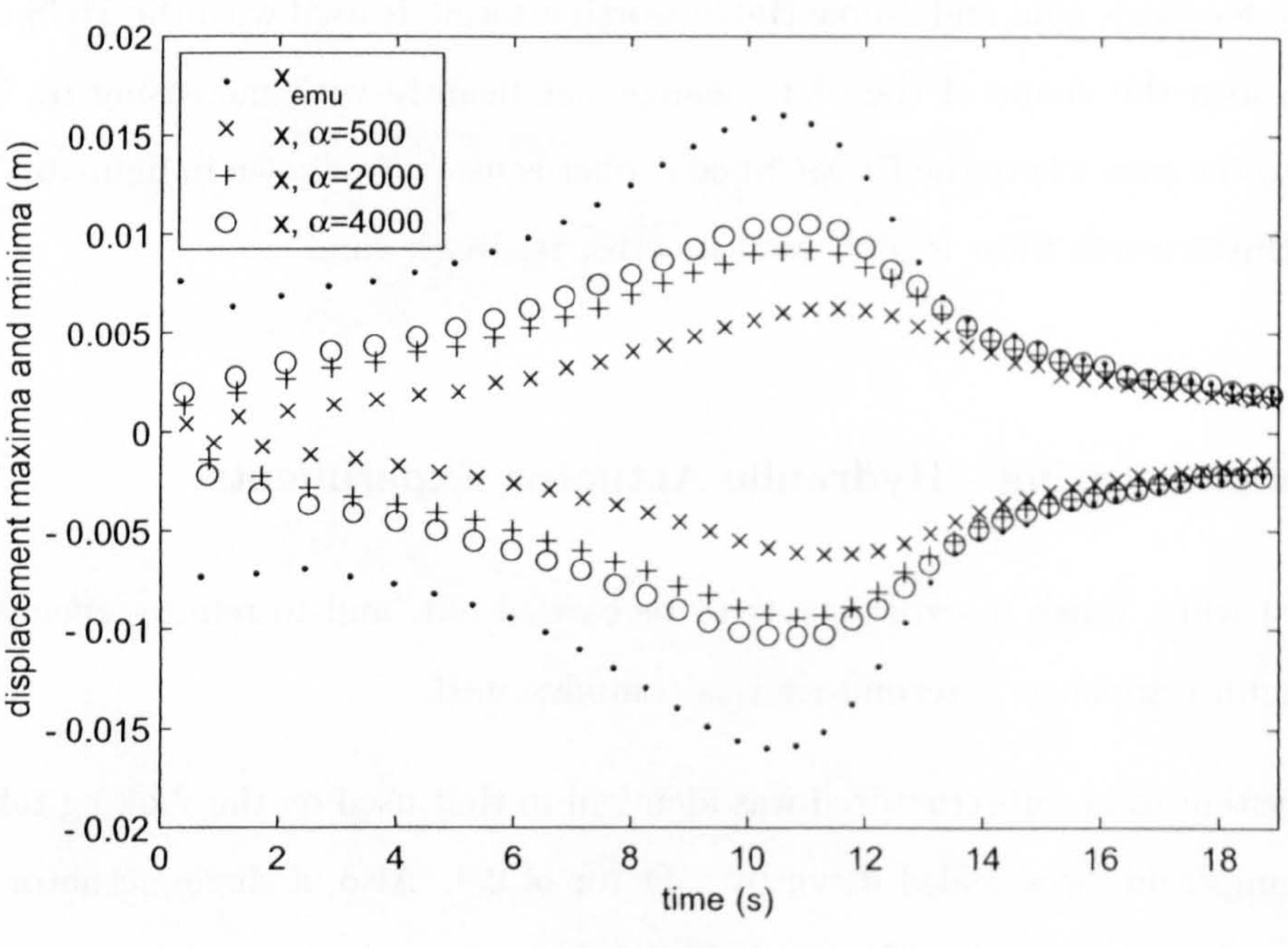

(b) Er-MCSI Controller

Figure 6.17: Shaking table displacement peaks for tests using 2-pole Butterworth low-pass filters with no error feedback gain, for a range of values of α, using (a) the MCS controller and (b) the Er-MCSI controller

The physical substructure contains the actuator, test specimen and an inner-loop proportional controller. The force required to apply a displacement x to the mass was measured, using a load cell connected between the mass and the actuator, and passed to the numerical model. The actuator and test specimen are shown in Figure 6.18.

The mass was free to move horizontally on linear bearings supported by two rails.

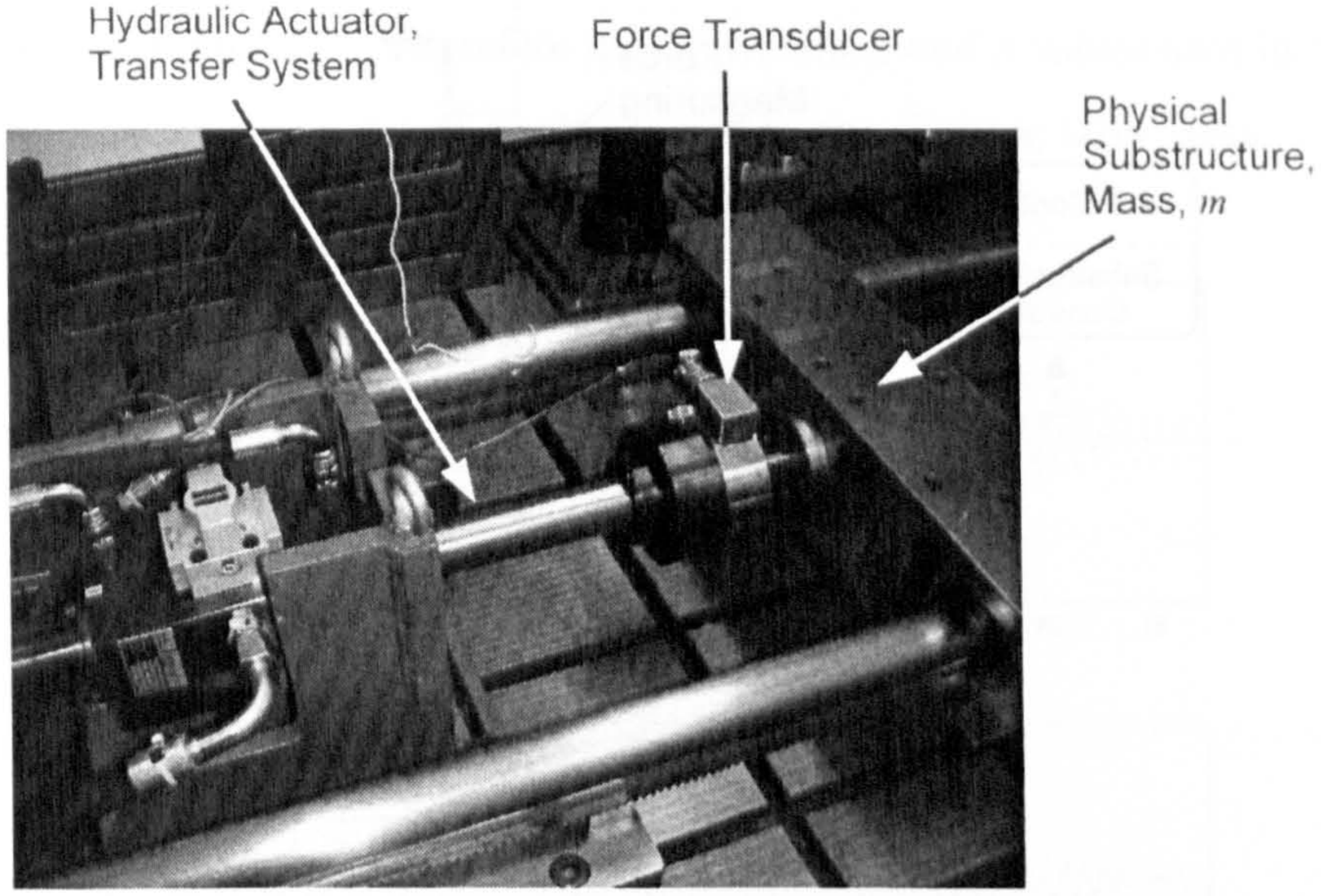

Figure 6.18: The test specimen and actuator

6.7.1 Shaking Table and Actuator Comparison

Before examining the results of the substructuring tests conducted using the actuator, it was useful to compare the performance of the shaking table and the actuator used for the tests presented here. To compare the performance during substructuring tests, it was necessary to set the proportional gain of the inner-loop controller for the actuator such that the plant dynamics are similar to those for the table when used in a single axis. It was also necessary to consider the implication of the demand being scaled by a factor of 0.4 for the actuator tests with respect to the amplitude of the shaking table tests.

Referring to section 6.4.1 a first order approximation to the table and inner loop controller may be expressed as:

$$G_t(s) = \frac{0.264}{s + 7.91} \tag{6.15}$$

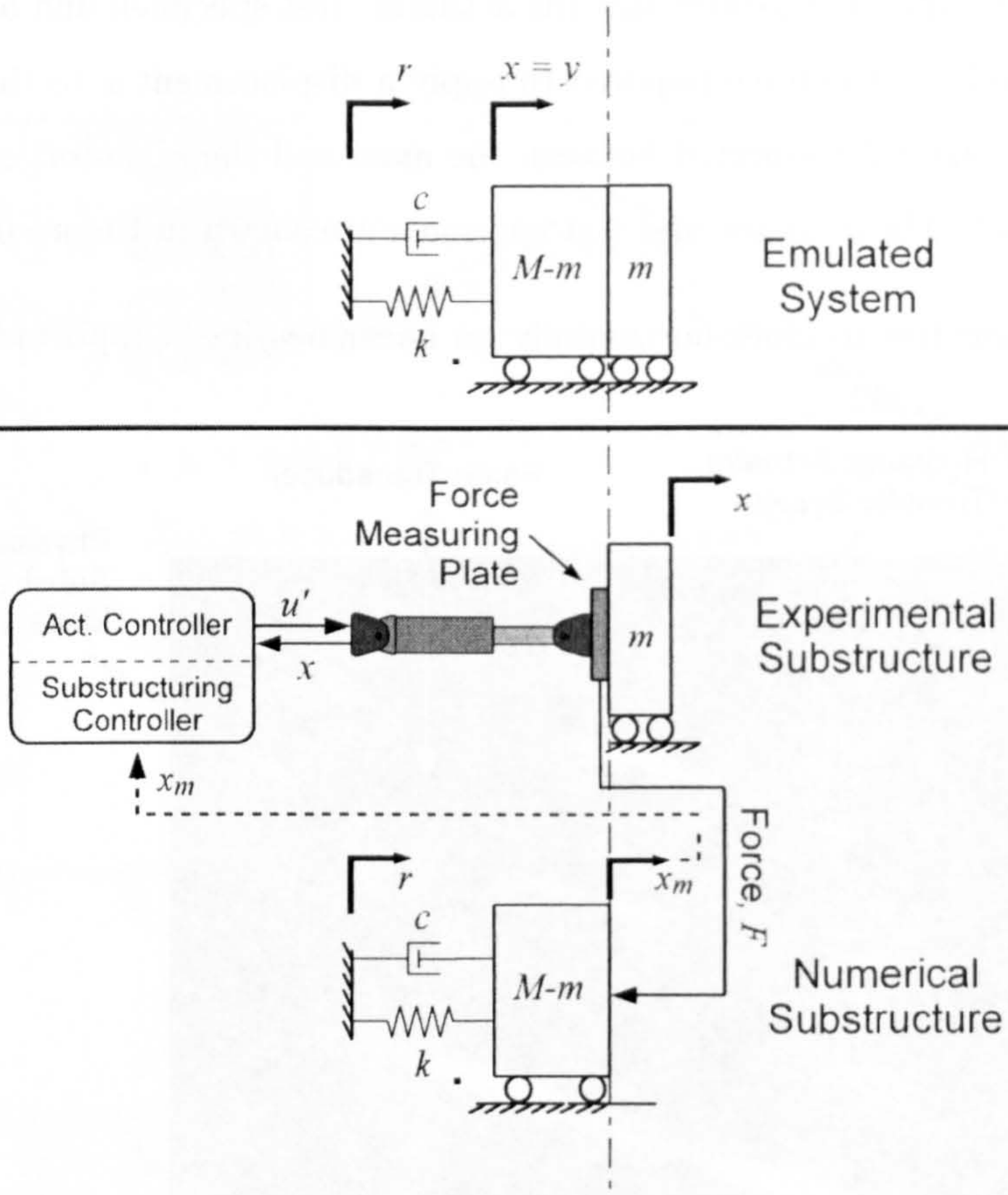

Figure 6.19: Breakdown of the emulated system into the physical and numerical substructures

where s is the Laplace transform variable. This transfer function represents the dynamics between the outer-loop control signal u (V) and the resulting displacement of the shaking table x (m). The result of system identification tests conducted on the actuator for various inner-loop gains was that the actuator dynamics may be approximated as:

$$G_a(s) = \frac{5}{s} \tag{6.16}$$

It follows that the plant dynamics between the outer-loop control signal u (V) and the displacement of the actuator x (m), that is the dynamics of the actuator and inner-loop controller, may be expressed as:

$$G_p(s) = \frac{5K_pK_t}{s + 5K_p} \tag{6.17}$$

where K_p is the inner-loop proportional gain and K_t is the gain of the displacement transducer, $K_t = 0.005$ m/V. Therefore to emulate the first-order response of the shaking

table, tests were conducted using the actuator with $K_p = 1.58$ and an additional gain applied to the outer loop control signal u of 6.68.

To compensate for the difference in the amplitude of the demand, r, between the actuator and the shaking table tests it was necessary to scale α and β for the actuator. By converting the MCS algorithm into non-dimensional form using R_0, the initial amplitude of the demand r, as the length dimension, it can be shown that the only effect of modifying R_0 is to scale α and β by R_0^{-2}. Therefore the equivalent α and β values used in the actuator tests must be 6.25 times greater than those used in the shaking table tests.

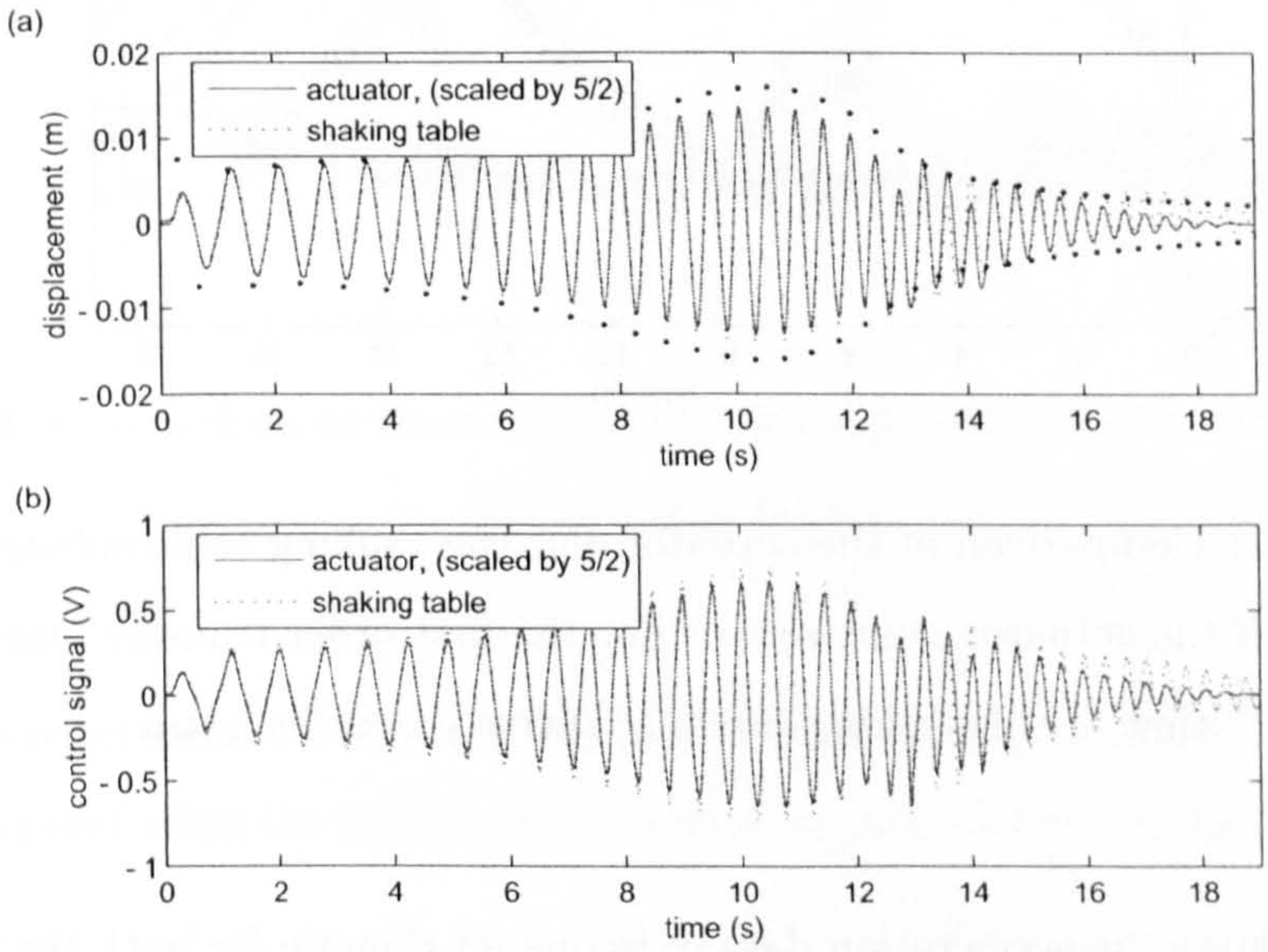

Figure 6.20: Comparison of the actuator and the shaking table substructuring experiments, with the actuator gains set so that the first order transfer function matches that of the shaking table, a) displacement and b) control signals

Experiments on the shaking table revealed that the optimum value of α using the MCS controller was 10000. Above this value instability occurred due to an oil column resonance within the actuators at approximately 23Hz. Figures 6.20 (a) and (b) show the displacement, x, and the control signal, u, for both the shaking table and the actuator tests, with the actuator data scaled by 5/2 to compensate for the demand being scaled relative to the shaking table. The dots correspond to the displacement maxima and minima for the emulated system. For the first 13s there is good agreement between the two sets of displacement data. At this point there is a sudden change in the form of the adaptive gains, as shown in Figure 6.21. It is thought that behaviour is due to large phase difference

between the numerical substructure output and the demand, which is discussed later, in section 6.7.2

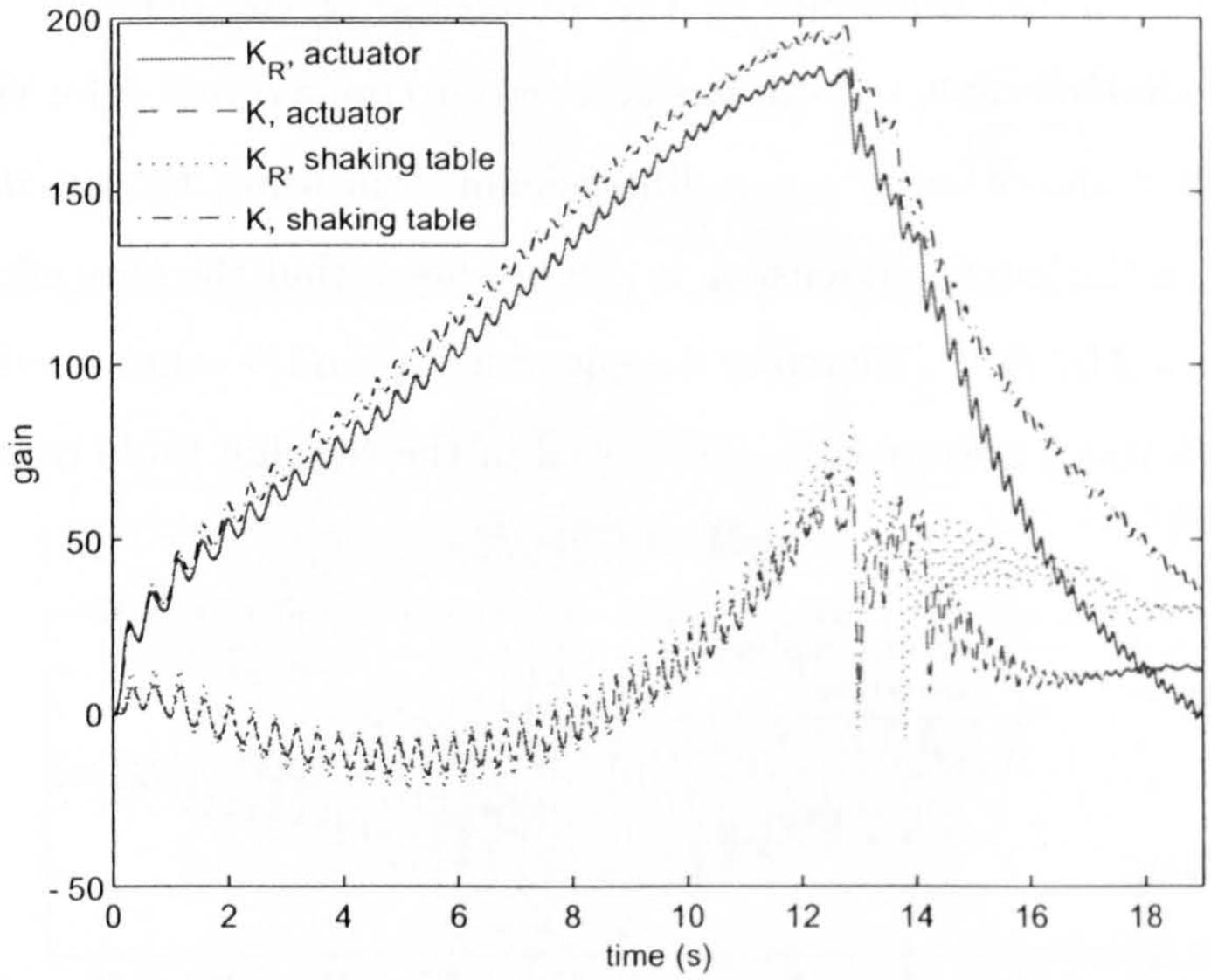

Figure 6.21: Comparison of the actuator and the shaking table substructuring experiments, with the actuator gains set so that the first order transfer function matches that of the shaking table, adaptive controller gains

Figure 6.22 shows the acceleration data in frequency domain for both the test with the shaking table and for that with the actuator. There is significant acceleration content at around 23Hz for the shaking table test which is thought to be due to oil column resonance. When the actuator was used as the transfer system, it was possible to increase α above the level at which instability occurred using the shaking table.

The best results were achieved with $\alpha = 250000$. Figure 6.23 shows the displacement data for the actuator with $\alpha = 62500$, corresponding to the maximum α value when using the shaking table and $\alpha = 500000$. The performance of the controller is much improved with the higher adaptive effort. This demonstrates that the oil column resonance has a detrimental effect on the performance of the shaking table substructuring experiments by limiting the maximum utilisable adaptive effort.

These comparative tests have demonstrated broadly similar behaviour of the substructuring system using the actuator or the shaking table as the transfer system when a first order approximation to the dynamics of the actuator emulate that of the shaking table.

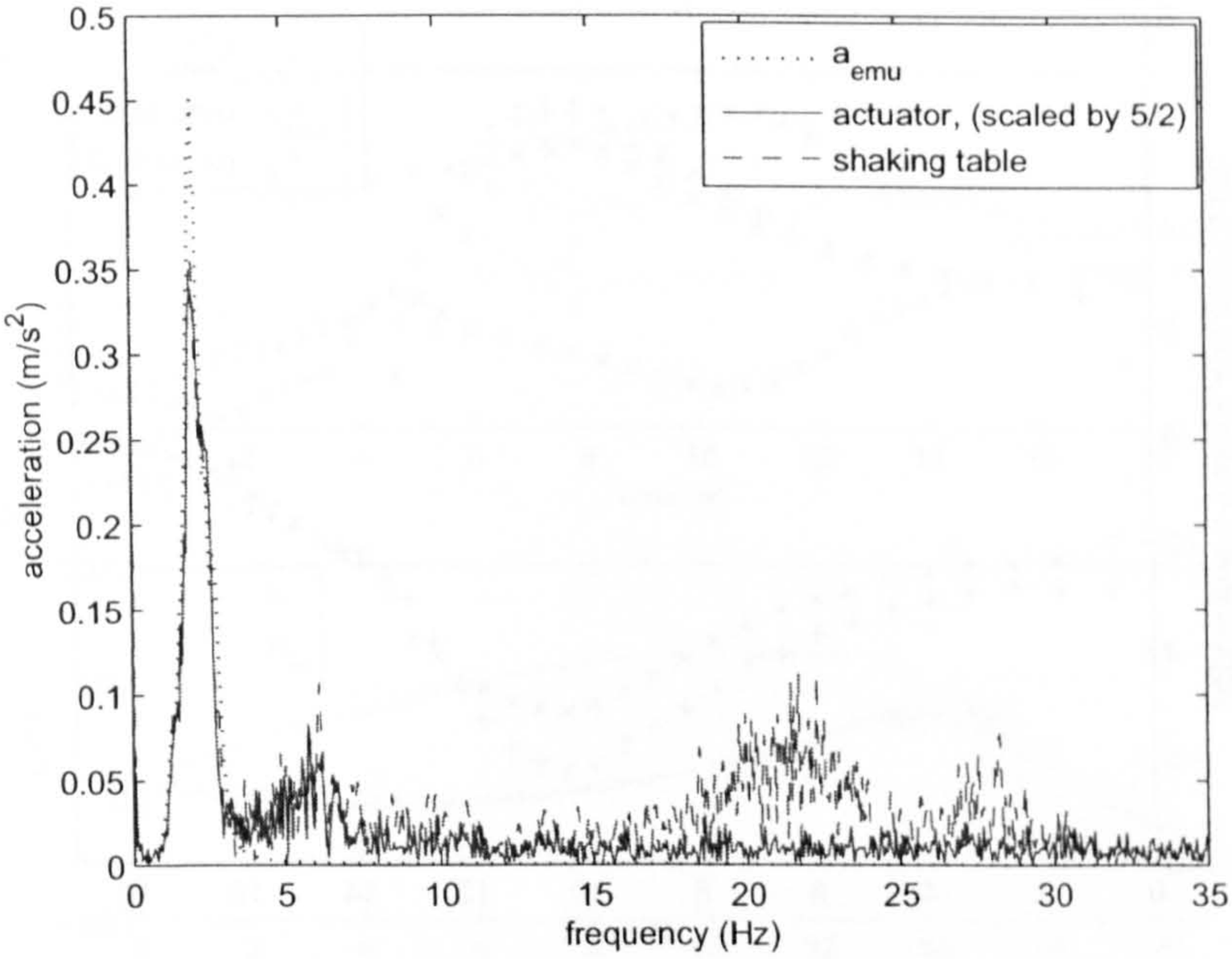

Figure 6.22: Comparison of the actuator and shaking table substructuring experiments, acceleration signals

However due to oil column resonance, the maximum utilisable values of the adaptive effort, α and β, are lower when the shaking table is used, leading to less satisfactory performance.

6.7.2 MCS Adaptive Controller

A series of substructuring tests were conducted using the actuator transfer system, firstly with the substructuring MCS controller and then with various modified control strategies. Results for the substructuring MCS controller using the maximum utilisable value of α ($\alpha = 1.2 \times 10^6$) for $K_p = 4$ are shown in Figure 6.24 (a). The displacement results match the desired displacement closely for the first 13s, however after this time there is a period of about 4s where there is less positive agreement between the displacement of the test specimen mass and that of the emulated system. During this period the gains undergo significant change as shown in Figure 6.24. Gain K_R which had settled to approximately a constant value before 13s suddenly decreases rapidly and K which was increasing with time suddenly oscillate about a constant value before decreasing. To understand this undesirable "gain jumping" behaviour, it is useful to simplify the system. It is beneficial to consider the case where the substructure mass is 0kg, resulting in no

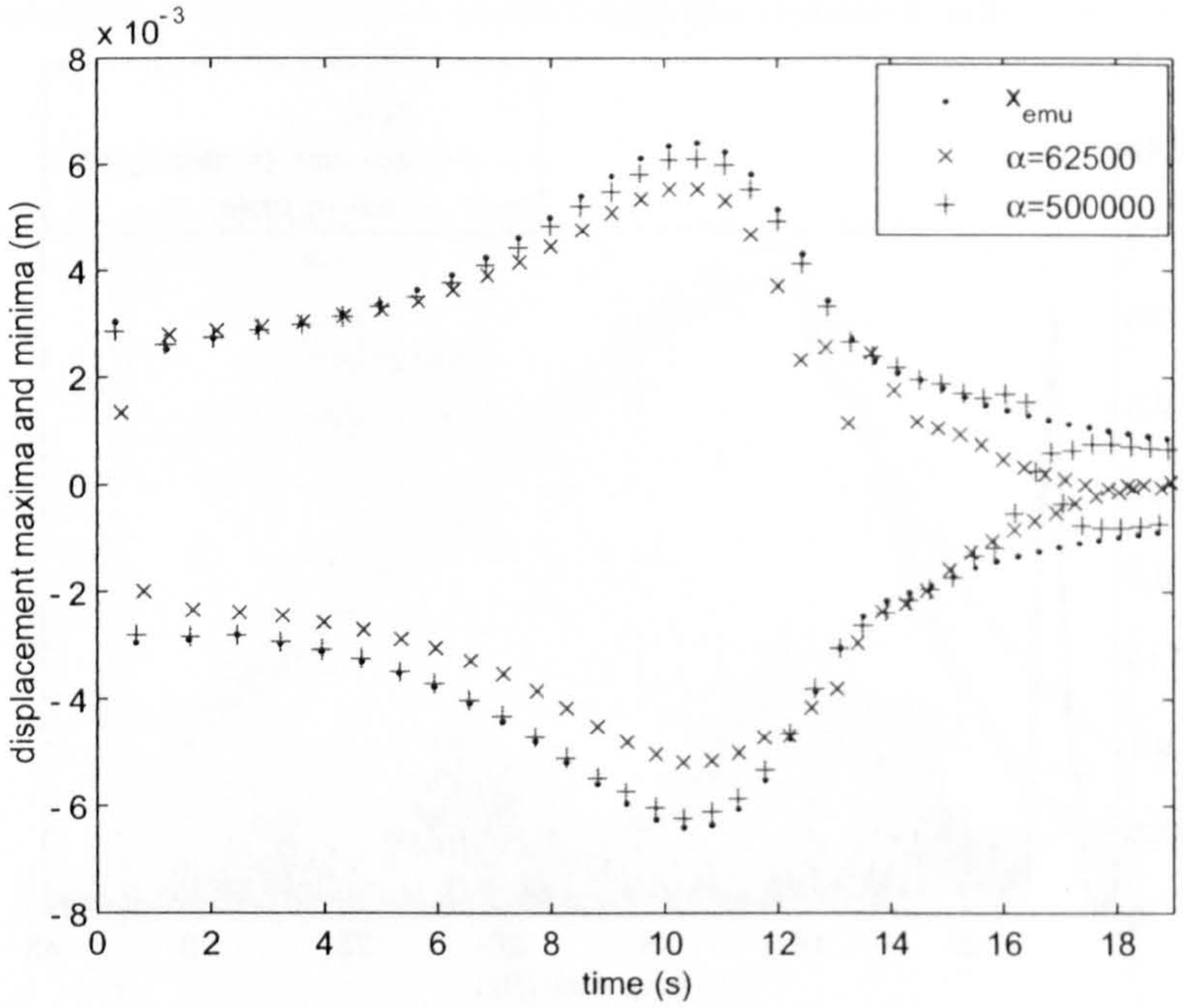

Figure 6.23: Displacement maxima and minima of the hydraulic actuator (with gains set so that the first order transfer function matches that of the shaking table) at the equivalent of the maximum utilisable α value for the shaking table, $\alpha = 62500$, and at the maximum utilisable value for the actuator, $\alpha = 500000$, compared with the maxima and minima for the emulated system

force feedback from the physical substructure to the numerical substructure (in this case the numerical model is identical to the emulated system). A further simplification is made by conducting the experiment in simulation using SIMULINK. In the simulation, the physical substructure is modelled as the first order system $G_p(s)$ using equation 6.17, thereby eliminating actuator non-linearities and transducer noise. Figure 6.25 shows a schematic of the simulation. The only difference between this set-up and the standard MCS controller is that the reference model has been substituted by the emulated system, resulting in zero force transfer between the plant and the numerical substructure. The standard controller the reference model would be first order since the plant and controller are first order and would be given by:

$$G(s) = \frac{b_m}{s + a_m} \tag{6.18}$$

where the model parameters are $b_m = a_m = 4/t_s$ and t_s is the setting time of the model. However the emulated system is second order with an underdamped response, resulting in

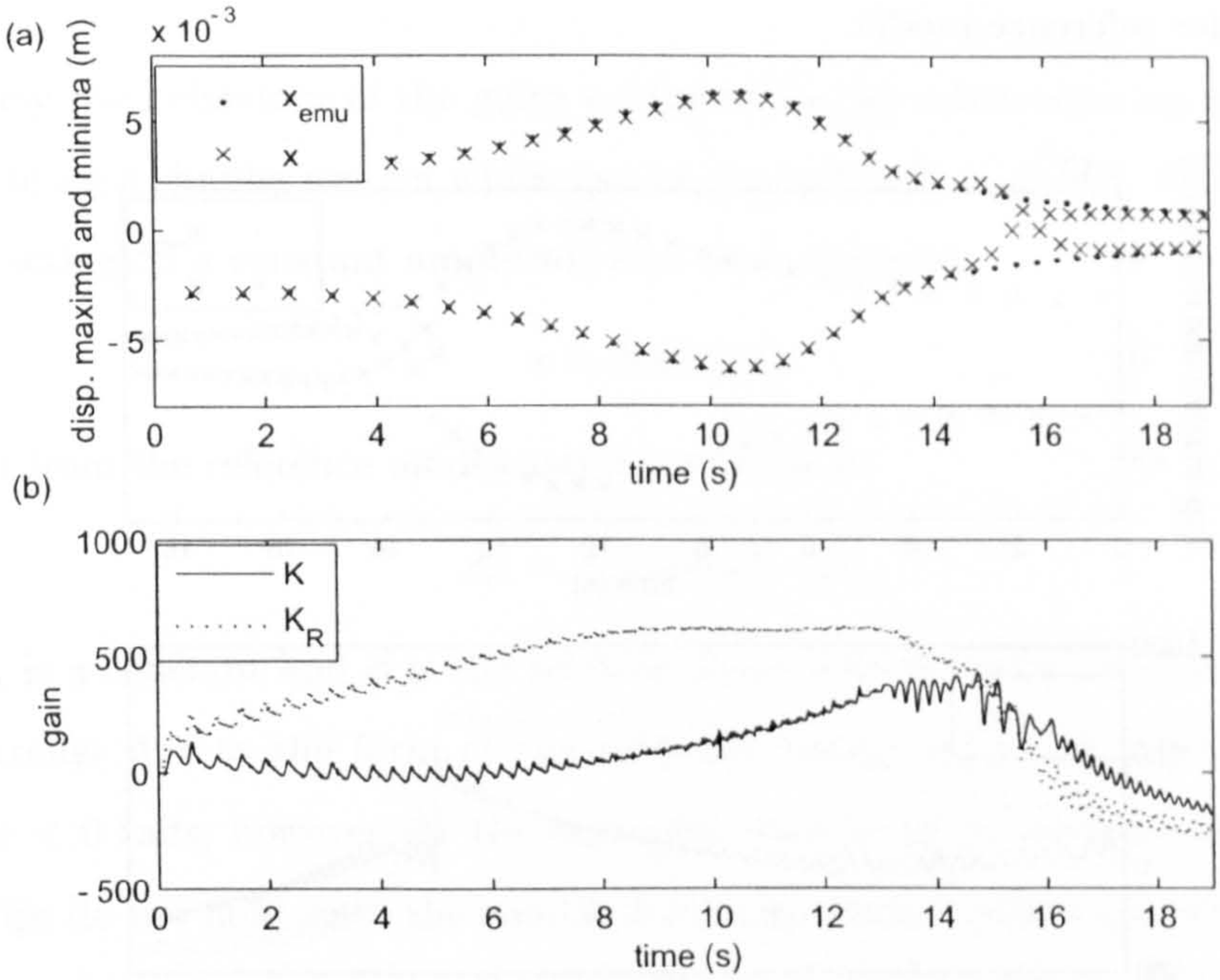

Figure 6.24: MCS control with the maximum utilisable α value, a) displacement maxima and minima and b) adaptive gains

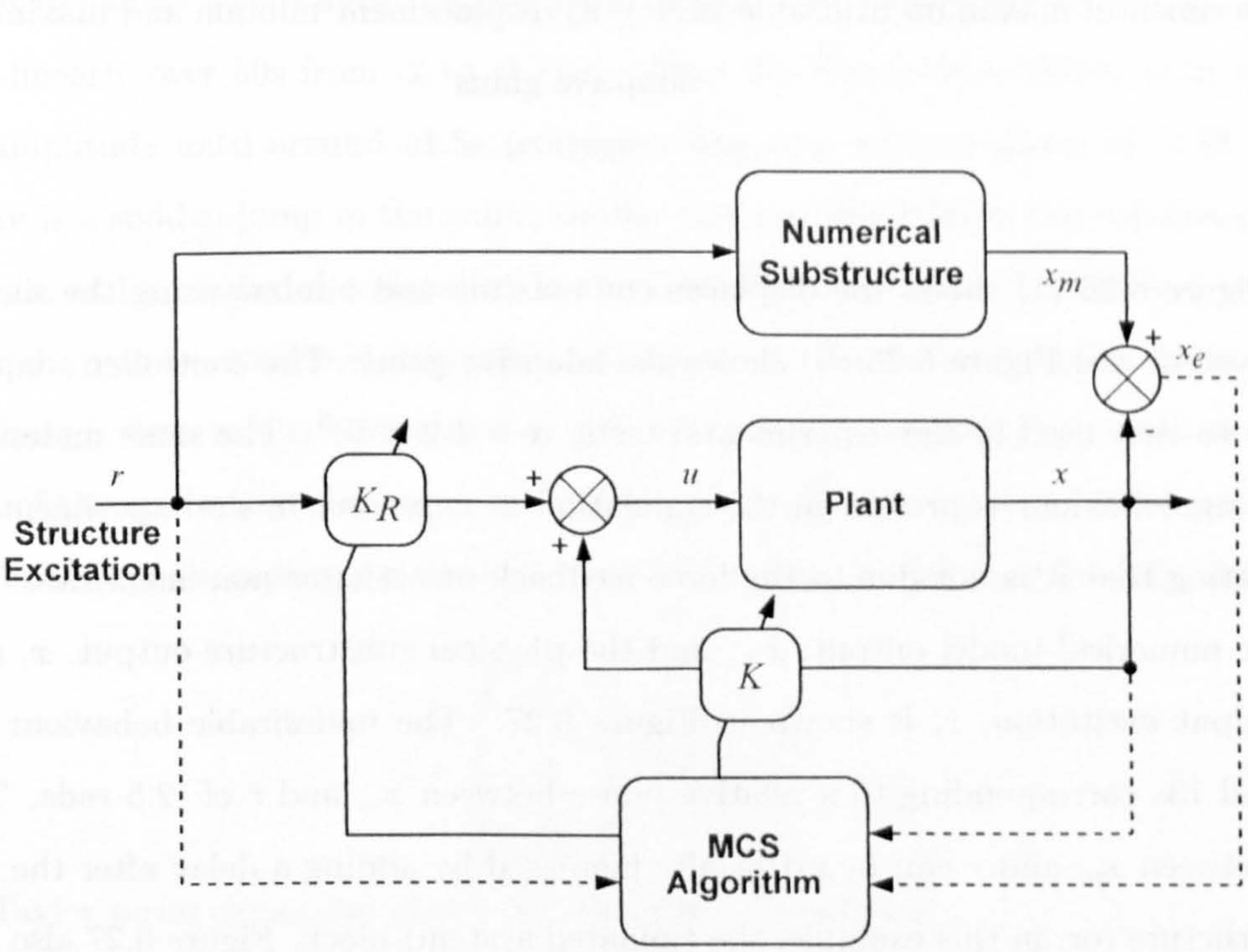

Figure 6.25: Block diagram of the MCS algorithm when used as a substructuring controller, with 0 kg mass in the physical substructure

gains in excess of unity and phase lags up to π rads rather than a maximum of $\pi/2$ rads with a first order reference model.

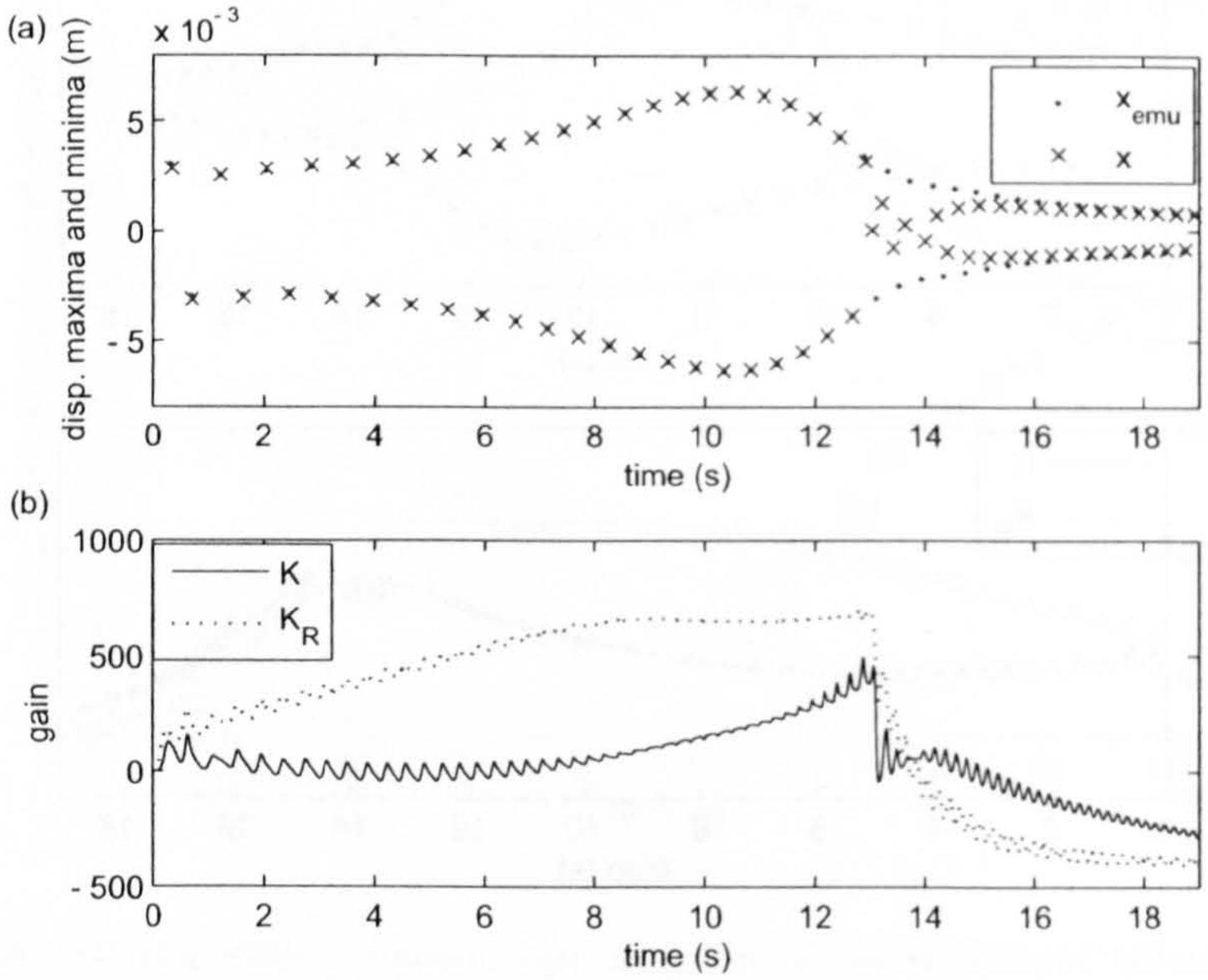

Figure 6.26: Simulation of 0 kg substructure, MCS control with $\alpha = 1.2 \times 10^6$ (the experimental maximum utilisable value), a) displacement minima and maxima and b) adaptive gains

Figure 6.26 (a) shows the displacement maxima and minima using the simulation of the system and Figure 6.26 (b) shows the adaptive gains. The controller adaptive effort is set to that used in the experimental tests, $\alpha = 1.2 \times 10^6$. The same undesirable gain jumping behaviour is present in the simulation as is present in the experimental system, indicating that it is not due to the force feedback or actuator non-linearities. The phase of the numerical model output, x_m, and the physical substructure output, x, relative to the input excitation, r, is shown in Figure 6.27. The undesirable behaviour begins at around 13s corresponding to a relative phase between x_m and r of -2.5 rads. The phase lag between x_m and r can be artificially increased by adding a delay after the numerical substructure (or, in this example, the emulated system) block. Figure 6.27 also shows the relative phases of x and x_m with respect to r for the case where a delay of 0.05 and 0.1s was imposed on the numerical substructure output. There is a deterioration of the agreement between x and x_m when the relative phase decreases below approximately -2.5 rads for each case.

Qualitative Analysis of Gain Jump

Qualitatively the behaviour of the gains exhibited by the substructuring systems may be replicated using a simpler system which can be theoretically analysed. Consider the MCS controller acting on a constant amplitude sine wave demand:

$$r = R\sin(\omega t) \tag{6.19}$$

the output from the reference model may be written as:

$$x_m = X_m \sin(\omega t - \phi) \tag{6.20}$$

where X_m is a constant and ϕ is the relative phase between r and x_m. For the standard MCS controller due to the form of the reference model (equation 6.18), $X_m < R$ and $-\pi/2 < \phi < 0$ rads, however for the examples considered in the previous section these relationships do not hold since the emulated system which replaces the reference model is second order (therefore $-\pi < \phi < 0$ rads). Figure 6.28 shows the error x_e and the gains for a signal with changing phase lag, for the case where $R = 0.002$, $X_m = 0.004$, $\omega = 4\pi$ and $\alpha = 10^6$ (values of the same order as those in the substructuring experiment) with the same plant dynamics as the substructuring simulation. The phase lag between x_m and r decreases linearly over 50s from -2 to -3 rads. After 35s the error oscillates with slowly increase amplitude until around 41.5s (corresponding to a relative phase of -2.83 rads) when there is a sudden jump in the gains, similar to those observed in the substructuring experiments, and a marked deterioration in the control performance. The error dynamics of the system may be examined using the approximation that since the rate of change in relative phase is slow, at any one point it may be considered constant. It is useful to study dynamics of the stationary point corresponding to steady gains and zero error based on a localised linear approximation to the error dynamics. The system may be defined in the form:

$$\dot{\xi} = \begin{pmatrix} \dot{x}_e \\ \dot{K} \\ \dot{K}_R \end{pmatrix} = f(\xi, t) \tag{6.21}$$

Using a Taylor series expansion about the stationary point gives:

$$\dot{\xi} \simeq (\xi_0) + Df_\xi(\xi_0)(\xi - \xi_0) \tag{6.22}$$

where $Df_\xi(\xi_0)$ is the Jacobian matrix evaluated at ξ_0, $\xi_0 = \begin{pmatrix} 0 & K^* & K_R^* \end{pmatrix}^T$ is the stationary point and K^* and K_R^* being defined as the constant gains to which the system settles. With the dynamics in this form, for the system to settle to the stationary

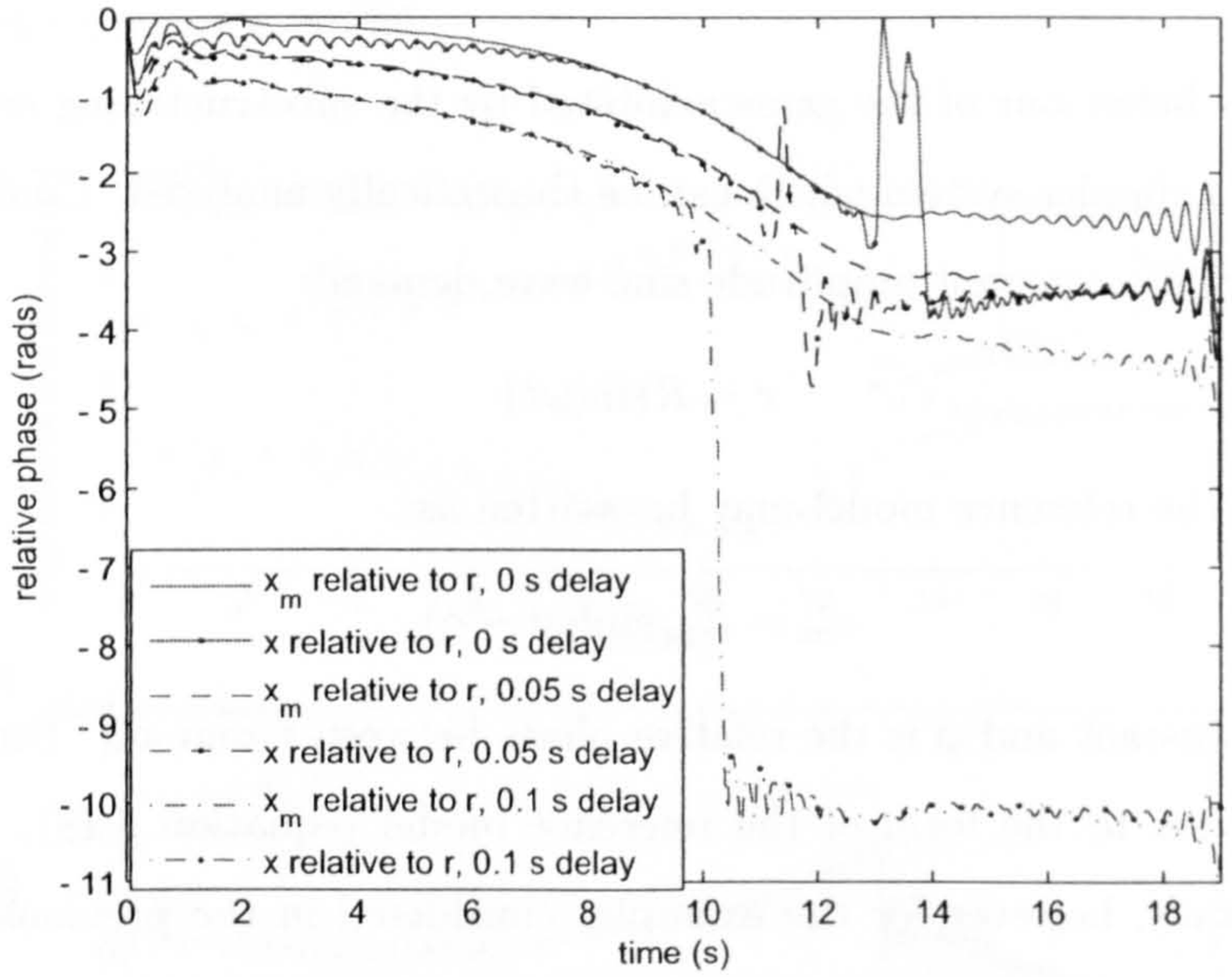

Figure 6.27: Simulation of 0 kg substructure, MCS control with $\alpha = 1.2 \times 10^6$ (the experimental maximum utilisable value), with a range of phase delays imposed on the numerical substructure, relative phase

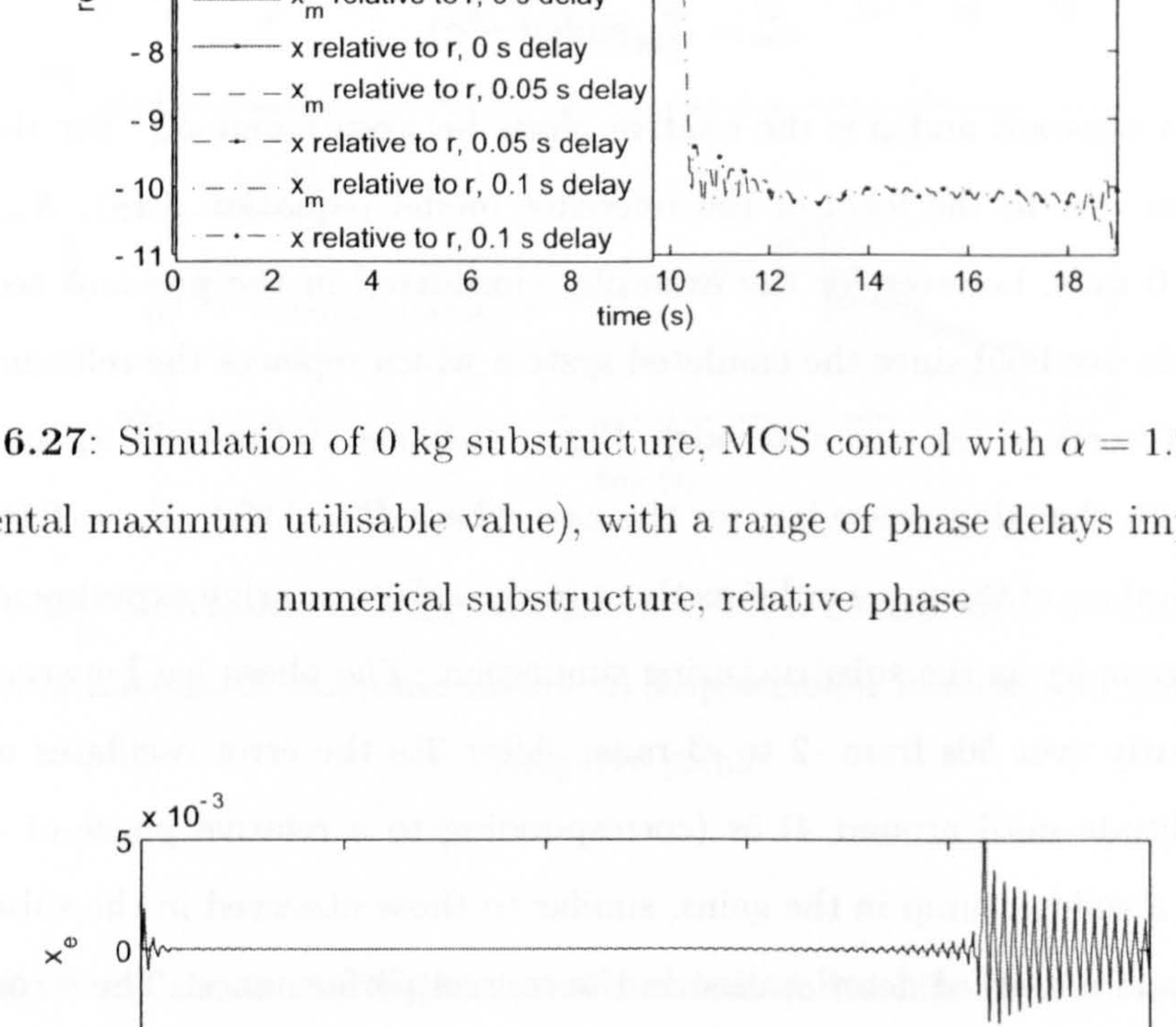

Figure 6.28: Simulation to demonstrate gain jump behaviour for a simple system with gradually decreasing phase

point, $f(\xi_0) = 0$. The eigenvalues of the Jacobian matrix at the stationary point may be determined as a measure of the localised stability of the system. If the real parts of the eigenvalues are negative then the system will settle to the stationary point.

The error dynamics may be written as:

$$\dot{x}_e = \dot{x}_m - \dot{x} \tag{6.23}$$

Using equations 6.8 and 6.9 the derivative of the gains may be written as:

$$\dot{K} = \alpha C_e \left(x_e x_m - x_e^2\right) + \beta C_e \left(2x_e\dot{x} + \dot{x}_m x_m - \dot{x}_m x_e - \dot{x}x_m\right) \tag{6.24}$$

$$\dot{K}_R = \alpha C_e x_e r + \beta C_e \left(x_e\dot{r} + r\dot{x}_m - r\dot{x}\right) \tag{6.25}$$

For convenience the substitution of the plant output has not been made but may be written as:

$$\dot{x} = -a\left(x_m - x_e\right) + brK_R + b\left(x_m - x_e\right)K \tag{6.26}$$

where $a = 5K_p$ and $b = 5K_pK_t$. Using these four equations the system may be written in the form of equation 6.21. At the stationary point since $f(\xi_0) = 0$, an equation for the steady state gains K^* and K_R^* may be derived:

$$f\left(\dot{\xi}_0\right) = \begin{pmatrix} \dot{x}_m - \dot{x}|_{\xi_0} \\ \beta C_e x_m \left(\dot{x}_m - \dot{x}|_{\xi_0}\right) \\ \beta C_e r \left(\dot{x}_m - \dot{x}|_{\xi_0}\right) \end{pmatrix} = 0 \tag{6.27}$$

giving:

$$\dot{x}_m = -ax_m + brK_R^* + bx_m K^* \tag{6.28}$$

Substituting in equations 6.19 and 6.20 gives:

$$K^* = \frac{a}{b} - \frac{\omega\cos(\phi)}{b\sin(\phi)} \tag{6.29}$$

$$K_R^* = \frac{X_m\omega}{bR\sin(\phi)} \tag{6.30}$$

which correspond to the Erzberger gains. Figure 6.28 shows the theoretical stationary point gains in comparison with those generated in simulation for the case where the frequency is approximately constant and the phase slowly decreases with time. There is very good agreement for the period up to approximately 35s. After this point there are oscillations of increasing amplitude on the simulation gains until around 41.5s where the

gain jump occurs. During the period of close agreement with the theoretical gains, the error in the simulation is very small confirming that the system is at the stationary point.

At the stationary point ξ_0, the Jacobian matrix may be written as:

$$Df_\xi(\xi_0) = \begin{bmatrix} bK^* - a & -bx_m & -br \\ \alpha C_e x_m + \beta C_e\left(\dot{x}_m - x_m\left(a - bK^*\right)\right) & -\beta C_e b x_m^2 & -\beta C_e b x_m r \\ \alpha C_e r + \beta C_e\left(\dot{r} - r\left(a - bK^*\right)\right) & -\beta C_e b x_m r & -\beta C_e b r^2 \end{bmatrix} \tag{6.31}$$

and the resulting equation for the eigenvalues may be derived as:

$$\lambda\left[\lambda^2 + \left(a - bK^* + b\beta C_e\left(x_m^2 + r^2\right)\right)\lambda + b\left(\alpha C_e\left(x_m^2 + r^2\right) + \beta C_e\left(\dot{x}_m x_m + \dot{r} r\right)\right)\right] = 0 \tag{6.32}$$

where λ is the eigenvalue. Therefore, there is always one eigenvalue at zero, and the other two are time varying. The real parts of these two eigenvalues are plotted over a cycle of the demand r in figure 6.29.

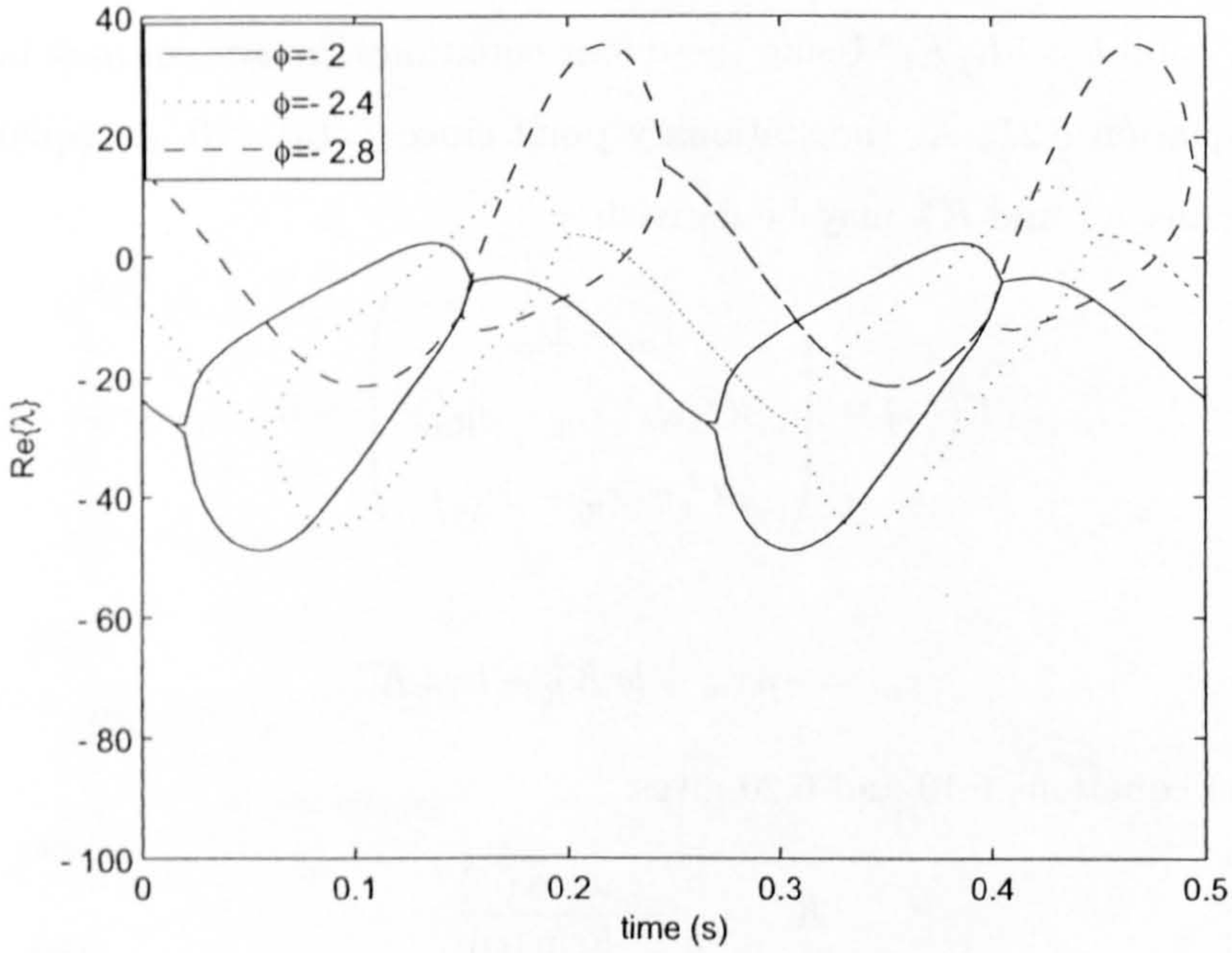

Figure 6.29: Real part of eigenvalues over a cycle for various phase delays

The eigenvalues oscillate with twice the frequency of the demand and for the majority of the time, for the cases where $\phi = -2$ and $\phi = -2.4$ (which correspond to time 25 and 35s in the simulation) the real component of the eigenvalues are negative. For the case where $\phi = -2.4$ the oscillations in the gains and the error observed in the simulation are

at twice the demand frequency, corresponding to the eigenvalue oscillation frequency. The exponential growth associated with the eigenvalue with a positive real part is compensated for by the exponential decay of the eigenvalue over the rest of the cycle while the real part is negative, resulting in a limit cycle around the stationary point. For $\phi = -2.8$ (corresponding to 45s) there is a marked increase in the real component of the eigenvalues indicating that settling at the stationary point is not possible. It is therefore reasonable to assume that the jump in gains is caused by a destabilisation of the stationary point due to the increase in phase. It should be noted that this does not correspond to a destabilisation of the system, just that the system will not settle to the stationary point, global asymptotic stability of the system has been demonstrated [208]. It should also be noted that as well as phase, the eigenvalues are affected by other parameters including signal amplitude and frequency, however in simulation the phase seems to have the most significant effect.

6.7.3 MCS with Additional Adaptive Gain, MCSE

One possible way of overcoming the problem of poor control performance of the substructuring experiments over 13 to 17s is to use a third control variable. Tests were conducted with x_e being used as the additional control variable, resulting in the control equation:

$$u(t) = K(t)x(t) + K_R(t)r(t) + K_e(t)x_e(t) \tag{6.33}$$

where the adaptive gain K_e is based on the displacement error at the interface x_e:

$$K_e(t) = \int_0^t \alpha y_e(\tau)x_e(\tau)d\tau + \beta y_e(t)x_e(t) \tag{6.34}$$

The reason for making this modification to the control strategy is through inspection of the resulting equation for the eigenvalues close to the stationary point. In this case, the system must be written in the form:

$$\dot{\xi} = \begin{pmatrix} \dot{x}_e \\ \dot{K} \\ \dot{K}_R \\ \dot{K}_e \end{pmatrix} = f(\xi, t) \tag{6.35}$$

with the stationary point $\xi_0 = \begin{pmatrix} 0 & K^* & K_R^* & K_e^* \end{pmatrix}^T$. Equations 6.23, 6.24 and 6.25 remain the same, however an equation for K_e^* is now required:

$$K_e^* = \alpha C_e x_e^2 + 2\beta C_e x_e (\dot{x}_m - \dot{x}) \tag{6.36}$$

and equation 6.26 is modified to:

$$\dot{x} = -a\left(x_m - x_e\right) + brK_R - b\left(x_m - x_e\right)K + Bx_eK_e \tag{6.37}$$

At the stationary point $f(\xi) = 0$, which gives:

$$f\left(\dot{\xi}_0\right) = \begin{pmatrix} \dot{x}_m - \dot{x}|_{\xi_0} \\ \beta C_e x_m \left(\dot{x}_m - \dot{x}|_{\xi_0}\right) \\ \beta C_e r \left(\dot{x}_m - \dot{x}|_{\xi_0}\right) \\ 0 \end{pmatrix} = 0 \tag{6.38}$$

This result imposes the same conditions on K^* and K_R^* as before (equations 6.29 and 6.30). However no condition is imposed on K_e^*. There is therefore a line of stationary points upon which K^* and K_R^* are defined using equations 6.29 and 6.30 with K_e^* being able to take any value. The eigenvalues for the Jacobian evaluated at a stationary point are given by:

$$\lambda^2\left[\lambda^2 + \left(a - bK^* + bK_e^* + b\beta C_e\left(x_m^2 + r^2\right)\right)\lambda + b\left(\alpha C_e\left(x_m^2 + r^2\right) + \beta C_e\left(\dot{x}_m x_m + \dot{r}r\right)\right)\right] = 0 \tag{6.39}$$

Figure 6.30 shows the error and gains for simulation using the modified controller. Although towards the end of the simulation there is a deterioration in the control, it is superior to that achieved using the MCS controller. Figure 6.31 show the eigenvalue plots generated using equation 6.39 with K_e^* values measured from the simulation, for the three relative phases considered before, $\phi = -2$, $\phi = -2.4$ and $\phi = -2.8$. These values of ϕ correspond to adaptive error gains of approximately $K_e^* = 285$, $K_e^* = 285$ and $K_e^* = 400$. Comparing them to those for the MCS controller, Figure 6.29, it can be seen that the effect of the adaptive gain is to lower the real component of the eigenvalues over the cycle of the demand, accounting for the more desirable behaviour during the simulation.

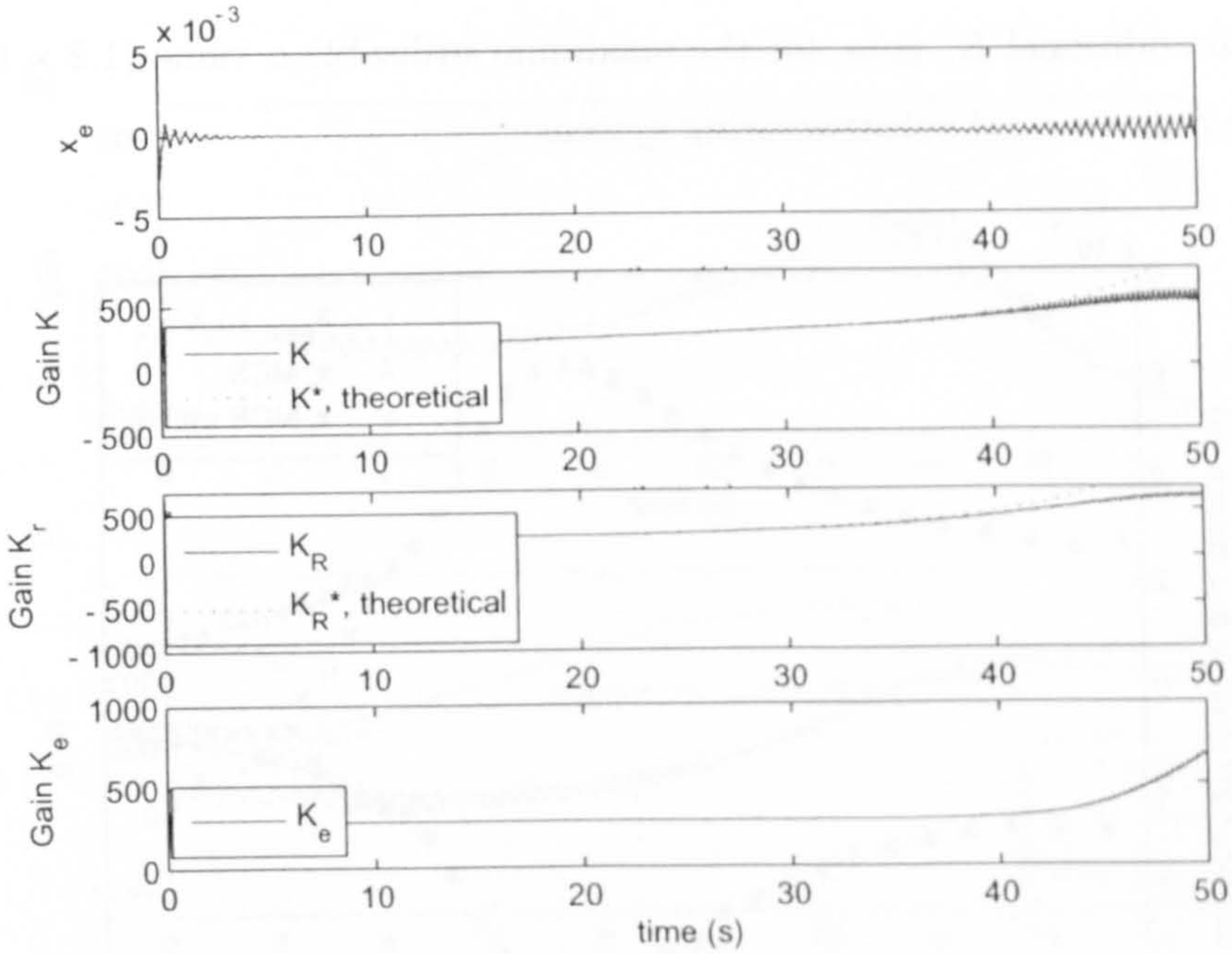

Figure 6.30: Simulation of the simple system with gradually decreasing phase using the MCS controller with an adaptive error gain

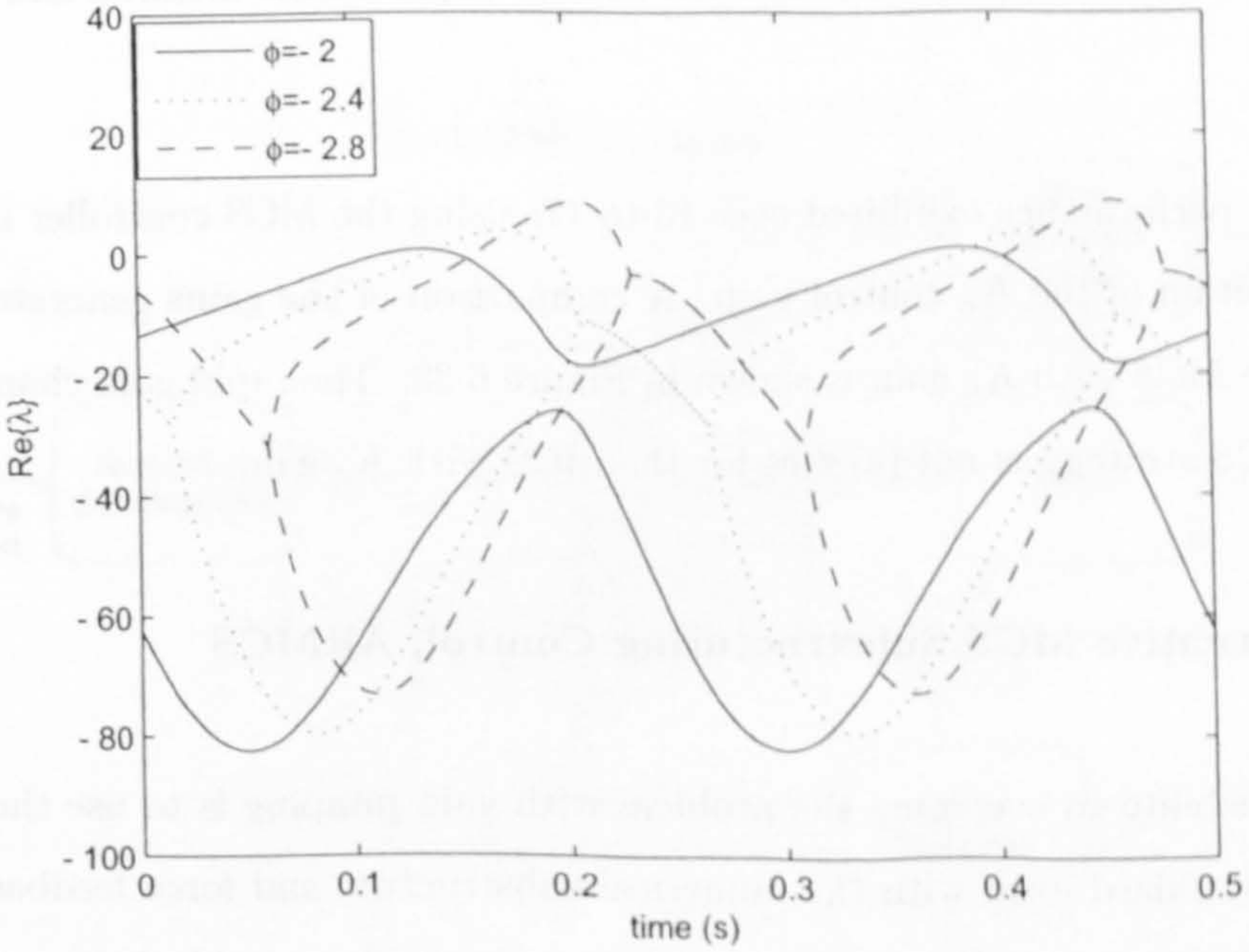

Figure 6.31: Real part of eigenvalues over a cycle for various phase delays using the MCS controller with an adaptive error gain

Figure 6.32 shows the displacement minima and maxima for the MCS controller and the MCS with additional K_e gain, for the maximum utilisable α value (1.2×10^6 in both cases) for the experimental substructuring system.

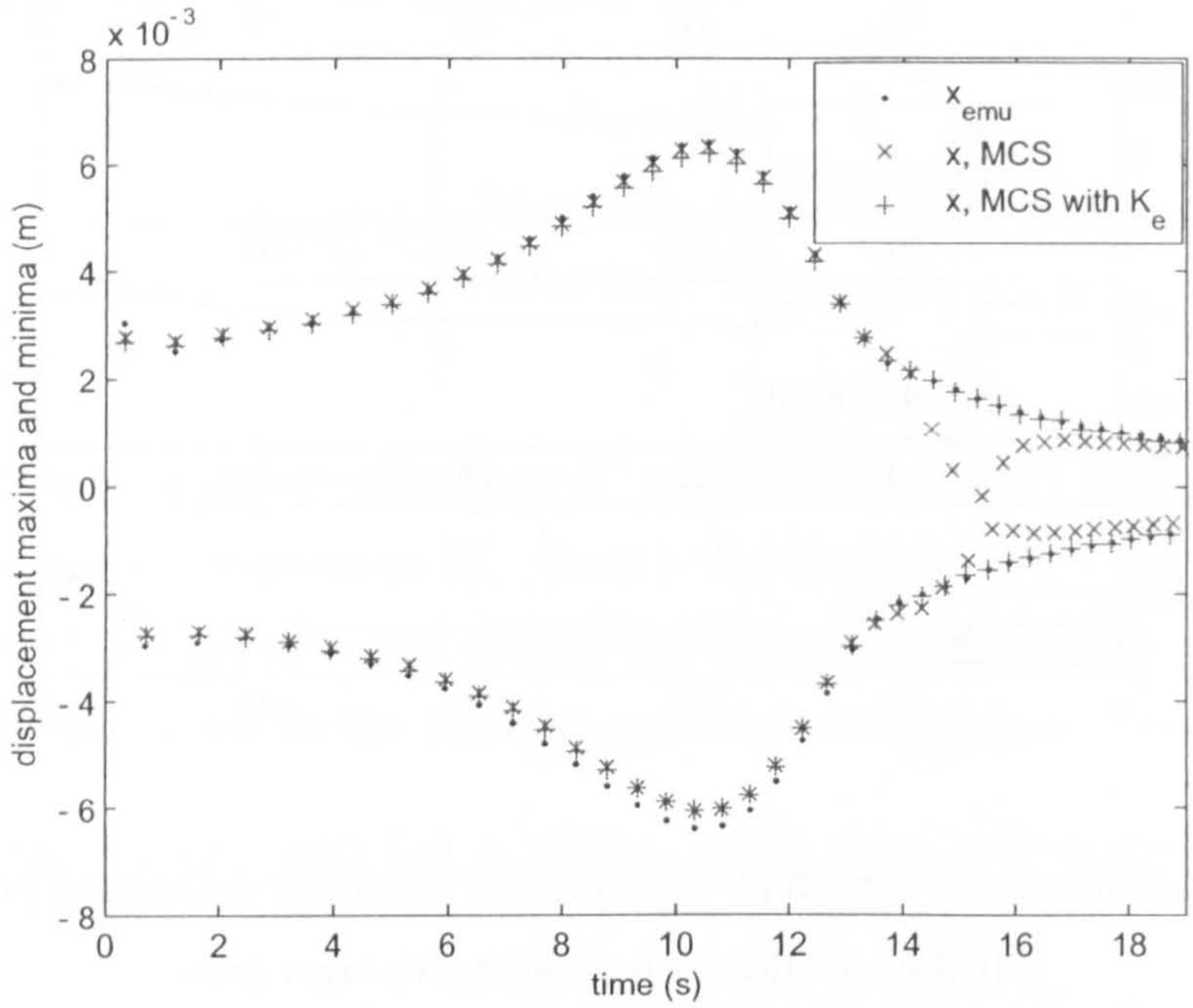

Figure 6.32: MCS and MCS with adaptive error feedback (MCSE), using maximum utilisable value of α (1.2×10^6 in both cases), displacement maxima and minima

The poor performance exhibited over 13 to 17s using the MCS controller is eliminated with the addition of the K_e control gain. A comparison of the gains generated using the MCS and the MCS with K_e gain is shown in Figure 6.33. The rapid gain change after 13s using the MCS strategy is not present for the MCS with K_e gain.

6.7.4 Alternative MCS Substructuring Control, AltMCS

A second possibility to overcome the problem with gain jumping is to use the MCS controller in its standard form with the numerical substructure and force feedback wrapped around the adaptive controller. Figure 6.34 shows the strategy in block form.

Within the dashed box is the standard MCS controller, with a force feedback to the numerical substructure outside the controller and a slight change to the variable names (the demand is r' and the reference model output is x'_m rather than r and x_m respectively).

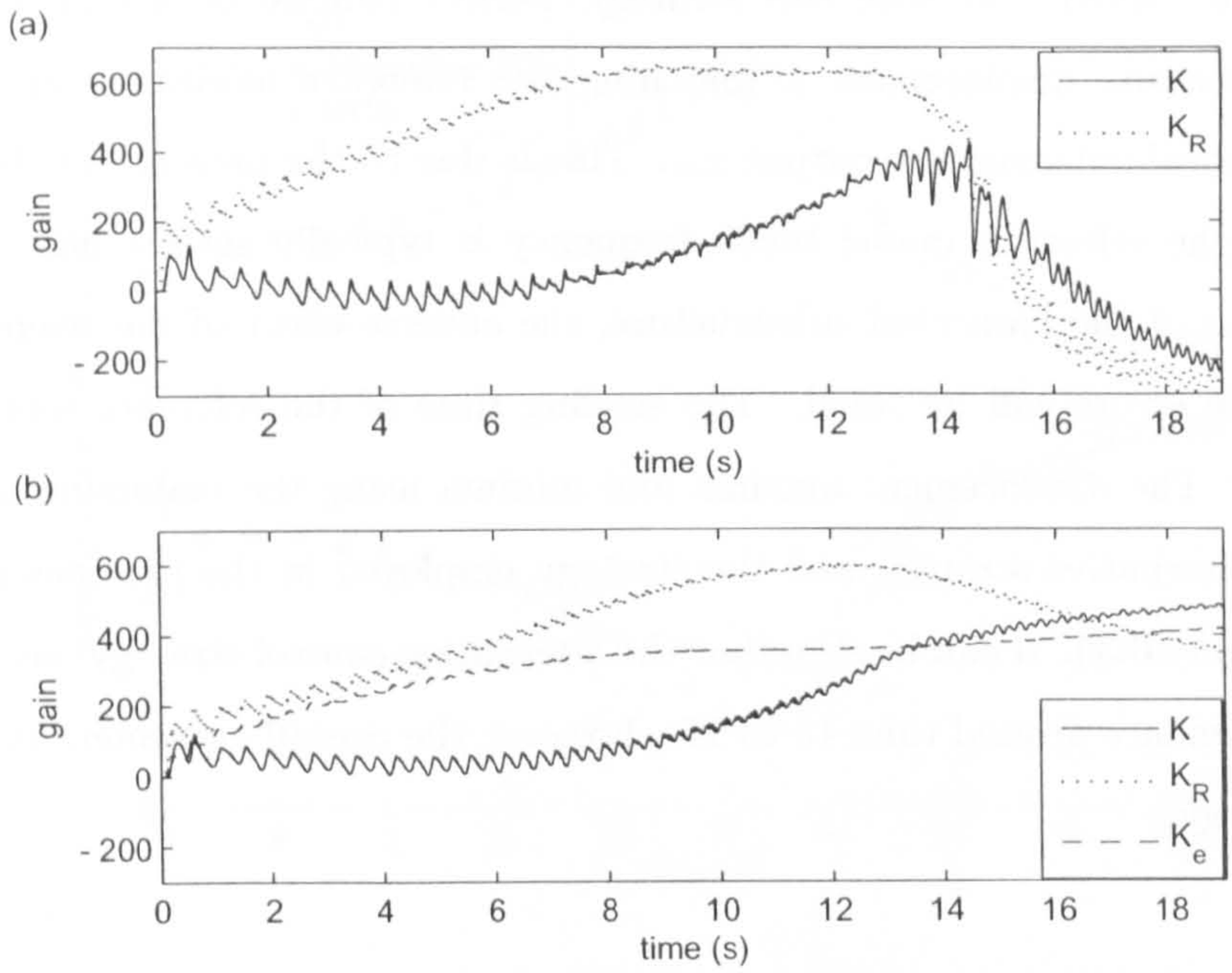

Figure 6.33: a) MCS and b) MCS with adaptive error feedback (MCSE), using maximum utilisable value of α (1.2×10^6 in both cases), adaptive gains

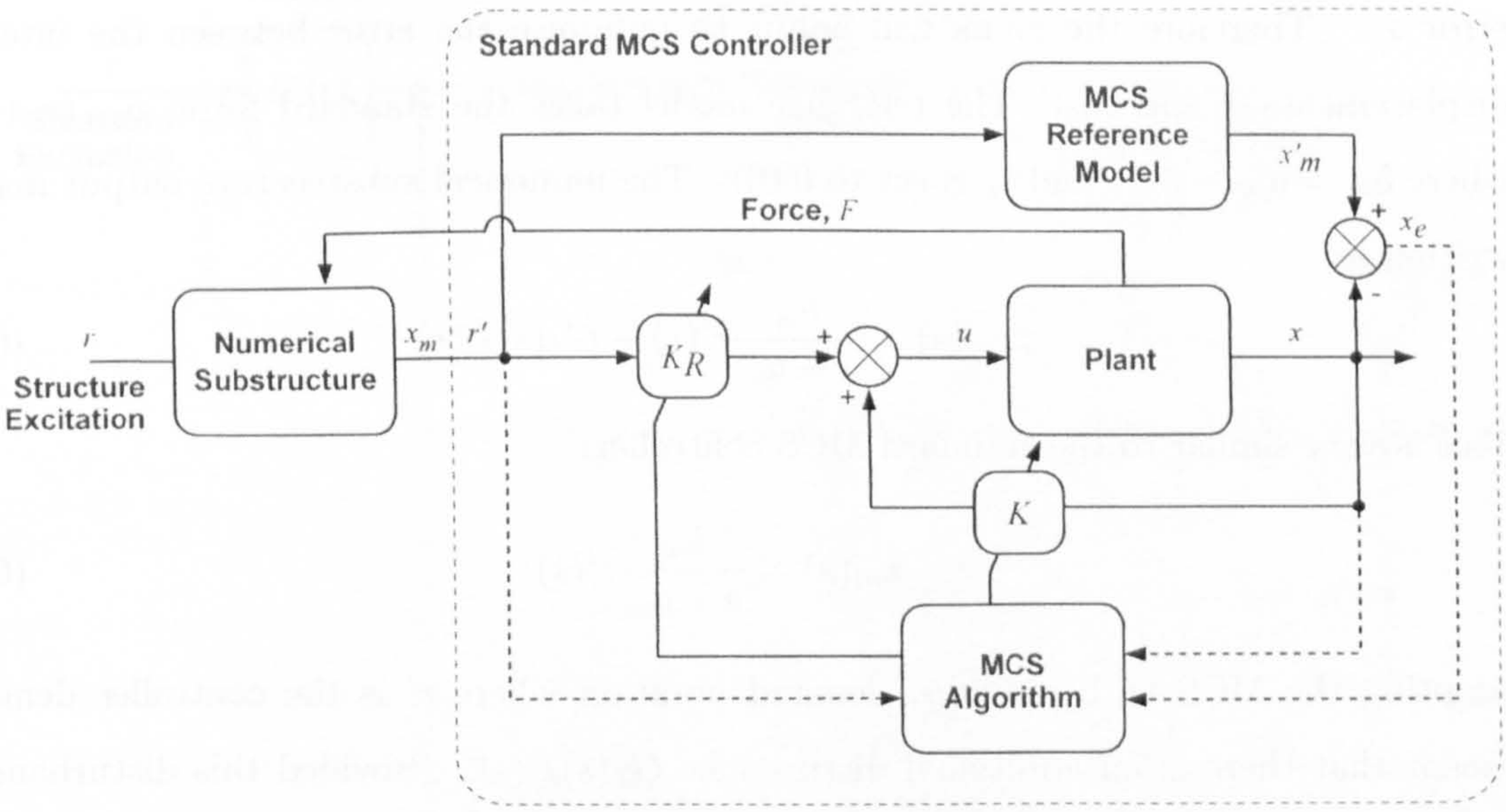

Figure 6.34: Block diagram of the alternative MCS substructuring controller, AltMCS

The output from the numerical substructure, x_m, forms the demand to the controller r'. It should be noted that with this strategy, perfect adaptation would result in the physical substructure displacement x matching the reference model output x'_m rather than the numerical substructure output x_m. This is due to the presence of the reference model. Since the reference model break frequency is typically set far higher than the expected output of the numerical substructure, the adverse effect of the reference model on the interface errors will be small. The settling time of the reference model was set to $t_s = 0.01$ s. The displacement maxima and minima using the maximum utilisable α value for the alternative strategy and the strategy employed in the previous section are compared in figure 6.35. It can be seen that the alternative control strategy has eliminated the poor performance around time 13 to 17s, however the overall agreement is inferior to the MCS strategy.

6.7.5 MCS with Modified Demand - MCSmd

A third way of overcoming the rapid gain changes which result in poor control over 13 to 17s using the MCS algorithm is to modify the demand input to the controller. A block diagram of the controller is shown in Figure 6.36, in which r' is the MCS controller demand. The numerical substructure output x_m is used to calculate the displacement error x_e. Therefore the gains will adapt to minimise the error between the interface displacements x and x_m. The reference model takes the standard form, $b_m/(s + a_m)$ where $b_m = a_m = 4/t_s$ and t_s is set to 0.01s. The numerical substructure output may be written as:

$$x_m(s) = \frac{b_m}{s + a_m} r'(s) - G_f(s)F(s) \tag{6.40}$$

This is very similar to the standard MCS controller:

$$x_m(s) = \frac{b_m}{s + a_m} r'(s) \tag{6.41}$$

adopting the MCS with modified demand notation where r' is the controller demand, except that there is an additional disturbance $G_f(s)F(s)$. Provided this disturbance is not large, the MCS with modified demand controller strategy will not be susceptible to the poor control caused by a large phase difference between the controller demand r and the numerical substructure output x_m since the maximum phase difference is 90° due to the reference model first order filter. The equation for $G_r(s)$ and $G_f(s)$ such that the

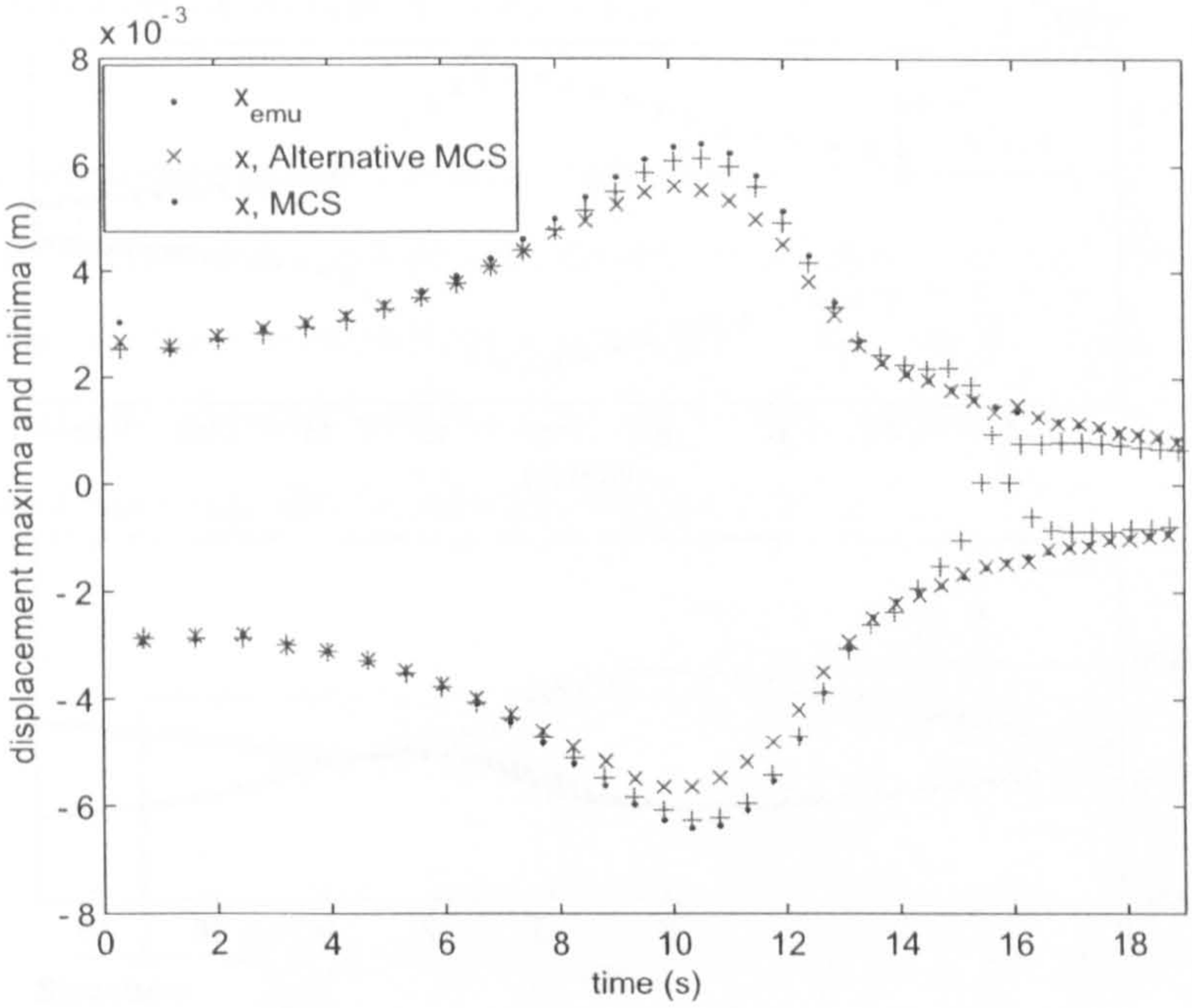

Figure 6.35: Displacement maxima and minima of substructuring experiments performed on a hydraulic actuator using maximum utilisable value of α with the standard and alternative MCS substructuring controllers, ($\alpha = 1 \times 10^6$ and $\alpha = 1.2 \times 10^6$ respectively)

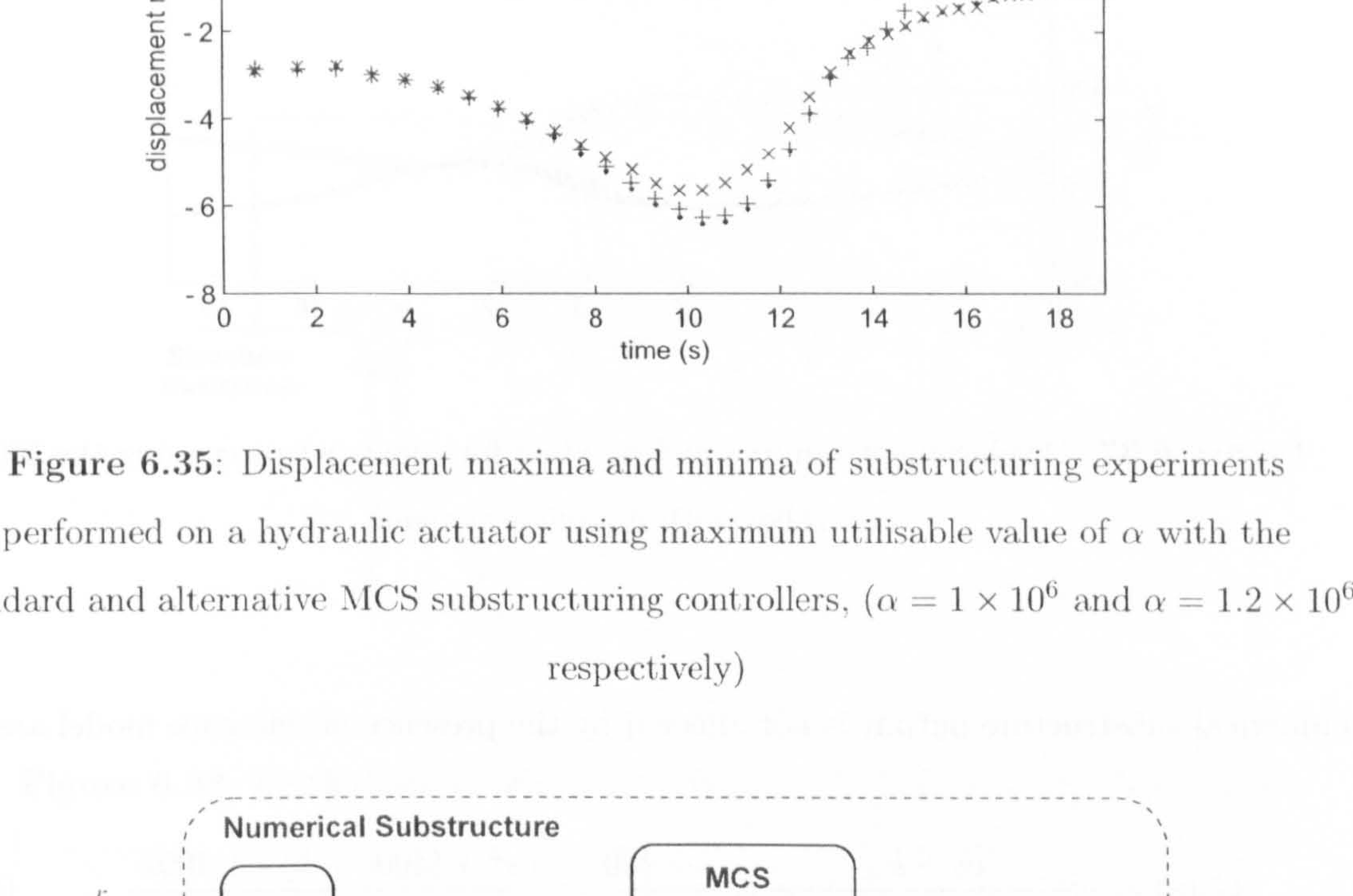

Figure 6.36: Substructuring using the MCS controller with modified demand, MCSmd

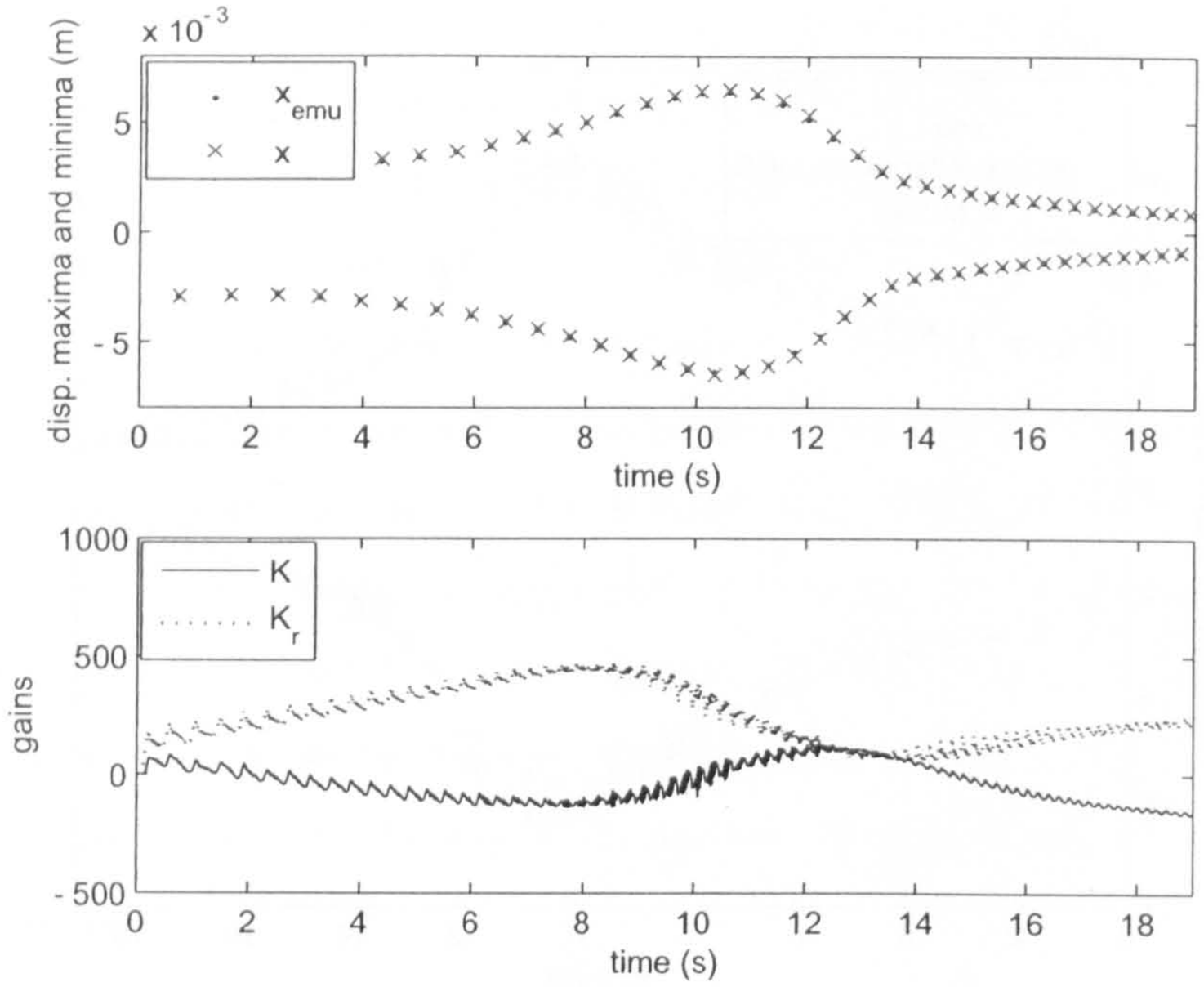

Figure 6.37: Displacement minima and maxima for substructuring using the MCS controller with modified demand

numerical substructure output is not affected by the presence of reference model are:

$$G_r(s) = \frac{cs + k}{(M - m)\, s^2 + cs + k} \times \frac{s + 400}{400} = \frac{cs^2 + (400c + k)\, s + 400k}{400\,((M - m)\, s^2 + cs + k)} \tag{6.42}$$

$$G_f(s) = \frac{1}{(M - m)\, s^2 + cs + k} \tag{6.43}$$

where M is the emulated system mass, m is the mass of the test specimen, c is the damping coefficient and k is the spring stiffness.

Figure 6.37 shows the test specimen displacement maxima and minima of the MCS with modified demand controller compared to the emulated displacement minima and maxima for the cases where the inner-loop gain is $K_p = 4$ and $K_p = 1$ with maximum utilisable adaptive weighting, $\alpha = 1.2 \times 10^6$ and $\alpha = 4 \times 10^6$ respectively. The performance of the controller is very good, resulting in minimal errors in the displacement of the test specimen compared to that of the emulated system.

6.7.6 Comparison of Adaptive and Linear Control Strategies

The potential advantage of the adaptive controller of a standard linear controller is now demonstrated. Section 6.4.1 details the design of a linear controller for the one degree of freedom substructured system tested here [204]. The linear design is based on the assumption that the physical substructure may be represented as a first-order system. The structure of the controller is shown in Figure 6.38.

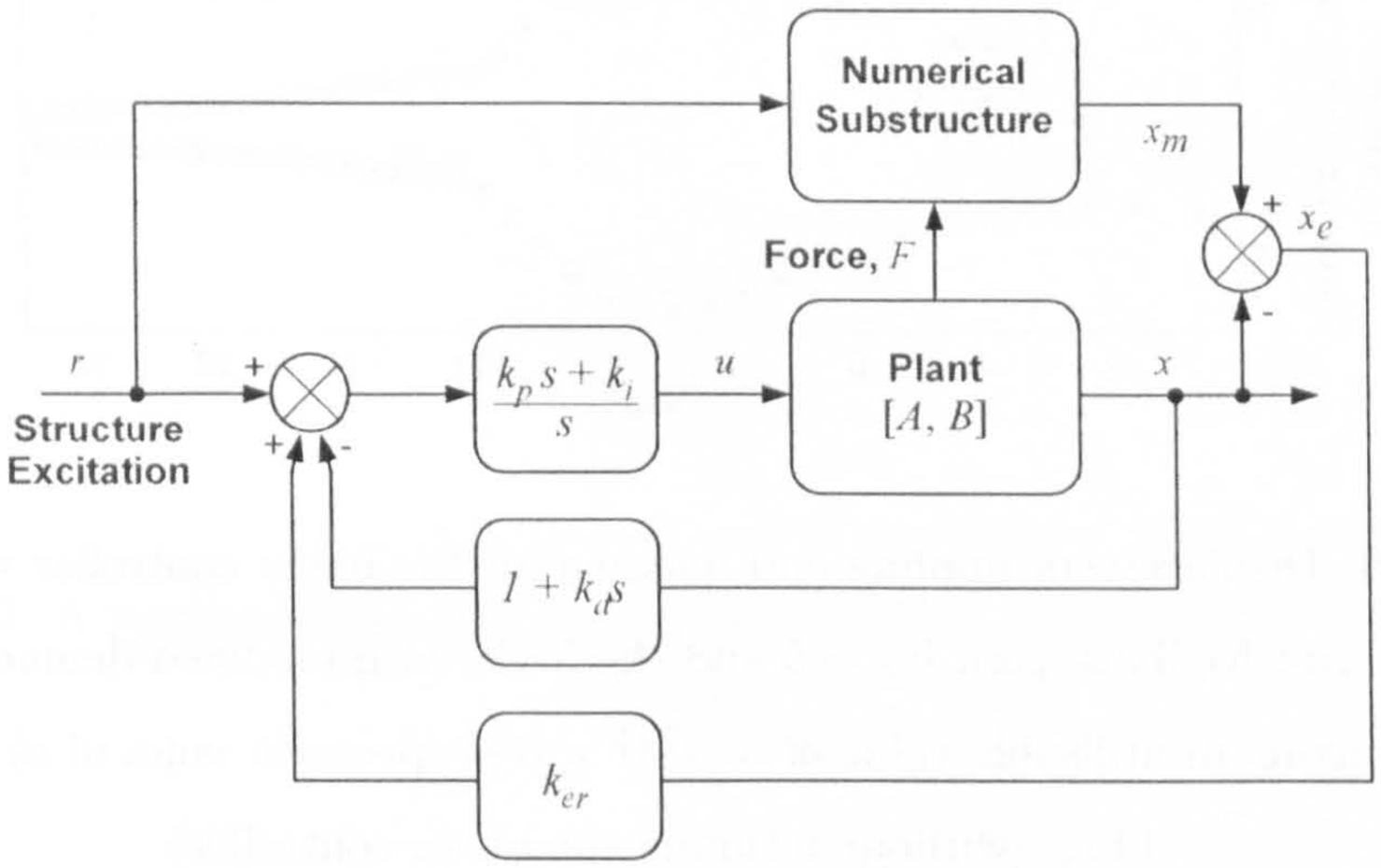

Figure 6.38: Block diagram of substructuring system using a linear controller

The controller has been based on a first-order linear model of the physical substructure dynamics, and may not prove robust to changes in plant parameters $\{a, b\}$ or model parameters $\{c, k, M\}$. To reduce the effect of parameter change, an error feedback strategy is used (k_{er} in Figure 6.38).

Tests were conducted with a inner-loop gain of $K_p = 1$ since higher gains resulted in instability of the outer-loop linear controller. Figure 6.39 (a) shows the displacement minima and maxima using the linear controller with an error feedback gain of $k_{er} = 5$ compared to the results using the MCS with modified demand controller and inner-loop gain of $K_p = 1$. Agreement with the emulated system displacements is very good using both the linear and the adaptive controllers. The drawback with the linear controller is that knowledge of both the emulated system dynamics and the transfer function dynamics are required to calculate the controller gains. This is in contrast to the adaptive controllers where no tuning is required. This point is demonstrated in Figure 6.39 (b) where the test

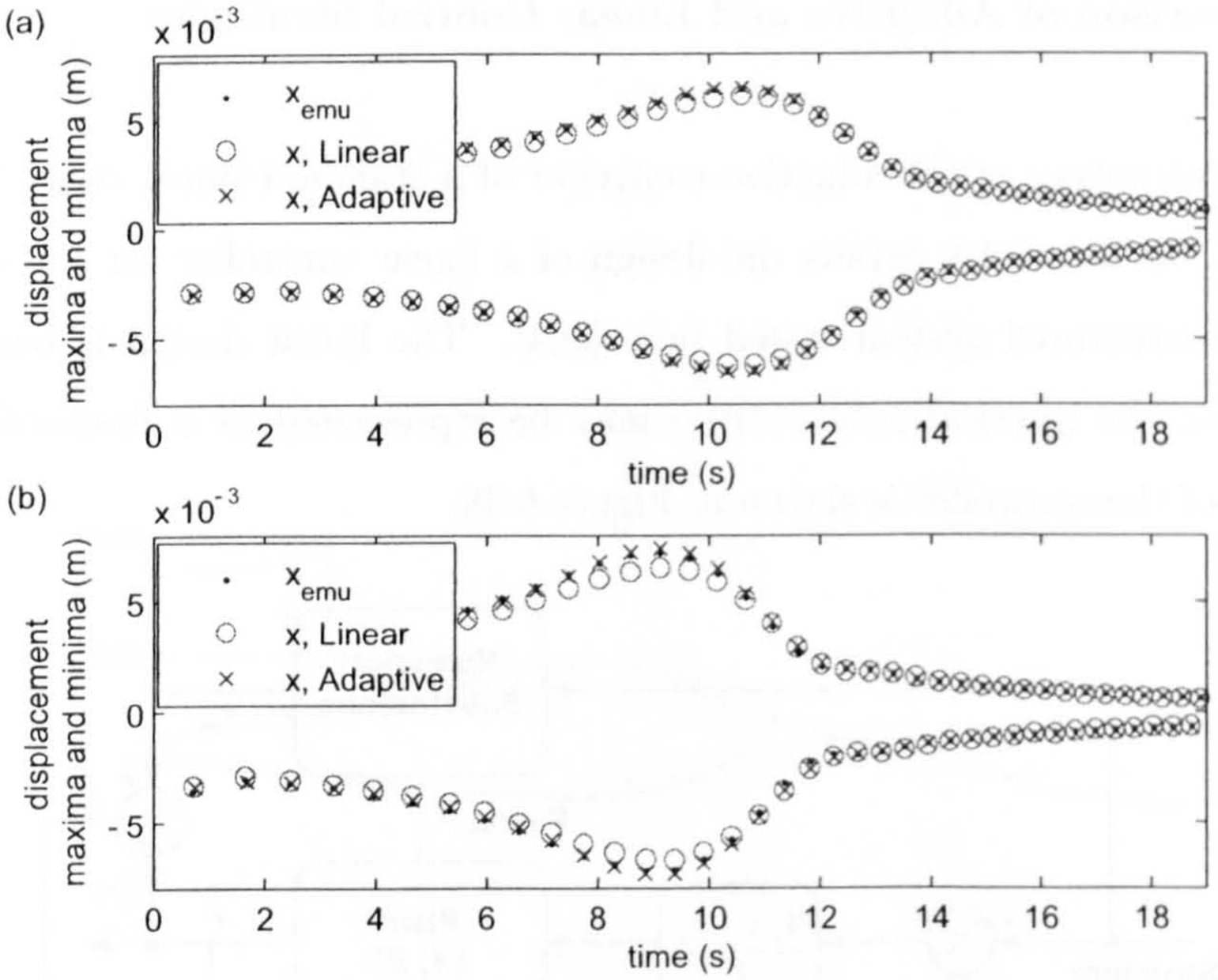

Figure 6.39: Displacement minima and maxima for the linear controller with maximum utilisable error feedback gain $k_{er} = 5$ and the MCS with modified demand controller using the maximum utilisable value of α, with a test specimen mass of a) 20 kg and b) 40 kg (without retuning the linear controller)

specimen mass has been increased to 40kg without retuning the linear controller. It can be seen that the added robustness provided by the error feedback gain is not sufficient to compensate for this change to the dynamics of the system resulting in errors between the substructured system and the emulated system. The adaptive controller performs well with only a slight over-prediction on the emulated system displacement peaks. This demonstration shows the potential for the adaptive controller to maintain good interface agreement despite large changes to the dynamics of the system without the need to retune the controller in comparison to the limited ability of the linear controller through the use of the error feedback gain k_{er}.

6.7.7 Er-MCSI controller

The substructuring system complete with the inner-loop proportional controller and the outer-loop Er-MCSI controller is represented in Figure 6.40.

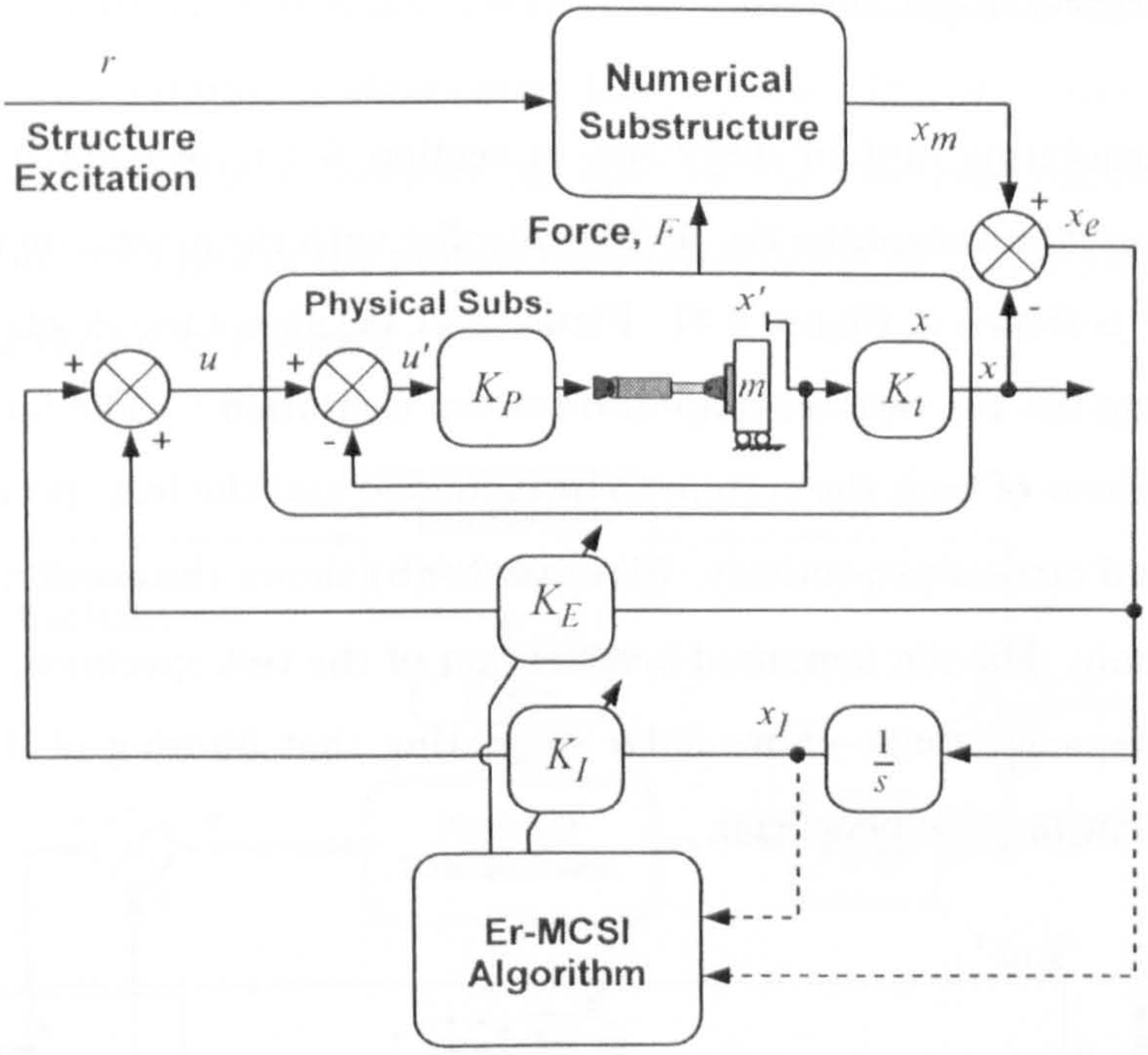

Figure 6.40: A representation of the substructuring system with Er-MCSI outer-loop control

The controller is discretised using the zero-order hold transform. The resulting equations for the gains are:

$$K_e(n+1) = K_e(n) + \beta y_e(n+1)x_e(n+1) - (\beta - \alpha\Delta)y_e(n)x_e(n) \tag{6.44}$$

$$K_I(n+1) = K_I(n) + \beta y_e(n+1)x_I(n+1) - (\beta - \alpha\Delta)y_e(n)x_I(n) \tag{6.45}$$

where subscript n indicates the sampling instant. The system was run with a sampling interval of 1ms. The empirical ratio $\alpha = 10\beta$ is used throughout. Tests are with a inner-loop gain of $K_p = 4$ unless otherwise stated.

Firstly experimental results are presented for the Er-MCSI controller. The effect of filtering of the measured force and displacement on the system is also studied. Filtering was successfully used to improve the control performance in substructuring tests on the shaking table. Then the effect of the inner-loop gain K_p and the use of forgetting factors are examined. Forgetting factors are a method of reducing adaptive gain wind-up by introducing a adaptive gain decay time. Finally the effect on the outer-loop controller of increasing the settling time of the physical substructure dynamics is investigated. This is achieved by altering the inner-loop proportional gain K_p.

Er-MCSI Outer-Loop Control

For the substructuring system described in section 6.3 implemented on the hydraulic actuator, the performance of the Er-MCSI controller with the maximum utilisable adaptive effort, $\alpha = 10^6$ is shown in Figure 6.41. Figure 6.41 (a) shows the displacement of the test specimen during the 19s variable-amplitude sweep excitation r. The minima and maxima of the displacement of both the system to be emulated and the test specimen is also shown via the dots and crosses respectively. Figure 6.41 (b) shows the acceleration signal in the frequency domain. For the measured acceleration of the test specimen, noise was present over a wide frequency range above 35Hz suggesting that filtering of the measured force and displacement may be beneficial.

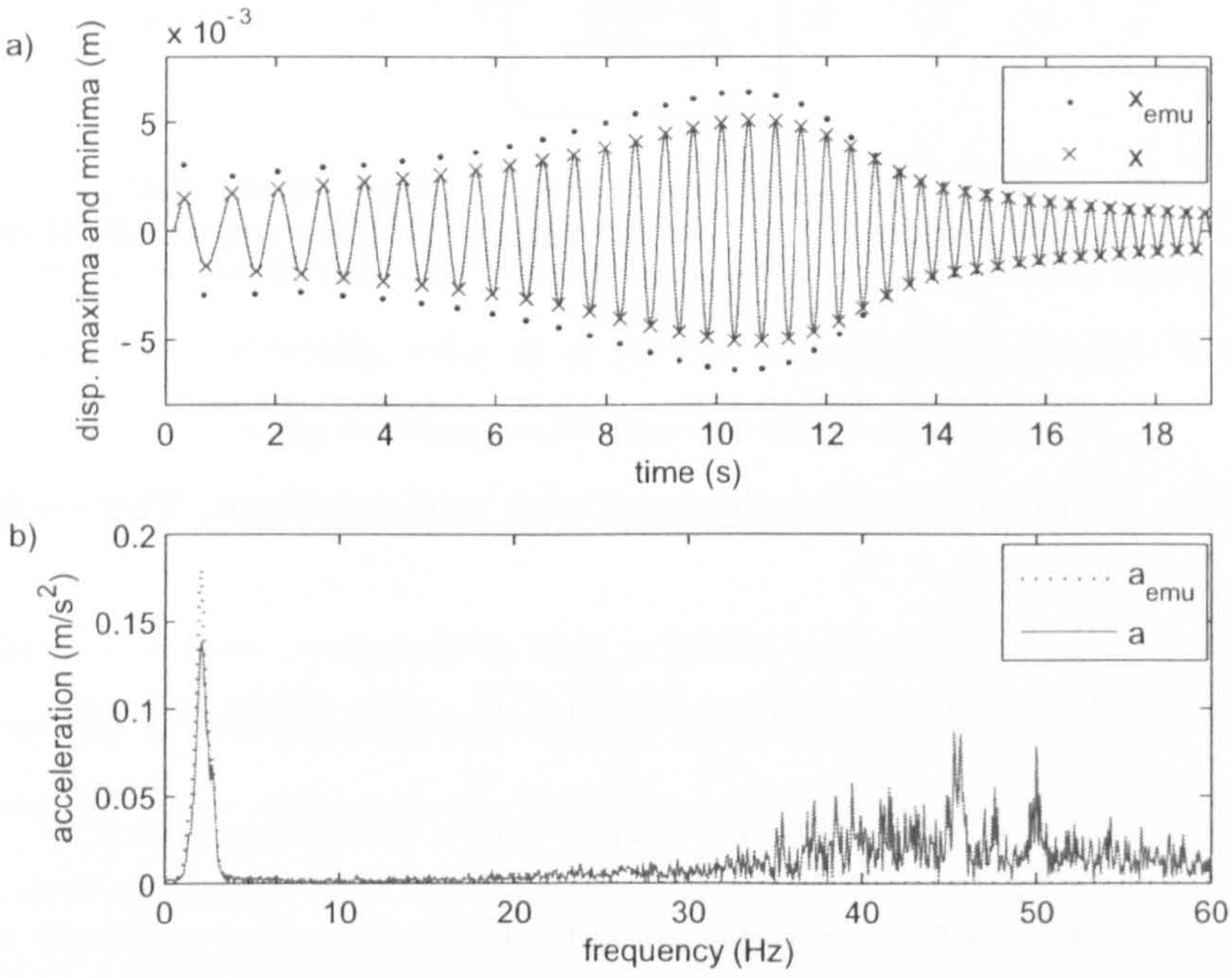

Figure 6.41: Er-MCSI control with $\alpha = 10^6$, a) actuator displacement and b) actuator acceleration

Filtering

In earlier tests conducted using the shaking table on the same substructure system (section 6.6.3) it was found that filtering of the measured signals significantly improved the performance of the outer-loop controller by allowing a far greater adaptive effort, i.e. larger

values of α and β. Identical filters are used for the force and the displacement to ensure that the lag due to the filtering is identical on both signals. The outer-loop controller will act to compensate for the lag induced by the filter on the measured displacement as well as effects due to the dynamics of the physical substructure. A block diagram of the system including filters is shown in Figure 6.42.

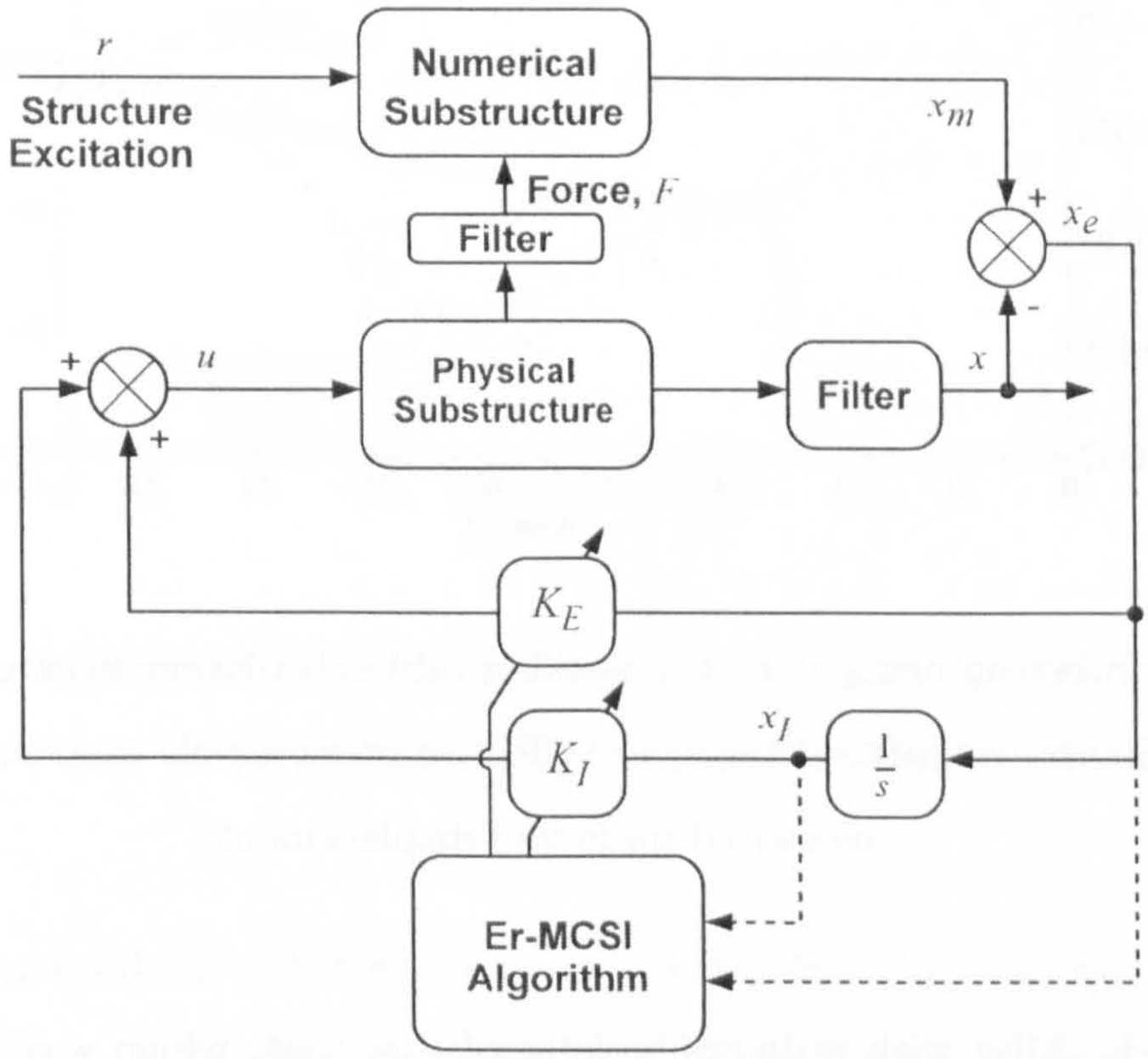

Figure 6.42: A representation of the substructuring system with Er-MCSI outer-loop control and filters

However it should be noted that the performance with filtering using the shaking table was only comparable to that without filtering using the actuator (shown in Figure 6.41). This can be seen from Figure 6.43, which shows the displacement minima and maxima for the shaking table experiments with no filter and with a pole cancellation filter (section 6.6.2). In the previous tests using the shaking table, two types of filter improved the control of the substructuring system, a pole cancellation filter and less successfully a second order Butterworth low-pass filter. A pole cancellation filter substitutes a pole-pair with a low damping ratio within the physical substructure, which results in a large sharp resonance peak, with a pole-pair with a higher damping ratio. For the shaking table a fourth order system identification between the control signal and the resulting displacement using Er-MCSI controller with the maximum utilisable value of α reveals that there

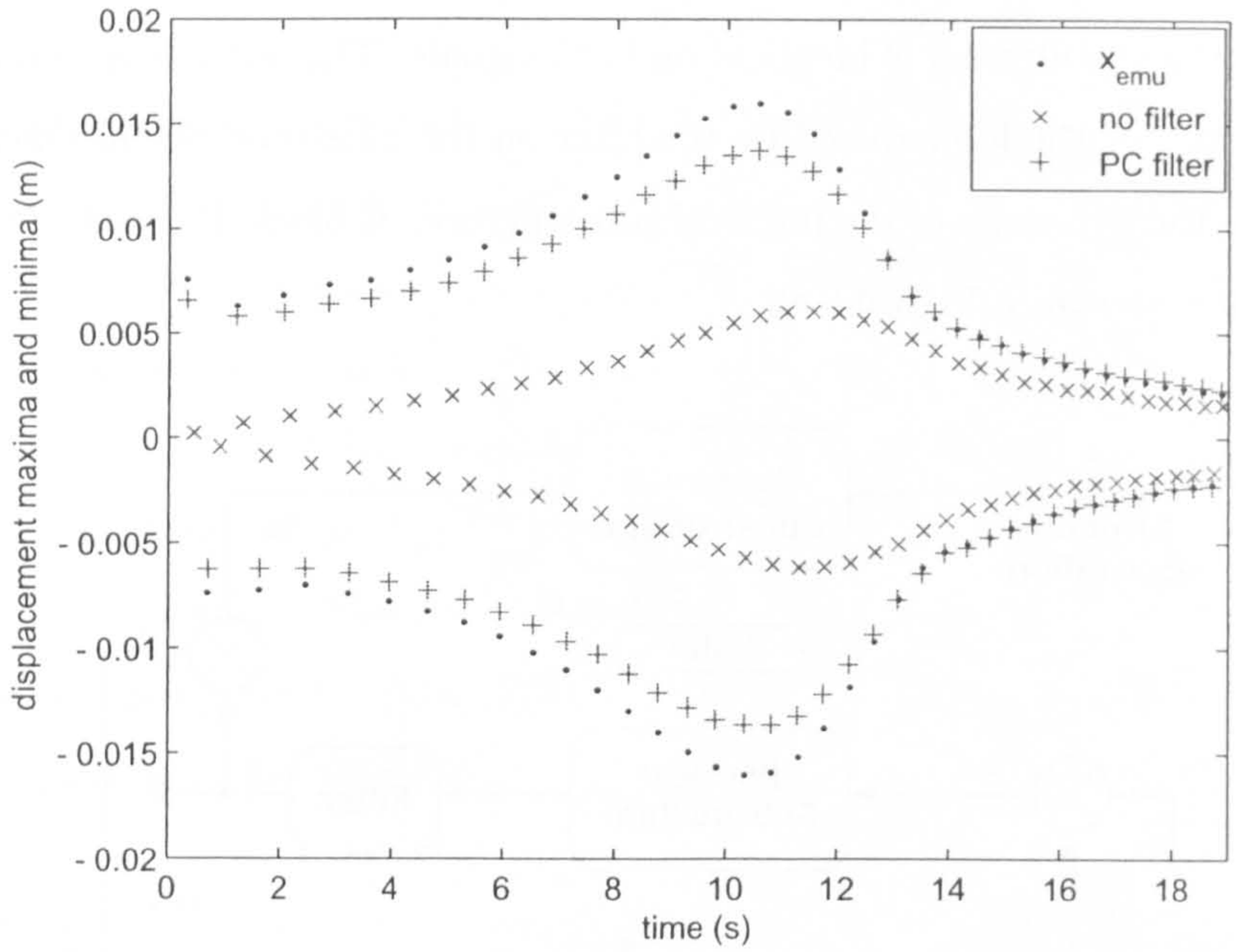

Figure 6.43: Substructuring using the shaking table, displacement maxima and minima using the maximum utilisable α value, the effect of using a pole cancellation filter on the measured force and displacement

is a resonance at 23Hz with a damping ratio of $\zeta = 0.04$, which was attributed to oil-column resonance within the actuators. However, for the actuator system a similar higher order system identification gives a transfer function of:

$$G_p(s) = \frac{371.3}{(s + 22.9)(s + 3157)} \tag{6.46}$$

which does not contain a resonance peak with low damping that could be replaced using the pole cancellation filter.

Bode plots of both system identifications are shown in Figure 6.44. Therefore a pole-cancellation filter is not suitable for the substructuring system using an actuator as the transfer system. Tests using a second order Butterworth low-pass filter with a cut-off of 30Hz were conducted. These revealed that the maximum utilisable value of α is significantly reduced when the filter is present, resulting in a degraded performance of the system.

Figure 6.45 shows the displacement peaks for the maximum utilisable value of $\alpha = 10^5$ and $\alpha = 10^6$ for the case with and without a filter respectively. With the filters present,

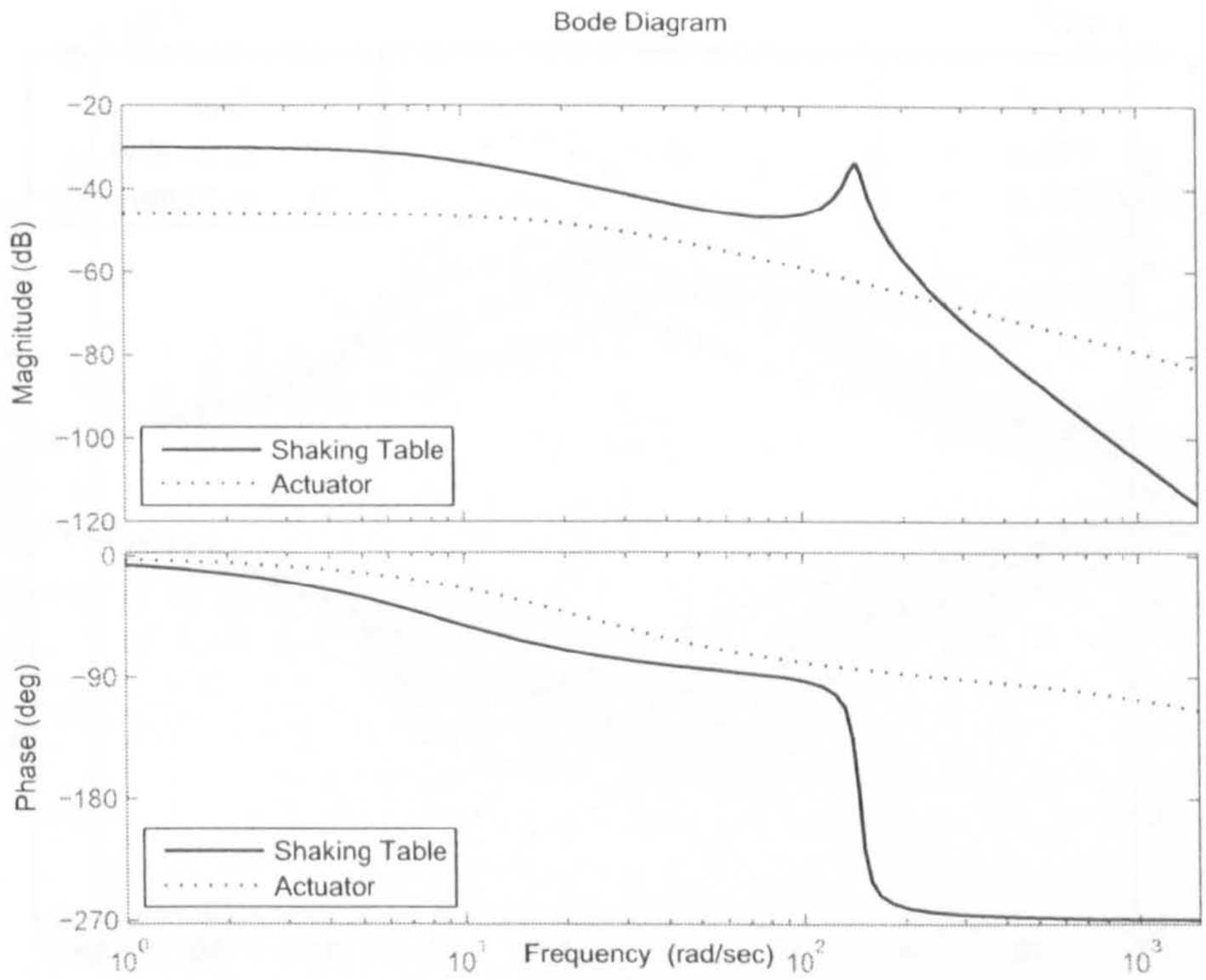

Figure 6.44: High order system identification for the shaking table and actuator systems during tests at the maximum utilisable value of α with the Er-MCSI controller

higher values of α result in a 20.5Hz resonance. Very similar results are obtained if the substructure mass is set to 0kg, indicating that the resonance is not due to the force feedback. It is thought that the resonance is due to the phase lag imposed on the test specimen displacement and force by the filters. With the shaking table experiments, higher-order dynamics in the form of the oil-column resonance are present in the system before the filtering is added. In this case, the addition of the filters is a compromise. The filters act to attenuate the effect of these higher-order dynamics by reducing the sharp 23Hz resonance peak, while at the same time introducing their own less severe higher-order dynamics.

Forgetting Factors

Forgetting factors are a mechanism by which gain wind-up can be counteracted. This is achieved by reducing the influence of past events on the current values of the adaptive gains. The equations for the gains, equations 6.44 and 6.45 are modified to:

$$K_e(n+1) = fK_e(n) + \beta y_e(n+1)x_e(n+1) - (\beta - \alpha\Delta)y_e(n)x_e(n) \tag{6.47}$$

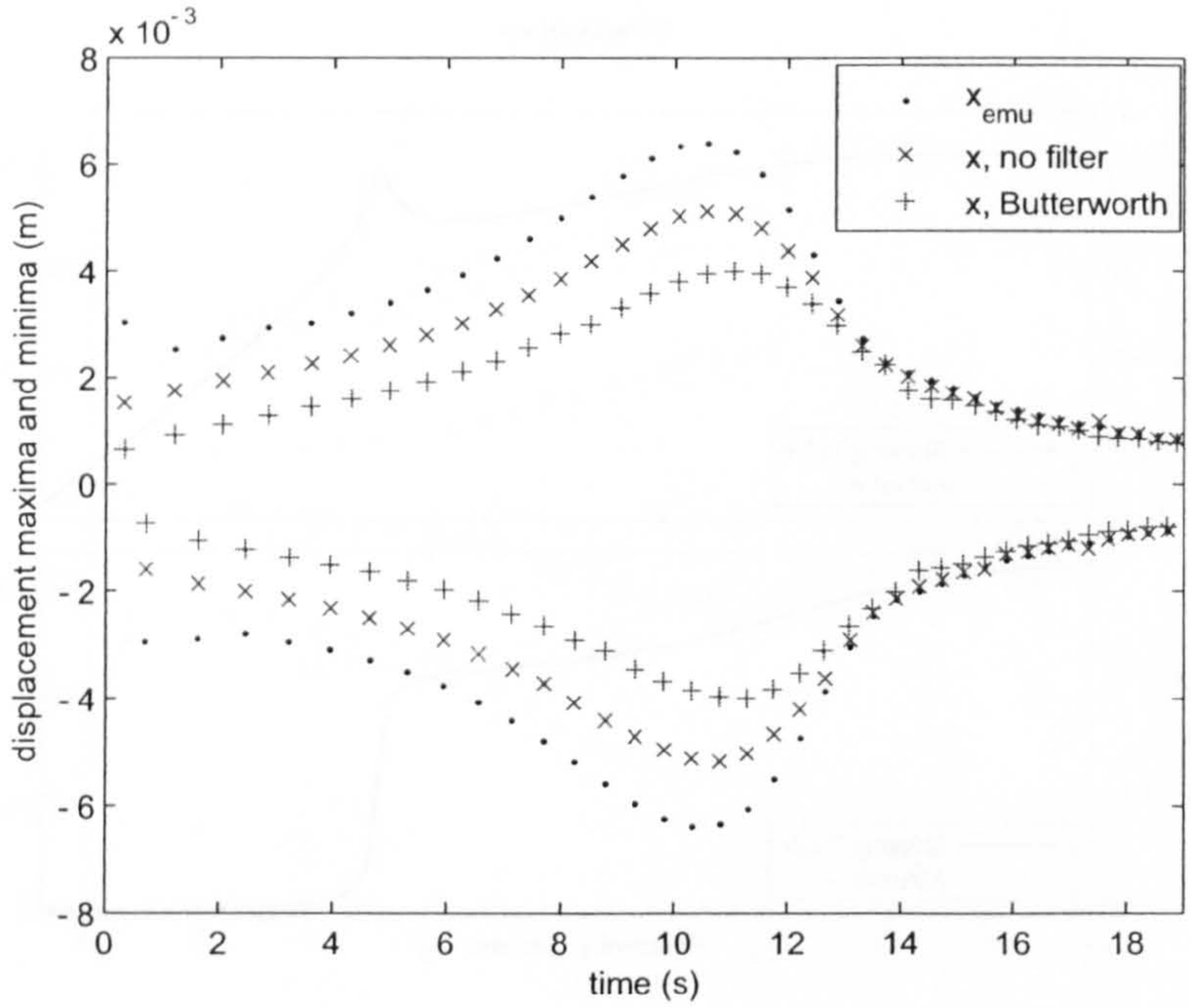

Figure 6.45: Er-MCSI control, the effect of applying a 2^{nd} order Butterworth low-pass filter to the displacement and force feedback signals, maximum utilisable value of α

$$K_I(n+1) = fK_I(n) + \beta y_e(n+1)x_I(n+1) - (\beta - \alpha\Delta)y_e(n)x_I(n) \tag{6.48}$$

where f is the forgetting factor. If f is unity then the forgetting factors have no effect, however if slightly less than one the current value of the gain is less dependent on the previous value. The forgetting factor acts as an adaptive gain decay time, the settling time of the decay may be expressed approximately as:

$$f = 1 - \frac{4\Delta}{t_s} \tag{6.49}$$

Figure 6.46 shows the displacement peaks for tests with maximum utilisable α values, $\alpha = 10^6$, $\alpha = 2 \times 10^6$, $\alpha = 8 \times 10^6$, $\alpha = 4 \times 10^6$, for forgetting factors $f = 1$, $f = 0.9999$, $f = 0.999$ and $f = 0.99$ respectively (or approximate decay times of ∞, 40, 4, 0.4s respectively).

Initially the effect of reducing the forgetting factor allowed a large value of α to be used, however this did not improve the resulting displacement peaks in comparison with the emulated system. This trend alters with a forgetting factor of $f = 0.99$ where the maximum utilisable α value halves relative to that for $f = 0.999$ and the displacement of the test specimen is not as close to that of the emulated system. It is concluded that

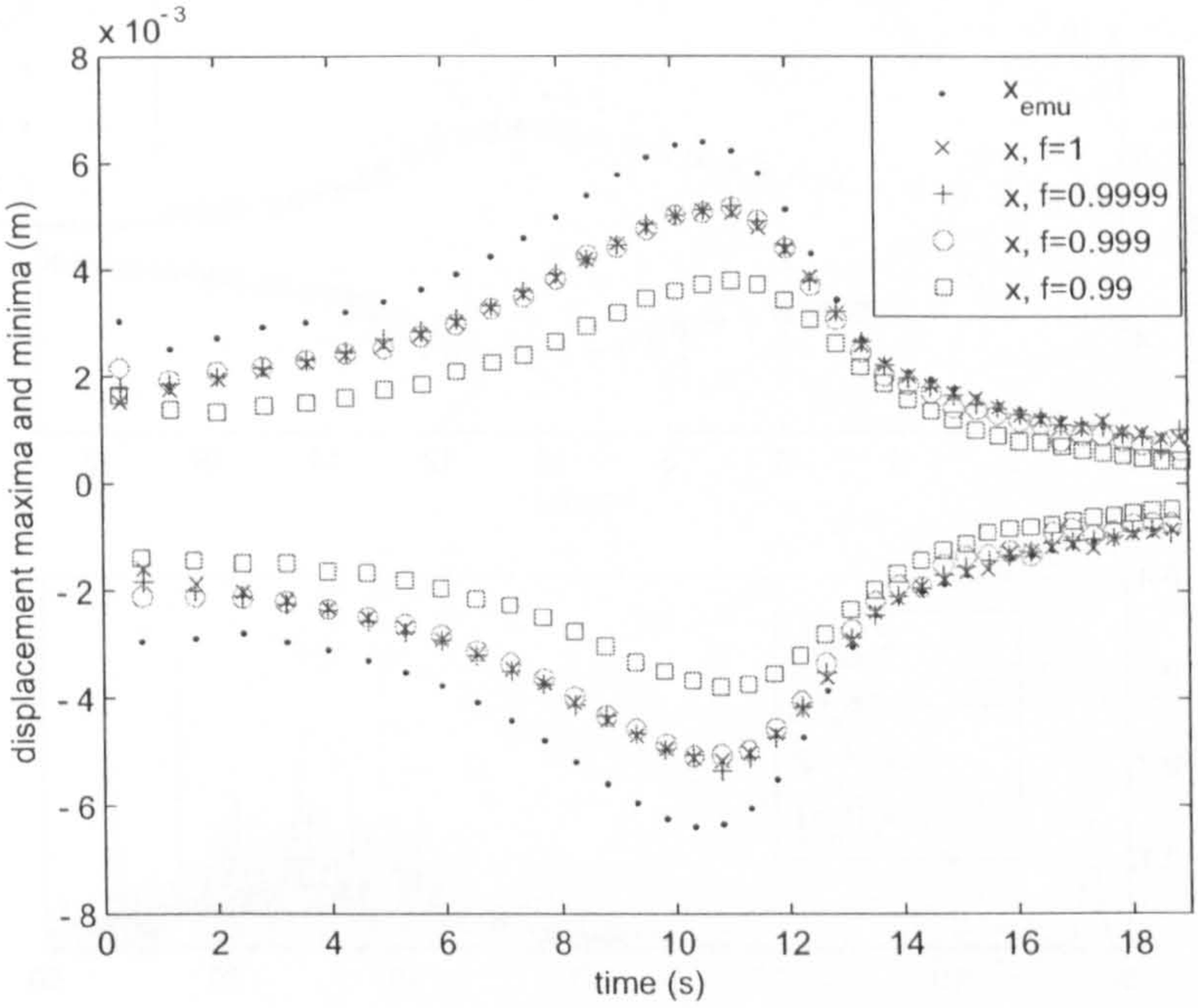

Figure 6.46: Er-MCSI control, the effect of forgetting factors, maximum utilisable value of α

forgetting factors are not a helpful mechanism for allowing improved Er-MCSI control of this system.

6.7.8 Inner Loop Proportional Gain

For the tests presented in the previous sections the value of the inner-loop gain was $K_p = 4$. The effect of altering the inner-loop gain K_p, and hence altering the settling time of the physical substructure, is now examined. Firstly it is worth considering the case where the adaptive weightings, α and β are kept constant, and inspecting the frequency content of the resulting test specimen motion. Figure 6.47 (a) shows the displacement maxima and minima of the test specimen for a range of values of K_p with $\alpha = 10^6$. The effect of changing K_p has only a minimal effect on the visible displacement performance of the substructuring system. However, if the acceleration of the mass (or force exerted on the mass) is considered, it can be seen that higher values of K_p result in greater high frequency vibration content, as is shown in Figure 6.47 (b).

This reduction in higher frequency content with reduced inner-loop gain allows higher

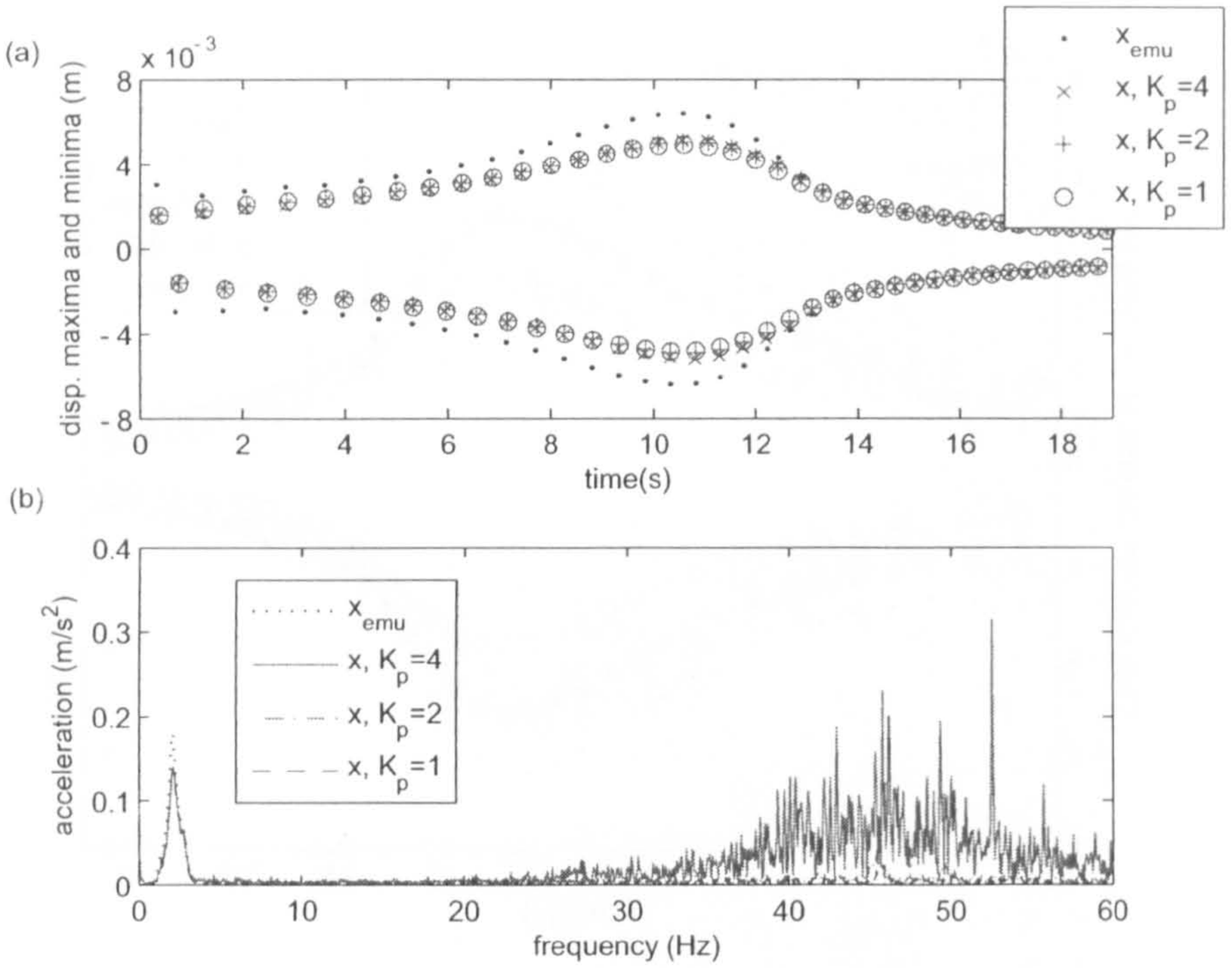

Figure 6.47: Effect of varying the inner-loop gain, K_p, on a) the displacement minima and maxima and b) the frequency content of the acceleration for $\alpha = 10^6$

adaptive gain weightings. Figure 6.48 shows the displacement results for various inner-loop gains using the maximum utilisable value for α, $\alpha = 2 \times 10^5$, $\alpha = 10^6$, $\alpha = 10^7$, $\alpha = 2 \times 10^7$ for $K_p = 8$, $K_p = 4$, $K_p = 1$ and $K_p = 0.5$ respectively. It can be seen that as K_p is reduced the substructuring results improve, although the rate of improvement is small for low values of K_p. It was found that tests with even lower inner-loop gains resulted in excessive drift prior to starting the test.

6.8 Conclusions

The real-time dynamic substructuring testing technique has been described as a general testing framework. Applicability to the machining industry has been highlighted citing specific applications of interest.

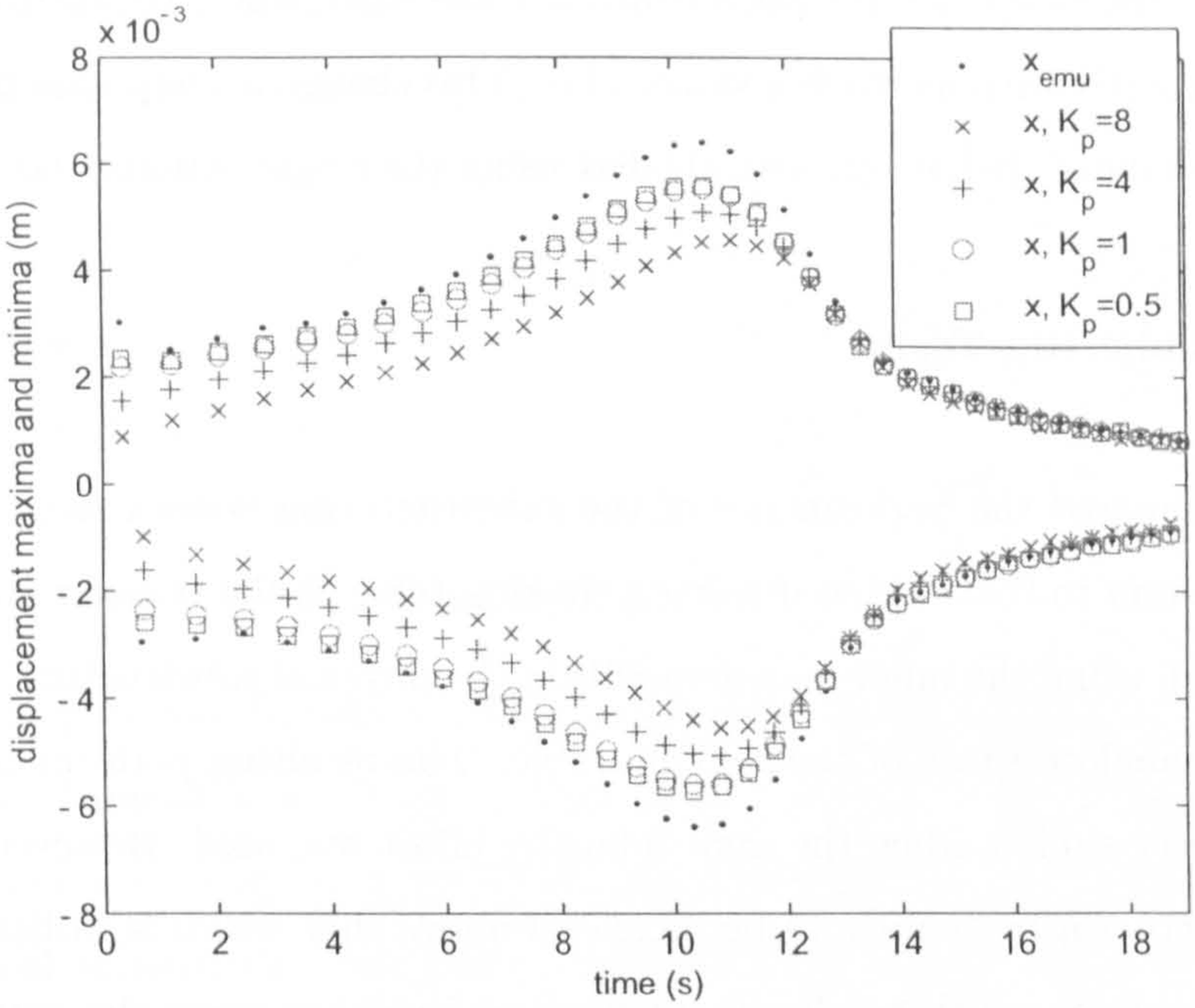

Figure 6.48: Er-MCSI control, the effect of inner loop gain K_p, maximum utilisable value of α

6.8.1 Shaking Table Tests

Substructuring experiments on a one degree-of-freedom mass spring damper system have been performed on the Bristol shaking table. In these experiments the experimental substructure consists of 20% of the mass with remainder being in the numerical substructure. These tests have shown that a linear control strategy based on a first order approximation to the plant dynamics combined with a high-gain error feedback works well for this linear substructure. Both the MCS and Er-MCSI adaptive controllers suffered from problems when implementing substructuring on the shaking table. Particularly, results were adversely affected by oil column resonance at 23 Hz, resulting in an underestimate of the system amplitude response.

Filtering of both the displacement and force feedback signals improved the performance of the adaptive controllers. As a result, tests using the Er-MCSI controller were most successful when pole cancellation filters were included.

It was found that the displacement prediction was roughly the same shape, but with increasing amplitude, for increasing α values when the Er-MCSI controller was used. This

is in contrast to the case when the MCS controller was used, where the displacement shape changed significantly with increasing values of α. This change in shape has been explained by the gain "jumping" behaviour investigated using the single actuator rig.

6.8.2 Hydraulic Rig Tests

Initial tests compared the performance of the substructuring system using a actuator as the transfer system to that achieved using a shaking table as the transfer system. For the actuator system, using the inner-loop gain within the physical substructure, the dynamics were tuned to emulate those of the shaking table. The resulting performance of the two systems were very similar when the same adaptive effort was used. However the adaptive effort for the actuator system could be increased above that which is utilisable using the shaking table system, which results in superior performance using the actuator system. It is thought that this is due to oil-column resonance within the shaking table dynamics which limits the maximum utilisable adaptive effort, and hence the controller performance.

Using the substructuring MCS controller, agreement between the emulated system and the test specimen displacements was good up to 13s. After this point there was a region of deteriorated performance, corresponding to a region of rapid changed in adaptive gains. This behaviour was reproduced in simulation with a 0kg test specimen, which has the effect of reducing the substructuring system to a standard control problem where the numerical model (which is now the same as the emulated system) generates a demand for the physical substructure to follow. This suggests that the undesirable behaviour was due to the modifications made to the MCS algorithm. In the example considered here, the unity-gain first-order reference model was replaced with a second-order numerical model. This modification meant that the relative phase between the numerical model output and input is potentially far higher and the gain of the numerical model is potentially greater than unity. The undesirable behaviour was reproduced in simulation for a simpler system with the relative phase linearly increasing with time. On this simple system a localised stability analysis was performed. This analysis revealed that with increasing phase the eigenvalues corresponding to the Jacobian matrix at the localised stationary point increased with increasing phase indicating a loss of localised stability about the stationary point.

Three tailored MCS substructuring control configurations, which potentially could

overcome this behaviour, were tried. Firstly an MCS controller with an additional adaptive error feedback gain, then an MCS algorithm in its standard form with the numerical model output acting as the demand to the controller and finally a formulation which used both a reference model and a modified numerical model (which incorporated a compensation for the reference model dynamics). The undesirable behaviour was not observed in any of these three systems, however overall only the latter two resulted in more accurate reproduction of the emulated system dynamics throughout the entire experiment when compared to the original MCS substructuring controller.

Finally the potential benefit of using an adaptive outer-loop controller over a linear controller was demonstrated. With the knowledge of the emulated system dynamics, a linear controller was designed to overcome the dynamics of a first order approximation to the physical substructure dynamics. The controller also included an error feedback gain to improve robustness to parameter changes. This controller performed well when applied to the substructuring example. However, when the mass of the test specimen was doubled without retuning the controller, the robustness provided by the error feedback gain did not prove sufficient to overcome the change in dynamics. This is in contrast to the adaptive controller which performed well for both cases. This demonstrates the ability of the adaptive controller to maintain good control performance despite large changes in the system dynamics. This is potentially useful for tests where sudden changes in dynamics might occur due to damage sustained by the test specimen, or where the dynamics of the transfer system are not fully understood.

In contrast to experiments performed on the shaking table it is demonstrated that filtering of the measured displacement and force from the test specimen on the hydraulic actuator does not improve the performance of the substructure system in comparison to the complete system which is being emulated. The reason for this is that there is no clear resonance in the dynamics of the physical substructure when the actuator is used. In fact, the use of second order Butterworth filters resulted in degraded performance. It is thought that this is because the presence of the filters has the effect of acting as higher order dynamics within the physical substructure which have been shown to adversely affect the performance of adaptive controllers. Tests showed that forgetting factors, which act as adaptive gain decay, did not improve the performance of the system. However there was a significant improvement in the performance of the substructuring system with the reduction of K_p, the inner-loop proportional gain. The experimental results presented

here with $K_p = 1$ are a significant improvement on the performance of the substructured system in comparison to those conducted using the shaking table.

Chapter 7

Conclusions and Further Work

SUMMARY: The main aspects of the thesis are summarised here along with proposals for extending the work.

7.1 Research Objectives

At the beginning of this thesis several objectives of the research were determined. These were:

1. Examine the current opportunities for use of adaptive controllers within the field of aerospace machining.

2. To develop an adaptive controller strategy that will vary the machining feed-rate to maintain a desired cutting power.

3. To demonstrate that the aforementioned adaptive controller strategy achieves its goal in the face both of geometrical variations in the cut and in power demand changes.

4. To develop a model that can be used in real-time to relate the mean cutting power to peak cutting force, the variable of interest to machining engineers.

5. To develop a software platform that will allow testing of the strategies for multi-dimensional cuts.

6. To investigate the use of adaptive controllers to improve the dynamic accuracy that can be achieved via the real-time substructuring technique.

7. To tailor the basic adaptive controller algorithm to improve stability when used in the real-time substructuring technique.

8. To demonstrate the potential of the real-time substructuring technique when applied to the field of metal machining.

Here the work is concluded with specific reference to the original objectives. Opportunities for further work is also discussed.

7.2 Current State of Machining Methods - Objective 1

A comprehensive literature review revealed that components that can be manufactured accurately and repeatedly are essential to meet the demands being imposed on airframe manufacturers as a result of the economic drivers that affect the aerospace market.

A technology that has proved beneficial in this area is that of accurate control in manufacture. With an increasing number of parts being milled from single pieces of metal, a particular area of interest is the application of control methods to improve the efficiency of the machining process, termed adaptive control with constraint (ACC). Essential to the success of this type of control is the reference model used to drive the controller algorithm design. The review demonstrated that empirical constants often figure in these reference models and their selection can be crucial to the performance of a particular algorithm.

MCS itself has a simple model and adaptation structure based on largely empirical constants and so was well suited to being applied to this field of ACC.

7.3 Regulation of a Metal Machining Process - Objectives 2-3

A method of inferring cutting power based on measurement of electrical power at the spindle has been presented. Using this power measurement, a controller strategy using a conventional fixed-gain controller and an adaptive controller based on the the MCS algorithm has been designed that regulates cutting power using the feed-rate as its control variable. The benefits of using an adaptive controller have been demonstrated, showing an adaptive controller to be most useful when cutting geometry changes significantly.

On the machine shop floor, such an adaptive scheme could be used in conjunction with

the conventional CNC cutting strategies to allow changes in feed-rate in order to optimise an entire cut. The CNC feed-rate could be selected as in the current manner yielding a single feed-rate for a single CNC block in the cut. The MCS algorithm could then be used to modify this single feed-rate to make better use of the available cutting spindle power for that block. The ability of MCS to function in this way has been demonstrated experimentally in this chapter. In addition to this the adaptive structure of MCS would also be able account for unexpected changes in geometry, wearing of the cutting tool and other factors. The ease with which the MCS algorithm can be implemented and tuned combined with its stable closed-loop performance during use has been demonstrated in this chapter. This highlights it for use in this area.

7.4 Process Demand Model Development - Objective 4

A framework for the development of a demand based on peak-tooth force has been initiated. Whilst accurate inferred reporting of peak-tooth loadings in real-time is always going to be a highly complex task, it is possible that some level of generalisation will produce results within acceptable limits. The relationships derived were not as simple as would be preferred and only apply for a small range of cutting conditions. A study that extends this study to a much larger range of cutting tool and workpiece geometries would be highly beneficial to this area of work.

7.5 Multi-axis Software Development - Objective 5

A high-level NC controller interface for the ControlLab32 suite of software has been designed providing the capability to perform cuts in both one and two degrees-of-freedom. The module allows the feed-rate to be continuously varied during the cut via an external or internal analogue signal. This module can be used to investigate the effect of variable dynamics due to profiled cutting on the adaptive controller during cutter.

The multi-axis module could also be used to investigate the benefits that MCS could offer with regard to reducing geometrical errors seen when cutting in more than one-degree of freedom. It is conceivable that an MCS inner-loop that regulates the feed-rate (or velocity) more accurately than the inner-loop controller of each degree-of-freedom could help to reduce inaccuracies seen when using conventional fixed-gain techniques.

7.6 Real-Time Substructuring - Objectives 6-8

Real-time substructure testing provides laboratories with the capability of testing entire structures without the need for the whole of those structures to be present within the laboratory. The relevance of real-time substructuring to the manufacturing engineer has been discussed with reference to specific examples.

A range of controller strategies have been presented and tested that control the transfer system within a substructuring experiment to ensure accurate reproduction of the emulated system dynamics. The advantage of using an adaptive controller over a fixed-gain, linear scheme for use as the substructuring controller have been demonstrated experimentally. Specifically, the adaptive algorithm allows accurate control, and hence reproduction of the emulated system dynamics, even when the transfer system (or plant) has been mis-modelled.

A localised stability analysis has been performed and highlights limitations that are imposed when using the standard MCS algorithm in a substructuring experiment. Three tailored adaptive controller structures have been designed and presented that each aim to overcome these limitations. The performance of these alternative strategies have been tested with the results demonstrating that each of them result in more stable closed-loop behaviour throughout the duration of the tests. Of these three tailored adaptive controllers two of them (MCS with additional gain and MCSmd) result in more accurate reproduction of the required emulated system dynamics when used in substructuring. In particular, MCSmd, offered much improved stability during substructuring tests and allowed the use of MCS in a much more conventional manner (i.e. by retaining the standard reference model structure used in conventional MCS).

7.6.1 Improvement of the Technique

As detailed above, three methods of altering the standard MCS algorithm to better suit the substructuring set-up have been proposed. The are:

- MCS with additional adaptive gain, MCSE
- Alternative MCS Substructuring control, AltMCS
- MCS with modified demand, MCSmd

The undesirable behaviour experienced when using a standard MCS scheme was not observed in any of these three systems, however overall only the latter two resulted in more accurate reproduction of the emulated system dynamics throughout the entire experiment when compared to the original MCS substructuring controller. Further, due to their structures, the stability of the AltMCS and MCSmd algorithm can be analysed in a similar manner to that of the standard MCS algorithm when used as a normal controller. This would indicate global asymptotic stability during operation and should be investigated.

Further work has already begun investigating the use of the MCSmd algorithm on structures with more than one degree-of-freedom. Presence of non-linearities within either or both of the numerical and physical substructures is also a current topic of investigation.

For wider adoption, the substructuring technique would benefit from use in applications that possess a higher bandwidth. These could include the machining applications mentioned in chapter 6, as well as studies including electric systems, e.g. electric motors, batteries, etc.. Actuator and transducer bandwidths as well as processor speed and analogue-to-digital, digital-to-analogue conversion times impose the limits on the highest frequency of an emulated system that can be successfully reproduced using substructuring. Use of novel actuation mechanisms, such as piezo-based actuators coupled with higher speed processors will open the doors for substructuring to these higher frequency applications.

References

[1] N. R. Augustine. *Augustine's laws*, pages 104–115. American Institute of Aeronautics and Astronautics, 6th edition, 1997.

[2] AECMA. Facts and Figures 2002. AECMA, Gulledelle 94-b.5,B-1200, Brussels, Belgium, September 2003.

[3] Michael Leasure. Aviation education multimedia library. Internet: http://www.tech.purdue.edu/at/courses/AEML/index.html, 2005.

[4] D. K. Y. Low, L. Li, and P. J. Byrd. Spatter prevention during the laser drilling of selected aerospace materials. *Journal of Materials Processing Technology*, 139:71–76, August 2003.

[5] I. E. Bottomley. Superplastic forming and diffusion bonding of aircraft structures. *Proceedings of the I Mech E, Part G - Journal of Aerospace Engineering*, 209(3):227–231, 1995.

[6] D. D. DiBitonto, P. T. Eubank, M. R. Patel, and M. A. Barrufet. Theoretical models of the discharge machining process I: A simple cathode erosion model. *Journal of Applied Physics*, 66(9):4095–4103, November 1989.

[7] Y. Koren. Control of machine tools. *Journal of Manufacturing Science and Engineering, Transactions of the ASME*, 119:749–755, November 1997.

[8] D. P. Stoten and H. Benchoubane. Empirical studies of an MRAC algorithm with minimal controller synthesis. *International Journal of Control*, 51(4):823–849, 1990.

[9] T. Williams, R. Maull, and B. Ellis. Strategic drivers in the aerospace industry. Technical report, University of Exeter, School of Business and Economics, 2000.

[10] Department For Transport. The future of air transport - White Paper - Annex A - Air travel forecasts. Report, 2003.

[11] Unknown. The super-jumbo of all gambles. *The Economist*, January 2005.

[12] M. Green. Highlights of recent laser materials processing activities. EULASNET, 7th International Meeting, November 2004.

[13] C. Y. Yeo, C. S. Tam, S. Jana, and M.W.S. Lau. A technical review of the laser drilling of aerospace materials. *Journal of Materials Processing Technology*, 42(1):15–49, April 1994.

[14] C. A. McNally, J. Folkes, and I. R. Pashby. Laser drilling of cooling holes in aero-engines: State of the art and future challenges. *Materials, Science and Technology*, 20(7):805–813, July 2004.

[15] B. S. Yilbas. Study of affecting parameters in laser hole drilling of sheet metals. *Journal of Engineering Materials and Technology, Transactions of the ASME*, 109(4):282–287, October 1987.

[16] B. S. Yilbas. Parametric study to improve laser hole drilling process. *Journal of Materials Processing Technology*, 70(1–3):264–273, October 1997.

[17] D. K. Y. Low and Li L. Comparison of intra- and inter-pulse modulation in laser percussion drilling. *Proceedings of the I Mech E, Part B - Journal of Engineering Manufacture*, 216(2):167–171, 2002.

[18] W. K. Hamoudi and B. G. Rasheed. Parameters affecting Nd:YAG laser drilling of metals. *International Journal for the Joining of Materials*, 7:63–69, 1995.

[19] S. Murphy. Laser drilling: Capabilities and trends. *Lasers and Applications*, 6(3):59–62, March 1987.

[20] S. Bandyopadhyay, J. K. Sarin Sundar, G. Sundararajan, and S. V. Joshi. Geometrical features and metallurigcal characterisitcs of Nd:YAG laser drilled holes in thick IN718 and Ti-6Al-4V sheets. *Journal of Materials Processing Technology*, 127(1):83–95, September 2002.

[21] S. O. Roos. Laser drilling with different pulse shapes. *Journal of Applied Physics*, 51(9):5061–5063, September 1980.

[22] K. T. Voisey, S. S. Kudesia, W. S. O. Rodden, D. P. Hand, J. D. C. Jones, and T. W. Clyne. Melt ejection during laser drilling of metals. *Materials Science and Enigneering A (Structural Materials: Properties, Microstructure and Processing)*, A356(1-2):414–424, September 2003.

[23] D. K. Y. Low, L. Li, and A. G. Corfe. The influence of assist gas on the mechanism of material ejection and removal during laser percussion drilling. *Proceedings of the I Mech E, Part B - Journal of Engineering Manufacture*, 214(7):521–527, 2000.

[24] A. Corcoran, L. Sexton, B. Seaman, P. Ryan, and G. Byrne. The laser drilling of multi-layer aerospace material systems. *Journal of Materials Processing Technology*, 123(1):100–106, April 2003.

[25] A. Sunwoo and R. Lum. Superplastic deformation enhanced diffusion bonding of aluminium 7475. *Scripta Metallurgica et Materialia*, 33(4):639–644, August 1995.

[26] R. Grimes. Superplastic forming: Evolution from metallurgical curiosity to major manufacturing tool? *Materials and Science Technology*, 19(1):3–20, January 2003.

[27] S. N. Patankar and T. M. Jen. "Superplastic forming" of commercial purity aluminium. *Scripta Materialia*, 38(1):145–148, December 1998.

[28] L P. Troeger and E. A. Starke. New process produces superplastic aerospace/automotive aluminium alloy. *Advanced Engineering Materials*, 2(12):802–806, 2000.

[29] X. J. Zhu, M. J. Tan, and W. Zhou. Enhanced superplasticity in commercially pure titanium alloy. *Scripta Materialia*, 52(7):651–655, April 2005.

[30] P. K. D. V. Yarlagadda, P. Gudimetla, and C. Adam. Finite element analysis of high strain rate superplastic forming (SPF) of Al-Ti alloys. *Journal of Materials Processing Technology*, 130-131:469–476, December 2002.

[31] G. A. Salishchev, R. M. Galeyev, O. R. Valiakhmetov, R. V. Safiullin, R. Y. Lutfullin, O. N. Senkov, F. H. Froes, and O. A. Kaibyshev. Development of Ti-6Al-4V sheet with with temperature superplastic properties. *Journal of Materials Processing Technology*, 116(2–3):265–268, October 2001.

[32] P. N. Comley. Manufacturing advantages of superplastically formed fine-grain Ti-6Al-4V alloy. *Journal of Materials Engineering and Performance*, 13(6):660–664, December 2004.

[33] L. D. Hefti. Advances in fabricating superplastically formed and diffusion bonded components for aerospace structures. *Journal of Materials Engineering and Performance*, 13(6):678–682, December 2004.

[34] Y. W. Xun and M. J. Tan. Applications of superplastic forming and diffusion bonding to hollow engine blades. *Journal of Materials Processing Technology*, 99(1):80–85, March 2000.

[35] L. Hefti. Advances in manufacturing superplastically formed and diffusion bonded components. In *Materials Science Forum*, volume 447-448 of *Superplasticity in Advanced Materials: 8th International Conference on Superplasticity in Advanced Materials, ICSAM 2003*, pages 177–182. Trans Tech Publications Ltd, Zurich-Ueticon, Switzerland, 2004.

[36] S. Lee. Thickness distribution in a superplastically formed rectangular pan under plane-strain conditions. *Journal of Materials Processing Technology*, 65(1–3):59–64, March 1997.

[37] D Garriga-Majo. Geometric analysis of thinning during superplastic forming. In *Materials Science Forum*, volume 357–359 of *Superplasticity in Advanced Materials: 8th International Conference on Superplasticity in Advanced Materials, ICSAM 2003*, pages 213–218. Trans Tech Publications Ltd, Zurich-Ueticon, Switzerland, 2000.

[38] K. S. Lee and L. Huh. Numerical simulation of the superplastic moving die forming process with a modified membrane finite element method. *Journal of Materials Processing Technology*, 113(1–3):754–760, June 2001.

[39] A. Huang, A. Lowe, and M. J. Cardew-Hall. Experimental validation of sheet thickness optimisation for superplastic forming of engineering structure. *Journal of Materials Processing Technology*, 112(1):136–143, May 2001.

[40] Y. H. Kim, J. Lee, and S. S. Hong. Optimal design of superplastic forming processes. *Journal of Materials Processing Technology*, 112(2–3):166–173, May 2001.

[41] K. F. Zhang, G. F. Wang, D. Z. Wu, and Z. R. Wang. Research on the controlling of the thickness distribution in superplastic forming. *Journal of Materials Processing Technology*, 151(1–3):54–57, September 2004.

[42] K. S. Lee and H. Huh. Simulation of superplastic forming/diffusion bonding with finite-element analysis using the convective coordinate system. *Journal of Materials Processing Technology*, 89-90:92–98, May 1999.

[43] A. Magurra, K. Ostolaza, and J.L. Alcaraz. Validation of In718 SPF and DB processes for the design of aircraft engine parts. *Journal of Materials Processing Technology*, 125-126:549–554, September 2002.

[44] L. Carrino, G. Giuliano, and C. Palmieri. On the optimisation of superplastic forming processes by the finite-element method. *Journal of Materials Processing Technology*, 143-144:373–377, December 2003.

[45] H. L. Xing, C. W. Wang, K. F. Zhang, and Z. R. Wang. Recent developments in the mechanics of superplasticity and its applications. *Journal of Materials Processing Technology*, 151(1–3):196–202, September 2004.

[46] Y. Kaneko, H. Yamada, T. Toyonaga, and K. Shoda. Performance of linear motor equipped die-sinking EDM. *International Journal of Electrical Machining*, 5:59–64, 2000.

[47] S. Cetin, A. Okada, and Y Uno. Electrode jump motion in linear motor equipped die-sinking EDM. *Journal of Manufacturing Science and Engineering, Transactions of the ASME*, 125(4):809–815, November 2003.

[48] M. R. Patel, M. A. Barrufet, P. T. Eubank, and D. D. DiBitonto. Theoretical models of the electrical discharge machining process II: The anode erosion model. *Journal of Applied Physics*, 66(9):4104–4111, November 1989.

[49] A. Singh and A. Ghosh. A thermo-electric model of material removal during electric discharge machining. *International Journal of Machine Tools and Manufacture*, 39:669–682, 1999.

[50] U. C. Tricarico, E. R. Delpretti, and D.F. Dauw. Geometrical simulation of the EDM die-sinking process. *Annals of the CIRP*, 37(1):191–196, 1988.

[51] Y. Zhao, X. Zhang, X. Liu, and K. Yamazaki. Geometric modelling of the linear motor driven electrical discharge maching (EDM) die-sinking process. *International Journal of Machine Tools and Manufacture*, 44:1–9, 2004.

[52] M. Kunieda and M. Kiyohara. Simulation of die-sinking EDM by discharge location searching algorithm. *International Journal of Electrical Machining*, 3:79–85, 1998.

[53] I. Puertas and C. J. Luis. A study on the machining parameters optimisation of electrical discharge machining. *Journal of Materials Processing Technology*, 143–144:521–526, December 2003.

[54] J. Qu, A. J. Shih, and R. O. Scattergood. Development of the cylindrical wire electrical discharge machining process, Part 1: Concept, design, and material removal rate. *Journal of Manufacturing Science and Engineering, Transactions of the ASME*, 124(3):702–707, August 2002.

[55] J. Qu, A. J. Shih, and R. O. Scattergood. Development of the cylindrical wire electrical discharge machining process, Part 2: Surface integrity and roundness. *Journal of Manufacturing Science and Engineering, Transactions of the ASME*, 124(3):708–714, August 2002.

[56] Y. S. Tarng, S. C. Ma, and L. K. Chung. Determination of optimal cutting parameters in wire electrical discharge machining. *International Journal of Machine Tools and Manufacture*, 35(12):1693–1701, 1995.

[57] I. Beltrami, A. Bertholds, and D. Dauw. A simplified post process for wire cut EDM. *Journal of Materials Processing Technology*, 58(4):385–389, April 1996.

[58] Y. S. Liao, J. T. Huang, and H. C. Su. A study on the machining parameters optimization of wire electrical discharge machining. *Journal of Materials Processing Technology*, 71(3):487–493, November 1997.

[59] A.B. Puri and B. Battacharyya. An analysis and optimisation of the geometrical inaccuracy due to wire lag phenomenon in WEDM. *International Journal of Machine Tools and Manufacture*, 43(2):151–159, 2003.

[60] N. Kinoshita, M. Fukui, and Y. Kimura. Study on wire-EDM: inprocess measurement of mechanical behaviour of electrode-wire. *Annals of the CIRP*, 33(1):89–92, 1984.

[61] D. F. Dauw and I. Beltrami. High-precision wire-EDM by on-line wire positioning control. *Annals of the CIRP*, 43(1):193–197, 1994.

[62] S. M. Shahruz. Vibration of wires used in electro-discharge machining (EDM). In *Proceedings of the IEEE Conference on Decision and Control*, volume 1, pages 815–820. IEEE, 2003.

[63] A. B. Puri and B. Bhattacharyya. Modelling and analysis of the wire-tool vibration in wire-cut EDM. *Journal of Materials Processing Technology*, 141:295–301, November 2003.

[64] M. T. Yan and P. H. Huang. Accuracy improvement of wire-EDM by real-time wire tension control. *International Journal of Machine Tools and Manufacture*, 44:807–814, 2004.

[65] N. Kinoshita, M. Fului, and G. Gamo. Control of wire-EDM preventing electrode from breaking. *Annals of the CIRP*, 31(1):111–114, 1982.

[66] K.P. Rajurkar, W. M. Wang, and R. P. Lindsay. On-line monitor and control for wire breakage in WEDM. *Annals of the CIRP*, 40(1):219–222, 1991.

[67] Y. S. Liao, Y. Y. Chu, and M. T. Yan. Study of wire breaking and monitoring of WEDM. *International Journal of Machine Tools and Manufacture*, 37(4):555–567, 1997.

[68] Y. F. Luo. Rupture failure and mechanical strength of the electrode wire used in wire EDM. *Journal of Materials Processing Technology*, 94(2–3):208–215, September 1999.

[69] K. P. Rajurkar, W. M. Wang, and W. S Zhao. WEDM-adaptive control with a multiple input model for identification of work-piece height. *Annals of the CIRP*, 46(1):147–150, 1997.

[70] K. P. Rajurkar, W. M. Wang, and J. A. McGeough. WEDM indentification and adaptive control for variable-height components. *Annals of the CIRP*, 43(1):199–202, 1994.

[71] M. T. Yan and Y. S. Liao. A self-learning fuzzy controller for wire rupture prevention in WEDM. *International Journal of Advanced Manufacturing Technology*, 11(4):267–275, 1996.

[72] M Kunieda and C. Fududate. High precision finish cutting by dry WEDM. *Annals of the CIRP*, 50(1):121–124, 2001.

[73] T. Wang, Y. Chen, and M. Kunieda. Study on wire-cut electrical discharge machining in gas. *Jixie Gongcheng Xuebao*, 39(8):76–80, 2003.

[74] Z. N. Guo, T. C. Lee, T. M. Yue, and W. S. Lau. Study on the machining mechanism of WEDM with ultrasonic vibration of the wire. *Journal of Materials Processing Technology*, 69(1–3):212–221, September 1997.

[75] D. Kremer and C. Lhiabet. A study on the effect of synchronizing ultrasonic vibrations with pulses in EDM. *Annals of the CIRP*, 40(1):211–214, 1991.

[76] D. Kremer, J.L. Lebrun, B. Hosari, and A. Mosan. Effect of ultrasonic vibrations on the performances in EDM. *Annals of the CIRP*, 38(1):199–202, 1989.

[77] V. S. Murti and P. K. Philip. A comparative analysis of machining characteristics in ultrasonic assisted EDM by the response surface methodology. *International Journal of Production Research*, 25:259–272, 1987.

[78] C. J. Luis, I. Puertas, and G. Villa. Material removal rate and electrode wear study on the EDM of silicon carbide. *Journal of Materials Processing Technology*, 164-165:889–896, May 2005.

[79] I. Puertas, C. J. Luis, and L. Alvarez. Analysis of the influence of EDM parameters on surface quality, MRR and EW of WC-Co. *Journal of Materials Processing Technology*, 153-154(1–3):1026–1032, November 2004.

[80] J. A. Sanchez, I Cabanes, L. N. Lopez de Lacalle, and A. Lamikiz. Development of optimum electrodischarge machining technology for advanced ceramics. *International Journal of Advanced Manufacturing Technology*, 18(12):897–905, 2001.

[81] Y. K. Lok and T. C. Lee. Processing of advanced ceramics using the wire-cut EDM process. *Journal of Materials Processing Technology*, 63(1–3):839–843, January 1997.

[82] D. F. Dauw, C. A. Brown, and J. P. Van. Surface topography investigations by fractal analysis of spark-eroded, electrically conductive ceramics. *Annals of the CIRP*, 39(1):161–165, 1990.

[83] N. Mohri, Y. Fukuzawa, T. Tani, and T. Sata. Some considerations to machining characterisitcs of insulating ceramics – towards practical use in industry. *Annals of the CIRP*, 51(1):161–164, 2002.

[84] N. Mohri, Y. Fukuzawa, T. Tani, N. Saito, and K. Furutani. Assisting electrode method for machining insulating ceramics. *Annals of the CIRP*, 45(1):201–204, 1996.

[85] John Wyatt. High performance machining historical and theoretical overview. IGDS Seminar - "High Performance Machining Historical and Theoretical Overview"- University of the West of England, 1999.

[86] S. Smith and J. Tlusty. Current trends in high-speed machining. *Journal of Manufacturing Science and Engineering, Transactions of the ASME*, 119(4(B)):664–667, November 1997.

[87] N. Tounsi and E. Elbestawi. Optimized feed scheduling in three axes machining. Part I: Fundamentals of the optimized feed scheduling strategy. *Journal of Machine Tools and Manufacture*, 43:253–267, 2003.

[88] A. Gashempoor, J. Jeswiet, and T. N. Moore. Automatic adjustment of cutting conditions in rough turning. *Proceedings of the I Mech E, Part B - Journal of Engineering Manufacture*, 217:1393–1400, 2003.

[89] J. H. Ko, W. S. Yun, and D.-W. Cho. Offline feed rate scheduling using virtual CNC based on an evaluation of cutting performance. *Computer-Aided Design*, 35:383–393, 2003.

[90] K. Hashmi, M. A. El Baradie, and M. Ryan. Fuzzy-logic based intelligent selection of machining parameters. *Journal of Materials Processing Technology*, 94:94–111, 1999.

[91] M. Tolouei-Rad and I. M. Bidhendi. On the optimization of machining parameters for milling operations. *International Journal of Machine Tools and Manufacture*, 37(1):1–16, 1997.

[92] T. Watanabe and S. Iwai. A control system to improve the accuracy of finished surfaces in milling. *Journal of Dynamic Systems, Measurement and Control, Transactions of the ASME*, 105(1):192–199, September 1993.

[93] M.-Y. Yang, T.-M. Lee, and J.-G. Choi. A new spindle current regulation algorithm for the CNC end milling process. *International Journal of Advanced Manufacturing Technology*, 19:473–481, 2002.

[94] K. D. Kim, M. S. Kim, and S. C. Chung. Real-time compensatory control of thermal errors for high-speed machine tools. *Proceedings of the I Mech E, Part B - Journal of Engineering Manufacture*, 218(8):913–924, August 2004.

[95] R. Ramesh, M. Mannan, and A. N. Poo. Error compensation in machine tools – A review – Part II: Thermal errors. *International Journal of Machine Tools and Manufacture*, 40:1257–1284, 2000.

[96] R. Ramesh, M. Mannan, and A. N. Poo. Error compensation in machine tools – A review – Part I: Geometric, cutting-force induced and fixture-dependent errors. *International Journal of Machine Tools and Manufacture*, 40:1235–1256, 2000.

[97] E. S. Lee, S. H. Suh, and J. W. Shoh. A comprehensive method for calibration of volumetric positioning accuracy on CNC machines. *International Journal of Advanced Manufacturing Technology*, 14:43–49, 1998.

[98] J. Ni and S. M. Wu. An on-line measurement technique for machine volumetric error compensation. *Journal of Manufacturing Science and Engineering, Transactions of the ASME*, 115(1):85–92, February 1993.

[99] J. S. Chen, J. S. Yuan, J. Ni, and S. W. Wu. Real-time compensation for time-variant volumetric errors on a machine center. *Journal of Engineering for Industry, Transactions of the ASME*, 115(4):472–479, November 1993.

[100] A. C. Okafor and Y. M. Ertekin. Derivation of machine tool error models and error compensation procedure for three axes vertical machining center using rigid body kinematics. *International Journal of Machine Tools and Manufacture*, 40:1199–1213, 2000.

[101] B. T. Eman, B.T. Wu, and M. F. DeVries. A generalized geometric error model for multi-axis machines. *Annals of the CIRP*, 36(1):253–256, 1987.

[102] J Denavit and R. S. Hartenberg. A kinematic notation for lower-pair mechanisms based on matrices. *Journal of Applied Mechanics, Transactions of the ASME*, 22(2):215–221, 1955.

[103] A. K. Srivastava, S. C. Veldhuis, and M. A. Elbastawit. Modelling geometrical and thermal errors in a five-axis CNC machine tool. *International Journal of Machine Tools and Manufacture*, 35(9):1321–1337, 1995.

[104] V. Kiridena and P. M. Ferreira. Mapping the effects of positioning errors on the volumetric accuracy of five-axis CNC machine tools. *International Journal of Machine Tools and Manufacture*, 33(3):417–437, 1993.

[105] J. Mou. A systematic approach to enhance machine tool accuracy for precision manufacturing. *International Journal of Machine Tools and Manufacture*, 37(5):669–685, 1997.

[106] J. Mou and C. R. Liu. An adaptive methodology for machine tool errors correction. *Journal of Engineering for Industry, Transactions of the ASME*, 117(3):389–399, August 1995.

[107] W. T. Lei and Y. Y. Hsu. Accuracy enhancement of five-axis CNC machines through real-time error compensation. *International Journal of Machine Tools and Manufacture*, 43:871–877, 2003.

[108] W. T. Lei and Y. Y. Hsu. Error measurement of five-axis CNC machines with 3D probeball. *Journal of Materials Processing Technology*, 139:127–133, 2003.

[109] W. T. Lei and Y. Y. Hsu. Accuracy test of five-axis CNC machine tool with 3D probeball. Part I: Design and modeling. *International Journal of Machine Tools and Manufacture*, 42:1153–1162, 2002.

[110] W. T. Lei and Y. Y. Hsu. Accuracy test of five-axis CNC machine tool with 3D probeball. Part II: Errors estimation. *International Journal of Machine Tools and Manufacture*, 42:1163–1170, 2002.

[111] J. Yuan and J. Ni. The real-time error compensation technique for CNC machining systems. *Mechatronics*, 8(4):359–380, June 1998.

[112] J. Jedrzejewski, J. Kaczmarek, Z. Kowal, and Z. Winiarski. Numerical optimisation of thermal behaviour of machine tools. *Annals of the CIRP*, 39(1):379–382, 1990.

[113] S. K. Kim and D. W. Cho. Real-time estimation of temperature distribution in a ball-screw system. *International Journal of Machine Tools and Manufacture*, 37(4):451–464, 1997.

[114] J. S. Chen. Fast calibration and modelling of thermally induced machine tool errors in real machining. *International Journal of Machine Tools and Manufacture*, 37(2):159–169, 1997.

[115] J. Mou. A method of using neural networks and inverse kinematics for machine tool error estimation and correction. *Journal of Manufacturing Science and Engineering, Transactions of the ASME*, 119(2):247–254, May 1997.

[116] C. Raksiri and M. Parnichkun. Geometric and force errors compensation in a 3-axis CNC milling machine. *International Journal of Machine Tools and Manufacture*, 44:1283–1291, 2004.

[117] A. Ouafi, M. Guillot, and A. Bedrouni. Accuracy enhancement of multi-axis CNC machines through on-line neurocompensation. *Journal of Intelligent Manufacturing*, 11(6):535–545, December 2000.

[118] Z. Lechniak, A. Werner, K. Skalski, and K. Kedzior. Methodology of off-line software compensation for errors in the machining process in the CNC machine tool. *Journal of Materials Processing Technology*, 76(1–3):42–48, April 1998.

[119] S. Bjrklund, P. Bjurstam, and A. Novak. Compensation of systematic errors in five-axis high speed machining. *International Journal of Production Research*, 40(15):3765–3778, 2002.

[120] D. Renton and M. A. Elbestawi. High-speed servo control of multi-axis machine tools. *International Journal of Machine Tools and Manufacture*, 40:539–559, 2000.

[121] M. Tomizuka. Zero phase error tracking algorithm for digital control. *Journal of Dynamic Systems, Measurement and Control, Transactions of the ASME*, 90(1):65–68, March 1987.

[122] Y. Koren and C. C. Lo. Advanced controllers for feed drive systems. *Journal of Dynamic Systems, Measurement and Control, Transactions of the ASME*, 102:265–272, 1992.

[123] S. S. Yeh and P. L. Hsu. An optimal and adaptive design of the feedforward motion controller. *IEEE/ASME Transactions on Mechatronics*, 4(4):428–439, December 1999.

[124] T. T. C. Tsang and D. W. Clarke. Generalised predictive control with input constraints. In *IEEE Proceedings*, volume 135 of *6*, pages 451–460, 1988.

[125] D. M. Alter and T. C. Tsao. Optimal feed-forward tracking control of linear motors for machine tool drives. In *Proceedings of the Americal Control Conference*, volume 1, pages 210–214, June 1995.

[126] C. Choi, T.-C. Tsao, and A. Matsubara. Control of linear motor machine tool feed drives for end milling: Robust MIMO approach. In *Proceedings of the American Control Conference*, pages 3723–3727. San Diego, California, USA, June 1999.

[127] D. Renton and M. A. Elbestawi. Motion control for linear motor feed drives in advanced machine tools. *International Journal of Machine Tools and Manufacture*, 41:479–501, 2001.

[128] H. Van Brussel, C.-H. Chen, and J. Swevers. Accurate motion controller design based on an extended pole placement method and a disturbance observer. *Annals of the CIRP*, 43(1):69–72, 1994.

[129] T. Umeno and Y. Hori. Robust speed control of DC servomotors using modern two degrees-of-freedom controller design. *IEEE Transactions on Industrial Electronics*, 38(5):363–368, 1991.

[130] K. Erkorkmaz and Y. Altintas. High speed CNC system design. Part III: High speed tracking and contouring control of feed drives. *International Journal of Machine Tools and Manufacture*, 41:1637–1658, 2001.

[131] A. T. Elfizy, G. M. Bone, and M. A. Elbestawi. Model-based controller design for machine tool direct feed drives. *International Journal of Machine Tools and Manufacture*, 44:465–477, 2004.

[132] S. Jee and Y. Koren. Adaptive fuzzy logic controller for feed drives of a CNC machine tool. *Mechatronics*, 14:299–326, 2004.

[133] Y. Koren. Cross-coupled bi-axial computer control for manufacturing systems. *Journal of Dynamic Systems, Measurement and Control, Transactions of the ASME*, 102(4):265–272, 1980.

[134] P. K. Kulkarni and K. Srinivasan. Optimal contouring of multi-axial feed drive mechanisms. *Journal of Dynamic Systems, Measurement and Control, Transactions of the ASME*, 111(2):140–148, 1989.

[135] K. Erkorkmaz and Y. Altintas. High-speed contouring control for CNC machine tool. In *Proceedings of the ASME Dynamic Systems and Control Division*, volume DSC 64, pages 463–469. 1998 ASME International Mechanical Engineering Congress and Exposition, 1998.

[136] Y. Altintas, K. Erkorkmaz, and W.-H. Zhu. Sliding mode controller design for high speed drives. *Annals of the CIRP*, 49(1):265–270, 2000.

[137] M. Tomizuka. Robust digital motion controllers for mechanical systems. *Robotics and Autonomous Systems*, 19:143–149, 2000.

[138] C. Lo. Real-time generation and control of cutter path for 5-axis CNC machining. *International Journal of Machine Tools and Manufacture*, 39:471–488, 1999.

[139] K. Nakazawa. Improvement of adaptive control of milling machine by non-contact cutting force detector. *Proceedings of the 16th International Machine Tool Design and Research Conference*, pages 109–116, 1975.

[140] R. Bedini, G. G. Lisini, and P. C. Pinotti. Experiments on adaptive control of a milling machine. *Journal of engineering for Industry, Transactions of the ASME*, 98(1):239–245, February 1976.

[141] J. Tlusty and M. A. A. Elbestawi. Analysis of transients in an adaptive control servomechanism for milling with constant force. *Journal of Engineering for Industry, Transactions of the ASME*, 99(3):766–772, August 1977.

[142] O. Masory and Y. Koren. Adative control system for turning. *Annals of the CIRP*, 29(1):281–284, 1980.

[143] A. G. Ulsoy, Y. Koren, and F. Rasmussen. Principal developments in the adaptive control of machine tools. *Journal of Dynamic Systems, Measurement and Control, Transactions of the ASME*, 105:107–112, June 1983.

[144] L. K. Lauderbaugh and A. G. Ulsoy. Dynamic modelling for control of the milling process. *Journal of Engineering for Industry, Transactions of the ASME*, 110:367–375, November 1988.

[145] G. Stute and F. R. Goetz. Adaptive control system for variable gain in ACC systems. In *Proceedings of the 16th International Machine Tool Design and Research Conference*, pages 117–121, 1975.

[146] M. Tomizuka and S. Zhang. Modelling and conventional control/adaptive PI control of a lathe cutting process. *Journal of Dynamic Systems, Measurement and Control, Transactions of the ASME*, 110(4):350–354, Decemeber 1988.

[147] M. Tomizuka, J.-H. Oh, and D. Dornfield. Model reference adaptive control of the milling process. In *Control of Manufacturing Processes and Robotic Systems*, pages 55–63, 1983.

[148] L.K. Danesshmend and H. A. Pak. Model reference adaptive control of feed force in turning. *Journal of Dynamic Systems, Measurement and Control, Transactions of the ASME*, 108(3):215–222, September 1986.

[149] L. K. Lauderbaugh and A. G. Ulsoy. Model reference adaptive force control in milling. *Journal of Engineering for Industry, Transactions of the ASME*, 111(1):13–21, February 1989.

[150] Y. Koren. Adaptive control systems for machining. *Manufacturing Review*, 2(1):6–15, March 1989.

[151] S. J. Rober and Y. C. Shin. Control of cutting force for end milling processes using an extended model reference adaptive control scheme. *Journal of Manufacturing Science and Engineering, Transactions of the ASME*, 118(3):339–347, August 1996.

[152] J. W. Barthel and Y. C. Shin. Adaptive control of non-minimum phase processes with application to the end milling processes. In *Proceedings of the American Control Conference, San Francisco, USA*, pages 2449–2454, 1993.

[153] S. J. Huang and Y. W. Lin. Application of a grey predictor and fuzzy speed regulator in controlling a retrofitted machining table. *International Journal of Machine Tools and Manufacture*, 36(4):477–489, April 1996.

[154] T. Luo, W. Lu, K. Krishnamurthy, and B. McMillin. Neural network approach for force and contour error control in multi-dimensional end milling operations. *International Journal of Machine Tools and Manufacture*, 38(10-11):1343–1359, 1998.

[155] M. Liang, T. Yeap, S. Rahmati, and Z. Han. Fuzzy control of spindle power in end milling processes. *International Journal of Machine Tools and Manufacture*, 42:1487–1496, 2002.

[156] R. G. Landers and A. G. Ulsoy. Model-based machining force control. *Journal of Dynamic Systems, Measurement and Control, Transactions of the ASME*, 122:521–527, September 2000.

[157] M. A. Elbestawi and R. Sagherian. Parameter adaptive control in peripheral milling. *International Journal of Mahcine Tools and Manufacture*, 27(3):399–414, 1987.

[158] R. G. Landers, A. G. Ulsoy, and Y.-H. Ma. A comparison of model-based machining force control approaches. *International Journal of Machine Tools and Manufacture*, 44:733–748, 2004.

[159] K. Warwirck, G. W. Irwin, and K. J. Hunt. *Neural networks for control and systems*, volume 46 of *IEE control engineering series*. Peregrinus, on behalf of the Institution of Electrical Engineers, 1992.

[160] S. J. Huang and C. Y. Shy. Intelligent control for handling motion non-linearity in a retro-fitted machining table. *IEE Proceedings: Control Theory and Applications*, 145(4):403–408, 1998.

[161] L. Zuo, T. Cheng, J. Zuo, Y. Liu, and S. Yang. Hierarchical intelligent control system for milling machine. *Proceedings of the IEEE International Conference on Intelligent Processing Systems*, 1:813–817, 1998.

[162] I. D. Landau. A survey of model reference adaptive techniques, theory and applications. *Automatica*, 10:353–379, 1974.

[163] I. D. Landau. *Adaptive control: The model reference approach*. Marcel Dekker, 1979.

[164] D. P. Stoten and H. Benchoubane. Robustness of a minimal controller synthesis algorithm. *International Journal of Control*, 51(4):851–861, 1990.

[165] H. Benchoubane and D.P. Stoten. The decentralised minimal controller synthesis algorithm. *International Journal of Control*, 56(4):967–983, 1992.

[166] S.P. Hodgson and D.P. Stoten. Passivity-based analysis of the minimal control synthesis algorithm. *International Journal of Control*, 69(5):633-646, 1998.

[167] E. Gomez Gomez. *Application of the MCS algorithm to the control system of the bristol shaking table.* PhD thesis, University of Bristol, UK, 1999.

[168] M. DiBernado. *Adaptive control and analysis of nonlinear chaotic dynamical systems.* PhD thesis, Univeristy of Bristol, UK, 1998.

[169] D. P. Stoten. An overview of the minimal control synthesis algorithm. Technical report, Institute of Mechanical Engineers Conference on Aerospace Hydraulics and Systems, London, 1993.

[170] H. Ernst and M. E. Merchant. Chip formation, friction and high quality machined surfaces. *American Society of Metals, Surface Treatment of Metals*, 29:299–336, 1941.

[171] M. E. Merchant. Basic mechanics of the metal cutting process. *Journal of Applied Mechanics, Transactions of the ASME*, 11:A168–A175, 1944.

[172] M. E. Merchant. Mechanics of the cutting process I: Orthogonal cutting and a type 2 chip. *Journal of Applied Physics*, 16(5):267–275, May 1945.

[173] M. E. Merchant. Mechanics of the metal cutting process II: Plasticity conditions in orthogonal cutting. *Journal of Applied Physics*, 16(6):318–324, 1945.

[174] E. H. Lee and B. W. Shaffer. The theory of plasticity applied to a problem of machining. *Journal of Applied Mechanics, Transactions of the ASME*, 73:405–413, 1951.

[175] W. B. Palmer and P. L. B. Oxley. Mechanics of orthogonal machining. *Proceedings of the Institute of Mechanical Engineers*, 173(24):623–639, 1959.

[176] R.G. Fenton and P. L. B. Oxley. Mechanics of orthogonal machining: Prediction of chip geometry and cutting forces from work-material properties and cutting conditions. *Proceedings of the I Mech E, Part 1*, pages 927–942, 1969.

[177] W. F. Hastings, P. Mathew, and P. L. B. Oxley. A machining theory for predicting chip geometry, cutting forces, etc. from work material properties and cutting conditions. *Proceedings of the Royal Society of London, Series A (Mathematical and Physical Sciences)*, 371(1747):569–587, August 1980.

[178] O. W. Boston and C. E. Kraus. The elements of milling. *Transactions of the ASME*, 54:71–104, 1932.

[179] O. W. Boston and C. E. Kraus. The elements of milling, Part 2. *Transactions of the ASME*, 56:355–371, 1934.

[180] M. E. Martellotti. An analysis of the milling process. *Transactions of the ASME*, 63:677–701, November 1941.

[181] M. E. Martellotti. An analysis of the milling process, Part II - down milling. *Transactions of the ASME*, 67:233–251, May 1945.

[182] J. Tlusty and P. MacNiel. Dynamics of cutting forces in end milling. *Annals of the CIRP*, 24(1):21–25, 1975.

[183] W. A. Kline and R. E. DeVor. The effect of run-out on cutting geometry and forces in end milling. *International Journal of Machine Tool Design and Research*, 23(2–3):123–140, 1983.

[184] J. W. Sutherland and R. E. DeVor. An improved method for cutting force and surface error prediction in flexible end milling systems. *Journal of Engineering for Industry, Transactions of the ASME*, 108(4):269–279, November 1986.

[185] F. M. Kolarits and W. R. DeVries. Mechanistic dynamic model of end milling for process controller simulation. *Journal of Engineering for Industry, Transactions of the ASME*, 113(2):176–183, May 1991.

[186] S. Smith and J. Tlusty. An overview of modelling and simulation of the milling process. *Journal of Engineering for Industry, Transactions of the ASME*, 113(2):169–175, May 1991.

[187] Y. Altintas, D. Montgomery, and E. Budak. Dynamic peripheral milling of flexible structures. *Journal of Engineering for Industry, Transactions of the ASME*, 114(2):137–145, May 1992.

[188] F. Ismail, M.A. Elbestawi, R. Du, and K. Urbasik. Generation of milled surfaces including tool dynamics and wear. *Journal of Engineering for Industry, Transactions of the ASME*, 115(3):245–252, August 1993.

[189] Y. Altintas and P. Lee. A general mechanics and dynamics model for helical end mills. *Annals of the CIRP*, 1996.

[190] A. J. L. Harrison and D.P. Stoten. Generalised finite difference methods for optimal estimation of derivatives in real-time control problems. *Proceedings of the I Mech E, Part I - Journal of Systems and Control Engineering*, 209(2):67–78, 1995.

[191] K. Takanashi and M. Nakashima. Japanese activities on online testing. *Journal of Engineering Mechanics*, 113(7):1014–1032, July 1987.

[192] H. Zhang, S. Ming, and S. Weng. Hardware-in-the-loop simulation study on the fuel control strategy of a gas turbine engine. *Journal of Engineering for Gas Turbines and Power*, 127(3):693–695, May 2005.

[193] G. Stoeppler, T. Menzel, and S Douglas. Hardware-in-the-loop simulation of machine tools and manufacturing systems. *IEE Computing and Control Engineering*, 16(1):10–15, 2005.

[194] S. W. K. Chan and J. R. Davidson. Development of a hardware in the loop engine simulation facility. *AIAA Paper*, 1985.

[195] K. L. Hall. What is hardware in the loop simulation? *Simulation Series*, 18(4):62–65, 1987.

[196] G. Pritschow and S. Rock. "Hardware-in-the-loop" simulation of machine tools. *Annals of the CIRP*, 53(1):295–598, 2004.

[197] A. Ganguli, A. Deraemaeker, M. Horodinca, and A. Preumont. Active damping of chatter in machine tools - Demonstration with a "Hardware-in-the-Loop" simulator. *Proceedings of the I Mech E, Part I - Journal of Systems and Control Engineering*, 219(5):359–369, 2005.

[198] S. Smith and D. Dvorak. Tool path strategies for high speed milling aluminium workpieces with thin webs. *Mechatronics*, 8:291–300, 1998.

[199] W. M. Sim, R. C. Dewes, and D. K. Aspinwall. An integrated approach to the high speed machining of moulds and dies involving both a knowledge-based system and a chatter detection and control system. *Proceedings of the I Mech E, Part B - Journal of Engineering Manufacture*, 216(1):1635–1646, 2002.

[200] David Michael Williams. *Numerical modelling of real-time substruture testing.* PhD thesis, Keble College, Oxford University, 2000.

[201] T. Horiuchi, M. Inoue, T. Konno, and Namita. Real-time hybrid experimental system with actuator delay compensation and its application to a piping system with energy absorber. *Earthquake Engineering and Structural Dynamics, 28(10):1121–1141, October 1999.*

[202] T. Horiuchi, M. Nakagawa, M. Sugano, and T. Konno. Development of a real-time hybrid experimental system with actuator delay compensation. In *Proceedings of the 11th World Conference on Earthquake Engineering, Acapulco*, page Paper 660. Oxford: Pergamon., 1996.

[203] M. I. Wallace, D. J. Wagg, and S. A. Neild. An adaptive polynomial based forward prediction algorithm for multi-actuator real-time dynamic substructuring. *Accepted for publication in Proceedings of the Royal Society of London*, 2005.

[204] D. P. Stoten, S. A. Neild, and D Drury. Dynamic substructuring via the adaptive MCS algorithm. In *Third World Conference on Structural Control, Como, Italy*, volume 2, pages 819–825, 2002.

[205] S. A. Neild, D. P. Stoten, D. Drury, and D. J. Wagg. Control issues relating to real-time substructuring experiments using a shaking table. *Earthquake Engineering and Structural Dynamics*, 34:1171–1192, 2005.

[206] D. P. Stoten. Fusion of kinetic data using composite filters. *Proceedings of the I Mech E - Part I - Journal of Systems and Control Engineering*, 215:483–497, 2001.

[207] S. A. Neild and D. P. Stoten. The error-based minimal control synthesis algorithm with integral action. *Proceedings of the I Mech E, Part I - Journal of Systems and Control Engineering*, 217(3):187–201, 2003.

[208] D. J. Wagg and D. P. Stoten. Substructuring of dynamic systems via the adaptive minimial control synthesis algorithm. *Earthquake Engineering and Structural Dynamics*, 30:865–877, 2001.